UNIVERSITÉ DE SHERBROOKE
Faculté de génie
Département de génie mécanique

# PRÉDICTION PAR TRANSFERT INVERSE DE L'ÉVOLUTION TEMPORELLE DU FRONT DE SOLIDIFICATION : APPLICATIONS AUX RÉACTEURS MÉTALLURGIQUES ET À LA CRYOCHIRURGIE

Thèse de doctorat
Spécialité : Génie mécanique

Mohamed HAFID

Jury : Marcel LACROIX (directeur)
Martin DÉSILETS
Mikhail SORIN
Louis GOSSELIN

Sherbrooke (Québec) Canada

Mai 2017

# RÉSUMÉ

Ce projet de recherche porte sur deux problématiques différentes, cependant, elles partagent les mêmes phénomènes physiques. Il s'agit de la prédiction inverse de l'évolution temporelle du front de solidification : (1) dans les réacteurs métallurgiques à haute température et (2) dans les tissus vivants pendant la cryochirurgie.

**Problématique #1 :** Afin de réduire l'érosion et l'agression chimique des parois internes de briques réfractaires par la matière en fusion au sein des réacteurs métallurgiques, on laisse croître par changement de phase solide/liquide une couche protectrice sur leur surface interne (Figure 1.**1**). Cette couche joue un rôle extrêmement important, car elle assure l'intégrité de l'installation et prolonge sa durée de vie. Toutefois, une couche protectrice trop épaisse réduit le volume utile de réacteur et diminue ainsi la production industrielle. Le défi, pour l'industriel, consiste alors à exploiter ces réacteurs tout en maintenant une couche dont l'épaisseur est optimale. L'environnement hostile qui règne au cœur du réacteur interdit toutefois les mesures directes. Les sondes qu'on y plonge sont détruites. Pour remédier à ce problème, l'industriel recourt à la simulation numérique et, plus récemment, à une approche par transfert inverse.

Cette thèse présente une procédure inverse de transfert de chaleur qui permet, à partir des mesures de température non invasives provenant d'un thermocouple situé dans les parois extérieures de briques, de prédire simultanément les paramètres thermiques inconnus ainsi que l'épaisseur de la couche protectrice au sein des réacteurs métallurgiques. La technique inverse repose sur la méthode de *Levenberg-Marquardt* (LMM) combinée avec la méthode de *Broyden* (BM).

**La Problématique #2** aborde quant à elle la cryochirurgie. C'est une technique récente, peu invasive, qui utilise le froid extrême pour détruire les tissus indésirables tels que les tumeurs (Figure 1.**8**). Elle s'adresse donc à des tumeurs internes et externes. L'objectif de la cryochirurgie est de détruire les tumeurs tout en minimisant les dommages des tissus sains adjacents. La fiabilité de cette technique dépend d'un certain nombre de paramètres thermiques tels que la température de la cryosonde, les propriétés thermiques des tissus, la durée de congélation, etc. Pour y parvenir, des méthodes expérimentales et numériques ont été développées. Cependant, chaque méthode a ses propres limites. En effet, le problème majeur est associé à la méconnaissance de certains paramètres thermiques, ce qui rend l’analyse de la transmission dans les tissus biologiques difficile. Pour pallier ces limites et améliorer la technique de cryochirurgie, une approche novatrice est retenue : il s’agit du transfert de chaleur inverse. À partir de mesures thermiques de températures provenant d’un thermocouple implanté dans la tumeur, cette approche permet de prédire les paramètres inconnus tels que la perfusion sanguine et, ensuite, de déterminer l’évolution temporelle de l’interface de congélation et la distribution de la température dans le tissu.

**Mots-clés :** Transfert de chaleur inverse, Méthode de *Levenberg-Marquardt*, Méthode de *Broyden*, Changement de phase, Réacteur métallurgique, Couche protectrice, Cryochirurgie, Interface de congélation.

# REMERCIEMENTS

Je remercie très chaleureusement mon directeur de recherche, professeur **Marcel LACROIX**, qui m'a constamment aidé, encouragé et guidé durant ces années. Je le remercie également pour sa confiance, sa disponibilité et son professionnalisme.

J'exprime tous mes remerciements à l'ensemble des membres du jury : Le professeur **Martin DÉSILETS**, le professeur **Mikhail SORIN** et le professeur **Louis GOSSELIN**, d'avoir accepté de juger ma thèse.
Mes remerciements vont particulièrement à mes parents, qui m'ont continuellement encouragé et soutenu tout au long de ces années. Sans vous rien n'aurait été possible. J'adresse des remerciements à mes frères et mes sœurs, qui m'ont beaucoup soutenu.

Je désire aussi remercier fortement le professeur **Sébastien PONCET** pour l'opportunité de l'article des coulis de glace que j'ai fait avec votre étudiante Senda TRABELSI. Merci Senda pour les dîners (couscous, chorba, bourek …).

Mes remerciements vont également à mes professeurs de l'Université Larbi Ben M'hidi OEB : Abdelbaki MAMERI, Tayeb OUKSEL, Mahfoudi CHAWKI, Athmane HARIZI, Bachir BENABBAS, Miloud GUEMINI, Ali BOUCHOUCHA, Berkani OUALID … qui m'ont fourni les outils en génie nécessaires à la réussite de mes études doctorales.

Mes remerciements s'adressent aussi à mes amis et collègues à l'Université de Sherbrooke qui m'ont apporté leur support intellectuel et moral pendant ces années. Merci à Christopher REDDICK, Mohamed KHENNICH, Charly KONE, Nidhal BOUSLAMA, Karim MASMOUDI, Imrane K. A. M., Mohsen ARIANA, Jean Paul L. F., Ahmed LAICHAOUI, Kamal Ben M., Abdelhakim LIMANE, Redha ESSELAMI, Rabah HAMMOUD, Mohammed CHERIF, Mohamed H., Marco BOUFFARD… Merci aussi à Marc LEBREUX pour les conseils de publication.

Je tiens également à exprimer mes vifs remerciements et reconnaissances envers mes amis à Montréal : Imad, Driss, Wail, Nadjib, Zaki, Djamel, Omar, Oussama, Athmane, Moussa, Moetazz, Kada, … Un grand merci pour leurs encouragements.

Ces remerciements ne seraient pas complets sans une pensée pour mes amis en Algérie : Moussa, Khaled, Raho, Aissa, El-hadj Marrouche, Nazim, Yacine, Youghourta, Ahmed, Fethi, Adel, Amar, Djmoui, houcine, les deux Oussama, Hamza, Karim, Imad….

Je souhaite remercier tout le membre du personnel de la faculté de génie, en particulier Jason GAUTHIER pour sa gentillesse et sa disponibilité.

Finalement, je remercie toutes les personnes ayant participé de près ou de loin dans l'élaboration de cette thèse.

Les travaux présentés dans cette thèse ont été financés par une bourse **CRSNG**, Le **C**onseil de **R**echerches en **S**ciences **N**aturelles et en **G**énie du **C**anada.

NSERC
CRSNG

# TABLE DES MATIÈRES

# LISTE DES FIGURES

# LISTE DES TABLEAUX

# 1. INTRODUCTION

## 1.1. Problématique #1 : Les réacteurs métallurgiques

### 1.1.1. Mise en contexte

Les réacteurs métallurgiques, tels que les fours à arc électrique et les cuves d'électrolyse, sont des fours de transformation qui nécessitent des puissances électriques élevées [1, 2]. La Figure 1.1 présente un schéma typique d'un four à arc électrique qui consiste à fondre et affiner les métaux tels que le minerai, la ferraille, la fonte brute et le verre. Les électrodes de haute tension (une seule électrode est présentée dans la Figure 1.1) déchargent leur courant électrique dans un bain de scories. La chaleur dissipée par effet Joule est nécessaire pour le processus de fusion. Après la réaction de fusion, le métal plus dense s'enfonce et s'accumule au fond du bain. Le chargement de minerai continu est réalisé par des ouvertures dans la voûte [3]. Le taraudage de laitier et de métal s'effectue à des intervalles réguliers à travers des perforations dans les parois latérales.

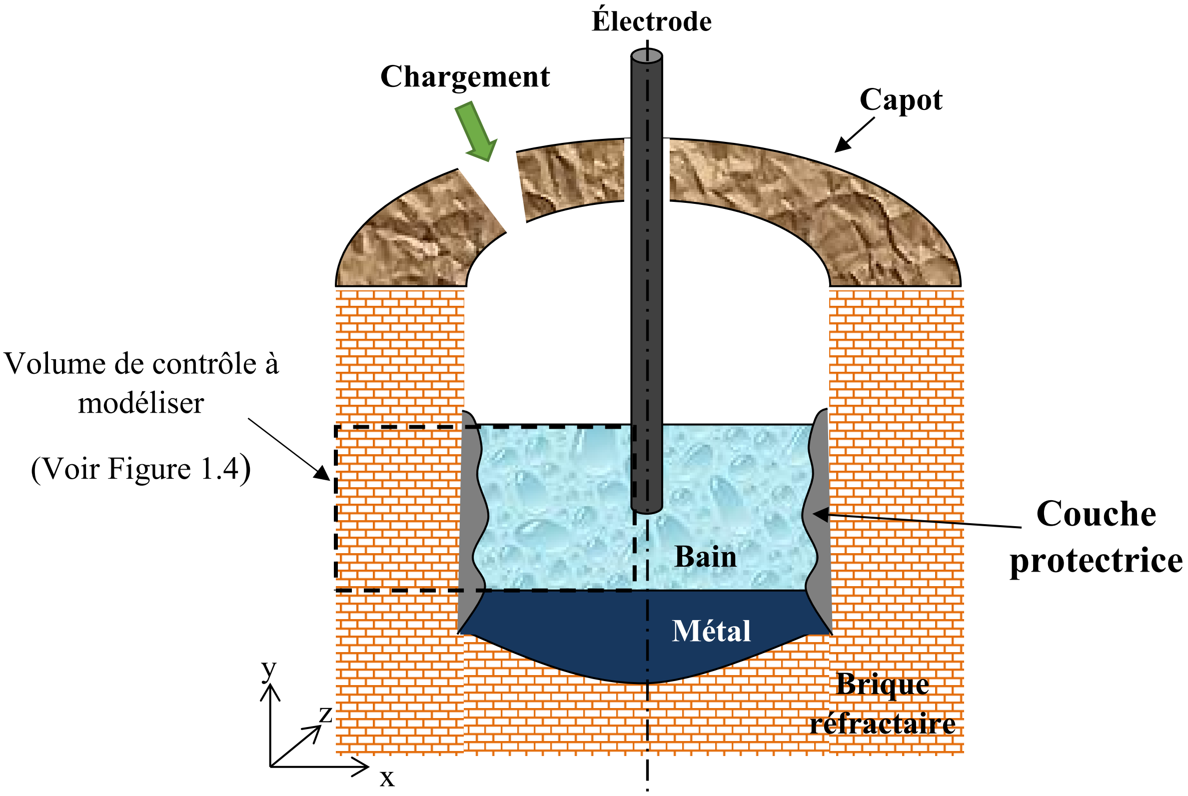

**Figure 1.1** Représentation schématique d'un four à arc électrique.

Figure 1.2 illustre une cuve d'électrolyse utilisée dans la production de l'aluminium à partir de l'alumine ($Al_2O_3$). L'alumine est dissoute dans le bain électrolytique qui est constitué principalement de cryolite[1] à haute température (entre 950 °C et 1 000) [4]. À l'aide de courant électrique de grande intensité qui circule entre l'anode et la cathode, l'aluminium est produit par la réduction de l'alumine dissoute [5]. Enfin, l'aluminium liquide qui s'accumule sur la cathode est extrait périodiquement par siphonage. Ce procédé est connu sous le nom de 'procédé de *Hall-Héroult*' [2].

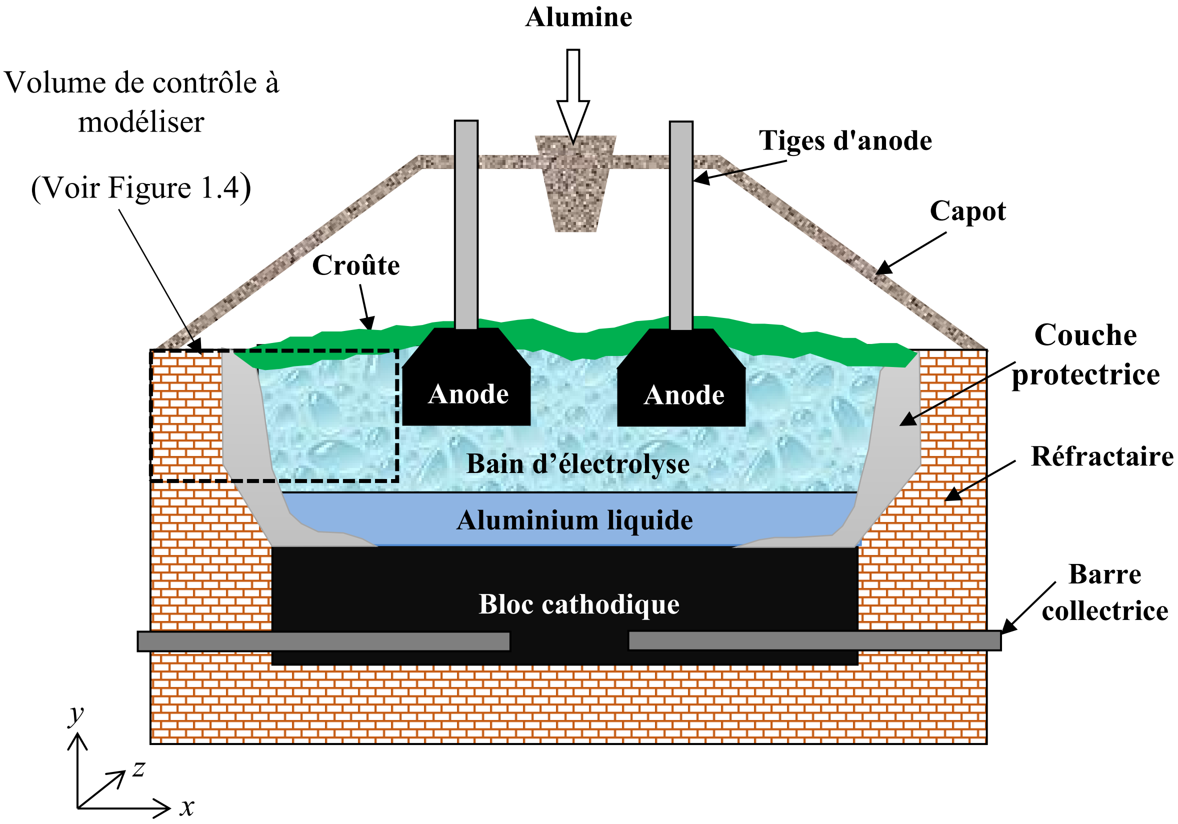

**Figure 1.2** Représentation schématique d'une cuve d'électrolyse.

À l'heure actuelle, l'industrie métallurgique représente l'un des consommateurs les plus gourmands en électricité. Par exemple en utilisant le procédé d'électrolyse Figure 1.2, il faut environ 13,5 à 14 MWh d'énergie électrique pour produire une tonne d'aluminium, ce

---

[1] Cryolite : Espèce minérale composée de fluorure double de sodium et d'aluminium, dont la formule chimique est $Na_3AlF_6$.

qui génère 2 à 3 tonnes de $CO_2$ [2]. En réalité, 40% à 50% de l’énergie électrique consommée par ces réacteurs est éventuellement perdue sous forme de chaleur i.e. la moitié de cette énergie sert réellement à la production [6]. À ce stade, l’innovation des réacteurs métallurgiques est primordiale notamment avec le problème de réchauffement climatique et l’augmentation des coûts énergétiques [7, 8].

Un phénomène fascinant de changement de phase solide/liquide qui se manifeste dans ces réacteurs métallurgiques est la formation d’une couche solide sur la surface intérieure des parois de briques réfractaires. Cette couche, appelée également revêtement protecteur ou encore gelée protectrice, se forme quand la matière en fusion entre en contact avec les parois internes du réacteur. Elle joue un rôle extrêmement important, car elle assure l’intégrité de l’installation et prolonge sa durée de vie [9, 10]. En effet, l'absence de cette couche laisse la matière en fusion en contact direct avec les parois internes de briques réfractaires, ce qui provoque le phénomène d’érosion-corrosion de ces parois [11]. Cette situation conduit à un vieillissement prématuré des réacteurs [9, 12].

La couche protectrice contribue également à l’efficacité énergétique des réacteurs en réduisant les pertes de chaleur au profit du milieu extérieur. En effet, l’absence de cette couche entraine, dans les cellules d’électrolyse, des courants électriques horizontaux indésirables, et par conséquent, l’efficacité énergétique de l’installation diminue [2, 13].

Toutefois, une couche trop épaisse réduit le volume utile du réacteur et diminue ainsi la production industrielle. Le défi, pour l’industriel, consiste alors à exploiter ces réacteurs en maintenant une couche dont l’épaisseur est optimale, c’est-à-dire une épaisseur qui protège les parois internes de briques réfractaires sans nuire à la production industrielle. Il est donc incontournable d’évaluer et de contrôler l’épaisseur de cette couche.

Cependant, il est très difficile, voire impossible, de mesurer en temps réel l’épaisseur de la couche protectrice. Actuellement, la méthode utilisée pour mesurer l’épaisseur de cette couche consiste à mesurer manuellement la variation de l’épaisseur en submergeant une sonde mécanique dans la matière en fusion (voir Figure 1.3) [14, 15].

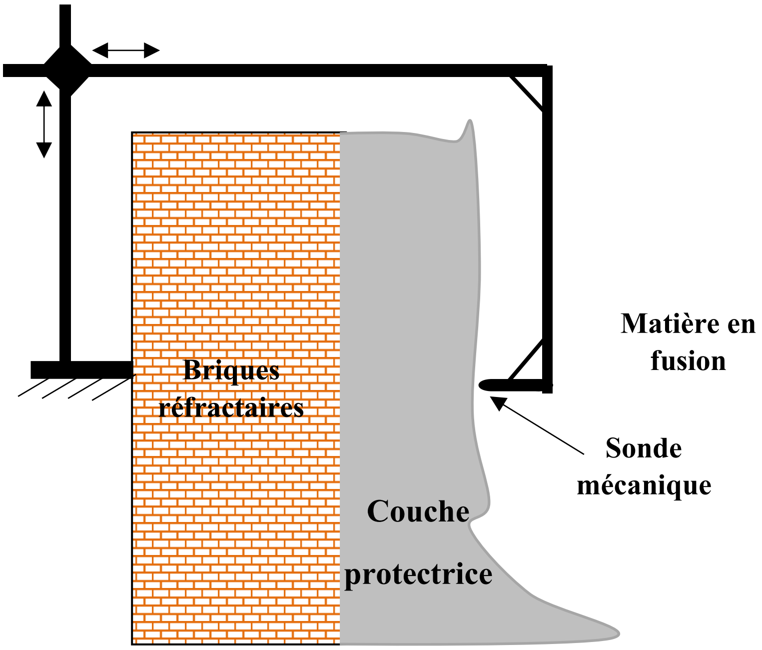

**Figure 1.3** Mesure de l'épaisseur du revêtement par une sonde mécanique.

Malheureusement, l'environnement hostile qui règne au cœur du réacteur interdit les mesures directes. Les sondes qu'on y plonge sont détruites. Les mesures faites sont souvent imprécises. De surcroît, cette méthode exige l'ouverture du capot du réacteur, ce qui augmente les pertes de chaleur et de masse au profit du milieu extérieur [16].

L'objectif principal de la présente problématique est de répondre à la question suivante : Comment serait-il possible de mesurer et prédire autrement l'épaisseur de cette couche protectrice au sein des réacteurs métallurgiques à haute température ?

### 1.1.2. Définition du projet de recherche

La première partie de la thèse vise à développer une méthode de mesure non-invasive (indirecte) pour prédire l'évolution temporelle du front de solidification de la couche protectrice au sein des réacteurs métallurgiques. La Figure 1.4 illustre le modèle direct du réacteur. La couche protectrice représente la phase solide du matériau à changement de phase (MCP). Dans ce modèle direct, toutes les propriétés thermo-physiques, la géométrie du domaine, les conditions initiales et aux limites sont bien connues. Le flux de chaleur $q''(t)$ imposé à la frontière droite représente la puissance thermique injectée au réacteur. L'autre frontière (la frontière gauche) représente le refroidissement par convection des parois externes du réacteur, dont la température du fluide de refroidissement est $T_\infty$ et le coefficient de transfert de chaleur $h_\infty$.

L'objectif de ce modèle consiste alors à calculer le champ transitoire de température $T(x,t)$ ainsi que l'évolution temporelle du front de solidification de la couche protectrice $E(t)$.

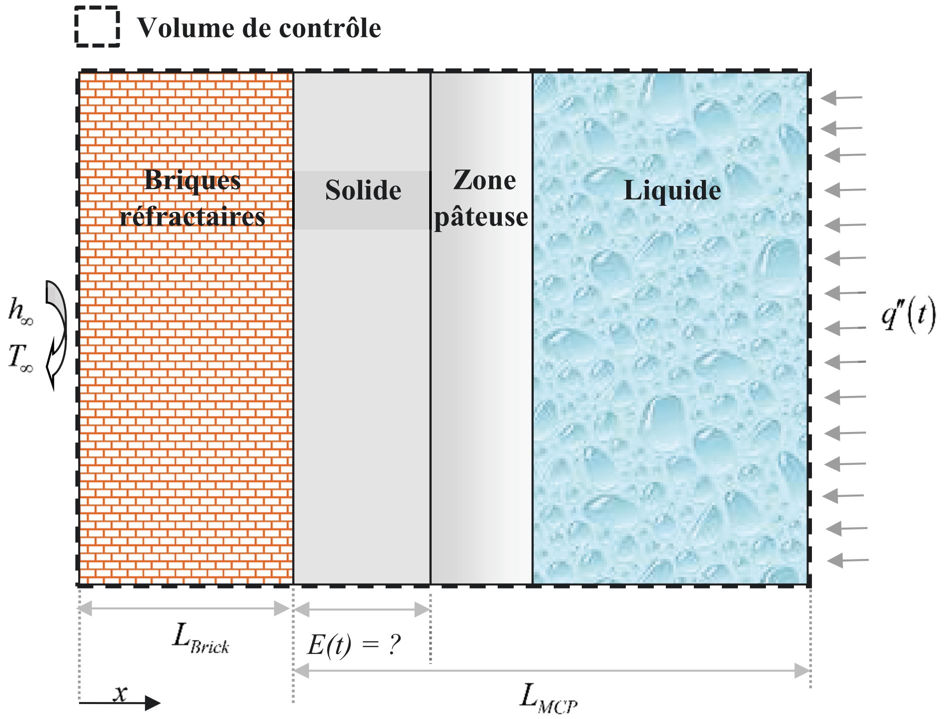

**Figure 1.4** Problème direct du réacteur. Tous les paramètres sont connus ; *E(t)* est prédit en discrétisant l'équation de conservation de l'énergie par la méthode des volumes finis.

Dans le modèle inverse certains paramètres thermiques tels que le flux de chaleur au centre du réacteur $q''(t)$, les conductivités thermiques du matériau à changement de phase (MCP) et le coefficient de transfert de chaleur $h_\infty$ sont inconnus (Figure 1.5). Pour prédire ces paramètres, on utilise de mesures thermiques $Y(x,t)$ provenant d'un capteur situé dans les parois extérieures de briques réfractaires. À partir de ces mesures minimalement invasives et de la méthode inverse basée sur l'algorithme de *Levenberg-Marquardt* (LM), les paramètres thermiques inconnus du réacteur peuvent être identifiés, et par conséquent, l'épaisseur de la couche de gelée peut être prédite en utilisant le modèle direct.

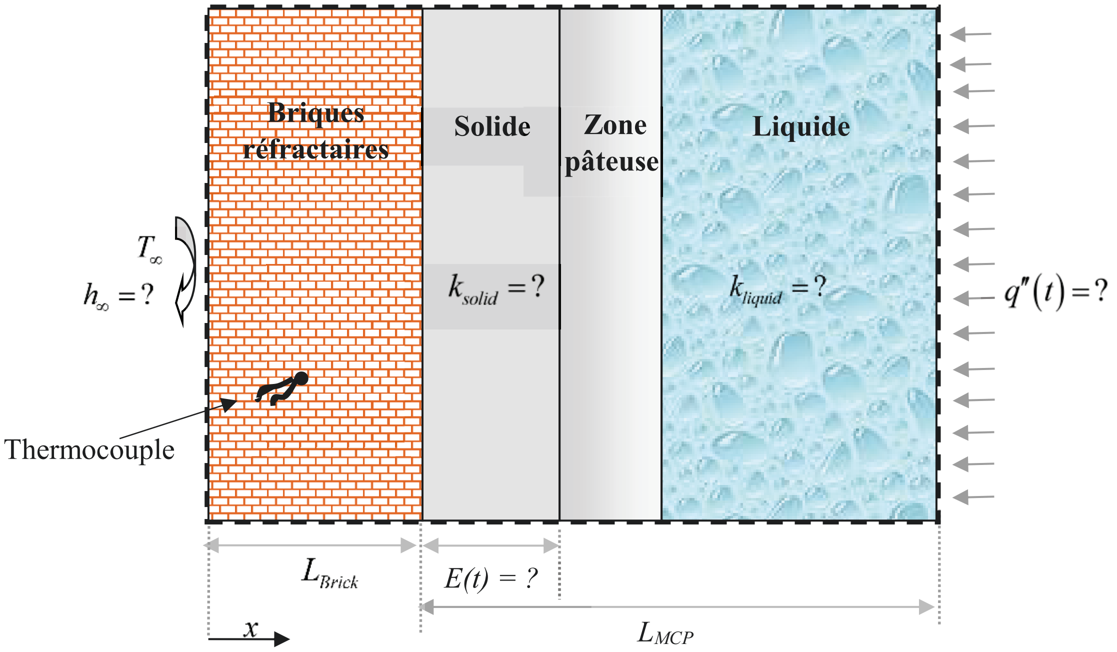

**Figure 1.5** Problème inverse du réacteur. $q''(t)$, $h_\infty$ et $k$ sont inconnus. Ils sont prédits à partir de mesures de température $Y(x,t)$ provenant de capteur situé dans la paroi de briques. Après avoir estimé ces paramètres inconnus, $E(t)$ est calculé en utilisant le modèle direct.

### 1.1.3. Objectifs du projet de recherche

Les objectifs principaux concernant cette problématique sont les suivants :

- ✓ Développer une méthode inverse pour prédire l'épaisseur de la couche protectrice à partir de mesures non-invasives de température provenant de capteurs situés dans les parois externes de réacteur ;
- ✓ Développer un modèle basé sur le transfert de chaleur inverse pour détecter le phénomène d'érosion au niveau des parois internes de briques réfractaires ;
- ✓ Prédire les propriétés thermo-physiques du matériau à changement de phase (MCP) et de brique réfractaire ;
- ✓ Prédire la résistance thermique de contact ($R_c$) entre le MCP et la brique réfractaire ;
- ✓ Prédire les paramètres polynomiaux de la conductivité thermique du MCP en fonction de la température.

Afin de concrétiser les objectifs principaux cités ci-dessus, des objectifs secondaires sont à déterminer

- ✓ Modéliser le réacteur métallurgique avec un modèle mathématique direct ;
- ✓ Modéliser le phénomène de changement de phase non-isotherme de la formation transitoire de la couche protectrice au sein des réacteurs métallurgiques ;
- ✓ Valider le modèle mathématique à l'aide de résultats issus de la littérature ;
- ✓ Minimiser le temps de calcul de la procédure inverse ;
- ✓ Étudier la performance, la robustesse et la stabilité de la méthode inverse.

### 1.1.4. Contributions originales

La procédure inverse de transfert de chaleur permettant d'estimer l'épaisseur de la couche protectrice au sein des réacteurs métallurgiques, a été abordée par plusieurs chercheurs à l'Université de Sherbrooke [17-20]. Dans tous ces travaux, les seules préoccupations soulevées étaient la prédiction du flux thermique au centre du réacteur et l'évolution temporelle de l'épaisseur de la couche protectrice.

Pour le présent projet de recherche, les contributions originales dans le domaine du transfert de chaleur inverse dans les réacteurs métallurgiques sont multiples et complémentaires :

- ✓ Développer une méthode inverse qui permet de détecter et de calculer l'épaisseur érodée de parois internes de briques réfractaires sans recourir aux modèles complexes de l'érosion ;
- ✓ Appliquer une procédure inverse qui combine la méthode de *Levenberg-Marquardt* et la méthode de *Broyden* afin de prédire l'épaisseur de couche protectrice dans les réacteurs métallurgiques ;
- ✓ Prédire la résistance thermique de contact $R_c$ entre le *MCP* et la brique réfractaire ;
- ✓ Prédire la conductivité thermique dans la phase solide et liquide de MCP, et dans la brique réfractaire ;
- ✓ Prédire les paramètres polynomiaux de la conductivité thermique de MCP qui dépendent de la température.

La Figure 1.6 montre les différents domaines impliqués dans la première problématique.

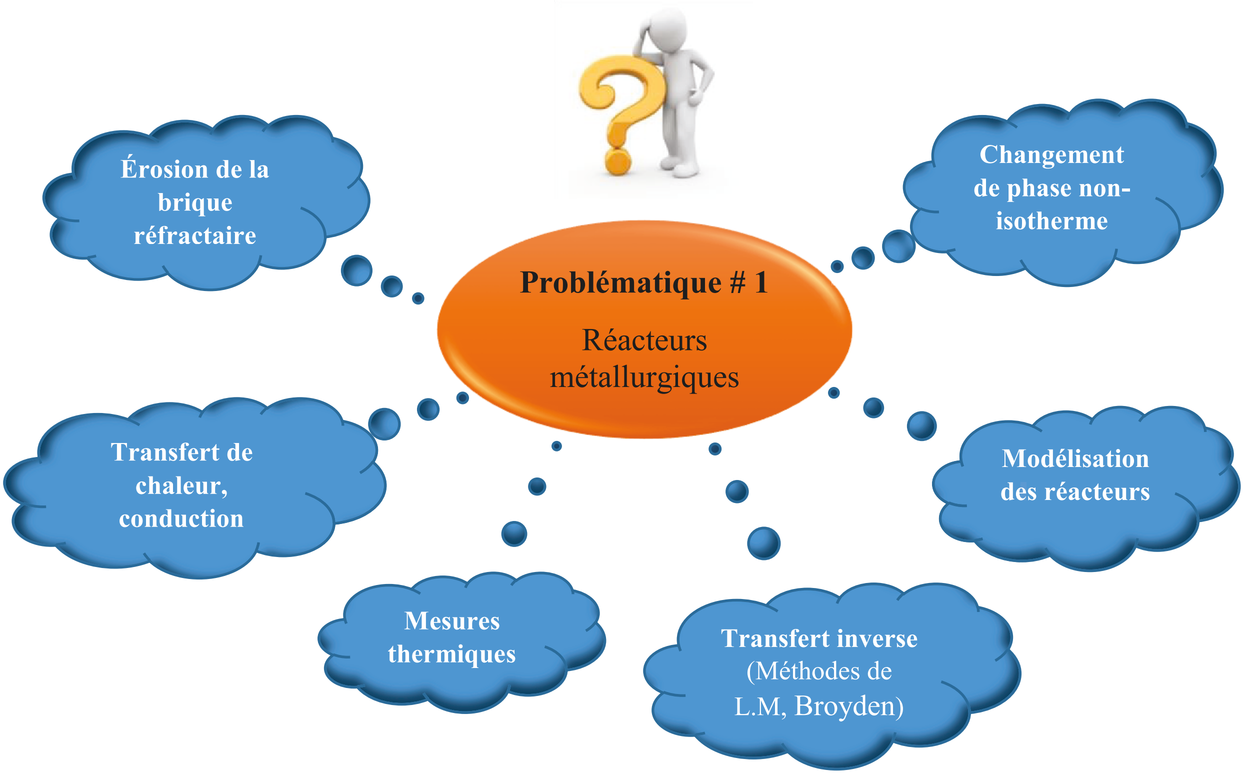

**Figure 1.6** Combinaison des domaines impliqués dans la problématique #1 (Réacteurs).

## 1.2. Problématique #2 : La cryochirurgie

### 1.2.1. Mise en contexte

Selon Statistique Canada, en 2016, environ deux Canadiens sur cinq développeront un cancer au cours de leur vie, et environ un Canadien sur quatre en décédera (Figure 1.7). En effet, on estime que 202 400 Canadiens développeront un cancer et que 78 800 en décéderont [21].

D'autre part, d'autres statistiques canadiennes en 2012, ont révélé que le cancer est la principale cause de décès chez les enfants de moins de 15 ans. De plus, d'après les années potentielles de vie perdues (APVP)[2], le cancer représente la principale cause de décès prématuré [22].

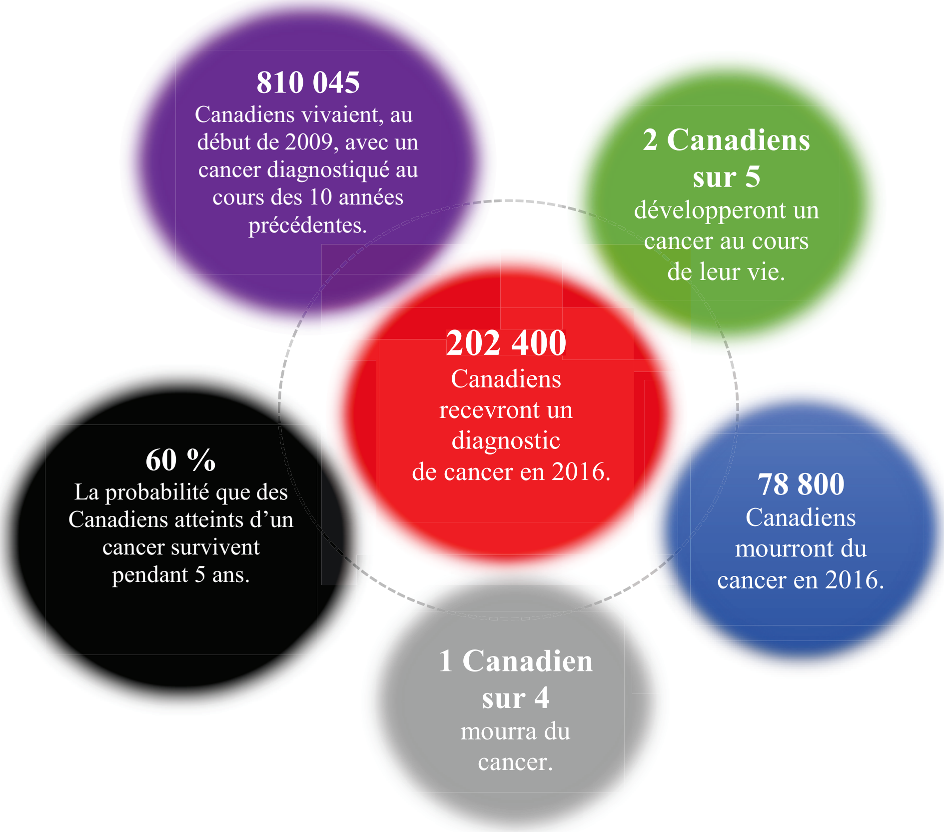

**Figure 1.7** Statistiques canadiennes sur le cancer (2016) [21].

---

[2] Les Années Potentielles de Vie Perdues (APVP) correspondent au nombre d'années de vie « perdues » lorsqu'une personne meurt « prématurément » de n'importe quelle cause avant l'âge de 75 ans.

Dans un contexte où le cancer continue de gagner du terrain au Canada, les chercheurs se retrouvent face à des défis de taille. Pour y faire face, souvent les médecins utilisent la chirurgie classique ou la chimiothérapie. Mais, ces méthodes présentent parfois des complications comme l'infection, l'hémorragie et les douleurs, etc. Pour pallier à ces complications, une alternative prometteuse moins invasive et moins agressive a été développée. Il s’agit de **la cryochirurgie**.

La cryochirurgie appelée aussi cryothérapie, est une technique destinée à la destruction des tissus indésirables (tumeurs et cancers) par le froid extrême. Elle est connue depuis les années 1970 [23]. Elle peut s’appliquer dans le traitement des tumeurs internes comme celles des os, du rein et de la prostate ou des tumeurs externes comme celles de la peau. Cette technique est privilégiée par rapport à la chirurgie traditionnelle. Elle minimise les douleurs et les cicatrices.

L’intervention chirurgicale se déroule sous anesthésie locale et sous le contrôle de scanner. La première étape consiste, à l’aide de l’imagerie médicale, à introduire une cryosonde[3] pour atteindre la tumeur. La cryosonde est alimentée par un fluide cryogénique (l’azote liquide ou l'argon) qui s’y décompresse en créant de très basses températures. Par conséquent, une boule de glace se forme autour de la cryosonde qui va englober la tumeur et la détruire (Figure 1.8).

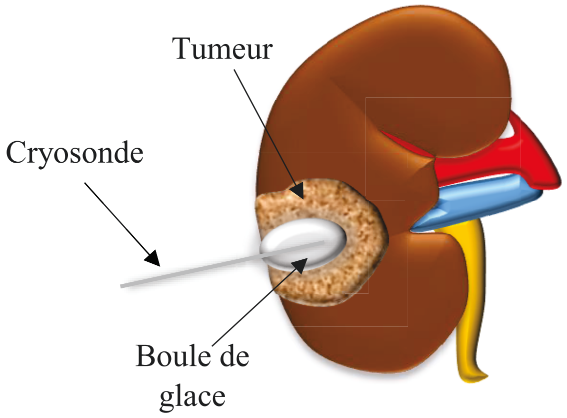

**Figure 1.8** Traitement de tumeur du rein par la cryochirurgie.

---

[3] Cryosonde : Petit appareil cylindrique creux dans lequel un fluide cryogénique s’écoule avec un débit contrôlé.

La destruction cellulaire se fait par plusieurs processus biologiques tels que la cristallisation de l'eau cellulaire, l'éclatement des cellules par le phénomène d'osmose[4], et d'ischémie[5] par le biais de thromboses vasculaires [24]. Les cellules détruites sont ensuite attaquées et éliminées par le système immunitaire [25].

Afin d'appliquer la cryochirurgie d'une façon sûre et efficace i.e. assurer la destruction complète des tissus indésirables et réduire les dommages des tissus sains, il est indispensable d'évaluer la température dans ces tissus.

Le contrôle de la cryochirurgie s'effectue habituellement avec des techniques expérimentales telles que l'imagerie médicale [26] et l'implantation des thermocouples dans le tissu [27]. Malheureusement, toutes ces techniques sont incapables de fournir la distribution entière de la température dans le tissu. De ce fait, les spécialistes de la cryothérapie doivent recourir à la modélisation numérique [28, 29]. Toutefois, cette dernière souffre de problèmes associés à la méconnaissance des paramètres thermiques des tissus indésirables (tumeur) comme, entre autres, la perfusion sanguine et la conductivité thermique. En effet, ces paramètres peuvent varier d'un patient à l'autre selon différents facteurs tels que l'état d'avancement de la tumeur, l'âge et la masse corporelle.

Il est possible de déterminer expérimentalement ces paramètres thermiques. Des techniques expérimentales ont été considérées, telles que les sondes à cuivre dans la mesure de la conductivité thermique de tissu [30] et la technique *Laser Doppler Imaging* (LDI)[6] dans la détermination de la perfusion sanguine [31]. Cependant, hélas, ces techniques présentent des complications. Elles nécessitent des équipements sophistiqués, et ne peuvent pas être utilisées pendant la chirurgie [32, 33].

L'objectif principal de la présente étude est de répondre à la question suivante : Comment serait-il possible de modéliser la cryothérapie avec des paramètres inconnus ?

---

[4] Osmose : Phénomène de diffusion de la matière entre deux milieux de concentrations différentes séparés par une paroi semi-imperméable.

[5] Ischémie : Insuffisance de la circulation sanguine dans un organe du corps entrainant une baisse de l'oxygénation, voire l'arrêt de sa fonction.

[6] LDI : Technique non invasive utilisée pour mesurer la perfusion sanguine en appliquant le principe du Doppler.

### 1.2.2. Définition du projet de recherche

L'objectif de la deuxième partie de la thèse est de développer une méthode basée sur le transfert de chaleur inverse pour prédire les paramètres thermiques inconnus des tissus (perfusion sanguine et conductivité thermique) et, par la suite, évaluer l'évolution temporelle de l'interface de congélation et le champ de température dans les tissus. Tel que mentionné à la première problématique, dans le modèle direct (Figure 1.9), toutes les propriétés thermo-physiques, la géométrie du domaine, les conditions initiales et aux limites sont connues. Le champ de température *T(x,t)* ainsi que l'évolution temporelle de l'interface de congélation *s(t)*, sont calculés en résolvant numériquement l'équation de *Pennes* avec changement de phase.

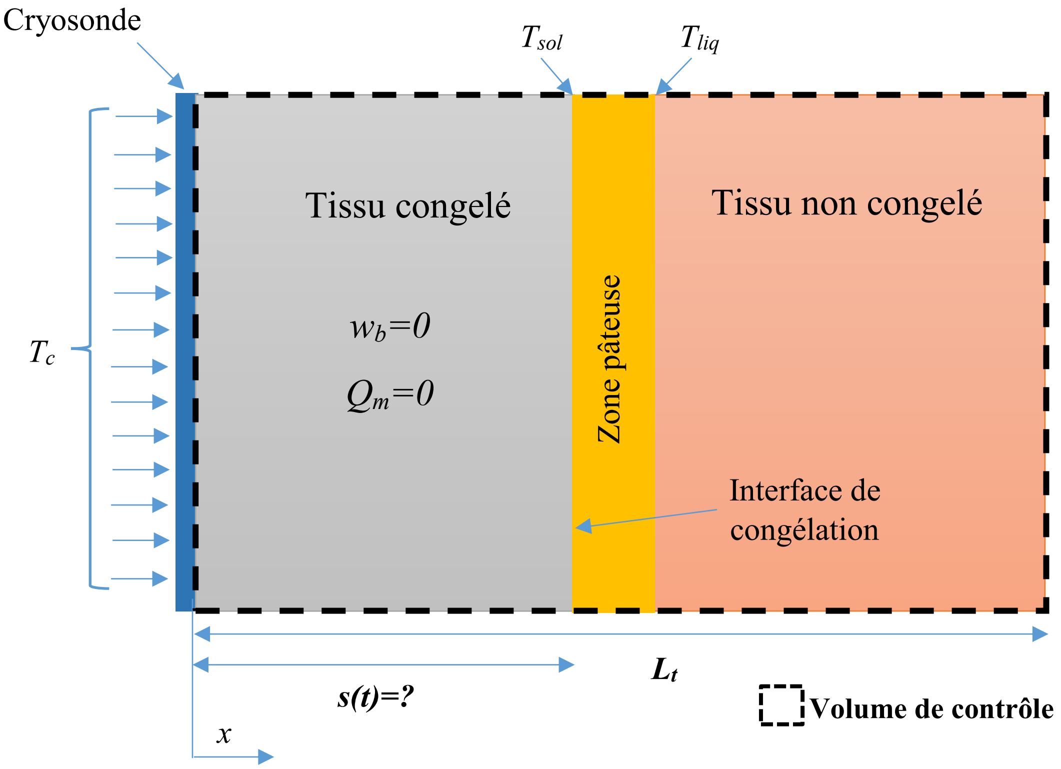

**Figure 1.9** Problème direct de cryothérapie : tous les paramètres sont connus ; *T(x,t)* et *s(t)* sont prédits en discrétisant l'équation de *Pennes* par la méthode des volumes finis.

Dans le problème inverse (Figure 1.10) certains paramètres comme le taux de perfusion sanguine et la conductivité thermique des tissus sont inconnus. À partir de mesures des températures *Y(x,t)* provenant d'un thermocouple implanté dans le tissu indésirable (tumeur), l'algorithme de la méthode inverse peut prédire ces paramètres inconnus et, par la suite calculer le champ de température *T(x,t)* et l'évolution temporelle de l'interface de congélation *s(t)*.

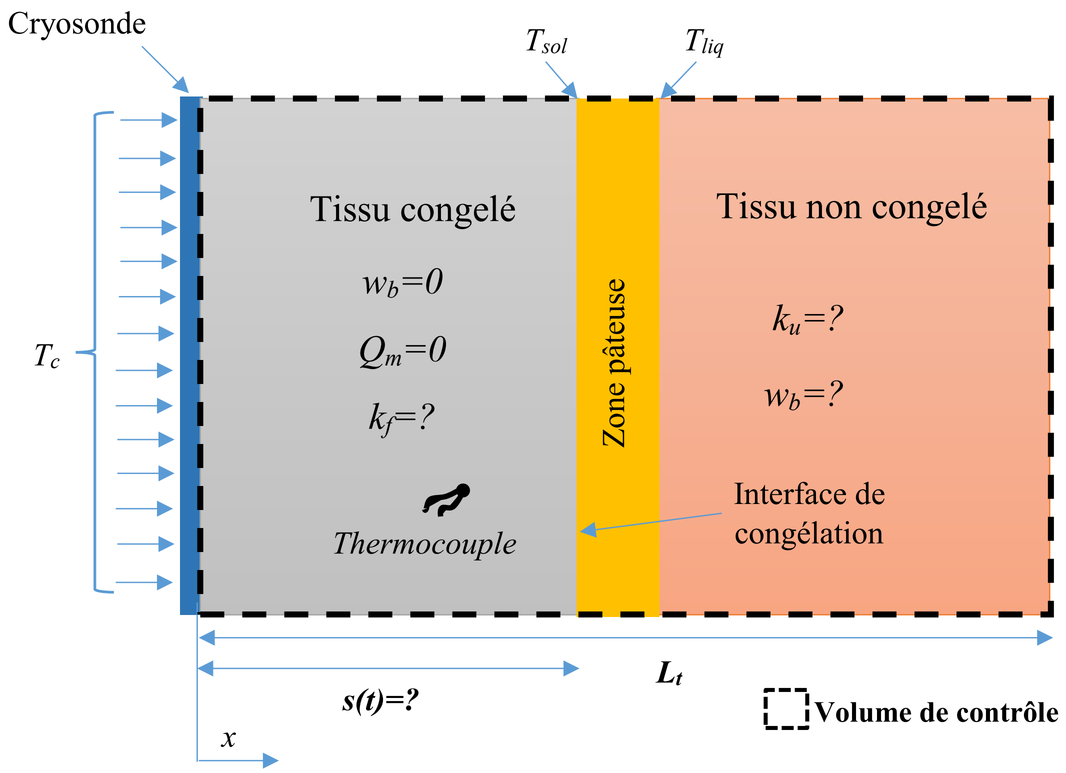

**Figure 1.10** Problème inverse : *k et* $w_b$ sont inconnus. Ils sont prédits à partir de mesures de température *Y(x,t)* provenant de thermocouple. Après avoir estimé ces paramètres inconnus, *T(x,t)* et *s(t)* prouvent être calculés en utilisant le modèle direct.

### 1.2.3. Objectifs du projet de recherche

Les objectifs principaux de la présente problématique sont les suivants :

- ✓ Développer une nouvelle technique basée sur le transfert de chaleur inverse pour procurer une meilleure application de la cryochirurgie ;
- ✓ Prédire les paramètres thermiques (la conductivité thermique et la perfusion sanguine) d'un tissu lors du processus de congélation ;

- ✓ Déterminer le champ de température *T(x,t)* et l'évolution temporelle de l'interface de congélation *s(t)* dans un tissu vivant.

Pour y parvenir, les objectifs secondaires sont les suivants :

- ✓ Modéliser le transfert de chaleur dans les tissus biologiques (modèle de *Pennes*) ;
- ✓ Modéliser le phénomène de changement de phase non-isotherme pendant la cryochirurgie ;
- ✓ Valider le modèle mathématique avec les résultats disponibles dans la littérature ;
- ✓ Minimiser le temps de calcul de la procédure inverse ;
- ✓ Vérifier la performance, la robustesse et la stabilité de la méthode inverse pour les différents scénarios envisagés.

### 1.2.4. Contributions originales

La présente problématique porte sur le transfert de chaleur inverse en cryochirurgie. L'originalité est que cette méthode sera appliquée au contrôle et à l'amélioration de la cryochirurgie.

Les contributions originales spécifiques de la présente problématique sont multiples :

- ✓ Développer une méthode inverse qui permet de prédire les paramètres thermiques inconnus d'un tissu biologique durant la cryochirurgie ;
- ✓ Appliquer un algorithme inverse qui combine la méthode de *Levenberg-Marquardt* et la méthode de *Broyden* en cryochirurgie ;
- ✓ Développer une méthode inverse comme alternative à l'imagerie médicale afin de suivre le mouvement de l'interface de congélation pendant la cryochirurgie.

La Figure 1.11 montre les différents domaines impliqués afin de répondre à cette problématique

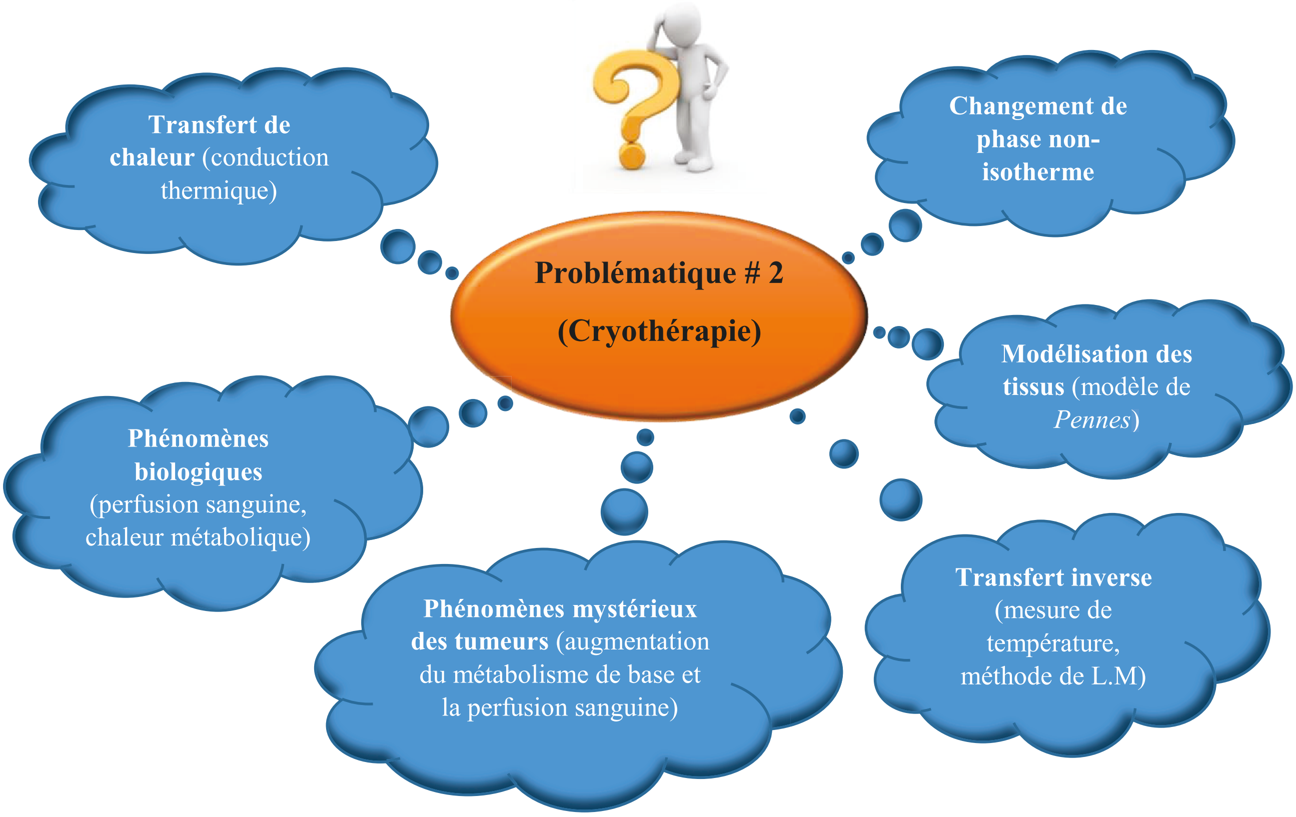

**Figure 1.11** Combinaison des domaines découlant de la problématique #2 (cryothérapie).

## 1.3. Plan du document

Ce document est divisé systématiquement en deux parties. La première partie est consacrée au transfert inverse dans les réacteurs métallurgiques. La deuxième partie présente, quant à elle, le transfert inverse en cryothérapie.

À la suite de l'introduction (chapitre#1), une revue de la littérature du problème de revêtement protecteur dans les réacteurs métallurgiques et du problème de traitement des tumeurs par cryothérapie est effectuée. Elle est dédiée à la synthèse des travaux antérieurs afin de justifier les objectifs du projet.

Le troisième chapitre inclut le premier article publié dans le journal *Applied Thermal Engineering*, dans lequel un procédé de transfert thermique inverse est présenté pour prédire les caractéristiques thermiques (le flux de chaleur et les conductivités thermiques de (1) la paroi de briques, (2) la couche protectrice et (3) la matière en fusion) et l'épaisseur de la couche protectrice d'un réacteur métallurgique [34].

Le quatrième chapitre expose le deuxième article publié dans le journal *Applied Thermal Engineering*. Cet article aborde le problème d'érosion de la paroi interne de la brique réfractaire d'un four de fusion. En outre, l'influence de plusieurs paramètres thermiques tels que la résistance thermique de contact entre le MCP et la brique réfractaire, la conductivité thermique et le nombre de *Biot* sur les prédiction inverse est examinée [35].

Le chapitre 5 comprend un troisième article soumis au journal *Applied Thermal Engineering*. Cet article met en lumière la prédiction des paramètres polynomiaux de la conductivité thermique de MCP qui dépendent de la température [36].

Le chapitre 6, quant à lui, élucide une application à la cryothérapie. Un quatrième article soumis au *Journal of Thermal Biology* dévoile une nouvelle technique basée sur le transfert de chaleur inverse pour contrôler et améliorer la cryochirurgie [37].

Enfin, le dernier chapitre présente les conclusions de cette thèse et les travaux futurs.

Deux autres articles qui expliquent davantage la première problématique sont présentés en annexe. Le premier article en annexe consiste à prédire en premier lieu les caractéristiques thermiques (flux de chaleur et conductivités thermiques de briques réfractaires et de MCP) puis l'évolution temporelle de la couche protectrice dans un réacteur métallurgique à haute température [38] (Annexe A). Le deuxième article en annexe développe quant à lui le phénomène d'érosion dans les fours de fusion [39] (Annexe B).
Enfin, un autre article sur le transfert inverse en cryothérapie est présenté dans l'annexe C. Cet article prédit la chaleur métabolique et la perfusion sanguine dans les tumeurs [40].

Ce premier chapitre est clos avec un schéma de la relation entre les deux problématiques abordées dans la thèse (Figure 1.12).

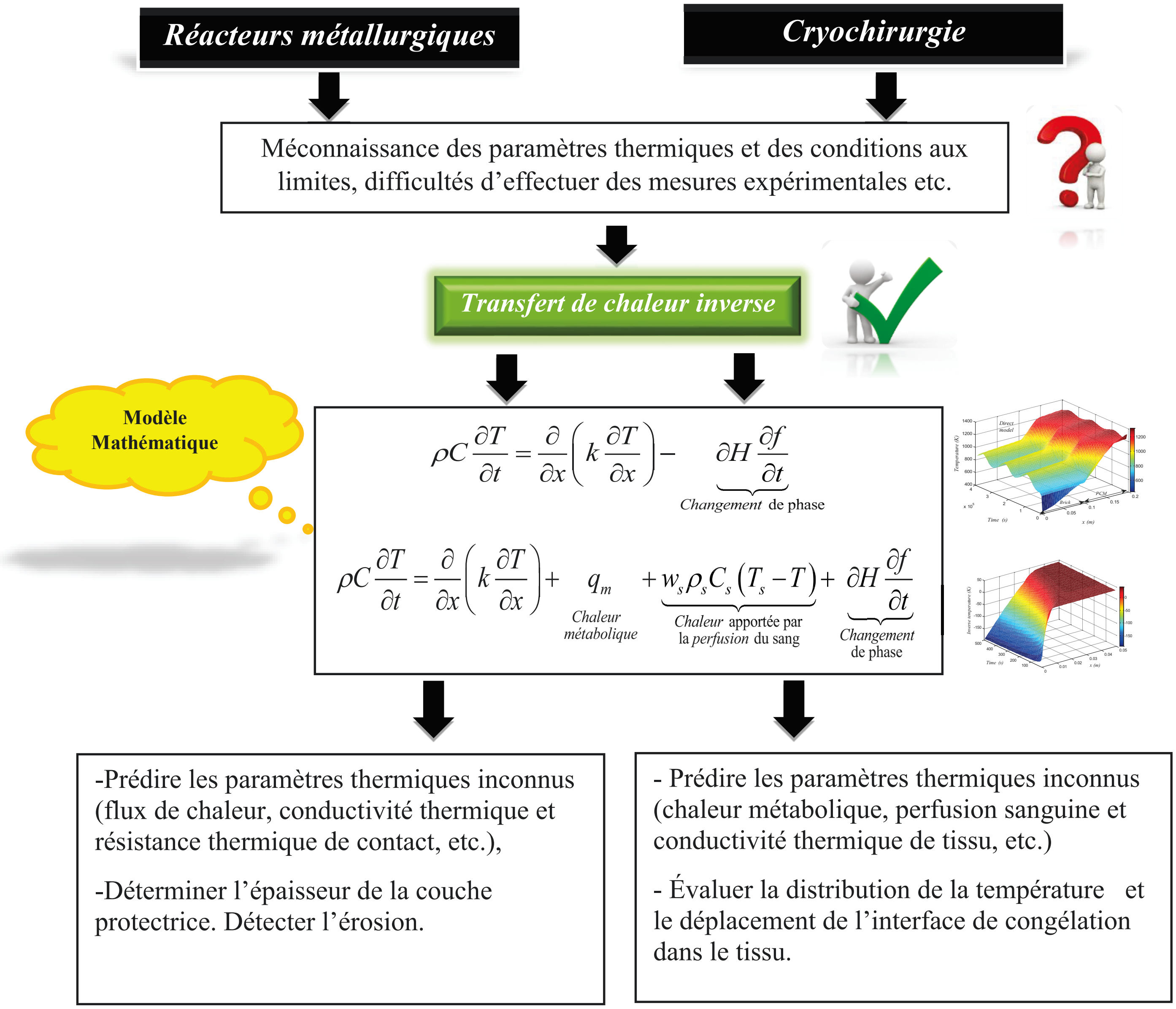

Méconnaissance des paramètres thermiques et des conditions aux limites, difficultés d'effectuer des mesures expérimentales etc.

$$\rho C\frac{\partial T}{\partial t}=\frac{\partial}{\partial x}\left(k\frac{\partial T}{\partial x}\right)-\underbrace{\partial H\frac{\partial f}{\partial t}}_{\textit{Changement}\text{ de phase}}$$

$$\rho C\frac{\partial T}{\partial t}=\frac{\partial}{\partial x}\left(k\frac{\partial T}{\partial x}\right)+\underset{\substack{\textit{Chaleur}\\ \textit{métabolique}}}{q_m}+\underbrace{w_s\rho_s C_s\left(T_s-T\right)}_{\substack{\textit{Chaleur}\text{ apportée par}\\ \text{la }\textit{perfusion}\text{ du sang}}}+\underbrace{\partial H\frac{\partial f}{\partial t}}_{\substack{\textit{Changement}\\ \text{de phase}}}$$

-Prédire les paramètres thermiques inconnus (flux de chaleur, conductivité thermique et résistance thermique de contact, etc.),

-Déterminer l'épaisseur de la couche protectrice. Détecter l'érosion.

- Prédire les paramètres thermiques inconnus (chaleur métabolique, perfusion sanguine et conductivité thermique de tissu, etc.)

- Évaluer la distribution de la température et le déplacement de l'interface de congélation dans le tissu.

**Figure 1.12** Aperçu du projet de recherche.

# 2. ÉTAT DE L'ART

## 2.1. Problématique #1 : Les réacteurs métallurgiques

Comme nous avons vu dans l'introduction, la couche protectrice dans les réacteurs métallurgiques à haute température joue un rôle extrêmement important. De nombreux travaux numériques et expérimentaux ont été faits afin d'évaluer l'épaisseur de cette couche.

### 2.1.1. Mesure directe de l'épaisseur de la couche protectrice

Dans le secteur métallurgique, la mesure de l'épaisseur de la couche protectrice au sein d'un réacteur métallurgique se fait habituellement à l'aide d'une sonde mécanique plongée dans le réacteur [10, 41-44]. Plus récemment, J. Floquet et al. ont effectué une mesure ultrasonore de l'épaisseur du front de solidification dans les réacteurs métallurgiques [45] et [46]. Dans le même contexte, C. Bertrand et al. ont pu déceler la formation d'un gel au sein d'un réacteur métallurgique cylindrique à l'aide d'une caméra thermique [47, 20].

Bien que cette technique (méthode de mesure invasive) soit capable de mesurer l'épaisseur de la couche protectrice, elle est rarement utilisée par l'industriel. En effet, les constatations de ces travaux expérimentaux révèlent que cette technique de mesure compte beaucoup d'inconvénients, entre autres, (1) c'est une méthode coûteuse. Etant donné que le bain de matières en fusion est un milieu très hostile, il endommage et parfois détruit les instruments de mesure (sonde mécanique, thermocouple, etc.) ; (2) Elle nécessite l'ouverture du réacteur, ce qui augmente les pertes de chaleur et les émissions de gaz nocifs ; (3) Elle demande aussi du personnel qualifié. Par conséquent, cette technique s'avère ni pratique, ni idéale pour mesurer l'épaisseur de la couche protectrice. De ce fait, l'industrie préconise la modélisation numérique.

### 2.1.2. Modélisation du front de solidification

Le tableau suivant montre quelques études numériques concernant la modélisation du front de solidification dans les réacteurs métallurgique :

**Tableau 2.1** Modélisation numérique de la couche protectrice (gelée).

| Auteurs | Modèles mathématiques |
|---|---|
| M. Dupuis, et al., 2004 [48], M. Dupuis & V. Bojarevics, 2005 [49] | 3D, régime stationnaire. |
| M. Dupuis & V. Bojarevics, 2006 [50] | 1D et 3D, régime stationnaire. |
| W. E. Haupin, 1971 [51],<br>J. Thonstad & S. Rolseth, 1983 [52] | 1D, régime stationnaire (résistances thermiques). |
| V. Gusberti, et al., 2012 [53],<br>E. Haugland, et al., 2003 [54]. | 3D, régime stationnaire (résistances thermiques). |
| M. P. Taylor, et al., 1983 [9] | 1D, régime instationnaire. |
| J. N. Bruggeman & D. J. Danka, 1990 [55] | 2D, régime stationnaire. |
| M. V. Romerio, et al., 2005 [56] | 3D, régime instationnaire. |

Dans le Tableau 2.1, la plupart des études portent sur des simulations numériques en régime stationnaire. Les auteurs n'ont pas pris en considération l'effet transitoire dans l'équation de la chaleur. De ce fait, ils n'ont pas pu prédire la variation temporelle de l'épaisseur de la couche protectrice. Pour ceux qui ont mené des simulations en régime transitoire, le modèle incluant le changement de phase donne de meilleures prédictions [9], [56]. Récemment, S. Kalaiselvam et al. ont réalisé une étude comparative pour prédire également le front de solidification dans un réacteur cylindrique. Ils ont affirmé que la modélisation du changement de phase est primordiale [57].

Pour pouvoir simuler le transfert de chaleur dans un réacteur métallurgique, il est nécessaire de connaitre la géométrie du domaine, les conditions initiales et les conditions aux limites (Problème direct). Or, dans l'industrie métallurgique, où les milieux sont extrêmement hostiles, ces conditions sont délicates à déterminer, voire inconnues. En effet, le flux de chaleur à l'intérieur du réacteur est inconnu. Sa valeur est influencée par plusieurs paramètres tels que l'état d'anode, la distance entre l'anode et la cathode, la quantité de minerai ajoutée, etc. [2]. De ce fait, il est très difficile de prédire l'évolution temporelle de l'épaisseur de la couche protectrice $E(t)$ qui protège les parois internes de briques. Pour répondre à ce problème, quelques auteurs ont suggéré de recourir au transfert inverse [17, 58-66].

### 2.1.3. Modélisation de la couche protectrice par le transfert inverse

Le tableau suivant montre quelques études sur la prédiction du flux de chaleur et l'épaisseur de la couche protectrice au sein des réacteurs à haute température, en utilisant des techniques inverses :

**Tableau 2.2** Prédiction de l'épaisseur de la couche protectrice par le transfert inverse.

| Auteurs | Type de capteur | Méthode inverse | Modèle Mathématique |
|---|---|---|---|
| O. Tadrari et M. Lacroix 2006 [17] | Thermocouple | Gradient conjugué | 1D, transitoire |
| M. LeBreux, et al. [58, 59, 61-63] | Capteur de flux de chaleur | Filtre de Kalman | 1D, transitoire |
| M. LeBreux, et al. [60] | Capteur de flux de chaleur | Filtre de Kalman | 2D, transitoire |
| M. A. Marois, et al. 2012 [64] | Thermocouple | Gradient conjugué | 1D, transitoire |
| M. A. Marois, et al., 2011 [65] | Thermocouple | Gradient conjugué | 1D, transitoire |
| M. A. Marois, et al., 2011 [66] | Thermocouple | *Levenberg-Marquardt* | 2D, transitoire |
| C. Bertrand, et al. 2013 [47] | Caméra infrarouge | Gradient conjugué | 2D, transitoire |
| C. K. Chen & C. R. Su , 2008 [67] | Thermocouple | Surfaces virtuelles | 2D, stationnaire |
| C. R. Su & C. K. Chen, 2007 [68] | Thermocouple | Surfaces virtuelles | 2D, stationnaire |
| S. Wang, et al., 2015 [69] | Thermocouple | Gradient conjugué | 2D, stationnaire |
| C. R. Su, et al., 2009 [70] | Thermocouple | Surfaces virtuelles | 2D, stationnaire |
| H. Farzan, et al., 2016 [71] | Capteur de flux de chaleur | Gradient conjugué | 2D, transitoire |

Il convient de noter que la majorité des travaux listés au Tableau 2.2 ont été développés avec l'unique objectif de prédire le flux de chaleur dans le réacteur $q''(t)$ et l'évolution temporelle du front de solidification de la couche protectrice $E(t)$. En 2006, Tadrari et Lacroix ont développé une méthode inverse pour prédire l'évolution temporelle de l'épaisseur de la couche protectrice dans un four à arc électrique [17]. Le modèle numérique est basé sur l'équation de la chaleur en régime transitoire. Le changement de phase du front de solidification de la couche protectrice est traité par la méthode enthalpique. La procédure inverse repose quant à elle sur la méthode du gradient conjugué avec l'équation adjointe. Cette étude révèle deux issues importantes. La première issue est que la prédiction de l'épaisseur de la couche protectrice demeure précise, même avec un signal bruité. La seconde issue concerne l'effet de la position du thermocouple. Les auteurs ont déduit que la position de thermocouple n'a pas d'influence significative sur la prédiction de l'épaisseur de la couche protectrice.

Une série d'études réalisée par LeBreux et al. aborde la même configuration [58-63]. Cette série d'études s'intéresse, dans une cellule d'électrolyse d'alumine, à l'évolution temporelle de l'épaisseur de gelée (couche protectrice). Mais, dans celle-ci, un filtre de Kalman a été développé pour réduire le temps de calcul nécessaire à la mise en oeuvre de la méthode inverse, et par conséquent, prédire l'épaisseur de gelée en temps réel. Les auteurs ont montré que le capteur de flux de chaleur donne de meilleures prédictions, et améliore la stabilité de la méthode inverse. Bien évidemment, un capteur de flux est composé d'une série de thermocouples.

Dans le même contexte, Marois et al. ont adopté la méthode du gradient conjugué avec un problème adjoint pour prédire l'épaisseur de gelée [64, 65]. Dans une autre étude effectuée sur une configuration 2D [66], les auteurs ont utilisé une approche pseudo 2D basée sur la technique de *Levenberg-Marquardt* pour résoudre le problème inverse. Ils ont constaté que cette approche permet de réduire le temps de calcul associé à la mise en oeuvre de la méthode inverse.

D'autre part, Bertrand et al. ont étudié le changement de phase de la cryolite dans un dispositif expérimental (réacteur à petite échelle) en utilisant un nouveau capteur de mesure [47]. Celui-ci est composé d'une caméra infrarouge couplée à un modèle inverse basé sur la méthode du gradient conjugué avec un problème adjoint.

D'autres études ont considéré la méthode des surfaces virtuelles pour prédire les géométries internes du four [67, 68, 70]. Néanmoins, cette méthode est en régime stationnaire. Elle ne permet pas de prédire la variation temporelle de l'épaisseur de la couche protectrice. Concernant le type de capteur utilisé dans la plupart des travaux listés dans le Tableau 2.2, les mesures thermiques ont été effectuées à l'aide des capteurs de température. Bien entendu, l'utilisation d'un capteur de température est simple, facile et bon marché [72, 73].

### 2.1.4. Effet de la température sur les propriétés thermiques

Dans les réacteurs métallurgiques à haute température, les propriétés physiques des matériaux sont affectées par la température. Wikström et al. ont mené une étude expérimentale et numérique pour déterminer le flux de chaleur au sein d'un four [74]. Ils ont conclu qu'il est primordial de prendre en compte l'effet de la température sur les propriétés thermiques (conductivité thermique et chaleur spécifique). Une autre étude similaire réalisée par Bideau et al. a confirmé cette conclusion [75].

Plusieurs méthodes inverses ont été développées pour estimer les propriétés thermiques qui dépendent de la température [76-79]. Généralement, la solution aux problèmes inverses en régime transitoire est complexe, en particulier si le problème implique le processus de changement de phase. Elle se complique davantage lorsque les mesures sont affectées en présence du bruit[7] [80]. En effet, l'estimation des propriétés thermiques qui dépendent de la température par des méthodes inverses est un défi.

### 2.1.5. Érosion dans les réacteurs

Un autre problème qui se manifeste dans les réacteurs métallurgiques à haute température est l'érosion de la paroi interne de la brique réfractaire. Ce phénomène se produit lorsque la couche protectrice de gelée est perdue et, par conséquent, la paroi interne de la brique devient soudainement exposée aux matières en fusion [81]. L'érosion du mur de brique est un processus lent et insidieux qui peut éventuellement conduire à la destruction de l'installation [82]. Le Tableau 2.3 montre quelques travaux associés à ce phénomène :

**Tableau 2.3** Études sur l'érosion dans les réacteurs.

| Auteurs | Méthodes menées |
|---|---|
| Wu, et al. [83] | *Boundary Element Method* (BEM) |
| Zhang, et al. [84], Chang, et al. [85] | 3D (CFD) |
| Guzmán, et al. [86], Li, et al. [87], Crudu, et al. [88], Kaur, et al. [89] | Études expérimentales |

---

[7] Bruit : Ensemble de perturbations de toute origine et de toute nature venant se superposer à un signal.

L’évaluation expérimentale et numérique s’avère donc très difficile pour détecter l’érosion à cause des hautes températures et de la variété des phénomènes physiques qui interviennent (transfert de chaleur et de masse, réactions chimiques, etc.). En effet, l’érosion de surfaces de briques dépend de plusieurs paramètres : la nature du matériau de la brique réfractaire, l`intensité du courant (température), la pression de fonctionnement, la nature des liquides et des gaz engagés dans les procédés mécaniques (contact, frottement, usure) etc. [90-92]. Cela, hélas, ne permet pas une description des phénomènes à partir de lois élémentaires, et c’est la raison pour laquelle on dénombre peu d’études à ce sujet dans la littérature technique.

## 2.2. Problématique #2 : La cryochirurgie

Tel qu’il a été discerné dans l’introduction, le suivi de l’interface de congélation est extrêmement important, afin d’appliquer la cryothérapie d’une manière efficace. Récemment, avec les progrès des techniques d'imagerie médicale, telles l’IRM (Imagerie par Résonance magnétique), l'échographie, les rayons X (Tableau 2.4), le recours à la cryothérapie est devenu abordable.

**Tableau 2.4** Techniques pour suivre l’interface de congélation au cours de la cryothérapie.

| Auteurs | Techniques de mesure de l’interface de congélation |
|---|---|
| G. Onik, et al. 1984 [93] | Sonde à ultrason |
| J. C. Saliken, et al., 1996 [94]<br>G. A. Sandison, et al., 1998 [95] | X-ray, CT[8] (Computed Tomography) |
| B. L. Daniel, et al., 1999 [26] | Imagerie par résonance magnétique (IRM) |

Le problème majeur de ces techniques d'imagerie médicale (Tableau 2.4) est qu’elles sont incapables de prédire l'emplacement exact des isothermes. Elles aident seulement à visualiser l'interface de la boule de glace englobant la tumeur (Figure 1.8). En effet, la limite de l'interface de la boule de glace est observable pour une température allant de -1 à -3 (°C). Alors que la température de destruction de certaines cellules comme les cellules épidermiques, peut descendre en dessous de -30 (°C). Effectivement, la cryosensibilité

---

[8] CT : Technique d'imagerie médicale basée sur l'absorption des rayons X par les tissus. Elle permet de visualiser des images transversales des tissus.

varie d’une cellule à une autre. De ce fait, l’évaluation de la température dans le tissu sain et tumoral est importante dans le processus de la cryochirurgie.
Pour s'attaquer au problème, et assurer un suivi en ligne de la température tissulaire pendant la congélation, des thermocouples sont utilisés. Ces derniers sont introduits dans le tissu sain et tumoral [27, 96-98].

Malheureusement, ces techniques comportent aussi des inconvénients, entre autres, (1) il est risqué d’implanter des thermocouples dans certains types de tissus tels que les tissus oculaires, osseux et nerveux, [99, 100]; (2) il est difficile de connaitre l'emplacement exact et le positionnement de ces thermocouples [98] ; (3) l’infection et l’hémorragie interne sont des complications possibles lors de l’implantation des thermocouples au niveau des tissus sains [100].
Pour éviter ces complications, on recourt à la modélisation numérique. Celle-ci est devenue un outil intéressant.

### 2.2.1. Modélisation de l’interface de congélation dans les tissus biologiques

Le transfert de chaleur dans les tissus biologiques est un processus complexe, car il implique une combinaison de plusieurs phénomènes thermiques tels que la conduction thermique, la convection, la perfusion du sang, et la production de chaleur métabolique. Au fil des années, plusieurs modèles mathématiques ont été développés pour décrire le transfert de chaleur à l'intérieur des tissus biologiques vivants. Ces modèles ont été largement utilisés dans l'analyse de la cryochirurgie et l'hyperthermie dans le traitement du cancer, la chirurgie au laser, la cryoconservation, le confort thermique et de nombreuses autres applications. Parmi ces modèles, on peut citer les modèles de : *Wulff* (1974), Klinger (1974), *Chen-Holmes* (1980), *Weinbaum-Jiji-Lemons* (1984) et *Pennes* (1948). [101] .

Le modèle de *Pennes* est le modèle le plus simple. Il a été introduit en 1948 par *Harry Pennes* pour la prédiction du transfert de chaleur dans l'avant-bras humain. Ce modèle a été largement utilisé par de nombreux chercheurs pour l'analyse des phénomènes de transfert de chaleur dans les tissus biologiques. Il décrit l'effet de la perfusion sanguine (débit sanguin) ainsi que la production de chaleur métabolique sur le transfert de chaleur dans les tissus vivants [101-103].

L'équation de *Pennes* pour un tissu vivant en une dimension est donnée par l'expression suivante

$$\rho C\frac{\partial T}{\partial t}=\frac{\partial}{\partial x}\left(k\frac{\partial T}{\partial x}\right)+q_m+\underbrace{w_s\rho_s C_s\left(T_s-T\right)}_{\textit{Chaleur}\ \text{apportée par la}\ \textit{perfusion}\ \text{du sang}} \tag{2.1}$$

Où

$$\begin{cases} T:\text{Température locale de tissu}\ (^\circ\text{C}) \\ T_s:\text{Température du sang artériel}\ (^\circ\text{C}) \\ w_s:\ \text{Taux de perfusion}\ (ml/s\ ml) \\ q_m:\ \text{Chaleur métabolique}\ (W/m^3) \\ \rho_s:\ \text{Densité du sang}\ (\text{kg}/\text{m}^3) \end{cases}$$

Le Tableau 2.5 montre quelques travaux portant sur la modélisation de l'interface de congélation, en utilisant le modèle de *Pennes*.

**Tableau 2.5** Modélisation de l'interface de congélation.

| Auteurs | Type de tumeur |
|---|---|
| J. Bastacky & B. Rubinsky, 1992 [104] | Tumeur du poumon |
| K. J. Chua, et al., 2007 [29] | Tumeur du foie |
| J. Zhang, et al., 2005 [105] | Cancer de la prostate |
| S. Kumar & V. K. Katiyar, 2007 [106] | Cancer du poumon |

J. Bastacky & B. Rubinsky ont déterminé les profils de température et l'évolution temporelle de l'interface de congélation dans un tissu pulmonaire sain qui contient une tumeur. Ils ont constaté que le déplacement de l'interface de congélation s'accélère brusquement à la transition entre la tumeur et le poumon sain (à cause de la grande différence de densité du tissu pulmonaire sain et du tissu tumoral) [104].

Un autre modèle numérique a été développé par K. J. Chua et al. pour étudier la vitesse de destruction cellulaire dans une tumeur du foie soumise à la cryochirurgie gel-dégel. L'équation de *Pennes* en régime transitoire a été discrétisée à l'aide de la méthode des volumes finis. Cette étude montre que l'utilisation de cycles de gel-dégel a le potentiel pour améliorer la destruction cellulaire dans les tissus cancéreux [29].

D’autre part, dans un processus de congélation de cancer de la prostate, J. Zhang et al. ont constaté que la circulation sanguine et la chaleur métabolique jouent un rôle important dans l’étude de la cryothérapie [105].

### 2.2.2. Influence de la perfusion sanguine et de la chaleur métabolique sur la cryothérapie

Dans les problèmes thermiques avec changement de phase, la génération de chaleur joue un rôle capital. En effet, la cryochirurgie est l'un des exemples qui implique la congélation des tissus biologique où la chaleur est produite par le métabolisme et la perfusion sanguine. Celles-ci ont fait l’objet de plusieurs travaux.

**Tableau 2.6** Études de l’influence de la perfusion sanguine et de la chaleur métabolique sur la cryothérapie.

| Auteurs | Paramètres étudiés | Méthode du calcul |
|---|---|---|
| R. Magleby, et al., 2008 [107] | Perfusion sanguine | CFD, 2D axisymétrique |
| Y. Rabin & A. Shitzer, 1998 [108] | Perfusion sanguine et chaleur métabolique | Différences finies, 3D |
| G. Zhao, et al., 2007 [109] | Perfusion sanguine et chaleur métabolique | Éléments finis, 2D axisymétrique |
| S. Singh & S. Kumar, 2013 [110] | Chaleur métabolique | 1D, analytique (*Quasi steady approximation*) |
| R. I. Andrushkiw, 1990 [111] | Perfusion sanguine et Chaleur métabolique | Différences finies |

R. Magleby et al. ont montré l’effet de la perfusion sanguine sur la cryothérapie au sein d’un tissu tumoral de poumon et de foie. Ils ont trouvé que le temps nécessaire pour geler ces tissus est variable en fonction de la nature du tissu ainsi que le taux de perfusion sanguine adopté [107].

Quant à l’influence de la chaleur métabolique, S. Singh & S. Kumar ont déterminé les profils de température et la position de l’interface de congélation durant la congélation

d’un tissu biologique. Ils ont montré que la vitesse de l’interface de congélation ralentit avec l'augmentation de la production de chaleur métabolique [110].
(G. Zhao et al.) et (Y. Rabin & A. Shitzer) ont démontré que les deux paramètres qui dominent le comportement des tissus sont la perfusion sanguine et la chaleur métabolique. Ils augmentent la difficulté de congélation du tissu pendant la cryochirurgie [108, 109].

Dans le cadre du traitement thermique par rayonnement électromagnétique, P. K. Gupta et al. ont utilisé trois modèles numériques (symétrie cartésienne, axisymétrique, et coordonnées sphériques) pour évaluer les champs de température dans un tissu biologique. Ils ont constaté que la température de la peau, la conductivité thermique et la perfusion sanguine ont une influence considérable sur le champ de température [112]. Une autre étude menée par P. K. Gupta et al. a permis de constater que les conditions aux limites et la chaleur interne du tissu (perfusion sanguine et chaleur métabolique) doivent être bien connues [113].

Le flux sanguin (perfusion sanguine) est une partie très décisive dans les fonctions vitales. Il joue un rôle capital dans la régulation de la température corporelle. En effet, 50 à 80 % de flux de chaleur dans le tissu est transporté dans le tissu par le flux sanguin [114]. Par conséquent, la connaissance de ce paramètre thermique est indispensable. Plusieurs techniques expérimentales ont été utilisées pour déterminer ce paramètre. À titre d’exemple, le Tableau 2.7 montre quelques techniques expérimentales pour mesurer la perfusion sanguine.

**Tableau 2.7** Techniques expérimentales pour mesurer la perfusion sanguine**.**

| Auteurs | Techniques de mesure |
|---|---|
| G. Delhomme, et al., 1992 [115] | Thermal Diffusion Probe (TDP) |
| C. Svedman, et al., 1998 [116] | Laser Doppler Flowmetry (LDF) |
| H. R. Schelbert, 2000 [33] | Positron Emission Tomography (PET) |

Toutes ces techniques expérimentales ont fait leurs preuves. Néanmoins, elles présentent des difficultés, entre autres, elles nécessitent des équipements sophistiqués et elles ne peuvent pas être utilisées pendant l’intervention chirurgicale. Par conséquent, on doit recourir, une autre fois, à la modélisation numérique. Mais, cette fois-ci, on utilisera une nouvelle approche basée sur le transfert de chaleur inverse.

### 2.2.3. Méthode inverse appliquée aux tissus biologiques

La méthode inverse a été également appliquée dans la détermination des propriétés thermiques de tissus biologiques :

**Tableau 2.8** Études sur le transfert de chaleur inverse.

| Auteurs | Paramètres estimés | Méthodes inverses menées |
|---|---|---|
| J. Iljaž & L. Škerget, 2014 [117] | La perfusion du sang | *Levenberg-Marquardt* |
| P. L. Ricketts, et al., 2008 [118] | La perfusion du sang | Alternating Direction Implicit (ADI) |
| Z. S. Deng & J. Liu, 2000 [119] | La perfusion du sang | DRBEM (the dual reciprocity boundary element method) |
| K. Das & S. C. Mishra, 2014 [120]<br>K. Das, et al., 2013 [121]<br>P. W. Partridge & L. C. Wrobel, 2007 [122] | La taille et la position de la tumeur | Algorithme génétique |
| K. Das & S. C. Mishra, 2015 [123] | La taille et la position de la tumeur | Curve fitting method |
| C. H. Huang & C. Y. Huang, 2007 [124] | Conductivité thermique et chaleur spécifique | *Levenberg-Marquardt* |
| A. Jalali, et al., 2014 [125] | Source de chaleur externe *Q(t)* :( hyperthermie) et le coefficient de transfert de chaleur *h(t)* | Gradient conjugué |

En utilisant la méthode de *Levenberg-Marquardt*, et à l'aide des mesures thermiques (températures), (J. Iljaž & L. Škerget) ont trouvé la clé pour la détermination de la perfusion artérielle d'un tissu biologique [117].

Une autre étude d'optimisation a été réalisée par P. L. Ricketts et al.. Dans cette étude, une combinaison est effectuée entre une étude expérimentale et numérique afin de développer un système de mesure de la perfusion sanguine au foie du rat [118].

Dans une série de travaux, toujours en utilisant le transfert de chaleur inverse, K. Das et al. ont pu estimer la taille et la position d'une tumeur à l'aide de mesures de température prises à la surface de la peau [120, 121, 123]. En effet, les paramètres thermiques des tissus biologiques comme la perfusion sanguine sont variables d'une personne à une autre. Ils varient en fonction de l'âge, du sexe, de la corpulence, du poids, de la taille et de l'état d'avancement de la tumeur, ainsi que du fonctionnement de la thyroïde[9]. La détermination de ces paramètres est davantage compliquée par la présence de tumeurs dont la croissance demeure énigmatique : division cellulaire aléatoire, dérèglement hormonal, dyspnée[10], etc. De surcroît, les paramètres thermiques des tumeurs diffèrent fréquemment de ceux des tissus sains [106].

Bref, il est difficile, voire impossible, d'énoncer une règle générale pour le calcul de ces paramètres thermiques chez les êtres humains. De ce fait, une grande incertitude s'installe dans le choix de ces paramètres.

Revenons sur la problématique de la cryothérapie. Afin d'appliquer celle-ci d'une façon convenable et efficace, il faut connaitre ces paramètres thermiques (perfusion sanguine, conductivité thermique, etc.). Or, dans toutes les études citées précédemment, aucune tentative n'a été faite pour estimer les paramètres thermiques au cours de la cryothérapie.
Le but de la présente étude est de remédier à cette situation en recourant au transfert de chaleur inverse.

---

[9] Thyroïde : Petite glande située dans le cou, en arrière de la pomme d'Adam.

[10] La dyspnée est une difficulté respiratoire.

# 3. PRÉDICTION INVERSE DES CARACTÉRISTIQUES THERMIQUES D’UN RÉACTEUR MÉTALLURGIQUE

## Avant-propos

**Auteurs et affiliation :**

**M. Hafid** : Étudiant au doctorat, Université de Sherbrooke, Faculté de génie, Département de génie mécanique.

**M. Lacroix** : Professeur, Université de Sherbrooke, Faculté de génie, Département de génie mécanique.

**Date d’acceptation :** 13 Juillet 2016

**État de l’acceptation :** Version finale publiée

**Revue :** Applied Thermal Engineering

**Référence :** [34]

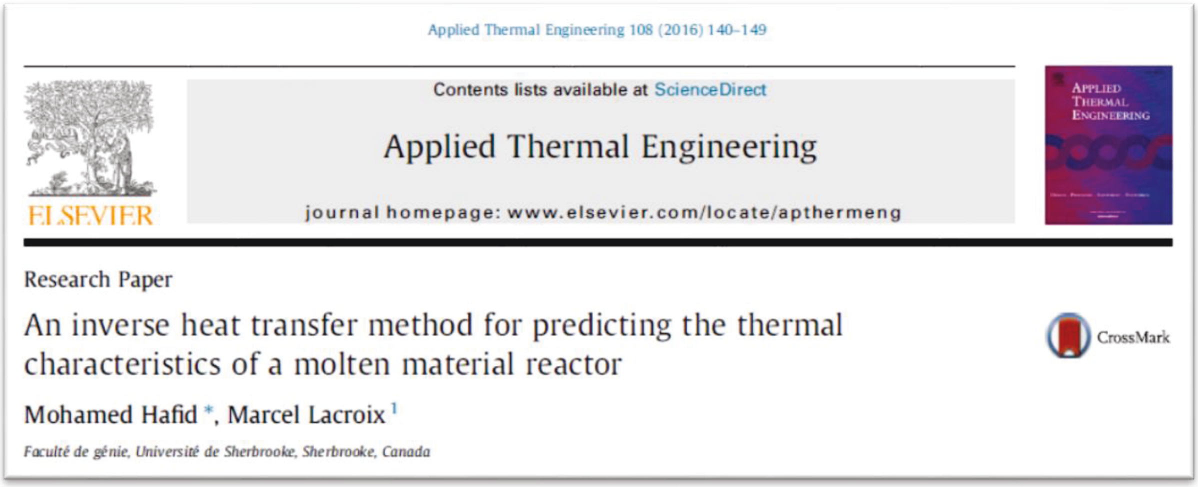

Applied Thermal Engineering 108 (2016) 140–149

Contents lists available at ScienceDirect

Applied Thermal Engineering

journal homepage: www.elsevier.com/locate/apthermeng

Research Paper

An inverse heat transfer method for predicting the thermal characteristics of a molten material reactor

Mohamed Hafid *, Marcel Lacroix [1]

*Faculté de génie, Université de Sherbrooke, Sherbrooke, Canada*

## Titre français

Méthode inverse de transfert thermique pour prédire les caractéristiques thermiques d'un réacteur métallurgique.

## Résumé français

Une procédure inverse de transfert thermique pour prédire la variation temporelle de l'épaisseur du revêtement protecteur qui recouvre les parois internes de briques réfractaires d'un réacteur métallurgique est présentée. La méthode inverse prédit simultanément la conductivité thermique de la paroi de la brique réfractaire, la conductivité thermique du revêtement protecteur, la conductivité thermique de la matière en fusion et le flux thermique à l’intérieur du réacteur. La méthode inverse repose sur la méthode de *Levenberg-Marquardt* (LMM) combinée à la méthode de *Broyden* (BM). L'effet (1) de l’initialisation des paramètres polynomiaux inconnus, (2) du bruit sur les données de températures enregistrées, (3) de l'emplacement de capteurs de température dans le mur de briques et (4) du nombre des températures enregistrées sur les prédictions inverse est étudié. Des recommandations concernant l'installation et le fonctionnement des capteurs de température sont énoncées.

## Mots clés

Transfert de chaleur inverse, Matériau à changement de phase, Méthode enthalpique, Méthode de *Levenberg-Marquardt*, Méthode de *Broyden*, Réacteur, Épaisseur du revêtement protecteur.

# Title

An Inverse Heat Transfer Method for Predicting the Thermal Characteristics of a Molten Material Reactor.

# Abstract

An inverse heat transfer procedure is presented for predicting the time-varying thickness of the protective bank that covers the lining of the refractory brick walls of a molten material reactor. The inverse method predicts simultaneously influential thermo-physical properties of the reactor such as the thermal conductivity of the refractory brick wall, the thermal conductivity of the solid and of the liquid layers of the phase change material, and the time-varying reactor heat load. The inverse method rests on the *Levenberg-Marquardt* Method (LMM) combined with the *Broyden* method (BM). The effect (1) of the initial guesses for the unknown LMM polynomial parameters, (2) of the noise on the recorded temperature data, (3) of the location of the temperature sensors embedded into the brick wall and (4) of the number of recorded temperature data on the inverse predictions is investigated. Recommendations are then made concerning the installation and the operation of the temperature sensors.

# Keywords

Inverse heat transfer, phase change material, enthalpy method, *Levenberg–Marquardt* method, *Broyden* method, reactor, bank thickness.

# Nomenclature

| | |
|---|---|
| $C_p$ | specific heat [J/kgK] |
| $dt$ | time step [s] |
| $f$ | liquid fraction |
| $h_\infty$ | heat transfer coefficient [W/m$^2$K] |
| $l$ | total number of measurements |
| $J$ | Jacobian matrix |
| $k$ | thermal conductivity [W/mK] |
| $L_{Brick}$ | width of the brick wall [m] |
| $L_{PCM}$ | width of the PCM layer [m] |
| $N$ | number of unknown parameters |
| $q''(t)$ | heat flux [W/m$^2$] |
| $\vec{P}$ | vector of unknown parameter |
| $PCM$ | phase change material |
| $RRMSE$ | relative root-mean-square errors [%] |
| $Error$ | estimation errors [%] |
| $E(t)$ | bank thickness [m] |
| $t$ | time [s] |
| $\hat{T}$ | estimated temperature [K] |
| W | weighting matrix |
| $x$ | Cartesian spatial coordinate [m] |
| $Y$ | measured temperature [K] |

**Greek symbols**

| | |
|---|---|
| $\varepsilon$ | small number |
| $\mu$ | damping parameter |
| $\rho$ | density [kg/m$^3$] |
| $\sigma$ | standard deviation of the measurement error |
| $\sigma_{\hat{P}_j}$ | standard deviation of the estimated parameter |
| $\Psi$ | sum of squares norm |
| $\xi$ | small number |
| $\delta H$ | enthalpy [J/m$^3$] |
| $\Delta$ | difference |
| $\Omega^k$ | diagonal matrix |
| $\lambda$ | heat of fusion [J/kg] |
| $\omega$ | random number |

**Subscripts**

| | |
|---|---|
| $0$ | initial value |
| $\infty$ | ambiant |
| $Brick$ | brick wall |
| exact | exact solution |
| $E(t)$ | bank thickness |
| $F$ | freezing point |
| $liq$ | liquidus |
| $PCM, liquid$ | liquid (PCM) |
| max | maximum |
| $P$ | parameter |
| $PCM$ | phase change material |
| $sol$ | solidus |
| $PCM, solid$ | solid (PCM) |

**Superscripts**

| | |
|---|---|
| $k$ | time iteration number |
| $T$ | transposed matrix |
| $\hat{}$ | estimated parameter |
| $\rightarrow$ | vector |
| $\leftrightarrow$ | matrix |

## 3.1. Introduction

Molten material reactors, such as melting furnaces [17, 58, 71, 126] and aluminum-electrolysis-cells [59-61] (Figure 3.1) are used for material processing that requires high powers and elevated temperature. Their applications are in the production of aluminum and the smelting of materials such as copper, steel, and nickel calcine.

A common feature of these reactors is the formation of a bank that covers the lining of their brick walls. This bank is essential for protecting the inside surface of the brick wall from the highly corrosive molten material [17, 58, 64]. The bank is formed when the molten material comes into contact with the cooled wall and solidifies. Maintaining this bank and controlling its thickness while the furnace is operated, is a challenging task. The hostile environment that prevails inside the reactor forbids direct measurements of the bank with submerged probes. The problem is further complicated by the fact that the bank thickness is time-varying. It depends on the boundary conditions at the walls, the power load delivered to the furnace, and the thermo-physical properties of the refractory brick wall and of the molten material.

The alternative approach for handling this problem rests on inverse heat transfer techniques. In this approach, the protective bank is predicted by means of temperatures and/or heat fluxes recorded by sensors embedded into the refractory brick walls. The data gathered by the sensors are fed to an inverse heat transfer algorithm that deducts the thermal conditions that exist inside the furnace. From there, the thickness of the protective bank may be estimated.

Over the last decade, few investigations have been conducted with inverse heat transfer methods for predicting the time-varying bank inside molten material reactors. These inverse methods are based on various algorithms such as the conjugate gradient method with the adjoint equation [17, 47, 64, 65], the Kalman Filter method (KF) [58-62, 127] and the *Levenberg–Marquardt* method [66]. All these methods proceed in the same manner. They focus on the inverse prediction of the power load, i.e., the time-varying heat flux at ($x=L_{Brick} + L_{PCM}$) (Figure 3.2). Once the heat flux is established, the protective bank thickness $E(t)$ is calculated using a direct method.

In all the aforementioned studies however, the thermal conductivities of the brick wall and of the PCM were fixed. In real situations, these conductivities are poorly known. For instance, the thermal conductivity of the brick wall may change as the bricks age. And the thermal conductivity of the phase change material (PCM) is often process dependent. As a result, the predicted time-varying bank thickness may be inaccurate when the wall and the PCM thermal conductivities are set in advance.

The present paper remedies this shortcoming. It pursues the previous studies by predicting simultaneously (1) the heat flux $q''(t)$, (2) the thermal conductivity of the refractory brick wall; and (3) the thermal conductivity of the liquid and of the solid phase of the PCM (Figure 3.2). Note that inverse heat transfer approaches have already been employed in the estimation of thermo-physical properties such as the heat transfer coefficient [128-131], the thermal conductivity [77, 131-135] and the heat flux [75, 136-139]. But none of these investigations has attempted to predict simultaneously the time-varying bank on the lining of a molten material reactor.

The paper is organized as follows. First, a one-dimensional phase change model based on the enthalpy method is presented and validated with data available in the open literature [140, 141]. The direct model is then implemented for the molten material reactor investigated in reference [61]. Second, an inverse heat transfer algorithm based on the *Levenberg-Marquardt* Method (LMM) is developed. The algorithm is combined to the *Broyden* method in order to reduce the computational time. Third, the overall inverse method is employed for the prediction of the thermo-physical properties of a reactor. Numerical simulations are then conducted for different operating scenarios. The effect (1) of the guessed initial *Levenberg-Marquardt* parameters, (2) of the position of the embedded temperature sensor into the wall, (3) of the number of collected temperature data and (4) of the noise on the inverse predictions is investigated.

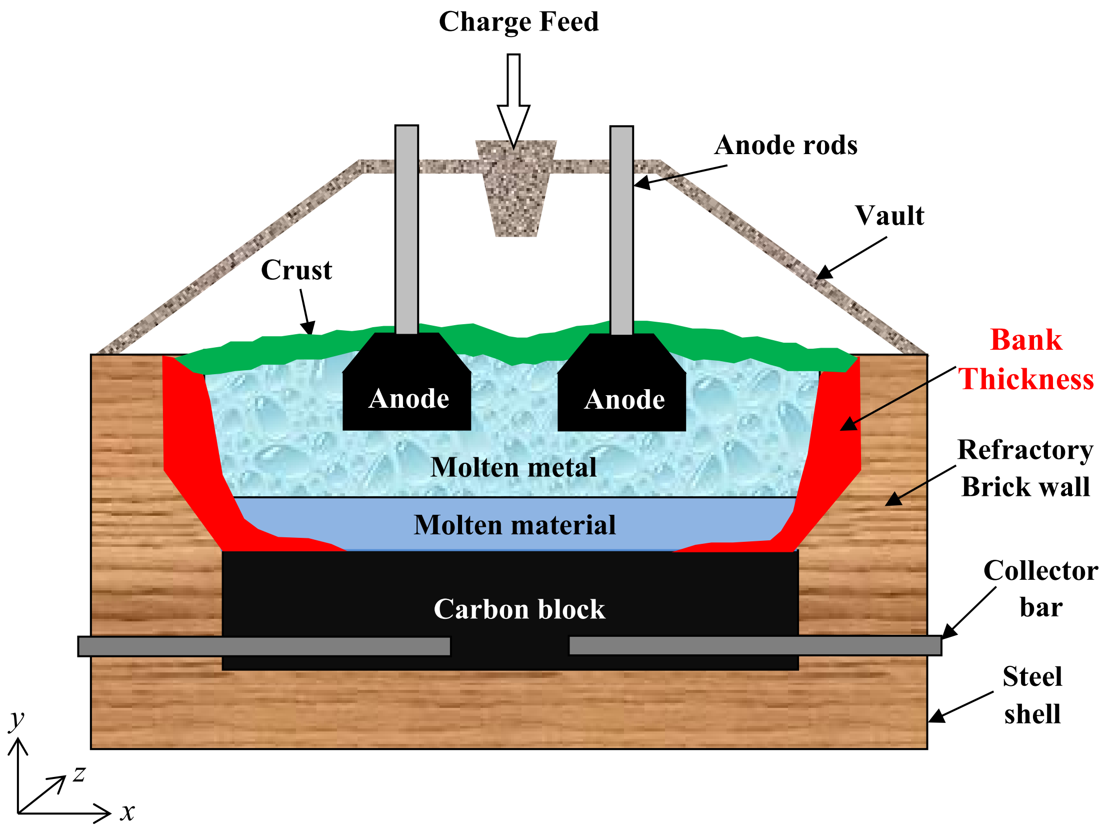

**Figure 3.1** Cross view of a typical molten material reactor. The thermal load is provided by the anodes.

## 3.2. Problem statement and assumptions

The one-dimensional phase-change problem for the protective bank of the molten material reactor is depicted in Figure 3.2. Here, the phase change phenomenon is non-isothermal, i.e., the melting process is delineated by three distinct zones: a solid phase layer, a solid/liquid phase layer or a mushy zone and a liquid phase layer. The lining of the refractory brick wall ($x=L_{Brick}$) is coated with a protective bank whose thickness is $E(t)$. $E(t)$ is the distance that separates the inner surface of the brick wall to the solidus of the Phase Change Material.

At the left boundary ($x=0$), the surface of the brick wall is cooled with an air stream. The outside air temperature is $T_\infty$ and the convective heat transfer coefficient $h_\infty$. At the right boundary ($x= L_{Brick} + L_{PCM}$), a time-varying heat flux $q''(t)$ is imposed over the time interval $t\epsilon[0, 400000\ (s)]$. A sensor, embedded into the refractory brick wall, captures and records the transient temperature $Y(t_i)$ (Figure 3.2).

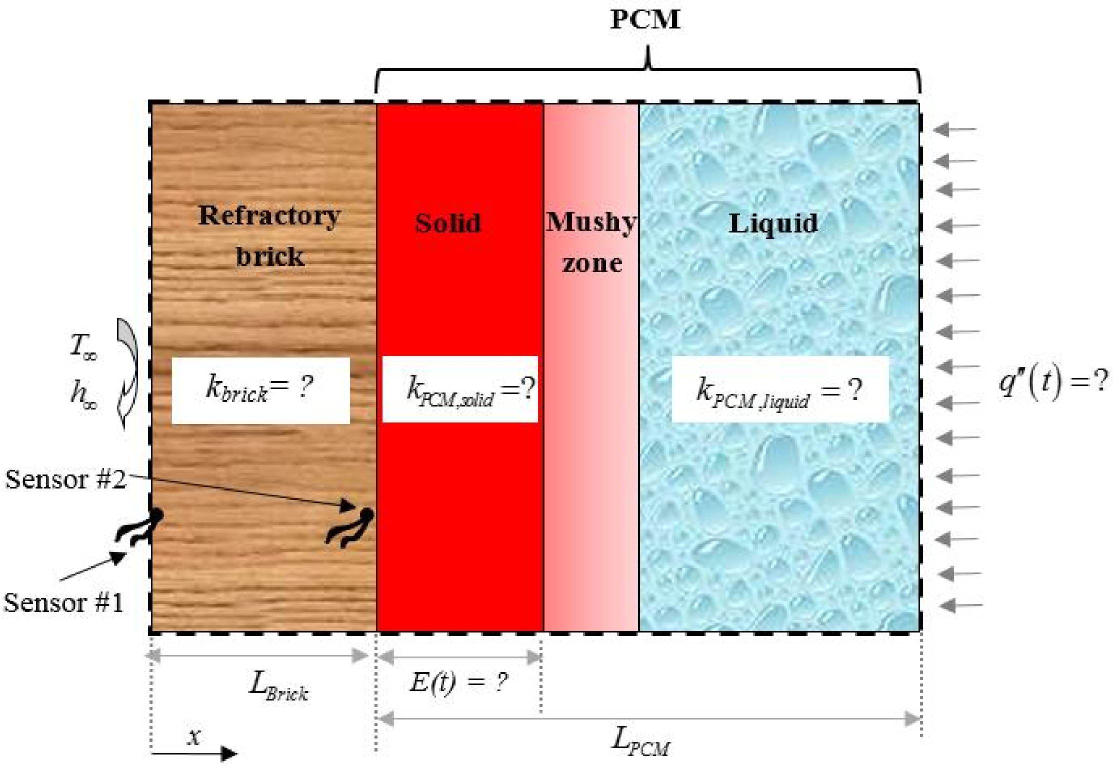

**Figure 3.2** Schematic of the 1D phase-change inverse problem. Here, $k_{Brick}$, $k_{PCM,solid}$, $k_{PCM,liquid}$ and $q''(t)$ are unknown. They are determined from temperatures recorded by a sensor embedded into the refractory brick wall.

The mathematical model for the phase change rests on the following assumptions [17, 58, 59, 61, 62, 64, 65]:

- The thickness (*x* direction) of the PCM layer and of the brick wall ($L_{brick}$+$L_{PCM}$) is small in comparison to the height (*y* direction, i.e., the vertical direction) and the depth (*z* direction, i.e., the direction perpendicular to schematic in Figure 3.2) of the reactor. Furthermore, the temperature gradients in the *x* direction are orders of magnitude larger than those in the *y* and *z* directions. As a result, a one-dimensional *x* direction model is adopted in the present study (Figure 3.2).
- The heat transfer inside the liquid phase of the PCM is conduction dominated [17, 142].
- The phase change problem is non-isothermal. The melting phenomenon is delineated by three zones: a solid phase, a mushy zone and a liquid phase.
- The thermal properties of the PCM are temperature independent.
- The brick wall and the PCM are strongly pressed against each other. As result, the thermal contact resistance between both materials is neglected.

## 3.3. The direct model

In the direct one-dimensional phase-change problem, the geometric and the thermo-physical properties as well as the initial and the boundary conditions are completely specified. As a result, the governing heat diffusion equation, i.e

$$\rho C_p \frac{\partial T}{\partial t} = \frac{\partial}{\partial x}\left( k \frac{\partial T}{\partial x} \right) - \delta H \frac{\partial f}{\partial t} \tag{3.1}$$

may be solved for the temperature field *T(x,t)* and for the exact time varying thickness of the protective bank *E(t)*. The enthalpy $\delta H$ is defined as

$$\delta H = \rho (C_{p,PCM,liquid} - C_{p,PCM,solid}) T + \rho \lambda \tag{3.2}$$

The liquid fraction $f$ varies linearly between the solidus temperature $T_{sol}$ and the liquidus temperature $T_{liq}$ in the following manner:

$$f = F(T) = \begin{cases} 0 & T \le \mathrm{T}_{sol} \quad (\mathit{Solid}\ \text{region}) \\ \dfrac{T - T_{sol}}{T_{liq} - T_{sol}} & \mathrm{T}_{sol} \le T \le \mathrm{T}_{liq} \ (\mathit{Mushy}\ \text{region}) \\ 1 & T \ge \mathrm{T}_{liq} \quad (\mathit{Liquid}\ \text{region}) \end{cases} \tag{3.3}$$

At each time-step, the liquid fraction $f$ is updated iteratively [141]:

$$f^{k+1} \approx f^k + \left( \frac{dF}{dT} \right)^k \left( T^{k+1} - F^{-1}\left( f^k \right) \right) \tag{3.4}$$

$F$ is a function of the temperature *T*. $F^{-1}$ is the inverse function of *F*.

The boundary conditions at the left and the right sides of Figure 3.2 are given by:

$$\begin{cases} \left( k \dfrac{\partial T}{\partial x} \right)_{x=0} = h_\infty \left( T(0,t) - T_\infty \right) \\ \left( k \dfrac{\partial T}{\partial x} \right)_{x=L_{Brick}+L_{PCM}} = q''(t) \end{cases} \tag{3.5}$$

Equations (3.1)-(3.5) are solved numerically using a Finite-Volume Method (FVM) [143]. The scheme adopted for the time discretization is implicit. The phase change process is handled with the enthalpy method reported in reference [141].

The above one-dimensional phase-change model was validated with the 1-D test case for the solidification of the binary Al–4.5% Cu alloy reported in references [140, 141]. In this test case, the width of the PCM layer is set equal to $L_{PCM}=0.5\ (m)$. A Dirichlet boundary condition of $T=573\ (K)$ is assumed at the boundary $x=L_{Brick}$ (Figure 3.2) and the initial temperature of PCM is fixed at $T_{in}= 969\ (K)$.

Figure 3.3 illustrates the predicted solidus and liquidus fronts. It is seen that the time-varying phase fronts predicted from the direct model are in excellent agreement with the results generated from the semi-analytical heat balance integral method [140] and the source-based numerical method [141].

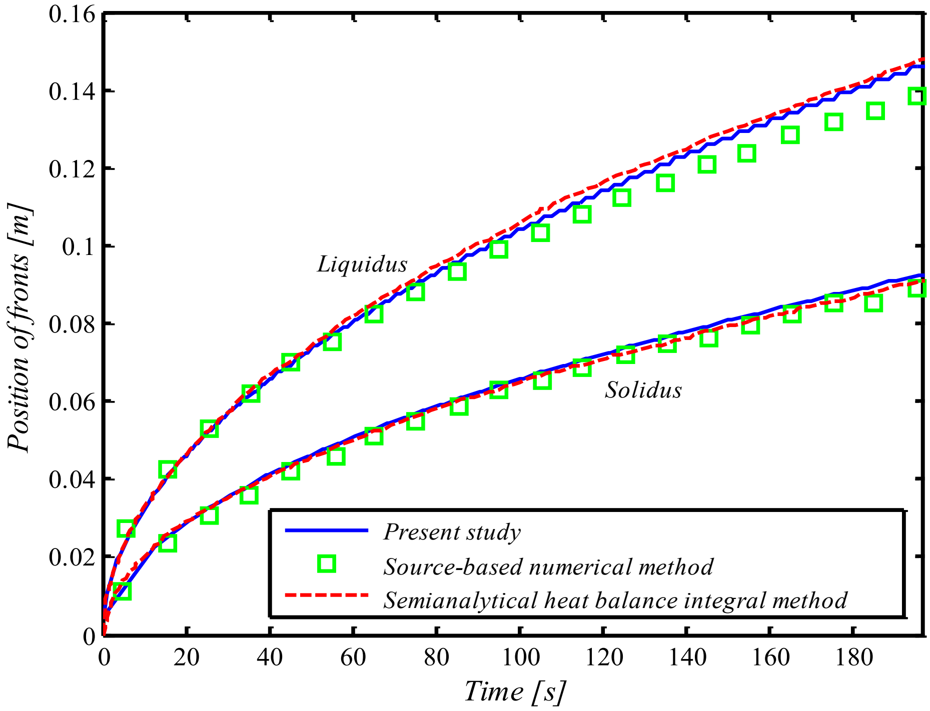

**Figure 3.3** Solidification of the binary Al–4.5% Cu alloy.

Next, the direct model was implemented for the molten material reactor illustrated in Figure 3.2. The operating thermal conditions for the reactor are reported in reference [61]. The width of the brick wall is set equal to $L_{Brick}=0.1(m)$ and the PCM layer is set equal to

$L_{PCM}=0.1(m)$ (Figure 3.2). The outside temperature is set equal to $T_\infty=300\ (K)$ and the outside convective heat transfer coefficient is fixed at $h_\infty=15\ (W/m^2\ K)$.

Several numerical simulations were performed to ensure that the predictions are grid space and time step independent. It was found that a mesh size $dx = 0.001\ (m)$ and a time step $dt = 100\ (s)$ is a good compromise for accuracy and CPU time requirements.

The thermo-physical properties of the brick wall and the PCM are summarized in Table 3.1 [61].

**Table 3.1** Thermo-physical properties for the reactor [61].

| Parameter | Value | Unit |
|---|---|---|
| $k_{BRICK}$ | 16.8 | W/m K |
| $C_{p,BRICK}$ | 875 | J/kg K |
| $\rho_{BRICK}$ | 2600 | kg/m$^3$ |
| $k_{PCM,solid}$ | 1 | W/m K |
| $k_{PCM,liquid}$ | 10 | W/m K |
| $C_{p,PCM,solid}$ | 1800 | J/kg K |
| $C_{p,PCM,liquid}$ | 1800 | J/kg K |
| $\rho_{PCM}$ | 2100 | kg/m$^3$ |
| $\lambda_{PCM}$ | 5.1 x 10$^5$ | J/kg |
| $T_{sol}$ | 1213 | K |
| $T_{liq}$ | 1233 | K |

The time-varying heat flux $q''(t)$ imposed at $(x=L_{Brick}+L_{PCM})$ is given by

$$q''(t) = Q_0 + Q_1 * \sin^2\left(\frac{3\pi.t}{t_{\max}}\right) \tag{3.6}$$

## 3.4. The inverse problem

In the inverse problem, the thermal conductivity of the brick wall $k_{Brick}$, the thermal conductivities of the solid and of the liquid PCM layers, i.e., $k_{PCM,solid}$ and $k_{PCM,liquid}$ respectively, and the heat flux $q''(t)$ are unknown. They are estimated from the inverse heat transfer procedure and fed to the direct model that calculates the time varying bank thickness *E(t)*.

The inverse model determines the unknown polynomial parameters for the heat flux and for the thermal conductivities $\vec{P}=\left[Q_0;\ Q_1;\ k_{brick};\ k_{PCM,solid};k_{PCM,liquid}\right]$. Once the polynomial parameters have been estimated, the bank thickness *E(t)* is determined with the direct model presented above.

The objective of the inverse algorithm is to minimize the following objective function:

$$\Psi\left(\vec{P}\right)=\left[Y_i-\hat{T}_i\left(\vec{P}\right)\right]^T W\left[Y_i-\hat{T}_i\left(\vec{P}\right)\right] \tag{3.7}$$

$\vec{P}=\left[Q_0;\ Q_1;\ k_{brick};\ k_{PCM,solid};k_{PCM,liquid}\right]$ is the set of the unknown polynomial parameters. $Y_i$ are the temperatures recorded by a sensor embedded into the brick wall. Temperature sensors i.e., thermocouples, are simple and inexpensive devices that are easy to install and to use. In the present study, these temperatures are 'generated' from the solution of the direct model for which all the properties and the boundary conditions of the problem have been specified. $\hat{T}\left(t_i,\vec{P}\right)$ are the estimated temperatures from the inverse model. They are determined from the solution of the direct problem by using the estimated values for the polynomial parameters. $W$ is the weighting matrix. Its elements equal to $diag\left(\sigma_i^2\right)^{-1}$, where $\sigma_i$ is the variance of the measurement error.

The method adopted for minimizing the objective function is the *Levenberg–Marquardt* Method (LMM). This method has been successfully applied to inverse heat transfer problems in the past [76, 144-149]. In the iterative scheme, the incremental value of the unknown parameters $\Delta P$, is defined as:

$$\Delta\vec{P}^k=\left[\left(\vec{J}^k\right)^T W\left(\vec{J}^k\right)+\mu^k\vec{\Omega}^k\right]^{-1}\left(\vec{J}^k\right)^T W\left(\vec{Y}_i-\vec{T}_i\left(\vec{P}^k\right)\right) \tag{3.8}$$

$\mu^k$ is a positive scalar called the damping parameter. The damping parameter is employed for convergence purposes. It ensures that the matrix $\left[\left(\vec{J}^k\right)^T W\left(\vec{J}^k\right)\right]$, in equation (3.8), is nonsingular. More details about the damping parameter are provided in [150]. $\vec{\Omega}^k$ is the diagonal matrix of $\left[\left(\vec{J}^{k}\right)^{T} W\left(\vec{J}^{k}\right)\right]$. $\vec{J}^{k}$ is the Jacobian matrix, also called the sensitivity matrix. It is written as

$$\vec{J}\left(\vec{P}\right)=\begin{pmatrix} \frac{\partial T_1}{\partial Q_0} & \frac{\partial T_1}{\partial Q_1} & \frac{\partial T_1}{\partial k_{brick}} & \frac{\partial T_1}{\partial k_{PCM,solid}} & \frac{\partial T_1}{\partial k_{PCM,liquid}} \\ \frac{\partial T_2}{\partial Q_0} & \frac{\partial T_2}{\partial Q_1} & \frac{\partial T_2}{\partial k_{brick}} & \frac{\partial T_2}{\partial k_{PCM,solid}} & \frac{\partial T_2}{\partial k_{PCM,liquid}} \\ \vdots & \vdots & \vdots & \vdots & \vdots \\ \frac{\partial T_I}{\partial Q_0} & \frac{\partial T_I}{\partial Q_1} & \frac{\partial T_I}{\partial k_{brick}} & \frac{\partial T_I}{\partial k_{PCM,solid}} & \frac{\partial T_I}{\partial k_{PCM,liquid}} \end{pmatrix} \tag{3.9}$$

$I$ is the total number of temperature recordings.

The Jacobian matrix, equation (3.9), plays a very important role in the estimation of the polynomial parameters. It carries important information about the behavior of the estimated temperatures with respect to the unknown parameter $P_j$. In fact, a successful estimation of these parameters depends on the magnitude of sensitivity coefficient $\partial T_i/\partial P_j$. For example, the larger the sensitivity coefficients, the easier it is to estimate the polynomial parameters.

There are several approaches for computing the sensitivity coefficients $\partial T_i/\partial P_j$ [151]. In this study, the sensitivity coefficients are approximated with a finite difference:

$$J_{ij}=\frac{\partial \hat{T}_i}{\partial P_j}\cong\frac{\hat{T}\left(t_i\ ;P_1,...,P_j+\left(\delta P_j\right),...P_N\right)-\hat{T}\left(t_i\ ;P_1,...,P_j-\left(\delta P_j\right),...P_N\right)}{2\left(\delta P_j\right)} \tag{3.10}$$

The parameter perturbation $\left(\delta P_j\right)$ is set to $\xi\left(1+\left|P_j\right|\right)$, where $\xi$ is a small number. The subscripts $i$ and $j$ indicate the time and the parameter, respectively.

In order to diminish the computational time devoted to the calculation of the sensitivity matrix, the Jacobian matrix is updated using the *Broyden* method [152]. Hence, for the first iteration, for every $\left(2\times N\right)$ iterations and for iterations that satisfy $\Psi\left(P+\Delta P\right)>\Psi\left(P\right)$, the sensitivity coefficients $\partial T_i/\partial P_j$ of the Jacobian matrix are estimated with equation (3.10). For every other iteration, the Jacobian matrix is updated using the *Broyden* expression:

$$J_k = J_{k-1} + \frac{\left(\left(\hat{T}_k - \hat{T}_{k-1}\right) - J_{k-1}\Delta P_{k-1}\right)\Delta P_{k-1}^T}{\Delta P_{k-1}^T \Delta P_{k-1}} \tag{3.11}$$

$J_{k-1}$ and $J_k$ are the Jacobian matrices at the previous and at the current iteration, respectively. $\Delta P_{k-1}$ is the incremental value of the unknown parameters defined in equation (3.8).

Convergence is declared when one of the following criteria is satisfied

$$\begin{cases} J^T \left\| Y\left(t_i\right) - \hat{T}\left(t_i, \vec{P}\right) \right\| < \varepsilon_1 \\ \left( \dfrac{P^{k+1} - P^k}{P^{k+1}} \right) < \varepsilon_2 \\ \Psi\left(P^{k+1}\right) < \varepsilon_3 \end{cases} \tag{3.12}$$

$\{\varepsilon_1 \; \varepsilon_2 \; \varepsilon_3\}$ are small numbers. In the present study, these parameters were fixed at $\{\varepsilon_1 = \varepsilon_2 = \varepsilon_3 = 0.001\}$.

The overall computational algorithm for the inverse problem is summarized as follows:

*Step 1:* Solve the direct problem (3.1)-(3.5) in order 'to generate' the temperature field $T_{exact}$.

*Step 2:* Choose an initial set of polynomial parameters and solve the inverse problem in order to obtain the estimated temperature field $\hat{T}\left(t_i, \vec{P}\right)$.

*Step 3:* Compute the objective function $\Psi\left(P\right)$ from equation (3.7).

*Step 4:* Check for the convergence with equation (3.12).

*Step 5:* Compute the sensitivity coefficients according to equation (3.10) or the *Broyden* update expression given by equation (3.11).

*Step 6:* Compute the increment $\Delta P$ for the estimated parameters from equation (3.8).

*Step 7:* Solve the direct problem with the new estimates $P^{k+1}$ in order to find $T(P^{k+1})$. Compute $\Psi\left(P^{k+1}\right)$ as defined in step 3.

*Step 8:* Check for convergence with equation (3.12). If convergence is not satisfied, go back to Step 5. Update the sensitivity coefficients and $\Psi\left(P\right)$.

*Step 9:* If convergence is achieved, the bank *E(t)* is determined from the direct model using the estimated polynomial parameters.

## 3.5. Statistical analysis

Once the objective function equation (3.7) is satisfied, a statistical analysis for the polynomial parameter estimation may be performed in order (1) to assess the accuracy and the uniqueness of the solution and (2) to obtain the confidence intervals. Moreover, the temperatures recorded by the sensor may be contaminated with measurement errors. For distributed measurement errors with zero mean and a constant variance $\sigma^2$, the standard deviation of the estimated parameters can be expressed as [151, 153]

$$\sigma_{\hat{P}_j} = \sigma \sqrt{diag\left\{\left(\frac{\partial T^T}{\partial P}\right)\left(\frac{\partial T}{\partial P^T}\right)\right\}^{-1}} \tag{3.13}$$

Assuming a normal distribution for the errors on the temperatures recorded and 99% confidence, the intervals for the computed quantities $P_j$ are given as

$$\text{Probability: } \left\{\left(\hat{P}_j - 2.576\ \sigma_{\hat{P}_j}\right) < P_{j,exact} < \left(\hat{P}_j + 2.576\ \sigma_{\hat{P}_j}\right)\right\} \cong 99\% \tag{3.14}$$

$\hat{P}_j$ are the estimated values of the unknown polynomial parameters, $P_{j,exact}$, for ($j=1...5$), and $\sigma_{\hat{P}_j}$ are the standard deviations obtained from equation (3.13).

## 3.6. Results and discussion

The inverse algorithm illustrated in Figure 3.4 was implemented in order to predict simultaneously the thermal conductivities ($k_{Brick}$, $k_{PCM,solid}$ and $k_{PCM,liquid}$) and the polynomial parameters of the heat flux *q"(t)* that prevail inside the reactor (Figure 3.2). Once these properties and parameters are estimated, the time-varying bank thickness *E(t)* is retrieved from the direct model presented in section 3.3.

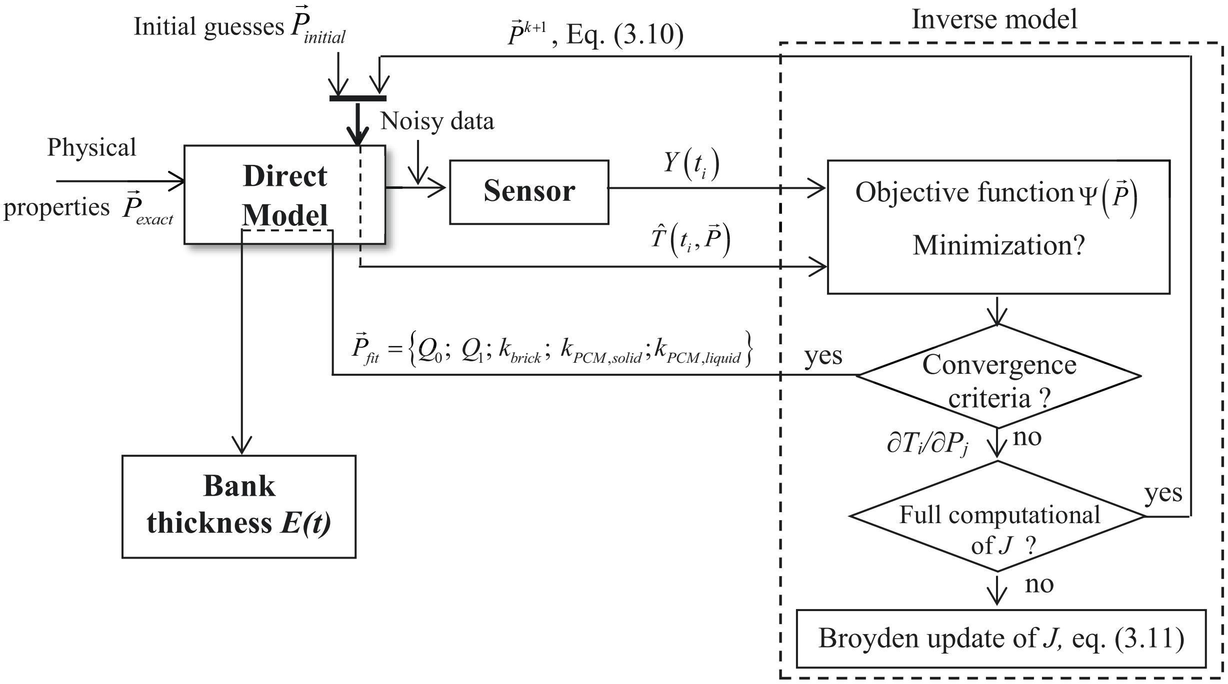

**Figure 3.4** Overall inverse heat transfer algorithm.

Note that the uniqueness and the accuracy of the inverse procedure have been thoroughly tested with noisy data and for different positions of the embedded sensor (*x=[0.025; 0.05; 0.075 (m)]*). It has been observed that the inverse predictions are, in all cases, in very good agreement with the exact solution. Due to the space restrictions, these results are not reported here.

The measured temperatures were collected with a sensor embedded into the refractory brick wall at two different locations: The first location, called ‘Sensor#1’, is close to the outer surface of the brick wall. The second position, 'Sensor#2', is close to the PCM (Figure 3.2). The total number of temperature data recorded during the time interval $t \epsilon [0, 400000\ (s)]$ is $I = 2000$.

For the sake of comparing the inverse predictions (the inverse model) to the exact solution (the direct model), three different estimation errors were adopted:

$$Error_P\ \% = 100 \times \frac{\left|P_{exact} - P_{inverse}\right|}{\left|P_{exact}\right|} \tag{3.15}$$

$$\mathrm{RRMSE}_{E(t)}\ \% = 100 \times \sqrt{\frac{1}{I}\sum_{i=1}^{I}\left(\frac{E(t_i)_{exact} - E(t_i)_{inverse}}{E(t_i)_{exact}}\right)^2} \tag{3.16}$$

$$\mathrm{Error}_{E(t_i)}\ \% = 100 \times \frac{\left|E(t_i)_{exact} - E(t_i)_{inverse}\right|}{\left|E(t_i)_{exact}\right|} \tag{3.17}$$

First, the effect of the initial guesses for the polynomial parameters $\vec{P} = \left[Q_0;\ Q_1;\ k_{brick};\ k_{PCM,solid}; k_{PCM,liquid}\ \right]$ was examined. The magnitude of the initial guesses was set at 1/3, 1/7 and 1/10 of that of the exact polynomial parameters $\vec{P}_{Exact} = \left[6000;\ 5000;\ 16.8;\ 1;10\ \right]$. The results of the investigation are summarized in Figure 3.5 and in Table 3.2. It is seen that convergence is achieved in all cases. Of course, convergence is slightly faster as the initial guesses are closer to the exact polynomial parameters (*Test 1)*. Simulations were performed with the Matlab software running on an Intel ® Core(TM) i5-2520M CPU @ 2.50GHz.

**Table 3.2** Number of iterations and CPU time for the three test cases.

| | **Initial guess** | **No. of iteration** | **CPU time (s)** |
|---|---|---|---|
| *Test 1* | *($P_{j,exact}$)*/3 | 21 | 2284.7 |
| *Test 2* | *($P_{j,exact}$)*/7 | 22 | 2364.8 |
| *Test 3* | *($P_{j,exact}$)*/10 | 24 | 2392.1 |

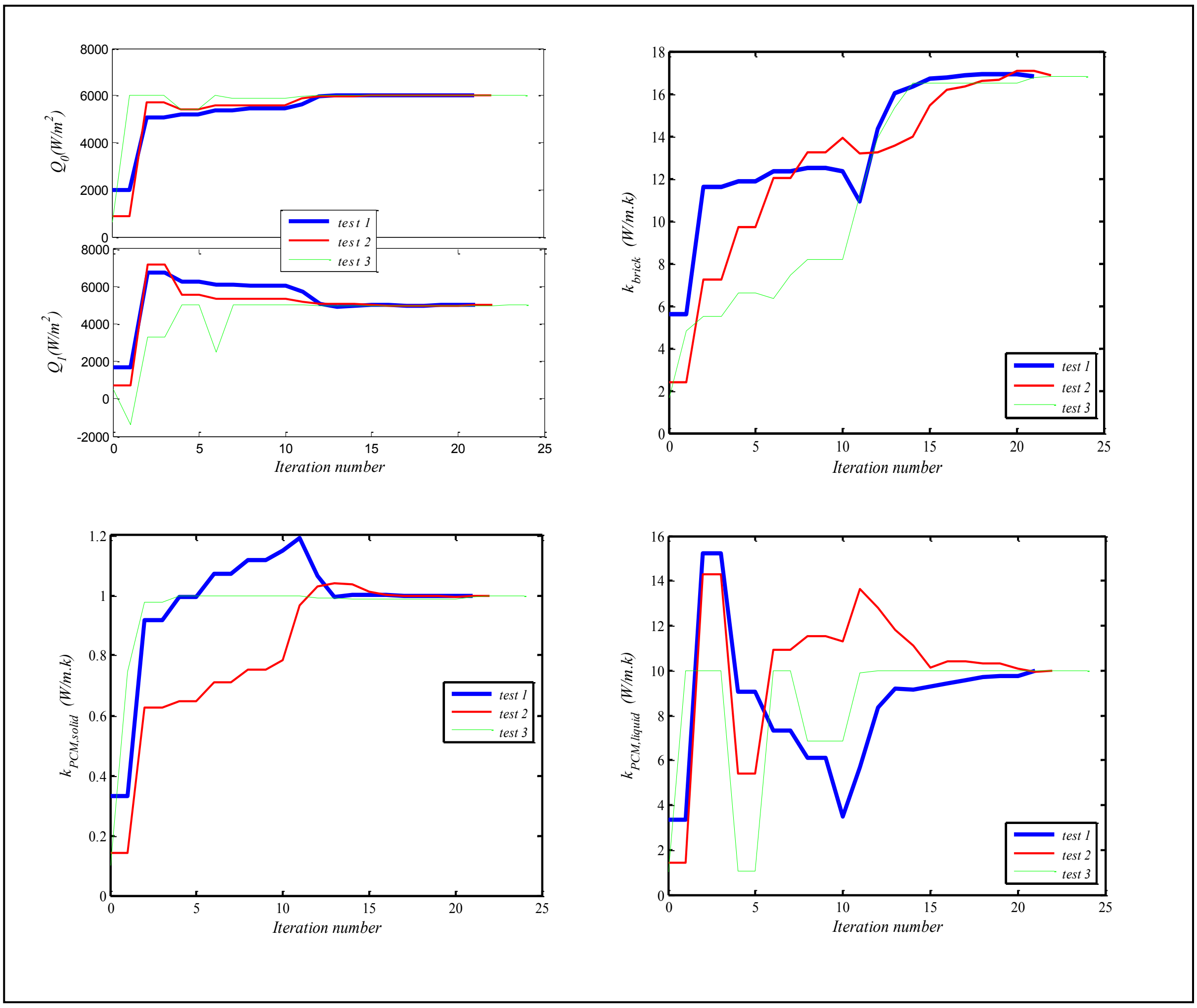

**Figure 3.5** Convergence of the parameters (Sensor#1, no noise).

Second, in the *Levenberg-Marquardt* Method (LMM), the finite-difference approximation of the sensitivity coefficients, equation (3.10), requires the solution of the direct problem ten times (2 times for each unknown parameter) per iteration. As a result, the computational effort may become prohibitive. To alleviate this problem, the sensitivity matrix was updated with the *Broyden* Method (BM) [154, 155]. In this study, the combination of the LMM to the BM (LMM/BM), calls the direct model 53 times while the LMM requires 70 calls. Consequently, the CPU time for the LMM/BM is 2285 (s) compared to 3536 (s) for the LMM. It is also observed that the LMM/BM requires more iteration than LMM [155].

The corresponding temperature distribution, estimated from the inverse model, is indistinguishable from the temperature distribution generated by the direct model (Figure 3.6).

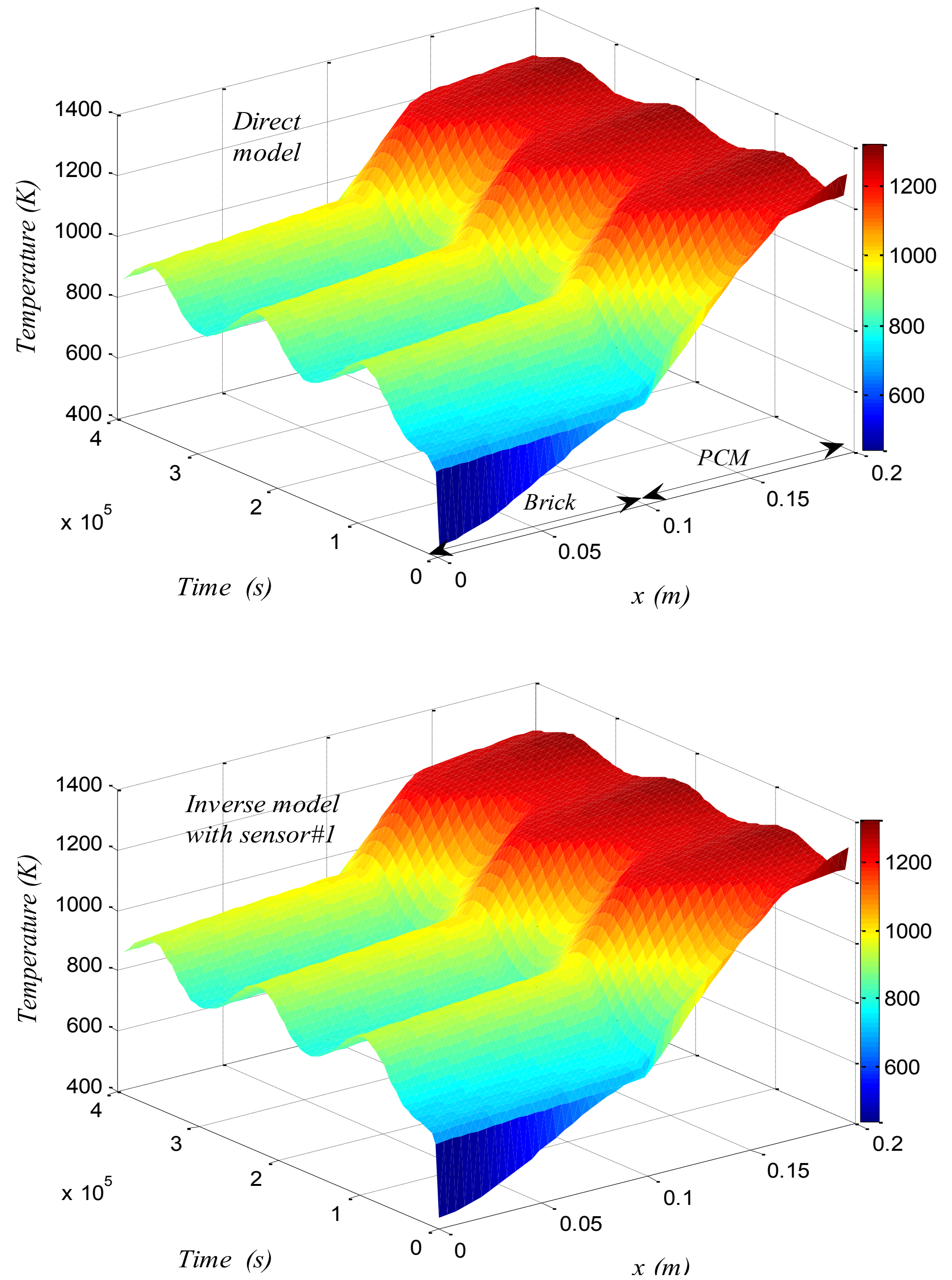

**Figure 3.6** Temperature distributions.

For the remainder of this paper, the initial parameter guesses for *'test* 1*'* and the LMM/BM will be retained in all simulations.

Next, the effect of the sensor location (Sensor#1 and Sensor#2) on the estimation of the unknown polynomial parameters was examined. The results are summarized Table 3.3. It is seen that the maximum error on the parameter estimation is less than 0.2%.

**Table 3.3** Polynomial parameters.

| | | ***Sensor#1*** | | ***Sensor#2*** | |
|---|---|---|---|---|---|
| | $P_{Exact}$ | $P_{Inverse}$ | $Error_P$ % | $P_{Inverse}$ | $Error_P$ % |
| $Q_0$ $(W/m^2)$ | 6000 | 6000.70 | 0.01 | 6001.09 | 0.02 |
| $Q_1$ $(W/m^2)$ | 5000 | 4998.63 | 0.03 | 4999.94 | 0.00 |
| $k_{brick}$ $(W/m\ K)$ | 16.8 | 16.82 | 0.12 | 16.83 | 0.18 |
| $k_{PCM,solid}$ $(W/m\ K)$ | 1 | 1.00 | 0.00 | 1.00 | 0.00 |
| $k_{PCM,liquid}$ $(W/m\ K)$ | 10 | 10.00 | 0.00 | 10.00 | 0.00 |

Once the polynomial parameters are identified (Table 3.3), the time-varying bank thickness *E(t)* is calculated from the direct model presented in section 3.3.

The exact and the estimated (from the inverse model) time-varying bank thicknesses are plotted in Figure 3.7. The inverse predictions are in perfect agreement with the direct model exact solution. In this case, the calculated relative root-mean-square error for the bank thickness ($RRMSE_{E(t)}$) is than 0.03%. The number of recorded temperature data was set to $I = 2000$.

The effect of the location of the temperature-sensor on the accuracy of the predicted bank thickness *E(t)* is depicted in Figure 3.8. As expected, sensor#2, located closer to the PCM, provides a slightly better estimation of the bank thickness [156]. But for both sensors, the $Error_{E(ti)}$ on the bank thickness remains less than 0.05%. Therefore, for practical reasons, sensor#1 is recommended over sensor#2. It is indeed easier and safer to install the sensor near the outer surface of the refractory brick wall. This observation should be of interest to the process industry.

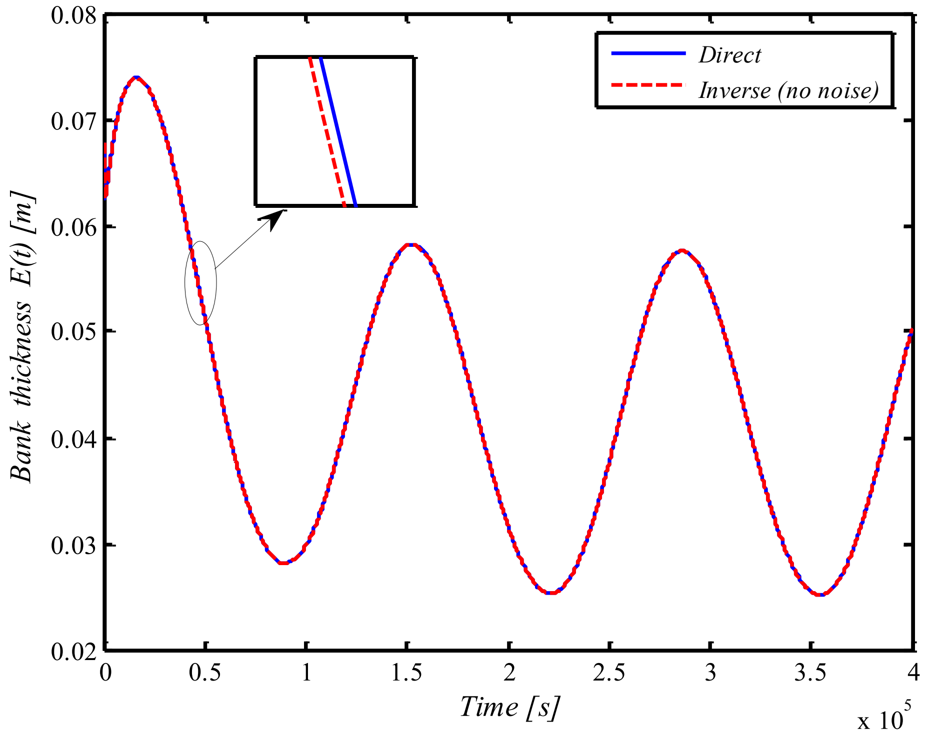

**Figure 3.7** Predicted time-varying bank thickness (sensor#1, no noise).

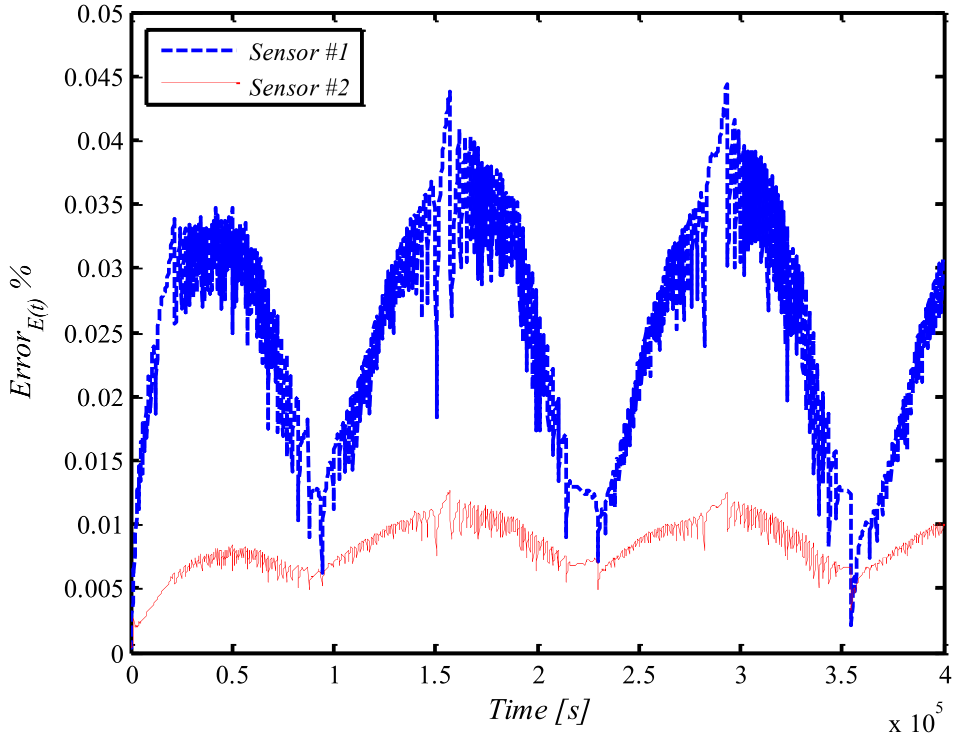

**Figure 3.8** Effect of the sensor position on the predicted bank thickness *E(t)*.

Table 3.4 and Figure 3.9 show the effect of the number of recorded temperature data *I* on the inverse predictions. As expected, the accuracy of the predictions is improved when *I* is raised from *250* to *2000*. The larger the number of recorded temperature data, the better. It is also noted that convergence cannot be achieved for *I* smaller than 200.

**Table 3.4** Effect of the number of recorded temperature data *I* on the predictions.

| | *ERROR$_P$ %* | | | | | *RRMSE$_{E(t)}$* | **CPU** |
|---|---|---|---|---|---|---|---|
| | $Q_0$ | $Q_1$ | $k_{brick}$ | $k_{PCM,solid}$ | $k_{PCM,liquid}$ | % | **time (s)** |
| *I=2000* | 0.01 | 0.03 | 0.12 | 0.00 | 0.00 | 0.03 | 2284.71 |
| *I=500* | 0.03 | 0.08 | 0.38 | 0.08 | 3.31 | 0.29 | 1795.45 |
| *I=250* | 7.44 | 17.88 | 54.03 | 30.43 | 18.54 | 10.92 | 4241.76 |

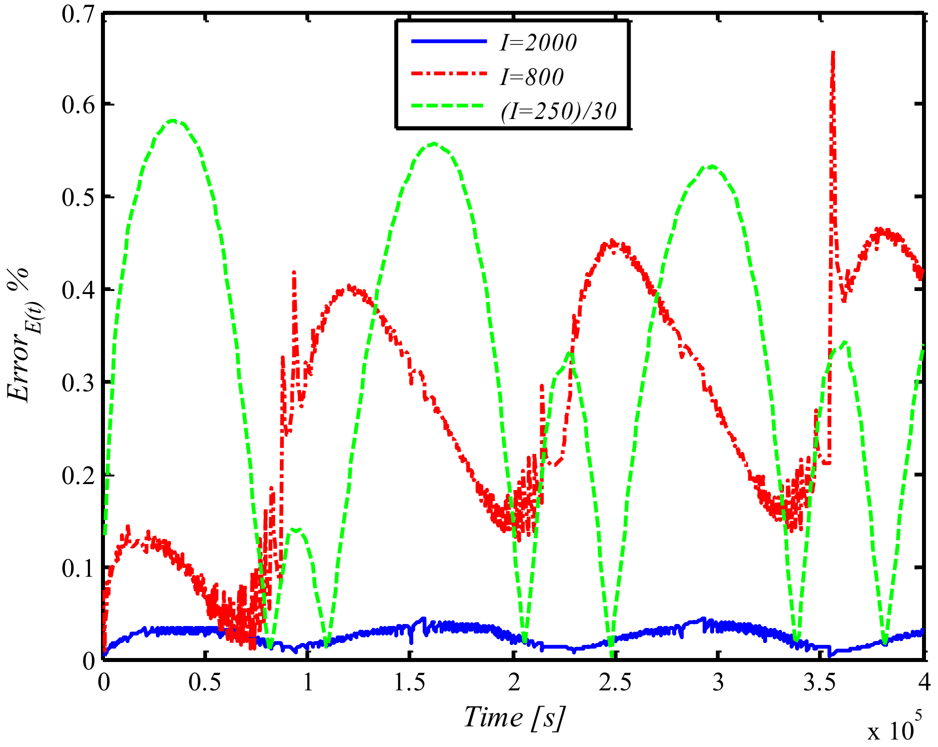

**Figure 3.9** Effect of the number of recorded temperature on the *Error$_{E(t)}$*.

In order to mimic the measurement errors on the recorded temperatures, a random error noise $\vec{\omega}_i$ was added to the exact temperature $\vec{T}_{exact}$ :

$$\vec{T}(\mathrm{t}_i) = \vec{T}_{exact}(\mathrm{t}_i) + \sigma\vec{\omega}_i \tag{3.18}$$

σ is the standard deviation of the measurement errors. In the present study, the maximum value for σ is set equal to 10%$T_{max}$ where $T_{max}$ is the maximum temperature measured by the sensor.

Figure 3.10 compares the noisy temperatures generated from the direct model to the estimated temperatures predicted by the inverse model using sensor#1. The confidence intervals ±2.576 $\sigma_{\hat{P}_j}$ are also shown. As expected, the confidence bounds widen when the noise level increases. It is seen also that the confidence bounds are narrow compared to the measurement noise. In fact, the standard deviation of the estimated parameters $\sigma_{\hat{P}_j}$ calculated with equation (3.13) is small when compared to the standard deviation of the measurement errors on the recorded temperatures σ.

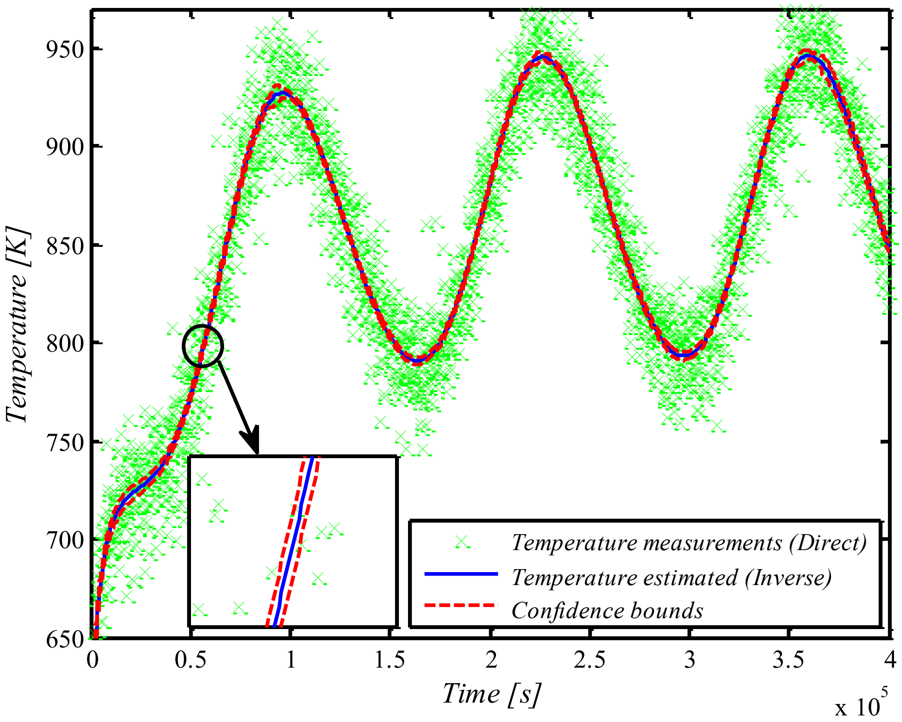

(a) ***σ=2% T*<sub></sub>**

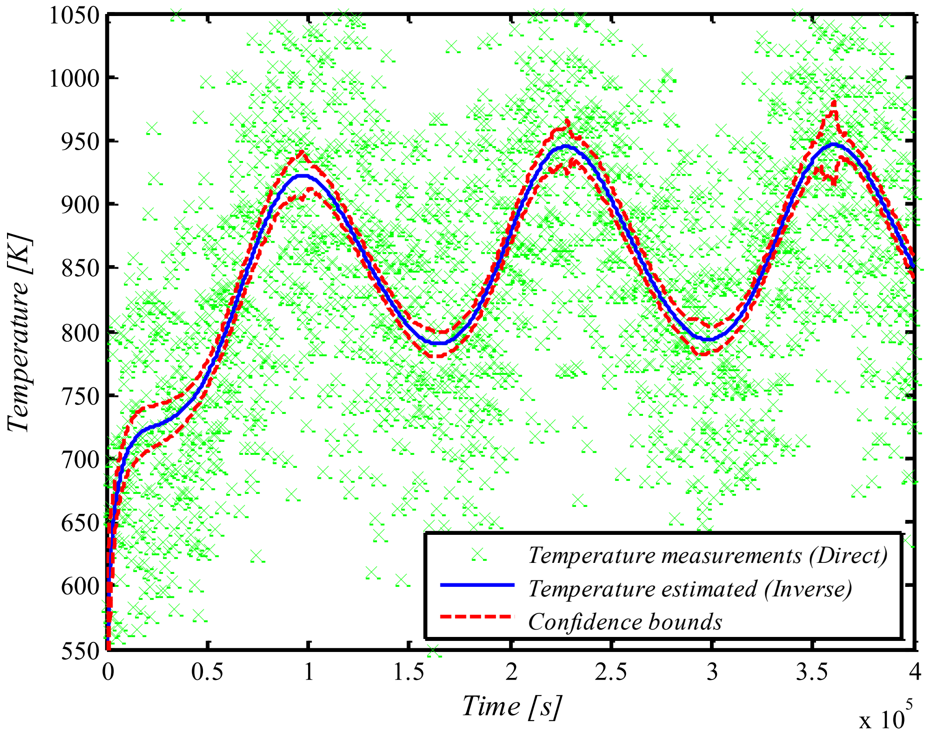

(b) ***σ*=10% *T*$_{max}$**

**Figure 3.10** Measured and predicted inverse temperatures using sensor#1.

Figure 3.11 illustrates the effect of the noise level on the predicted bank thickness *E(t)* using sensor #1. As the noise level rises from $2\%T_{max}$ to $10\%T_{max}$, the relative root-mean-square error for the bank thickness $RRMSE_{E(t)}$ increases from *2.61% to 7.80%*. Nonetheless, in all cases, the inverse model remains stable and relatively accurate.

Table 3.5 summarizes the effect of the noise level on the polynomial parameters using sensor #1. As expected, when the noise level is increased, the predictions worsen (particularly for the thermal conductivities).

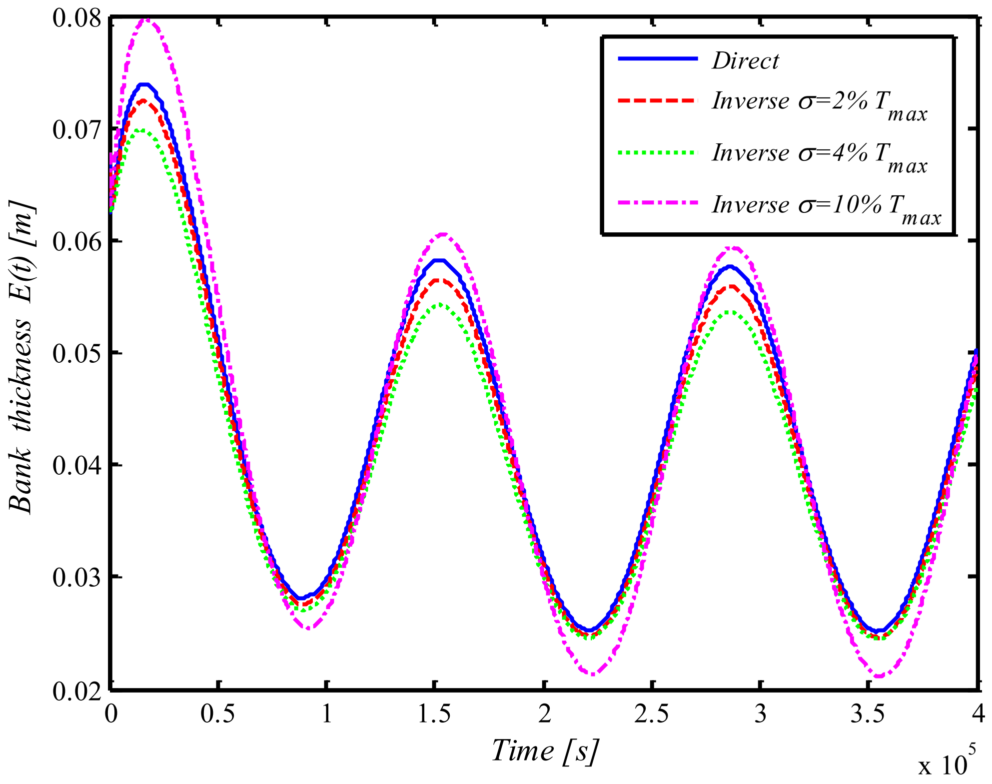

**Figure 3.11** Effect of noise on the predicted bank thickness with sensor #1.

**Table 3.5** Effect of noise on the prediction of polynomial parameters with sensor #1.

| | | $\sigma = 2\% T_{max}$ | | $\sigma = 4\% T_{max}$ | | $\sigma = 10\% T_{max}$ | |
|---|---|---|---|---|---|---|---|
| | $P_{Exact}$ | $P_{Inverse}$ | $Error_P$ % | $P_{Inverse}$ | $Error_P$ % | $P_{Inverse}$ | $Error_P$ % |
| $Q_0$ $(W/m^2)$ | 6000 | 6019.95 | 0.33 | 6084.62 | 1.41 | 5770.42 | 3.83 |
| $Q_1$ $(W/m^2)$ | 5000 | 4964.51 | 0.71 | 4874.03 | 2.52 | 5438.88 | 8.78 |
| $k_{brick}$ $(W/m\ K)$ | 16.8 | 18.92 | 12.62 | 30.59 | 82.08 | 7.72 | 54.05 |
| $k_{PCM,solid}$ $(W/m\ K)$ | 1 | 0.97 | 3.00 | 0.91 | 9.00 | 1.19 | 19.00 |
| $k_{PCM,liquid}$ $(W/m\ K)$ | 10 | 8.29 | 17.10 | 7.33 | 26.70 | 9.63 | 3.70 |

## 3.7. Conclusion

A simple and yet accurate inverse heat transfer procedure was presented for predicting the time-varying thickness of the protective bank that covers the lining of the brick walls of a molten material reactor. The inverse method predicts simultaneously influential thermo-physical properties of the reactor such as the thermal conductivity of the refractory brick wall $k_{Brick}$, the thermal conductivity of the solid and of the liquid layers of the phase change material $k_{PCM,solid}$ and $k_{PCM,liquid}$ respectively, and the time-varying reactor heat load $q''(t)$. The inverse method rests on the *Levenberg-Marquardt* Method (LMM) combined to the *Broyden* method (BM). The effect (1) of the initial guesses for the unknown LMM polynomial parameters, (2) of the noise on the recorded temperature data, (3) of the location of the temperature sensors embedded into the brick wall and (4) of the number of recorded temperature data on the inverse predictions was investigated. Analysis of the results yielded recommendations concerning the installation and the operation of the temperature sensors.

## Acknowledgements

The authors are grateful to the Natural Sciences and Engineering Research Council of Canada (NSERC) for the financial support.

# 4. PRÉDICTION INVERSE DE LA RÉSISTANCE THERMIQUE DE CONTACT ET DE L'ÉROSION

## Avant-propos

**Auteurs et affiliation :**

**M. Hafid** : Étudiant au doctorat, Université de Sherbrooke, Faculté de génie, Département de génie mécanique.

**M. Lacroix** : Professeur, Université de Sherbrooke, Faculté de génie, Département de génie mécanique.

**Date d'acceptation :** 25 Août 2016

**État de l'acceptation :** Version finale publiée

**Revue :** Applied Thermal Engineering

**Référence :** [35]

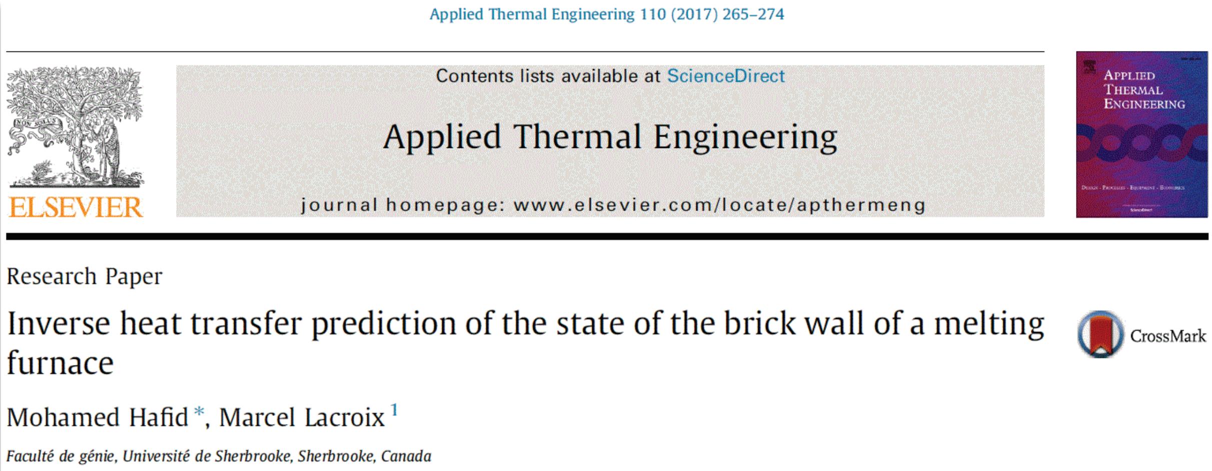

Applied Thermal Engineering 110 (2017) 265–274

Contents lists available at ScienceDirect

Applied Thermal Engineering

journal homepage: www.elsevier.com/locate/apthermeng

Research Paper

Inverse heat transfer prediction of the state of the brick wall of a melting furnace

Mohamed Hafid *, Marcel Lacroix [1]

*Faculté de génie, Université de Sherbrooke, Sherbrooke, Canada*

## Titre français

Prédiction par transfert inverse de l'état de la paroi de brique d'un four de fusion

## Résumé français

Une méthode de transfert de chaleur inverse pour prédire l'état de la paroi interne de briques réfractaires d'un four de fusion est présentée. À l’aide de mesures de température provenant d’un thermocouple implanté dans la paroi de brique, le procédé inverse est capable de prédire (1) l’évolution temporelle de l'épaisseur du banc qui recouvre l’intérieur de la paroi du four ; (2) la résistance thermique de contact entre le banc solidifié et la paroi de briques réfractaires et (3) l'érosion de la paroi interne de briques réfractaires. La procédure inverse repose sur l'algorithme de *Levenberg-Marquardt* combiné à la méthode de *Broyden*. L'effet (1) du bruit sur les mesures de température ; (2) de la diffusivité thermique de la paroi de briques réfractaires ; (3) de l'emplacement du capteur de température ; et (4) du nombre de Biot sur les prédictions inverses est étudié. Des recommandations pour la position optimale du capteur et son fonctionnement sont tirées.

## Mots clés

Méthode inverse, Changement de phase, Méthode de *Levenberg-Marquardt*, Méthode de *Broyden*, Four de fusion.

## Title

Inverse heat transfer prediction of the state of the brick wall of a melting furnace.

## Abstract

An inverse heat transfer method for predicting the state of the lateral refractory brick wall of a melting furnace is presented. By collecting temperature data with a thermocouple embedded into the brick wall, the inverse method is able to predict (1) the time-varying thickness of the protective bank that covers the inner lining of the furnace wall; (2) the thermal contact resistance between the inner lining and the protective bank; and (3) the possible erosion of the refractory brick wall. The inverse procedure rests on the *Levenberg Marquardt* algorithm combined with the *Broyden* method. The effect (1) of the noise on the collected temperature data; (2) of the thermal diffusivity of the brick wall; (3) of the location of the embedded temperature sensor; and (4) of the Biot number on the inverse predictions is investigated. Recommendations are made for the optimum position of the embedded sensor and its operation.

## Keywords

Inverse method; solid-liquid phase change; *Levenberg–Marquardt* Method; *Broyden* method; Melting furnace.

# Nomenclature

| | |
|---|---|
| $C_p$ | specific heat [J/kgK] |
| $dt$ | time step [s] |
| $f$ | liquid fraction |
| $h$ | heat transfer coefficient [W/m$^2$K] |
| $I$ | total number of measurements |
| $J$ | Jacobian matrix |
| $k$ | thermal conductivity [W/mK] |
| $L_{Brick}$ | width of the brick wall [m] |
| $L_{Erosion}$ | width of the erosion [m] |
| $L_{PCM}$ | width of the PCM layer [m] |
| $N$ | number of unknown parameters |
| $q^{"}(t)$ | heat flux [W/m$^2$] |
| $\vec{P}$ | vector of unknown parameter |
| $PCM$ | phase change material |
| $R_c$ | thermal contact resistance [K m$^2$/W] |
| $RRMSE$ | relative root-mean-square errors [%] |
| $Error$ | estimation errors [%] |
| $E(t)$ | bank thickness [m] |
| $t$ | time [s] |
| $\hat{T}$ | estimated temperature [K] |
| $x$ | Cartesian spatial coordinate [m] |
| $Y$ | measured temperature [K] |
| $\alpha$ | thermal diffusivity |
| $\varepsilon$ | small number |
| $\mu$ | damping parameter |
| $\rho$ | density [kg/m$^3$] |
| $\sigma$ | standard deviation of the measurement error |
| $\psi$ | sum of squares norm |
| $\xi$ | small number |
| $\delta H$ | enthalpy [J/m$^3$] |
| $\Delta$ | difference |
| $\Omega^k$ | diagonal matrix |
| $\lambda$ | heat of fusion [J/kg] |
| $\omega$ | random number |

**Subscripts**

| | |
|---|---|
| $0$ | initial value |
| $\infty$ | ambiant |
| $Brick$ | brick wall |
| exact | exact solution |
| $E$ | eutectic |
| $E(t)$ | bank thickness |
| $F$ | freezing point |
| $liq$ | liquidus |
| $liquid$ | liquid (PCM) |
| max | maximum |
| $PCM$ | phase change material |
| $P$ | parameter |
| $q^{"}(t)$ | heat flux |
| $R_c$ | thermal contact resistance |
| $sol$ | solidus |
| $solid$ | solid (PCM) |

**Superscripts**

| | |
|---|---|
| $k$ | time iteration number |
| $T$ | transposed matrix |
| $\hat{}$ | estimated parameter |
| $\vec{}$ | vector |
| $\overleftrightarrow{}$ | matrix |

## 4.1. Introduction

Melting furnaces such as electric arc furnaces (EAFs) are used for material processing that requires high power density and elevated temperatures. Some of their applications concern the smelting of copper, of nickel calcine, of steel and of pre-reduced iron ore and the melting/recycling of scrap metals. A schematic of a typical EAF is provided in Figure 4.1. High voltage electrodes (only one electrode is shown here) discharge their electric current into a bath of conducting slag. The current dissipates the heat (Joule effect) needed for the smelting process. The smelting reaction takes place in the slag layer and the denser metal sinks and accumulates at the bottom of the bath. Continuous loading of ore material is achieved though openings in the vault. Tapping of slag and metal is carried out at regular time intervals through perforated holes in the lateral walls. The furnace suffers heat losses though the vault via the freeboard gas above the slag layer. Heat is also lost by conduction through the refractory brick walls. Thermocouples are usually embedded into the vault and into the brick walls to monitor their temperature and, as it will be seen shortly, to provide information on the thermal conditions that prevail inside the furnace [17, 34, 58, 64].

An interesting solid/liquid phase change process that arises in these furnaces is the formation of a solid layer, called ledge or bank, on the inner surface of the refractory brick walls (Figure 4.1). The presence of this phase change material bank (PCM) is of the utmost importance [1, 71]. It protects the inner lining of the walls from the chemical attack of the molten material, thereby maintaining the integrity of the facility and prolonging its active life. On the other hand, too thick a bank is detrimental to the furnace output. It diminishes the bath volume available for smelting. Therefore, from an industrial point of view, the challenge is to operate the furnace by keeping a bank of optimum thickness that is a bank that protects the inner wall without hampering the furnace production.

Predicting the thermal behavior of banks inside EAFs is however a challenging problem. Their time-evolution depends on the complex heat transfer processes that prevail inside the molten bath as well as on the way the furnace is designed and operated. Measuring banks with probes plunged into the molten bath is impractical no to say dangerous. Simulating the heat transfer and the flow circulation inside the slag and the metal is feasible with modern CFD tools [157-163]. But this computational approach is time and resources consuming and it may not be the most suitable method to be implemented on line for the control system of an industrial facility. The most promising alternative appears to be the inverse heat transfer approach.

The prediction of phase change banks inside high temperature melting furnaces with inverse heat transfer methods has received increasing attention over the last decade [17, 34, 58-62, 64-66]. Sensors imbedded inside the refractory brick walls provide temperatures and/or heat fluxes to an inverse heat transfer algorithm that calculates the time-varying thickness of the bank.

In all the aforementioned studies however, the prediction of the thermal contact resistance between the brick wall and the bank was ignored. The erosion of the brick wall was also neglected.

The thermal contact resistance reflects the imperfect contact between two materials [164-167], in the present case these materials are the brick wall and the bank. The contact resistance attenuates the temperature and/or the heat flux signal captured by the sensor and fed to the inverse algorithm. As a result, the accuracy of the predictions of the bank made with the inverse algorithm is affected. In some cases, the predictions may even be worthless.

Another problem that arises in high temperature EAFs is the erosion of the inner lining of the refractory brick wall [83, 84, 88, 90, 92]. This phenomenon occurs when the bank is lost and the inside lining of the wall suddenly becomes exposed to the hostile molten material. Erosion of the brick wall is a slow and insidious process that may eventually lead to the destruction of the facility [86, 87, 89, 91].

These problems are addressed in the present study. An inverse heat transfer procedure is proposed for predicting simultaneously: (1) the time-varying lateral heat flux (and therefore the protective bank thickness) and the thermal contact resistance; and (2) the time-varying lateral heat flux and the erosion of the refractory brick wall. The numerical simulation of the solid/liquid phase change of the bank rests on the enthalpy method [168, 141]. The inverse algorithm employs the *Levenberg-Marquardt* Method (LMM) in conjunction with the *Broyden* method [152]. The numerical procedure is first validated. Next, it is employed to investigate the effect (1) of the noise on the collected temperature data; (2) of the thermal diffusivity of the brick wall; (3) of the location of the embedded temperature sensor; and (4) of the Biot number on the inverse predictions.

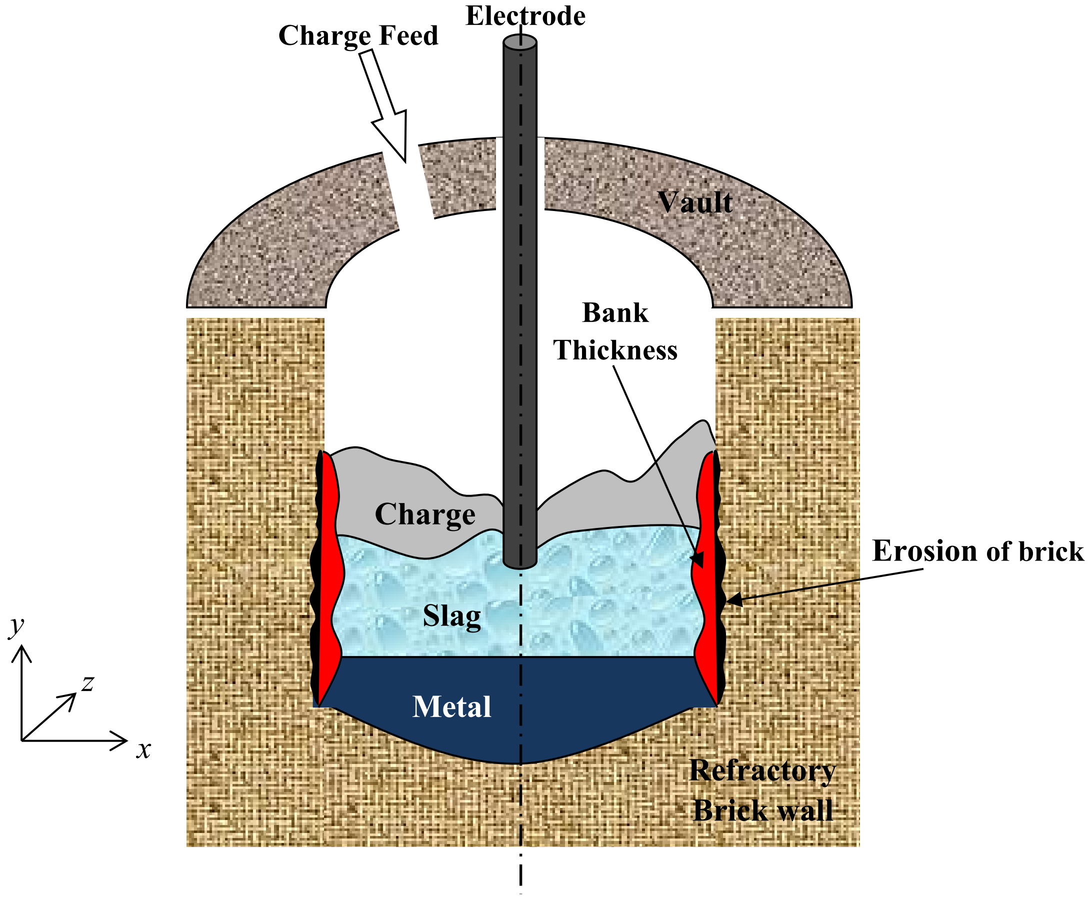

**Figure 4.1** Cross view of a typical electric arc melting furnace.

## 4.2. The direct problem

This section describes what is called the direct problem. In the direct problem, all the physical and the geometrical properties are known. The objective of the direct model is to determine the transient temperature field $T(x,t)$ and, from there, to calculate the time-varying thickness of the protective phase change material bank $E(t)$.

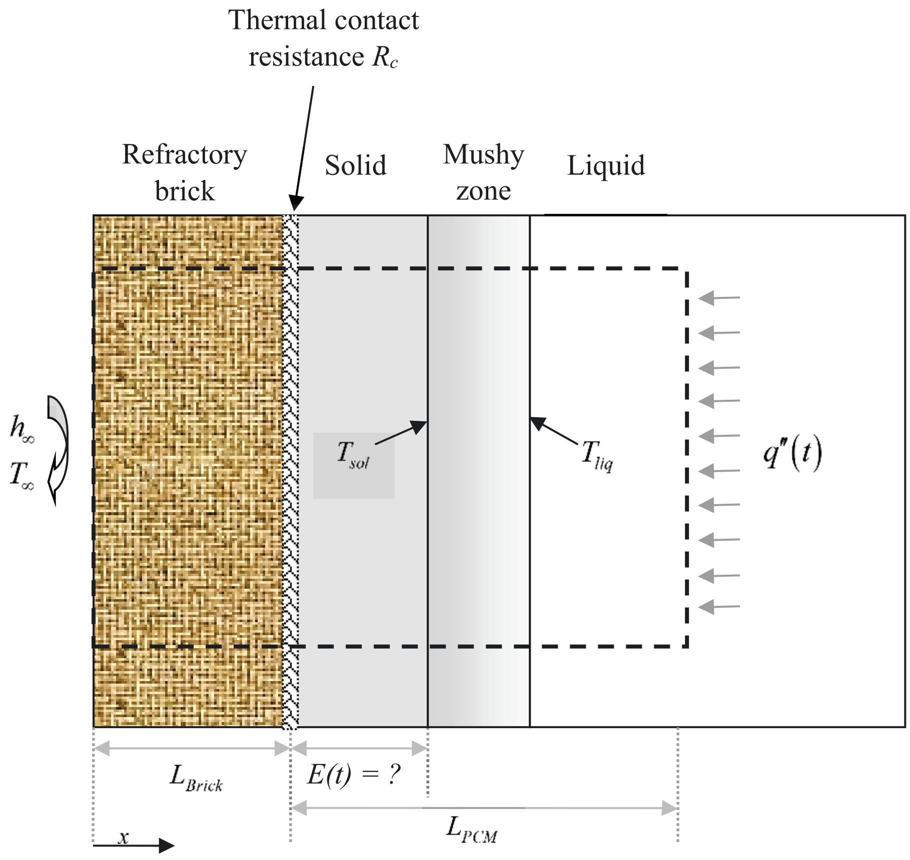

**Figure 4.2** Schematic of the direct problem. $q''(t)$ and $R_c$ are known. *E(t)* is unknown. It is predicted numerically with the direct model.

The direct model of Figure 4.2 rests on the following assumptions [17, 34, 58, 61, 62, 64]:

- The thickness $(L_{brick}+L_{PCM})$ of the brick wall and of the PCM layer (*x* direction) is small in comparison to the height (vertical direction) and the depth (direction perpendicular to the picture) of the furnace. Furthermore, the temperature gradients across the wall (*x* direction) are much larger than the temperature gradients in the other directions. Consequently, a one-dimensional model can be applied.
- The phase change problem is non-isothermal. The melting and the solidification processes occur over a temperature range.
- The thermal properties of the phase change material (PCM) are temperature independent. They may, however, be different for the solid and liquid phases.

- The heat transfer inside the liquid phase of the PCM (slag) is conduction dominated [17, 142].
- The thermal contact resistance $R_c$ between the refractory brick wall and the PCM is constant [62].

The outer surface of the refractory brick wall (*x=0*) is cooled by convection heat transfer. The convective heat transfer coefficient is $h_\infty$ and the constant outside temperature is $T_\infty$. At the right boundary, i.e., $x = L_{Brick} + L_{PCM}$, a time-varying heat flux $q''$(t) is imposed over the time interval $t = [0\ ;\ t_{\max}]$. The inner surface of the brick wall is covered by a protective bank whose time-varying thickness is *E(t)*. *E(t)* represents the position of the solidification front of the PCM. The PCM is composed of a solid layer, a mushy zone and liquid layer (Figure 4.2).

The governing heat diffusion equation for the refractory brick wall and for the PCM is stated as

$$\rho C_p \frac{\partial T}{\partial t} = \frac{\partial}{\partial x}\left( k \frac{\partial T}{\partial x} \right) - \delta H \frac{\partial f}{\partial t} \tag{4.1}$$

$f$ and $\delta H$ are the liquid fraction and the enthalpy, respectively. The enthalpy $\delta H$ is defined as $\delta H = \rho(C_{p,liquid} - C_{p,solid})T + \rho\lambda$.

The liquid fraction *f*, varies linearly between the solidus $T_{sol}$ and the liquidus $T_{liq}$ according to the following relationship:

$$f = F(T) = \begin{cases} 0 & T \le \mathrm{T}_{sol} \quad (Solid) \\ \dfrac{T - T_{sol}}{T_{liq} - T_{sol}} & \mathrm{T}_{sol} < T < \mathrm{T}_{liq}\ (Solid - liquid) \\ 1 & T \ge \mathrm{T}_{liq} \quad (Liquid) \end{cases} \tag{4.2}$$

The boundary conditions are:

$$\left( k \frac{\partial T}{\partial x} \right)_{x=0} = h_\infty \left( T(0,t) - T_\infty \right) \tag{4.3}$$

$$\left( k\frac{\partial T}{\partial x} \right)_{x=L_{Brick}+L_{PCM}} = q''(t) \tag{4.4}$$

A thermal contact resistance $R_c$ is applied at $x = L_{Brick}$, that is the gap between the refractory brick wall and the PCM:

$$-k_{Brick}\left.\frac{\partial T_1}{\partial x}\right|_{x=L_{Brick}}^{Brick} = -k_{PCM}\left.\frac{\partial T_2}{\partial x}\right|_{x=L_{Brick}}^{PCM} = \frac{T_{Brick}-T_{PCM}}{R_c} \tag{4.5}$$

Eqs. (4.1)-(4.5) are solved numerically using a time-implicit finite-volume method [143]. At each time-step, the liquid fraction $f$ is updated iteratively according to the enthalpy method [141].

$$f^{k+1} \approx f^k + \left(\frac{dF}{dT}\right)^k \left(T^{k+1} - F^{-1}\left(f^k\right)\right) \tag{4.6}$$

$F$ is a function of the temperature $T$ (see Eq. (4.2)). $F^{-1}$ is the inverse function of $F$.

The above numerical model was first validated with the one-dimensional solidification of a binary aluminium-copper alloy. This problem is reported in Voller V. R. [140, 141]. The thermophysical properties of the alloy are summarized in Table 4.1.

**Table 4.1** Thermophysical properties of the binary aluminum-Copper alloy [140, 141].

| Parameter | Value | Unit |
|---|---|---|
| $C_{p,\,solid}$ | 900 | J/kg K |
| $k_{solid}$ | 200 | W/m K |
| $\rho$ | 2800 | kg/m$^3$ |
| $C_{p,\,liquid}$ | 1100 | J/kg K |
| $k_{liquid}$ | 90 | W/m K |
| $\lambda$ | 3.9 x 10$^5$ | J/kg |
| $T_E$ | 821 | K |
| $T_F$ | 933 | K |
| $T_{liq}$ | 919 | K |

A Dirichlet boundary condition of $T = 573K$ is imposed at the boundary $x = L_{Brick}$ (Figure 4.2). The initial temperature is set equal to $T_{in} = 969$ K and the PCM layer thickness is set equal to $L_{PCM}$=0.5 m. The predicted solidus and liquidus fronts are depicted in Figure 4.3. It is seen that the predictions of the direct model are in excellent agreement with those of Voller.

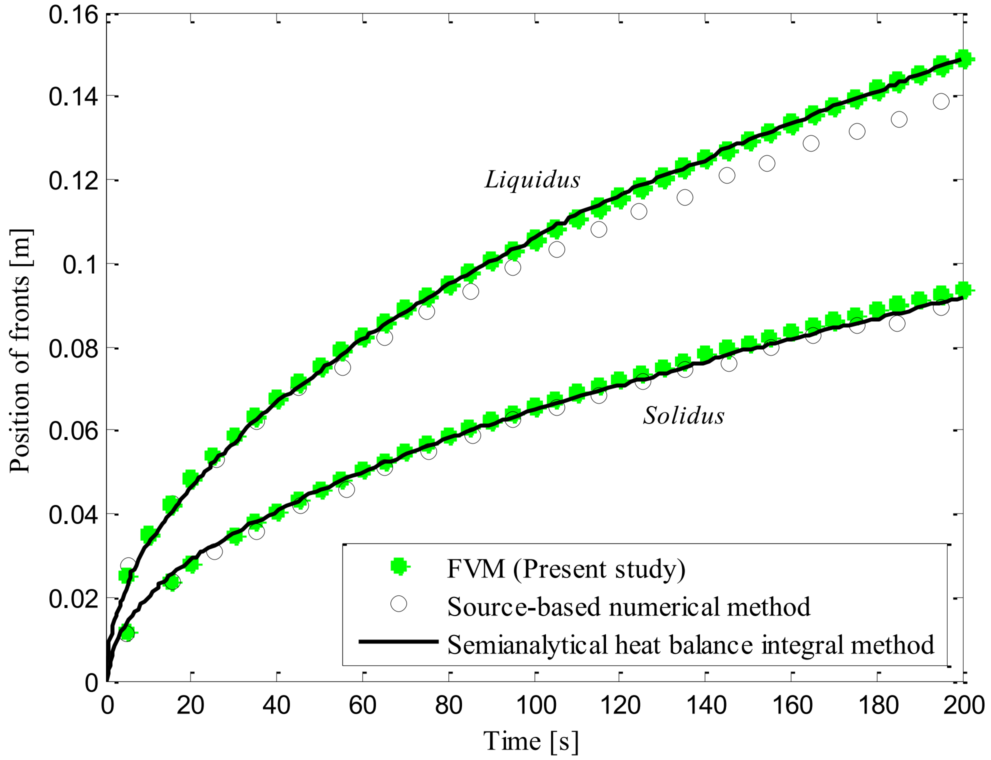

**Figure 4.3** Solidification of a binary Al–4.5%-Cu alloy: Comparison with the results reported by Voller [140, 141].

Next, the direct model was tested for a typical high-temperature melting furnace [34, 58]. In this case, the refractory brick wall is set equal to $L_{Brick}$ = $0.1m$ and the entire PCM layer (solid, mushy, and liquid) is set equal to $L_{PCM} = 0.1m$ (Figure 4.2). At $\left(x=0\right)$, i.e., the left boundary, the average heat transfer coefficient takes a value of $h_{\infty} = 15\ W/m^2.K$ and the outside temperature is fixed at $T_{\infty} = 300$ K. At $\left(x = L_{Brick} + L_{PCM}\right)$ , i.e., the right boundary, the heat flux $q''(t)$ is given by

$$q''(t) = \mathrm{P}_1 + P_2 * \sin^2\left(\frac{2\pi.t}{t_{\max}}\right) \qquad \text{at : } x = L_{Brick} + L_{PCM} \tag{4.7}$$

Also, the thermal contact resistance is set to

$$R_c = \mathrm{P}_3 \qquad \text{at : } x = L_{Brick} \tag{4.8}$$

The magnitude of the parameters $P_1$, $P_2$ and $P_3$ in Eqs. (4.7) and (4.8) are provided in Table 4.2.

**Table 4.2** Parameters for the simulation of a high-temperature melting furnace (direct problem).

| Parameter | Value | Unit |
|---|---|---|
| $P_1$ | 7000 | $W/m^2$ |
| $P_2$ | 3000 | $W/m^2$ |
| $P_3$ | 0.02 | $m^2$ K /W |

At the time $t = 0$ s. The initial bank thickness is $E(t = 0) = 0.023$ m. The thermophysical properties of the refractory brick wall and of the PCM are summarized in Table 4.3 [58].

**Table 4.3** Thermophysical properties of the refractory brick wall and of the PCM [34, 58].

| Parameter | Value | Unit |
|---|---|---|
| $k_{BRICK}$ | 16.8 | W/m K |
| $C_{p, BRICK}$ | 875 | J/kg K |
| $\rho_{BRICK}$ | 2600 | $kg/m^3$ |
| $k_{PCM,solid}$ | 1 | W/m K |
| $k_{PCM,liquid}$ | 10 | W/m K |
| $C_{p, PCM,solid}$ | 1800 | J/kg K |
| $C_{p, PCM,liquid}$ | 1800 | J/kg K |
| $\rho_{PCM}$ | 2100 | $kg/m^3$ |
| $\lambda_{PCM}$ | $5.1 \times 10^5$ | J/kg |
| $T_{sol}$ | 1213 | K |
| $T_{liq}$ | 1233 | K |

All numerical simulations were conducted with a grid size of 200 uniformly distributed control volumes inside the brick wall and the PCM layer. A time step of 100 s was employed to advance the solution from $t$=0 to $t_{\max} = 400000$ s. Additional numerical simulations were performed in order to make sure that the predictions are space and time-step independent.

Figure 4.4 reveals that the predicted time-varying bank thickness for $R_c \approx 0$ (no contact resistance) is similar to the predictions of Lebreux et al. [58-61], Marois et al. [64-66] and Bertrand et al. [47]. Indeed, in all these studies, the effect of the thermal contact resistance between the refractory brick wall and the PCM was ignored. Figure 4.4 clearly shows however that the effect of $R_c$ on the predicted bank thickness must be accounted for. For instance, for $R_c$ = 0.02 $m^2$.K /W, a difference of almost 2 cm in the predicted bank thickness is observed with the case for $R_c \approx 0$. This 2 cm solid layer may seem thin but in the industrial context of high-temperature melting furnaces, it is all it takes to maintain the structural integrity of the refractory brick wall. As a result, the thermal contact resistance will henceforth be retained.

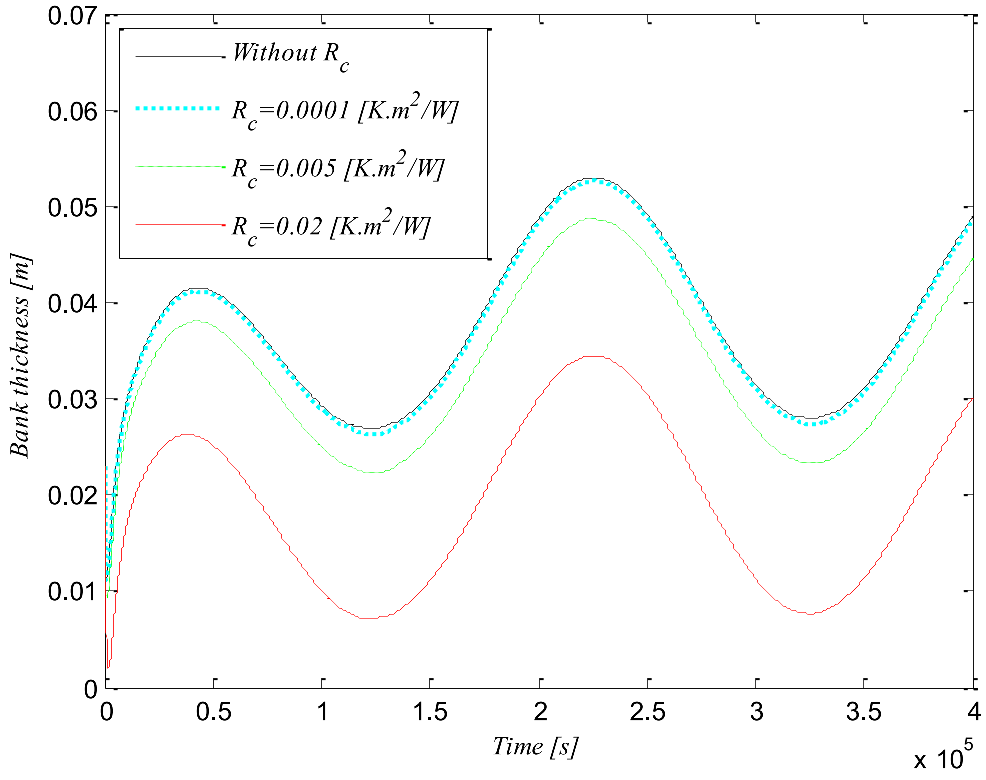

**Figure 4.4** Effect of the thermal contact resistance on the bank thickness.

## 4.3. Inverse problem

In the inverse problem, the heat flux $q''(\mathrm{t})$ (at $x = L_{Brick} + L_{PCM}$) and the thermal contact resistance $R_\mathrm{c}$ (at $x = L_{Brick}$) are unknown, i.e. *($P_1$, $P_2$, $P_3$)* in Eqs. (4.7) and (4.8) are unknown. The objective of the inverse method is to determine the unknown parameters for $q''(\mathrm{t})$ and $R_\mathrm{c}$ by using temperature measurements taken from a sensor embedded into the refractory brick wall (Figure 4.5). Once the heat flux $q''(\mathrm{t})$ and the thermal contact resistance $R_\mathrm{c}$ are estimated, the bank thickness $E(t)$ is determined from the Finite-Volume Model (FVM) presented in section 4.2.

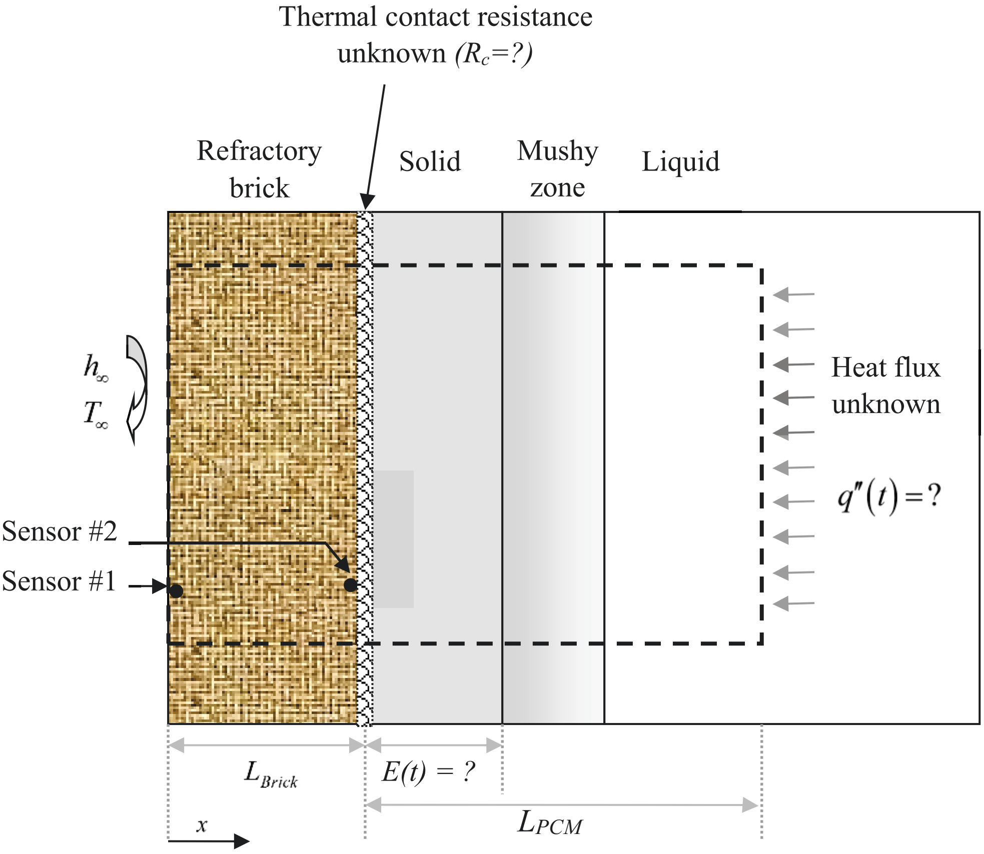

**Figure 4.5** The inverse problem: $q''(\mathrm{t})$ and $R_\mathrm{c}$ are unknown. They are determined from temperature measurements.

The solution for the inverse problem consists of minimizing the least square norm $\Psi\left(\vec{P}\right)$, where $P = (P_1, P_2, P_3)$ is the set of the unknown parameters:

$$\Psi\left(\vec{P}\right)=\sum_{i=1}^{I}\left[Y\left(t_i\right)-\hat{T}\left(t_i,\vec{P}\right)\right]^2 \tag{4.9}$$

Here $Y\left(t_i\right)$ are the temperatures measured with the sensor (Direct temperatures). In the present study, these temperatures are ‘generated’ from the solution of direct problem wherein the parameters vector $P = (P_1, P_2, P_3)$ are known (Table 4.2). $\hat{T}\left(t_i,\vec{P}\right)$ are the estimated temperatures from the inverse method. $I$ is the total number of measurements. The solution of the inverse problem is obtained when the least square norm $\Psi\left(\vec{P}\right)$ is minimized.

The present inverse problem is solved with the *Levenberg-Marquardt* parameter estimation method (LMM) [76, 144-148, 156]. This method is recommended when the unknown function can be parametrized. In this method, the incremental value of the unknown parameter $\Delta P$, is given by:

$$\Delta\vec{P}=\left[\left(\overleftrightarrow{J}^k\right)^T\overleftrightarrow{J}^k+\mu^k\overleftrightarrow{\Omega}^k\right]^{-1}\left(\overleftrightarrow{J}^k\right)^T\left(\vec{Y}-\vec{T}\left(\vec{P}^k\right)\right) \tag{4.10}$$

Here $\mu^k$ is a positive damping parameter. The choice and the update of this parameter is discussed in [150]. $\overleftrightarrow{\Omega}^k = diag\left[\left(\overleftrightarrow{J}^k\right)^T\overleftrightarrow{J}^k\right]$ is a diagonal matrix. The superscripts "↔" and "→" refer to the matrix and vector notation, respectively. The superscript "T" denotes the transpose of the matrix. $\overleftrightarrow{J}^k$ is the Jacobian matrix and it is defined as:

$$\overleftrightarrow{J}\left(\vec{P}\right)=\begin{pmatrix} \dfrac{\partial T_1}{\partial P_1} & \dfrac{\partial T_1}{\partial P_2} & \cdots & \dfrac{\partial T_1}{\partial P_N} \\ \dfrac{\partial T_2}{\partial P_1} & \dfrac{\partial T_2}{\partial P_2} & \cdots & \dfrac{\partial T_2}{\partial P_N} \\ \vdots & \vdots & & \vdots \\ \dfrac{\partial T_I}{\partial P_1} & \dfrac{\partial T_I}{\partial P_2} & \cdots & \dfrac{\partial T_I}{\partial P_N} \end{pmatrix} \tag{4.11}$$

The Jacobian matrix, also called the sensitivity matrix, plays a crucial role in the inverse problem of parameter estimation. There are several approaches for computing the Jacobian [151]. In the present study, the Jacobian ($\vec{J} \in R^{I*\mathrm{N}}$ where: $I$=800 and $N$=3) is approximated with a finite difference approximation. For example, the sensitivity coefficient is given by:

$$J_{ij} = \frac{\partial \hat{T}_i}{\partial P_j} \cong \frac{\hat{T}\left(t_i\ ; P_1, ..., P_j + \left(\delta P_j\right), ... P_N\right) - \hat{T}\left(t_i\ ; P_1, ..., P_j - \left(\delta P_j\right), ... P_N\right)}{2\left(\delta P_j\right)} \tag{4.12}$$

The subscripts $i$ and $j$ represent the time and the parameter, respectively. The parameter perturbation $\left(\delta P_j\right)$ is set to $\xi\left(1+\left|P_j\right|\right)$, where $\xi$ is a small number ($\xi = 0.001$).

At each iteration, the approximation of the sensitivity coefficients of the Jacobian matrix requires the solution of the direct problem 2*$N$ times ($N$=3). As a result, the finite difference approximation may become computationally prohibitive.

In order to reduce the computational effort, the Jacobian matrix is updated using the *Broyden* method [152]. This method has already been applied successfully in the field of inverse heat transfer [34, 154, 155]. In principle this method can be combined with the LMM to eliminate the need to compute the sensitivity coefficients at every iteration.

For the first iteration, for every *2*N* iterations and for iterations where $\Psi\left(P+\Delta P\right) > \Psi\left(P\right)$, the sensitivity coefficients of the Jacobian matrix are estimated with Eq. (4.12). For every other iteration, the Jacobian matrix is updated with the expression proposed by *Broyden*:

$$J_k = J_{k-1} + \frac{\left(\left(\hat{T}_k - \hat{T}_{k-1}\right) - J_{k-1}\Delta P_{k-1}\right)\Delta P_{k-1}^T}{\Delta P_{k-1}^T \Delta P_{k-1}} \tag{4.13}$$

$J_k$ and $J_{k-1}$ are the Jacobian matrices at the current and previous iteration, respectively. $\Delta P_{k-1}$ is the incremental value of the unknown parameters given by Eq. (4.10).

In order to obtain confidence intervals and confidence bounds for the estimated parameters, a statistical analysis is performed [151, 153]. It is assumed that the recorded temperatures are contaminated with measurement errors. For distributed measurement errors with zero mean and a constant variance $\sigma^2$, the standard deviation of the estimated parameters is given by

$$\sigma_{\hat{P}_i} = \sigma \sqrt{diag\left\{\left(\frac{\partial T^T}{\partial P}\right)\left(\frac{\partial T}{\partial P^T}\right)\right\}^{-1}} \tag{4.14}$$

Assuming a Gaussian distribution for temperature measurement errors and 99% confidence, the bounds for the computed quantities $P_i$ are determined as

$$\text{Probability}\left\{\left(\hat{P}_i - 2.576\ \sigma_{\hat{P}_i}\right) \le P_i \le \left(\hat{P}_i + 2.576\ \sigma_{\hat{P}_i}\right)\right\} \cong 99\% \tag{4.15}$$

$\hat{P}_i$ are the values estimated for the unknown parameters (*i=1; 2; 3*), and $\sigma_{\hat{P}_i}$ are the standard deviations obtained from Eq. (4.14).

The overall computational procedure using the *Levenberg-Marquardt* Method combined with the *Broyden* method is summarized as follows (Figure 4.6) :

Convergence of the LMM is declared when

$$\begin{cases} J^T \left\| Y(t_i) - \hat{T}(t_i, \vec{P}) \right\| < \varepsilon_1 \\ \left(\dfrac{P^{k+1} - P^k}{P^{k+1}}\right) < \varepsilon_2 \\ \Psi\left(P^{k+1}\right) < \varepsilon_3 \end{cases} \tag{4.16}$$

$\{\varepsilon_1;\ \varepsilon_2;\ \varepsilon_3\}$ are a small numbers.

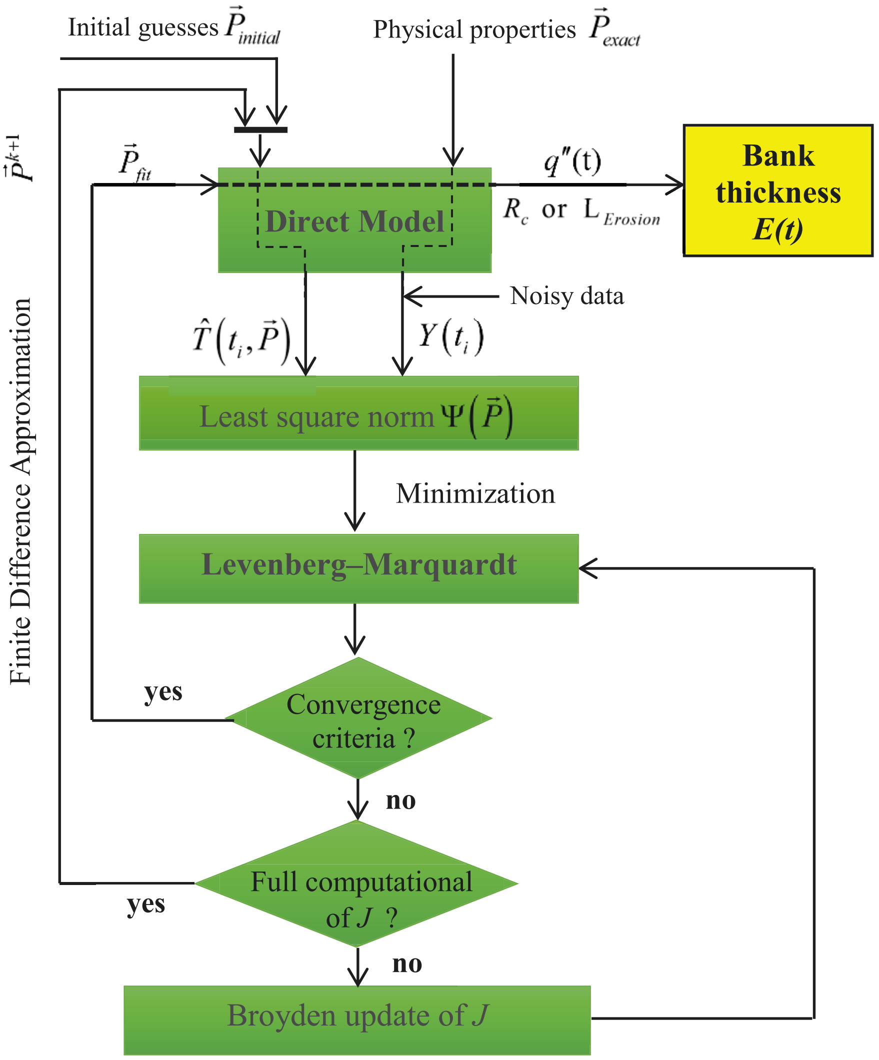

**Figure 4.6** Overall inverse calculation procedure.

## 4.4. Results and discussion

The above algorithm (Figure 4.6) for the inverse procedure was thoroughly applied to two different test cases.

The first test case is concerned with the simultaneous prediction of the unknown time-varying heat flux $q''(t)$ (at $x = L_{Brick} + L_{PCM}$) and the unknown thermal contact resistance $R_c$ between the refractory brick wall and the PCM (at $x = L_{Brick}$) (Figure 4.5).

In the second test case, the inverse procedure is employed to predict simultaneously the unknown time-varying heat flux and the unknown thickness of the eroded wall $L_{Erosion}$ (Figure 4.7).

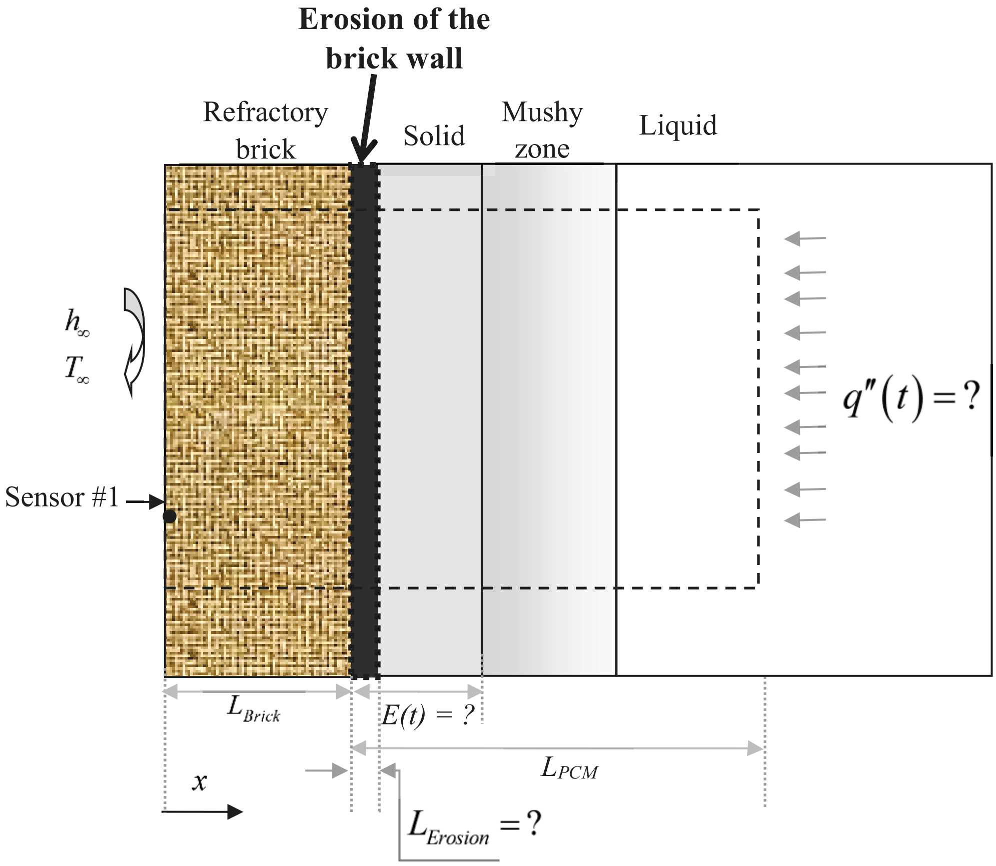

**Figure 4.7** The inverse problem of erosion. $q''$(t) and $L_{Erosion}$ are unknown. They are determined from the temperature measurements made with sensor#1.

Once (1) the heat flux $q''$(t) and (2) the thermal contact resistance $R_c$ or the thickness of the eroded wall $L_{Erosion}$ are estimated, the bank thickness *E*(*t*) is easily determined from the Finite-Volume Model (FVM) presented in section 4.2.

The transient temperatures measurements $Y(t_i)$ are taken with a sensor that may be placed at two different locations: The position called 'Sensor#1' is found at a depth of $x_1 = 0.5\times10^{-3}$ m inside the refractory brick wall. This location is close to the outside surface of the refractory brick wall (Figure 4.5). The position called 'Sensor#2' is found at a depth of $x_2 = 98.5 \times 10^{-3}$ m inside the refractory brick wall. This location is close to the inner lining of the refractory brick wall (Figure 4.5).

The total number of temperature recordings during an experiment (also called temperature measurements) is *I*=800 (the time-step is set equal to 500 s for a total time interval t=0, 400000 s).

The unknown time-varying heat flux $q''(\mathrm{t})$ and the unknown thermal contact resistance *R*c are parameterized with Eqs. (4.7) and (4.8), respectively.

Note that the accuracy and the uniqueness of the solution for the inverse problem have been thoroughly checked with noisy 'experimental measurements' and for different positions of the sensor embedded into the refractory brick wall. The extensive set of numerical experiments that were performed did not reveal the existence of multiple solutions.

For the sake of comparing the 'exact solution' provided by the direct model of section 4.2 and the 'estimated solution' obtained with the inverse model of section 4.3, the relative root-mean-square error (*RRMSE*) for the heat flux and the bank thickness are employed. These *RRMSEs* are defined as follows:

$$\mathrm{RRMSE}_{q''(t)}\,\% = 100 \times \sqrt{\frac{1}{I}\sum_{i=1}^{I}\left(\frac{q''(t_i)_{estimated} - q''(t_i)_{exact}}{q''(t_i)_{exact}}\right)^2} \tag{4.17}$$

$$\mathrm{RRMSE}_{E(t)}\,\% = 100 \times \sqrt{\frac{1}{I}\sum_{i=1}^{I}\left(\frac{E(t_i)_{estimated} - E(t_i)_{exact}}{E(t_i)_{exact}}\right)^2} \tag{4.18}$$

The error on the prediction of unknown parameters is also used. It is defined as:

$$Error_P\,\% = 100 \times \frac{\left\|P_{estimated} - P_{exact}\right\|}{\left\|P_{exact}\right\|} \tag{4.19}$$

Figure 4.8 compares the direct temperatures 'obtained with the direct model' to the inverse temperatures 'estimated by the inverse model'. The coincidence between both predictions is undisputable.

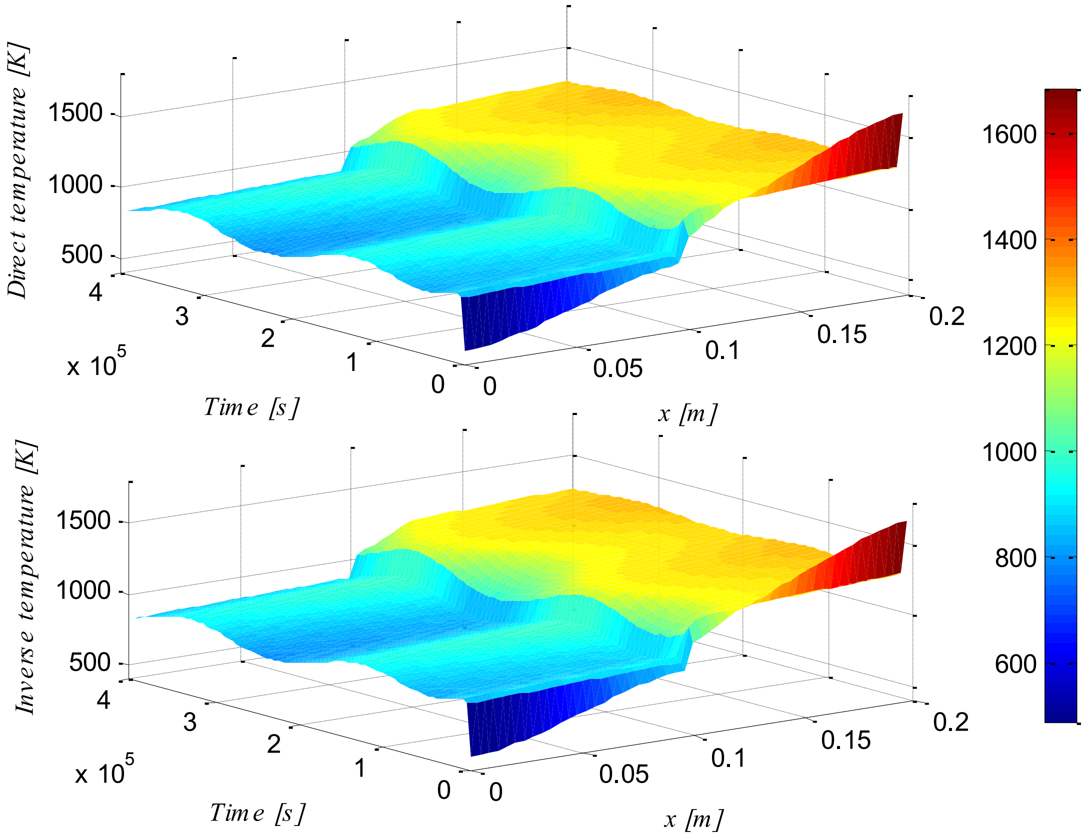

**Figure 4.8** Furnace temperature distributions, sensor#1, no noise.

### 4.4.1. Effect of temperature sensor location

Table 4.4 shows the effect of the sensor position (sensor#1 and sensor#2) and of the thermal diffusivity of the refractory brick wall on the accuracy of the predicted bank thickness $E(t)$, heat flux $q''(t)$ and thermal contact resistance $R_c$. It is seen that the effect of the sensor position on the accuracy of the predictions is insignificant [17, 34, 77]. As a result, sensor #1 is recommended over sensor#2. Not only does it provide equally accurate information but it is also much easier and safer to install a sensor near the outer surface of the brick wall.

On the other hand, as expected, the $\mathrm{RRMSE}_{E(t)}$, the $\mathrm{RRMSE}_{q''(t)}$ and the $Error_{R_c}$ slightly diminish as the thermal diffusivity of the brick wall increases.

**Table 4.4** Effect of the sensor position and of the thermal diffusivity of refractory brick on $\mathrm{RRMSE}_{E(t)}$, $\mathrm{RRMSE}_{q''(t)}$ and $Error_{R_c}$ ; no noise ( $\sigma = 0$ ).

| | **Thermal Diffusivity ($m^2/s$)** | **Position (mm)** | |
|---|---|---|---|
| | | 0.5 (Sensor#1) | 98.5 (Sensor#2) |
| ***RRMSE<sub></sub>*** | | | |

| | **Thermal Diffusivity ($m^2/s$)** | **Position (mm)** | |
|---|---|---|---|
| | | 0.5 (Sensor#1) | 98.5 (Sensor#2) |
| ***$RRMSE_{E(t)}$ %*** | $\alpha_{k_{Brick}=10} = 4.4*10^{-6}$ | 16.3 | 15.7 |
| | $\alpha_{k_{Brick}=16.8} = 7.4*10^{-6}$ | 5.3 | 5.2 |
| | $\alpha_{k_{Brick}=20} = 8.8*10^{-6}$ | 3.1 | 3.0 |
| ***$RRMSE_{q(t)}$ %*** | $\alpha_{k_{Brick}=10} = 4.4*10^{-6}$ | 0.1 | 0.1 |
| | $\alpha_{k_{Brick}=16.8} = 7.4*10^{-6}$ | 0.1 | 0.1 |
| | $\alpha_{k_{Brick}=20} = 8.8*10^{-6}$ | 0.0 | 0.0 |
| ***$Error_{Rc}$ %*** | $\alpha_{k_{Brick}=10} = 4.4*10^{-6}$ | 4.1 | 3.9 |
| | $\alpha_{k_{Brick}=16.8} = 7.4*10^{-6}$ | 3.5 | 3.5 |
| | $\alpha_{k_{Brick}=20} = 8.8*10^{-6}$ | 2.2 | 2.1 |

## 4.4.2. Effect of measurement noise

Noisy experimental data $\vec{T}(\mathrm{t}_i)$, i.e., measurements contaminated with errors, were also simulated. An error is added to $\vec{T}_{exact}(\mathrm{t}_i)$ (the temperature predicted by the direct model) in the following manner:

$$\vec{T}(\mathrm{t}_i) = \vec{T}_{exact}(\mathrm{t}_i) + \sigma\vec{\omega}_i \tag{4.20}$$

$\sigma$ is the standard deviation of the measurement errors. Its magnitude is set equal to 2% $T_{max}$. $T_{\max}$ is the maximum temperature measured by the sensor. $\vec{\omega}_i$ is a random number. This number is provided by a random number generator (for example, the *randn* function of Matlab).

Figure 4.9 compares the noisy temperature data generated with the direct model to the estimated temperatures predicted by the inverse model using sensor #1. The confidence bounds $\pm 2.576\ \sigma_{\hat{P}_i}$ are also shown.

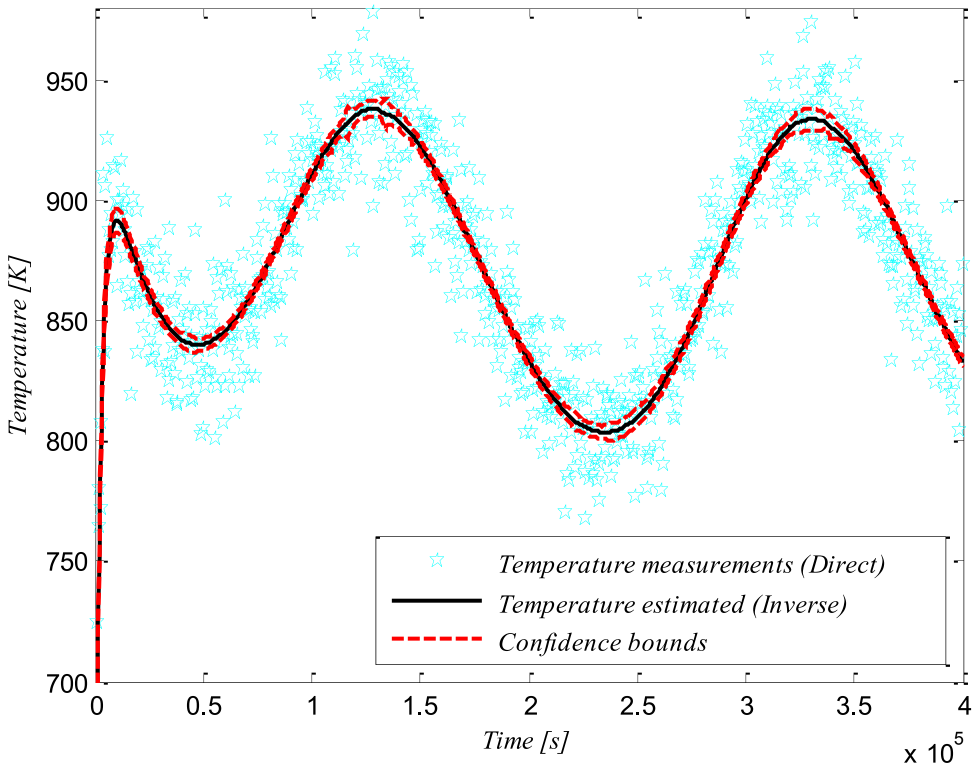

**Figure 4.9** Measured (direct model) and predicted temperatures (inverse model) obtained with sensor #1; $\sigma = 2\%\ T_{max}$.

Figures 4.10 and 4.11 show the effect of the noise level on the predicted time-varying bank thickness *E(t)* and heat flux $q''(\mathrm{t})$ using sensor #1. As expected, when the noise level rises to 2% $T_{max}$, the $RRMSE_{q''(t)}$, the $\mathrm{RRMSE}_{E(t)}$ and the $Error_{R_c}$ increase from *(0.1 %, 5.3 %, 3.5 %)* to *(0.2 %, 14.8 %, 9.5 %)*, respectively. Nevertheless, the inverse method remains stable and accurate in spite of the noisy signals.

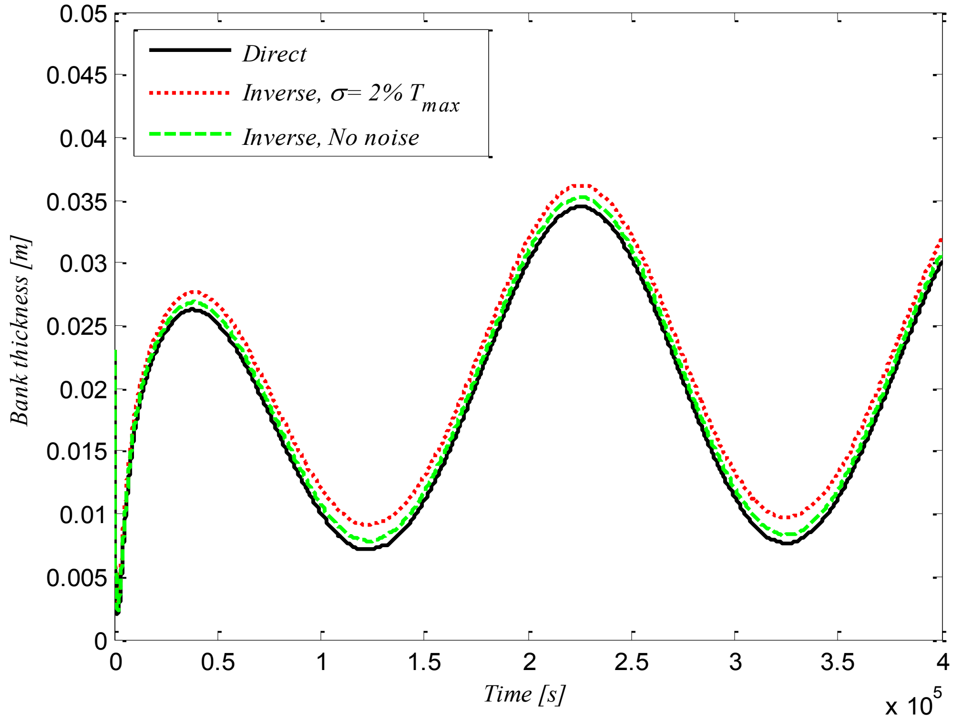

**Figure 4.10** Effect of the noise on the predicted bank thickness from sensor #1.

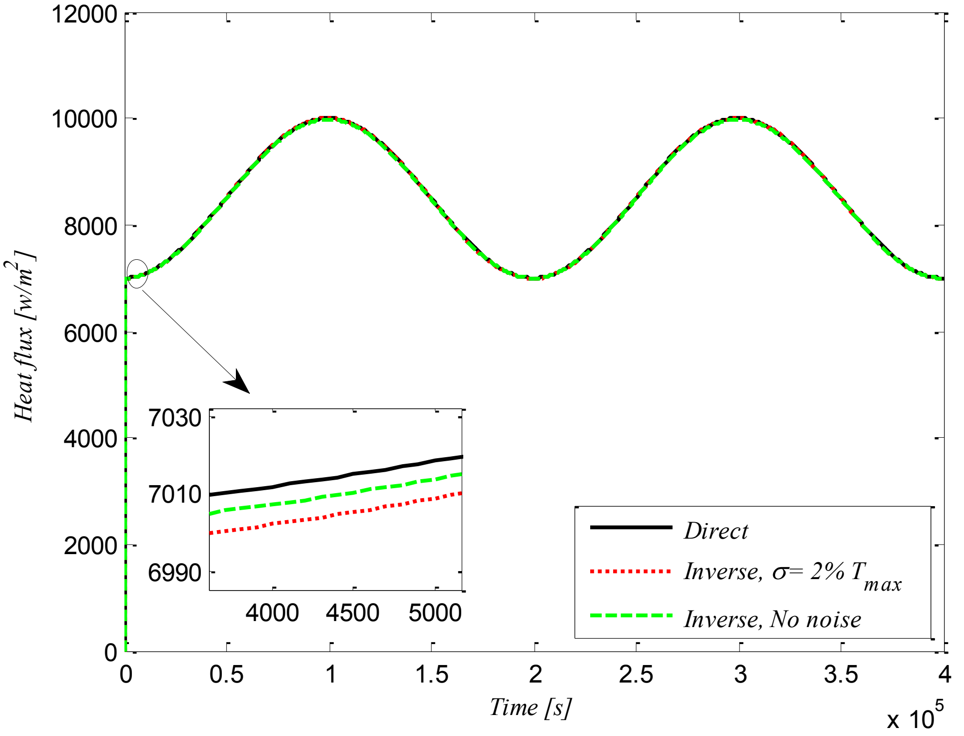

**Figure 4.11** Effect of the noise on the predicted heat flux $q''(t)$ from sensor #1.

### 4.4.3. Effect of the Biot number

The effect of the Biot number $Bi = \frac{h_\infty . L_{Brick}}{k_{Brick}}$ on the predicted bank thickness is depicted in Figure 4.12. When the Biot number is small ( $Bi \approx 0.09$ ), the inverse predictions from sensor #1 are excellent. A small Biot number represents the case of an air-cooled brick wall ( $h_\infty = 15\ W/m^2.K$ ). On the other hand, when the Biot number becomes large ( $Bi \approx 9$ ), the inverse predictions made with sensor #1 deteriorate. This is the case, for instance, with a water-cooled brick wall ( $h_\infty = 1500\ W/m^2.K$ ). The temperature signal captured by sensor #1, which is located close the outer surface of the brick wall, is contaminated by the high cooling rate of water. In this case, the use of sensor #2 (embedded deeper into the brick wall) is recommended. Note that as the Biot number increases, the heat losses through the lateral brick wall augment and, consequently, the bank becomes thicker.

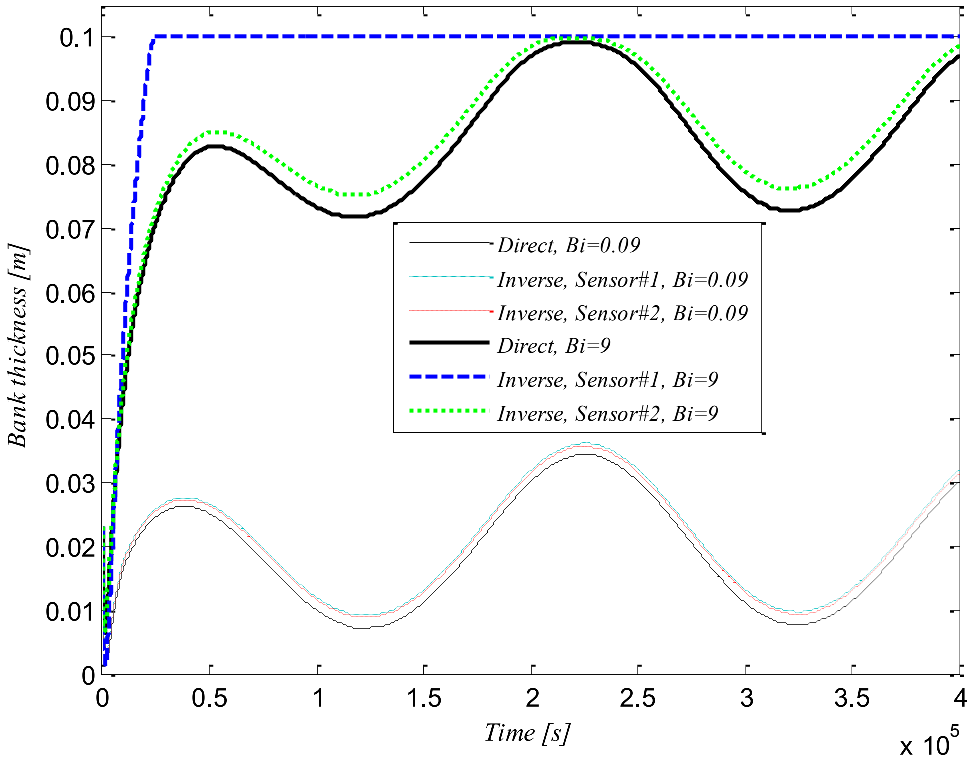

**Figure 4.12** Effect of the Biot number on the predicted bank thickness; $\sigma = 2\%\ T_{max}$

### 4.4.4. Erosion of the refractory brick wall

When the protective bank is lost, the inner lining of the refractory brick wall suddenly comes into direct contact with the molten material. As a result, the exposed wall becomes vulnerable to erosion.

Let us assume that the inner side of the refractory brick wall is eroded with $L_{Erosion}$=0.01 m. The space that used to be filled with brick material is now filled with molten PCM. This situation may be simulated numerically by letting the 'protective bank' move to the left, in the negative *x* values. Moreover, since erosion of the refractory brick wall is a slow process [86], [89], the eroded portion of the wall may be considered time-independent within the time-intervals simulated here (t=400000 s).

A test case for which the inverse model was used to predict simultaneously the heat flux $q''$(t) and the eroded portion of the brick wall $L_{Erosion}$ is presented next.

The direct model is first employed to generate the temperature data with sensor#1. The data are contaminated with noise levels of $\sigma = 2\%\ T_{max}$ and $\sigma = 4\%\ T_{max}$. For this simulation, the eroded portion of the wall $L_{Erosion}$ is fixed and the following heat flux $q''$(t) is imposed at $\left(x = L_{Brick} + L_{PCM}\right)$:

$$q''(t) = \underset{P_1}{7000} + \underset{P_2}{4000} * \sin^2\left(\frac{2\pi.t}{t_{\max}}\right) \tag{4.21}$$

$$\mathrm{L}_{Erosion} = 0.01\ \ \mathrm{m} = \mathrm{P}_3 \tag{4.22}$$

Furthermore, it is assumed that the thermal contact resistance between the brick wall and the PCM is known. It is set equal to $R_c$ = 0.02 m$^2$.K /W, a typical value. The physical proprieties of the eroded region are similar to that of the PCM. They are reported in Table 4.3.

In the inverse solution method, the heat flux $q''$(t) and the eroded portion of the wall $L_{Erosion}$ are predicted by determining the unknown parameters ($P_1$, $P_2$, $P_3$) in Eqs (4.21) and (4.22). Once these parameters are obtained, the time-varying bank thickness *E(t)* is calculated from the direct model described in section 4.2.

Table 4.5 summarizes the effect of the noise on the prediction of heat flux ($P_1$ and $P_2$) and of the eroded portion of the wall ($P_3$). The overall discrepancy between the inverse predictions and the exact solution is recorded for the prediction of the brick wall erosion, $\boldsymbol{Error}_{Erosion}$ =14%.

The inverse prediction of the bank thickness is compared to the exact solution in Figure 4.13. The erosion of the wall is depicted by the negative bank thickness (negative *x* direction, Figure 4.7).

This example exemplifies how the present inverse model can be used for preventive maintenance. It predicts the onset of wall erosion so that corrective actions may be taken to prevent further damages to the wall.

**Table 4.5** Parameters of the heat flux and the erosion.

| | | $\sigma = 2\% T_{max}$ | | $\sigma = 4\% T_{max}$ | |
|---|---|---|---|---|---|
| | $P_{Exact}$ | $P_{inverse}$ | $Error_P$ % | $P_{inverse}$ | $Error_P$ % |
| $P_1$ $W/m^2$ | 7000 | 7037.6 | 0.5 | 7028.7 | 0.4 |
| $P_2$ $W/m^2$ | 4000 | 3953.4 | 1.2 | 3887.0 | 2.8 |
| $P_3$ $m$ | $10*10^{-3}$ | $10.8*10^{-3}$ | 8.0 | $8.6*10^{-3}$ | 14.0 |

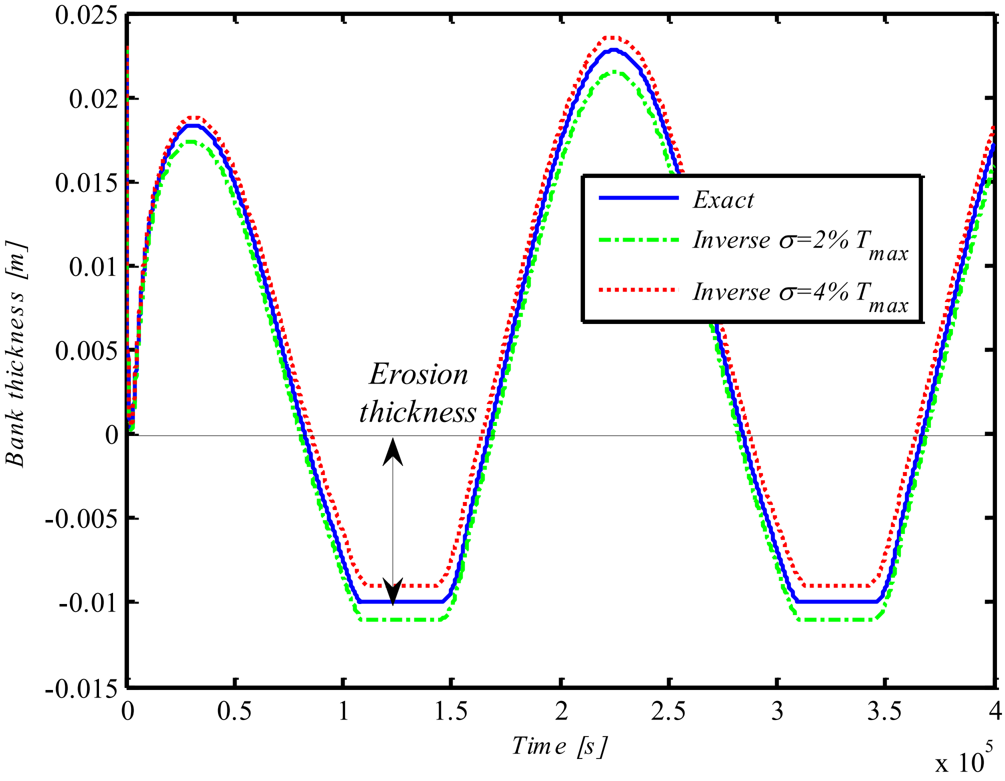

**Figure 4.13**. Predicted bank thickness with erosion.

## 4.5. Conclusion

An inverse heat transfer method for predicting the state of the lateral refractory brick wall of a melting furnace was presented. By collecting temperature data with a thermocouple embedded into the brick wall, the inverse method may predict (1) the time-varying thickness of the protective bank that covers the inner lining of the furnace wall; (2) the thermal contact resistance between the inner lining and the protective bank; and (3) the erosion of the refractory brick wall. The inverse procedure rests on the *Levenberg-Marquardt* algorithm combined with the *Broyden* method. The effect (1) of the noise on the collected temperature data; (2) of the thermal diffusivity of the brick wall; (3) of the location of the embedded temperature sensor; and (4) of the Biot number on the inverse predictions was investigated. Recommendations were made for the optimum position of the embedded sensor and its operation.

## Acknowledgements

The authors are grateful to the Natural Sciences and Engineering Research Council of Canada (**NSERC**) for the financial support.

# 5. PRÉDICTION INVERSE DES PARAMÈTRES POLYNOMIAUX DE LA CONDUCTIVITÉ THERMIQUE DE MCP EN FONCTION DE LA TEMPÉRATURE

## Avant-propos

**Auteurs et affiliation :**

**M. Hafid** : Étudiant au doctorat, Université de Sherbrooke, Faculté de génie, Département de génie mécanique.

**M. Lacroix** : Professeur, Université de Sherbrooke, Faculté de génie, Département de génie mécanique.

**Date de soumission** : 23 Décembre 2016

**Revue :** Applied Thermal Engineering

**Référence :** [36]

## Titre français

Prédiction des paramètres polynomiaux d’un four de fusion par le transfert de chaleur inverse.

## Résumé français

Une procédure de transfert thermique inverse permettant de prédire simultanément les paramètres thermiques d'un four de fusion est présentée. Ces paramètres sont (1) le coefficient de transfert thermique externe, (2) les paramètres polynomiaux de la conductivité thermique de MCP qui dépendent de la température et (3) le flux de chaleur du four. Une fois ces paramètres estimés, l’évolution temporelle de revêtement protecteur qui recouvre la surface interne de la paroi du four est prédite. Le changement de phase solide/liquide du MCP est modélisé par la méthode enthalpique. Le problème inverse repose sur la méthode de *Levenberg-Marquardt* (LMM) combinée à la méthode de *Broyden* (BM). L’effet de la position de capteur dans le mur de brique, de la fréquence d’acquisition des données et du bruit sur les mesures de température est étudié. Une analyse statistique pour l'estimation des paramètres est également effectuée. Des recommandations concernant l'emplacement du capteur et la fréquence d’acquisition des données sont faites.

## Mots clés

Transfert de chaleur inverse, Four de fusion, Changement de phase, Méthode de *Levenberg-Marquardt*, Méthode de *Broyden*, Revêtement protecteur.

# Title

Multi-Parameter Estimation of a Melting Furnace by Inverse Heat Transfer

# Abstract

An inverse heat transfer procedure is presented for predicting simultaneously operating and thermal parameters of a melting furnace. These parameters are the external heat transfer coefficient, the thermal conductivity of the phase change material (PCM) and the time-varying heat load of the furnace. Once these parameters are estimated, the time-varying protective PCM bank that coats the internal surface of the furnace wall can be predicted. The melting and solidification of the PCM is modeled with the enthalpy method. The inverse problem is handled with the *Levenberg-Marquardt* Method (LMM) combined to the *Broyden* method (BM). The models are validated and the effect of the position of the temperature sensor embedded in the furnace wall, of the data capture frequency and of the measurement noise, is investigated. A statistical analysis for the parameter estimation is also carried out. Recommendations are made concerning the location of the embedded sensor and the data capture frequency.

# Keywords

Inverse heat transfer; Melting furnace; phase change; *Levenberg–Marquardt* Method; *Broyden* Method; bank.

# Nomenclature

| | |
|---|---|
| $C_p$ | specific heat [J/kgK] |
| $dt$ | time step [s] |
| $f$ | liquid fraction |
| $h_\infty$ | heat transfer coefficient [W/m$^2$K] |
| $I$ | total number of measurements |
| $J$ | Jacobian matrix |
| $k$ | thermal conductivity [W/mK] |
| $L_{Brick}$ | width of the brick wall [m] |
| $L_{PCM}$ | width of the PCM layer [m] |
| $N$ | number of unknown parameters |
| $q''(t)$ | heat flux [W/m$^2$] |
| $\vec{P}$ | vector of unknown parameter |
| $PCM$ | phase change material |
| $RRMSE$ | relative root-mean-square errors [%] |
| $Error$ | estimation errors [%] |
| $E(t)$ | bank thickness [m] |
| $t$ | time [s] |
| $\hat{T}$ | estimated temperature [K] |
| $x$ | Cartesian spatial coordinate [m] |
| $Y$ | measured temperature [K] |

**Greek symbols**

| | |
|---|---|
| $\varepsilon$ | small number |
| $\mu$ | damping parameter |
| $\rho$ | density [kg/m$^3$] |
| $\sigma$ | standard deviation of the measurement error |
| $\psi$ | sum of squares norm |
| $\xi$ | small number |
| $\delta H$ | enthalpy [J/m$^3$] |
| $\Delta$ | difference |
| $\Omega^k$ | diagonal matrix |
| $\lambda$ | heat of fusion [J/kg] |
| $\omega$ | random number |

**Subscripts**

| | |
|---|---|
| 0 | initial value |
| $\infty$ | ambiant |
| $Brick$ | brick wall |
| exact | exact solution |
| $E(t)$ | bank thickness |
| $liq$ | liquidus |
| $liquid$ | liquid (PCM) |
| max | maximum |
| $P$ | parameter |
| $PCM$ | phase change material |
| $sol$ | solidus |
| $solid$ | solid (PCM) |

**Superscripts**

| | |
|---|---|
| $k$ | time iteration number |
| $T$ | transposed matrix |
| ^ | estimated parameter |
| → | vector |
| ↔ | matrix |

## 5.1. Introduction

Melting furnaces, such as electric arc furnaces, are used for material processing that requires high powers and elevated temperatures (Figure 5.1). Their main applications are the smelting of materials such as steel, copper and nickel calcine. High voltage electrodes discharge their electric load into the bath of electrically conducting slag (or phase change material PCM). The current is carried between the electrode tip and the slag to generate the heat required for the smelting process.

An interesting solid/liquid phase change phenomenon that arises in these furnaces is the formation of solid layer, called a bank, that covers the internal surface of the refractory brick walls. This bank plays a crucial role. It protects the brick walls from the highly corrosive molten material, thereby prolonging the life of the facility. Too thick a bank is however detrimental to the furnace throughput as the volume available for smelting is reduced. Keeping a bank of optimal size is therefore crucial for the safe and profitable operation of the smelting furnace.

It is extremely difficult to measure the bank thickness using probes submerged into the molten bath. The hostile conditions that prevail in the melt damage and destroy the probes. This method is time consuming, risky and often inaccurate. Moreover, the transient formation of the bank is a most complex process that depends on the power input, the boundary conditions and the thermophysical properties of the slag.

In recent years, the problem of bank formation inside high temperature melting furnaces has been tackled with various inverse heat transfer methods [17, 34, 35, 47, 58-66, 75]. The inverse heat transfer methods rest on the conjugate gradient method with the adjoint equation [17, 47, 64, 65, 71], the Kalman-filter method [58-63] and the *Levenberg-Marquardt* method [34, 35, 66, 75]. In these studies, the thermophysical properties of the materials and the operating conditions of the furnace are fixed. The focus is on the inverse prediction of the time-varying heat load of the furnace (the heat flux $q''(t)$ at $\left(x = L_{Brick} + L_{PCM}\right)$ (Figure 5.2). Once the heat load is determined, the time-varying bank thickness *E(t)* is predicted.

Recently, [34] have predicted the heat flux and thermal conductivity inside the molten material reactor. They assumed that the external heat transfer coefficient is known and thermal conductivity of bank is temperature independent. Indeed, inside high temperature reactors, it is important to consider the effect of temperature on the thermal conductivity.

The objective of the present investigation is to go one step further. It develops a *Levenberg-Marquardt* method (LMM) for the simultaneous inverse heat transfer prediction of several key parameters of the melting furnace: (1) the time-varying heat flux $q''(t)$; (2) the external heat transfer coefficient $h_\infty$; (3) the temperature-dependent thermal conductivity of the solid phase of the PCM and (4) thermal conductivity of the liquid phase of the PCM (Figure 5.4). Moreover, the LMM is combined with the *Broyden* method (BM) in order to reduce the computational time [152].

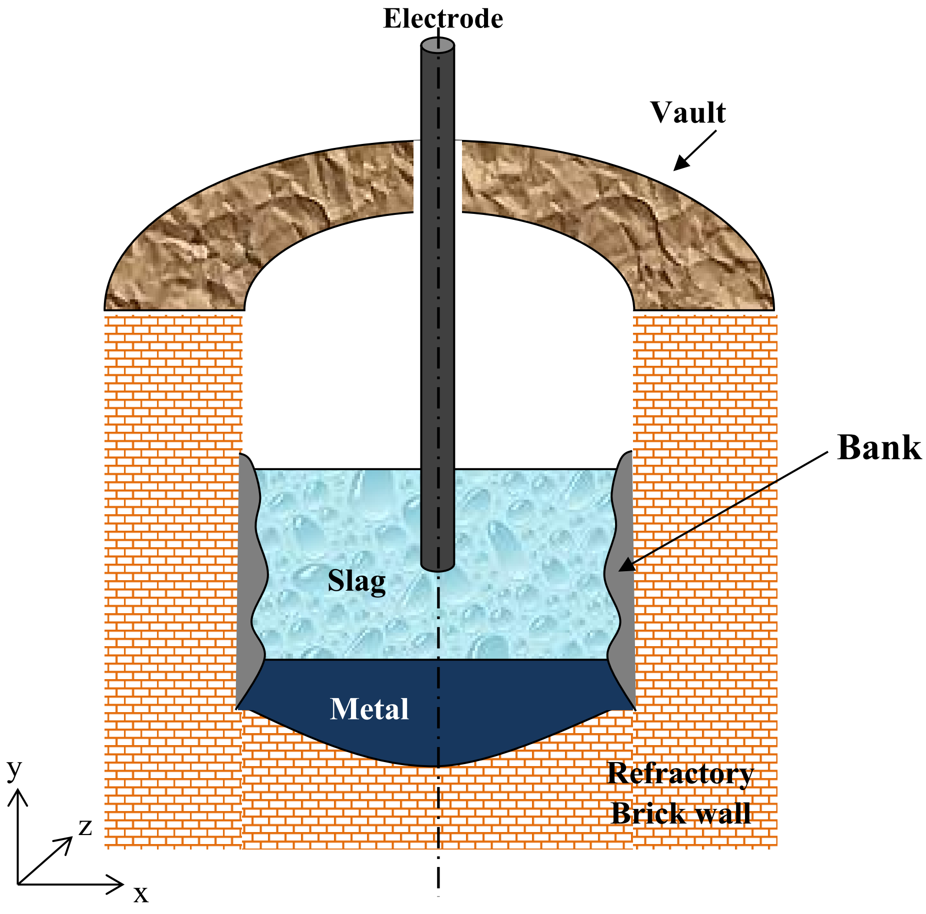

**Figure 5.1** Cross view of a melting furnace.

This paper is organized as follows. A mathematical model based on the enthalpy method is first presented for dealing with the melting-solidification problem [168]. The phase change model is validated with results available in the open literature [140, 141]. Next, the *Levenberg-Marquardt* Method (LMM) combined with the *Broyden* Method (BM) is deployed. The overall inverse method is then used to estimate the unknown parameters for typical operating conditions of a melting furnace. Finally, the effect of the location of the embedded temperature sensors, of the measurement noise and of the data-capture-frequency is investigated.

## 5.2. Direct problem

For the direct model, the geometry and the thermophysical properties of the furnace are known. The objective here is to compute the transient temperature field *T(x,t)* inside the furnace (the PCM and the lateral wall) and the time varying thickness of the protective bank *E(t)*.

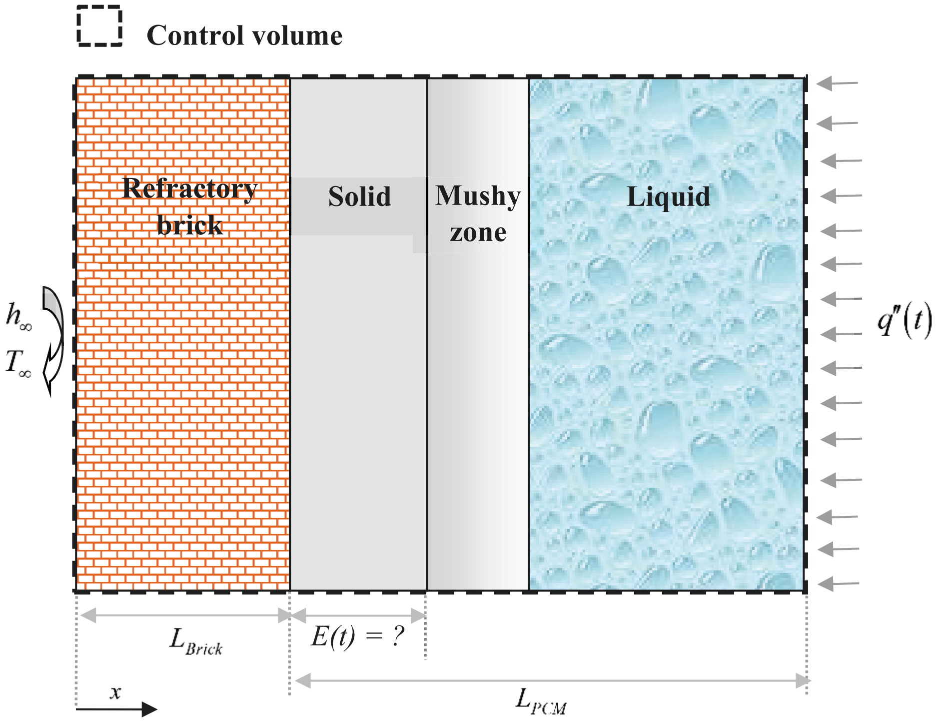

**Figure 5.2** Schematic of the 1-D direct problem.

Figure 5.2 shows a schematic of the 1-D direct problem. The left boundary condition (the external surface of the refractory brick wall, *x=0*) is cooled by convection heat transfer. The external convective heat transfer coefficient is $h_\infty$ and the external temperature is $T_\infty$. At the right boundary ($x = L_{Brick} + L_{PCM}$), a time-varying heat flux $q''$(t) is imposed over the time interval $t = \left[0\ ;\ t_f\right]$. The internal surface of the refractory brick wall is covered with a protective bank whose thickness *E(t)* is unknown and time-dependent. *E(t)* corresponds to the position of the solidification front of the PCM.

The mathematical model for the phase change problem rests on the following assumptions:

- The temperature gradients in the *x* direction of the furnace are much larger than those in the other directions. As a result, a one-dimensional analysis can be applied (Figure 5.2) [34, 35].
- The phase change problem is non-isothermal. The melting/solidification process of the bank takes place over a temperature range. The melting process is depicted by three zones: a solid phase, a solid/liquid phase or a mushy zone and a liquid phase.
- The thermal properties of the phase change material (PCM) are temperature independent except for the thermal conductivity in the solid state which is temperature-dependent.
- The heat transfer inside the liquid phase of the PCM (the slag) is conduction dominated [17, 142].
- The thermal contact resistance between the refractory brick wall and the PCM is neglected [34, 58, 65].

Based on the above assumptions, the governing heat diffusion equation is

$$\rho C_p \frac{\partial T}{\partial t} = \frac{\partial}{\partial x}\left(k\frac{\partial T}{\partial x}\right) - \delta H \frac{\partial f}{\partial t} \tag{5.1}$$

$\delta H$ and $f$ are the enthalpy and the liquid fraction of the PCM respectively. The same equation governs the conduction heat transfer through the refractory brick wall. In this case however, there is no phase change and, as a result, $\frac{\partial f}{\partial t} = 0$. The enthalpy $\delta H$ of the PCM is defined as $\delta H = \rho(C_{p,liquid} - C_{p,solid})T + \rho\lambda$. The liquid fraction $f$ is a function of temperature. It varies linearly between the solidus $T_{sol}$ and the liquidus $T_{liq}$ in the following manner:

$$f = F(T) = \begin{cases} 0 & T \le \mathrm{T}_{sol} \quad (\mathit{Solid}\ \text{region}) \\ \dfrac{T - T_{sol}}{T_{liq} - T_{sol}} & \mathrm{T}_{sol} \le T \le \mathrm{T}_{liq} \, (\mathit{Mushy}\ \text{region}) \\ 1 & T \ge \mathrm{T}_{liq} \quad (\mathit{Liquid}\ \text{region}) \end{cases} \tag{5.2}$$

At each time-step, *f* is updated iteratively according to the enthalpy method using the following expression [141].

$$f^{k+1} \approx f^{k} + \left(\frac{dF}{dT}\right)^{k} \left(T^{k+1} - F^{-1}\left(f^{k}\right)\right) \tag{5.3}$$

$F$ is a function of the temperature *T*. $F^{-1}$ is the inverse function of *F*.

The boundary conditions are:

$$\left(k \frac{\partial T}{\partial x}\right)_{x=0} = h_{\infty}\left(T(0,t) - T_{\infty}\right) \tag{5.4}$$

$$\left(k \frac{\partial T}{\partial x}\right)_{x=L_{Brick}+L_{PCM}} = q''(t) \tag{5.5}$$

Eqs. (5.1)-(5.5) are solved numerically using a time-implicit Finite-Volume Method (FVM) [143].

The accuracy of the FVM and enthalpy method was validated with results available in the open literature. For the sake of validation, the one-dimensional solidification problem of a binary alloy reported by Voller [140, 141] was simulated. The predicted solidus and liquidus fronts are shown in Figure 5.3. It is seen that the predictions of the 1-D direct model are in excellent agreement with those of Voller. More information about the validation is available in [35].

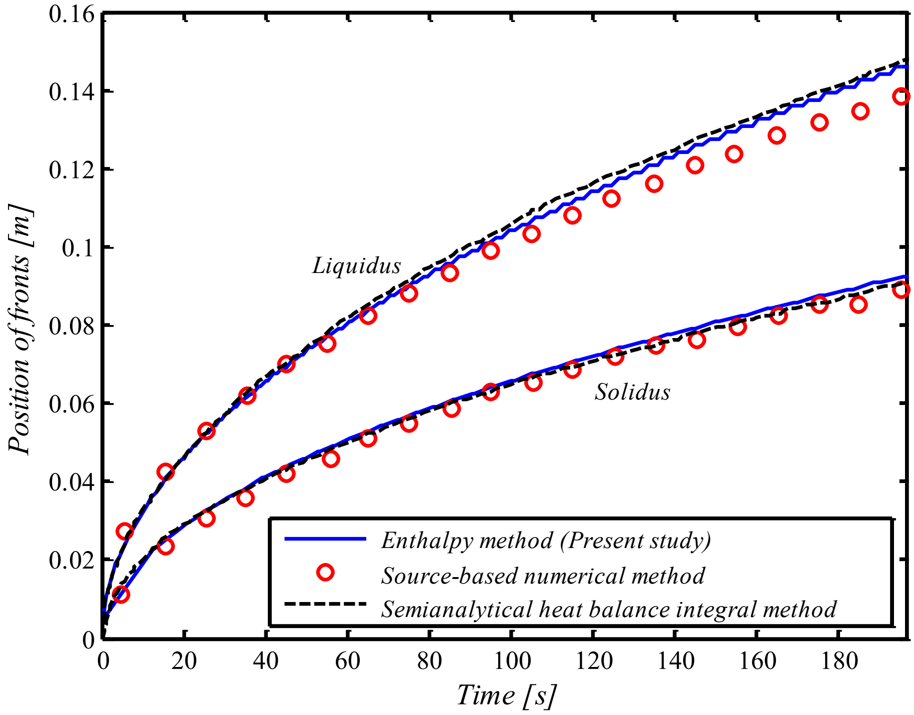

**Figure 5.3** Solidification of a binary *Al–4.5%*-Cu alloy: Comparison of the 1-D direct model (FVM) with the results reported by Voller.

Next, the 1-D direct model was implemented for the entire melting furnace (PCM and brick wall). The operating thermal conditions of the furnace are similar to those reported in [34, 35, 58]. The brick wall is set equal to $L_{Brick} = 0.1$ m and the thickness of the slag layer (solid, mushy, and liquid) is set equal to $L_{PCM} = 0.1$ m (Figure 5.2). At $(x = 0)$, the external temperature is set equal to $T_\infty = 300$ K and the external average heat transfer coefficient is fixed at $h_\infty = 15\ W/m^2.K$. At the right boundary $(x = L_{Brick} + L_{PCM})$, the time-varying heat flux $q''(t)$ is given by

$$q''(t) = q_0 + q_1 * \sin^2\left(\frac{2\pi.t}{t_{\max}}\right) \tag{5.6}$$

It is also assumed that the PCM thermal conductivity in the solid phase is temperature-dependent, whereas the thermal conductivity in liquid phase remains constant (in order to mimic the effect of the flow circulation).

$$\begin{cases} k_{solid} = k_{s_0} + k_{s_1}\left(\dfrac{T}{800}\right) \\ k_{liquid} = k_l \end{cases} \tag{5.7}$$

The parameters for the heat flux and the thermal conductivity in Eqs. (5.6) and (5.7) are taken as $\left[q_0;\ q_1;\ k_{s_0};\ k_{s_1};\ k_l\right] = \left[5000;\ 4000;\ 1;\ 0.1;\ 10\right]$ respectively. The remaining thermo-physical properties for the refractory brick wall and for the PCM are summarized in Table 5.1 [34, 35, 58].

The initial bank thickness is $E(t=0) = 0.0678\ \text{m}$, and the initial temperature for the brick wall and for the PCM $\left(0 < x < L_{Brick} + L_{PCM}\right)$ are set equal to:

$$T_0(x) = T(x,0) = \frac{x}{(L_{Brick} + L_{PCM})}\left(1400 - T_\infty\right) + T_\infty \tag{5.8}$$

**Table 5.1** Thermo-physical properties of the refractory brick wall and of the PCM.

| Parameter | Value | Unit |
|---|---|---|
| $k_{BRICK}$ | 16.8 | W/m K |
| $C_{p,BRICK}$ | 875 | J/kg K |
| $\rho_{BRICK}$ | 2600 | kg/m$^3$ |
| $k_{PCM,solid}$ | 1 | W/m K |
| $k_{PCM,liquid}$ | 10 | W/m K |
| $C_{p,PCM,solid}$ | 1800 | J/kg K |
| $C_{p,PCM,liquid}$ | 1800 | J/kg K |
| $\rho_{PCM}$ | 2100 | kg/m$^3$ |
| $\lambda_{PCM}$ | 5.1 x 10$^5$ | J/kg |
| $T_{sol}$ | 1213 | K |
| $T_{liq}$ | 1233 | K |

To ensure grid-space and time-step independence, all numerical simulations were conducted with a grid size of 200 control volumes distributed uniformly inside the refractory brick wall and inside the PCM layer. The time step was set equal to 100 s.

## 5.3. Inverse problem

It is assumed, in the inverse problem, that the heat flux $q''(\mathrm{t})$, the external heat transfer coefficient $h_\infty$ and the thermal conductivity of the solid $k_{solid}$ and of liquid phases $k_{liquid}$ of the PCM are unknown (the coefficients $\left[q_0;\ q_1;\ h_\infty;\ k_l;\ k_{s_0};\ k_{s_1}\right]$ in Eqs. (5.6) and (5.7) are unknown).

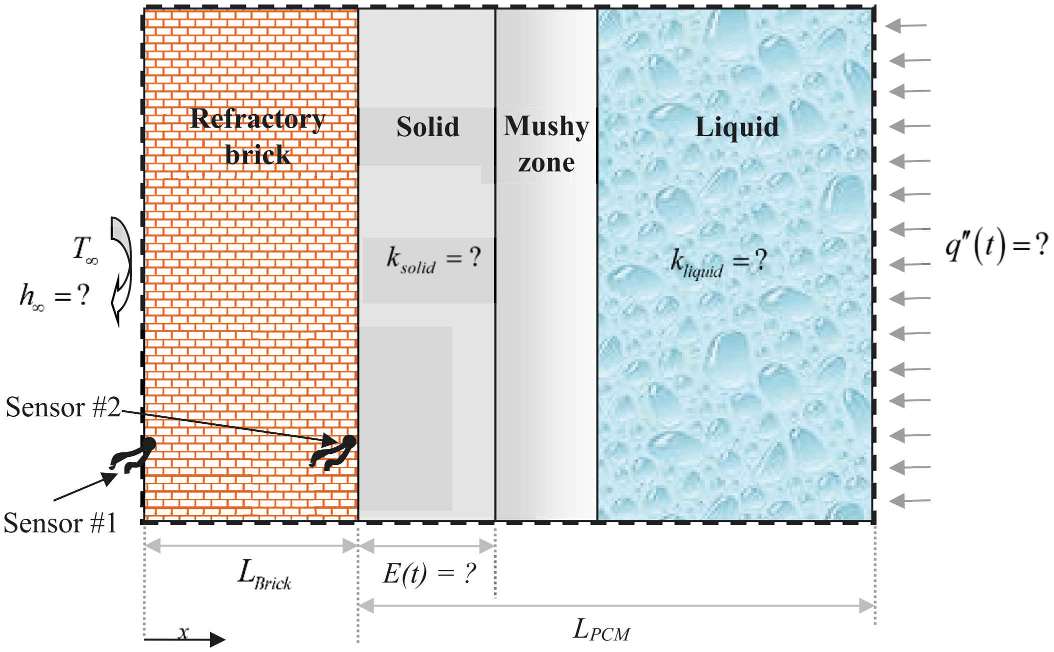

**Figure 5.4** The inverse problem: $q''(t)$, $\mathrm{k}_{solid}$, $\mathrm{k}_{liquid}$, and $\mathrm{h}_\infty$ are unknown. They are determined from temperatures measurements taken internal the refractory brick wall.

The objective of the inverse method is to determine the unknown coefficients $\vec{P}=\left[q_0;\ q_1;\ h_\infty;\ k_l;\ k_{s_0};\ k_{s_1}\right]$ by using temperature measurements taken from a sensor embedded into the brick wall (Figure 5.4). Once the time-varying heat flux $q''(\mathrm{t})$, the external heat transfer coefficient $h_\infty$ and the thermal conductivities ($k_{solid}$, $k_{liquid}$) are determined, the time-varying thickness $E(t)$ of the protective bank may be estimated from the 1-D direct model (FVM) presented above. The inverse procedure consists of transforming the problem into an optimum control problem which aims at minimizing the sum of the least square norm $\Psi(\vec{P})$ where $\vec{P}=\left[q_0;\ q_1;\ h_\infty;\ k_l;\ k_{s_0};\ k_{s_1}\right]$ is the vector of the unknown parameters:

$$\Psi\left(\vec{P}\right)=\left[Y_i-\hat{T}_i\left(\vec{P}\right)\right]^T W\left[Y_i-\hat{T}_i\left(\vec{P}\right)\right] \tag{5.9}$$

$Y_i$ are the temperatures measured with the sensor embedded into the brick wall. For the sake of the present study, these temperatures are 'generated' from the solution of the direct problem (section 5.2). $\hat{T}_i\left(\vec{P}\right)$ are the estimated temperatures from the inverse problem. $W$ is the weighting matrix. It is often taken as a diagonal matrix with its elements equal to $\left(\sigma^2\right)^{-1}$, where $\sigma$ is the variance of the measurement error. The superscript"T" denotes the transpose of the matrix. The solution of the inverse problem is obtained by minimizing $\Psi(P)$. The inverse problem is solved with the *Levenberg–Marquardt* Method (LMM). This method has been successfully applied to inverse problems in the past [76, 144, 145, 147-149, 169, 170-173]. In this iterative method, the incremental value of the unknown parameters $\Delta P$, is written as:

$$\Delta\vec{P}^k=\left[\left(\vec{J}^k\right)^T W\left(\vec{J}^k\right)+\mu^k\vec{\Omega}^k\right]^{-1}\left(\vec{J}^k\right)^T W\left(\vec{Y}_i-\vec{T}_i\left(\vec{P}^k\right)\right) \tag{5.10}$$

$\mu^k$ is a positive damping parameter. Its magnitude and update are discussed in [150]. $\vec{\Omega}^k=diag\left[\left(\vec{J}^k\right)^T\vec{J}^k\right]$ is a diagonal matrix. The superscript $k$ denotes the iteration number. The superscripts "$\vec{}$" and"$\ddot{}$" refer to the vector and matrix notation, respectively. $\vec{J}^k$ is the Jacobian matrix and it is defined as

$$\vec{J}\left(\vec{P}\right)=\begin{pmatrix}\dfrac{\partial T_1}{\partial P_1} & \dfrac{\partial T_1}{\partial P_2} & \cdots & \dfrac{\partial T_1}{\partial P_N}\\ \dfrac{\partial T_2}{\partial P_1} & \dfrac{\partial T_2}{\partial P_2} & \cdots & \dfrac{\partial T_2}{\partial P_N}\\ \vdots & \vdots & \ddots & \vdots\\ \dfrac{\partial T_I}{\partial P_1} & \dfrac{\partial T_I}{\partial P_2} & \cdots & \dfrac{\partial T_I}{\partial P_N}\end{pmatrix} \tag{5.11}$$

$I$ is the total number of measurements. $N$ is the number of unknown parameters. Here, ($N$=6) and $\vec{P} = \left[ q_0;\ q_1;\ h_\infty;\ k_l;\ k_{s_0};\ k_{s_1} \right]$.

There are several approaches for calculating the coefficients of the Jacobian matrix [151]. In the present work, the Jacobian ($\vec{J} \in \mathbb{R}^{I*N}$) is constructed with central finite difference approximations:

$$J_{ij} = \frac{\partial \hat{T}_i}{\partial P_j} \cong \frac{\hat{T}\left(t_i\ ; P_1,\ldots,P_j + \left(\delta P_j\right),\ldots P_N\right) - \hat{T}\left(t_i\ ; P_1,\ldots,P_j - \left(\delta P_j\right),\ldots P_N\right)}{2\left(\delta P_j\right)} \tag{5.12}$$

The subscripts $i$ and $j$ indicate the time and the parameter, respectively. The parameter perturbation $\left(\delta P_j\right)$ is set to $\xi\left(1+\left|P_j\right|\right)$, where $\xi$ is a small number.

The approximation of the sensitivity coefficients of the Jacobian matrix, Eq. (5.12), requires the solution of the direct problem 12 times per iteration. As a result, the finite difference approximation may become computationally prohibitive.

In order to diminish the computational time, the Jacobian matrix is updated using the *Broyden* Method (BM) [152]. The BM can be combined with the LMM to eliminate the need to compute the sensitivity coefficients at every iteration. This strategy has already been applied successfully in the field of inverse heat transfer problem (IHTP) [34, 35, 154, 155]. The sensitivity coefficients of the Jacobian matrix are estimated with a central difference approximation, Eq. (5.12), for the first iteration, for every 2*N iterations and for iterations in which $\Psi\left(P+\Delta P\right) > \Psi\left(P\right)$. For every other iteration, the Jacobian matrix is updated by the expression proposed by *Broyden*:

$$J_k = J_{k-1} + \frac{\left(\left(\hat{T}_k - \hat{T}_{k-1}\right) - J_{k-1}\Delta P_{k-1}\right)\Delta P_{k-1}^T}{\Delta P_{k-1}^T \Delta P_{k-1}} \tag{5.13}$$

$J_k$ and $J_{k-1}$ are the Jacobian matrices at the current and previous iteration, respectively. $\Delta P_{k-1}$ is the incremental value of the unknown parameters.

Convergence is declared when one of the following three criteria is satisfied:

$$\begin{cases} J^T \left\| Y(t_i) - \hat{T}(t_i, \vec{P}) \right\| < \varepsilon_1 \\ \left( \dfrac{P^{k+1} - P^k}{P^{k+1}} \right) < \varepsilon_2 \\ \Psi\left(P^{k+1}\right) < \varepsilon_3 \end{cases} \tag{5.14}$$

$\{\varepsilon_1 \ \varepsilon_2 \ \varepsilon_3\}$ are a small number, i.e., ($\varepsilon_1 = \varepsilon_2 = \varepsilon_3 = 0.001$).

## 5.3.1. Statistical analysis for parameter estimation

In order to assess the accuracy and the uniqueness of the inverse solution, a statistical analysis for parameter estimation is performed. It is assumed that the recorded temperatures are contaminated with measurement errors. For distributed measurement errors with zero mean and a constant variance $\sigma^2$, the standard deviation of the estimated parameters is given by

$$\sigma_{\hat{P}_i} = \sigma \sqrt{diag \left\{ \left( \frac{\partial T^T}{\partial P} \right) \left( \frac{\partial T}{\partial P^T} \right) \right\}^{-1}} \tag{5.15}$$

Assuming a normal (or Gaussian) distribution for temperature measurement errors and 99% confidence, the bounds for the computed quantities $P_i$ are determined as

$$\text{Probability} \left\{ \left( \hat{P}_i - 2.576\ \sigma_{\hat{P}_i} \right) < P_{i,exact} < \left( \hat{P}_i + 2.576\ \sigma_{\hat{P}_i} \right) \right\} \cong 99\% \tag{5.16}$$

$\hat{P}_i$ are the values estimated for the unknown parameters. $P_{i,exact}$ , for (*i=1,..., 6*), and $\sigma_{\hat{P}_i}$ are the standard deviations obtained from Eq. (5.15).

The overall computational algorithm for the inverse problem is summarized in Figure 5.5

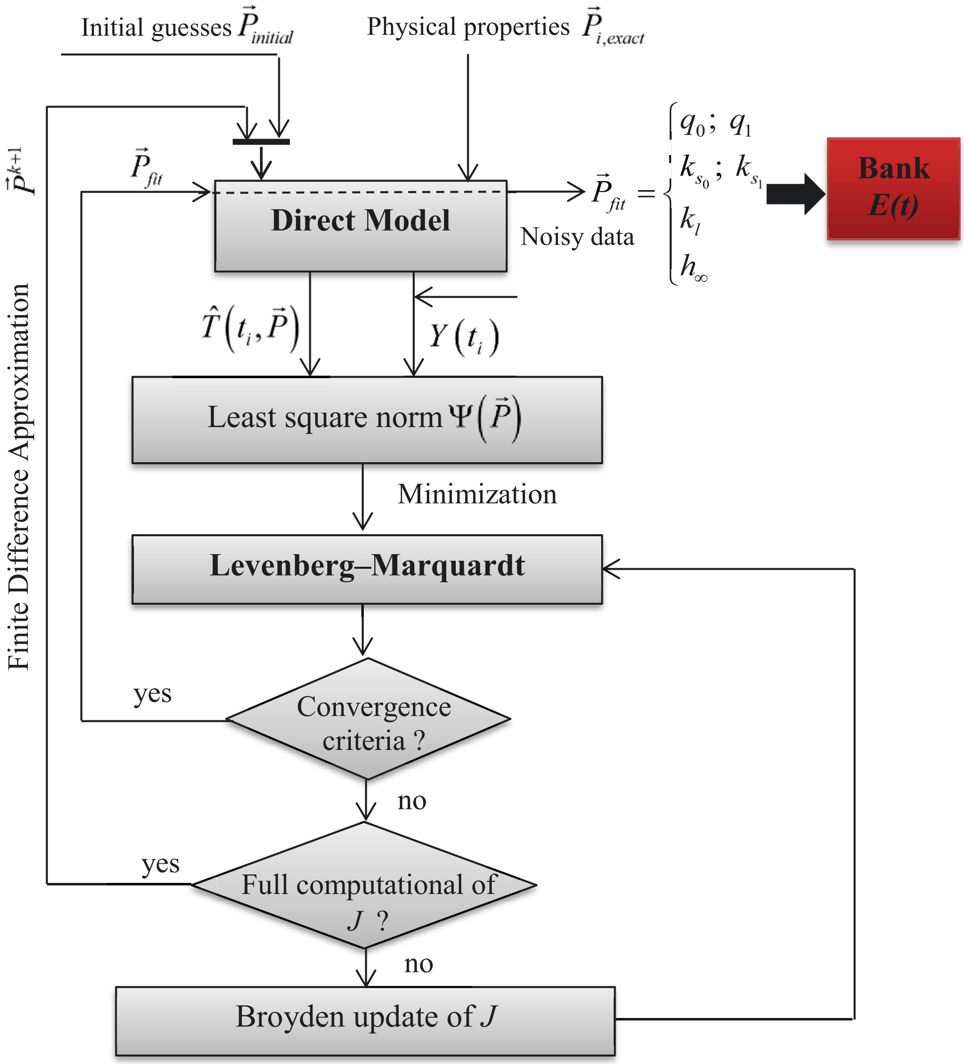

**Figure 5.5** Overall algorithm for the inverse method.

## 5.4. Results and discussion

The above inverse calculation algorithm (Figure 5.5) was thoroughly tested for estimating simultaneously the following unknown parameters:

- ✓ The heat flux $\left(q_0;\ q_1\right)$ at $x = L_{Brick} + L_{PCM}$;
- ✓ The external heat transfer coefficient $\left(h_\infty\right)$;
- ✓ The temperature-dependent thermal conductivity $\left(k_{s_0};\ k_{s_1}\right)$ in the solid PCM;
- ✓ The constant thermal conductivity $\left(k_l\right)$ in liquid PCM.

Once the unknown parameters $\left[q_0;\ q_1;\ h_\infty;\ k_l;\ k_{s_0};\ k_{s_1}\right]$ have been obtained from the inverse method, the time-varying bank thickness *E(t)* is calculated from the 1-D direct model (FVM) presented in section 5.2.

The unknown heat flux and thermal conductivities are parameterized with Eqs. (5.6) and (5.7), respectively.

The temperatures measurements $Y_i$ were taken with a sensor embedded in the wall at two different locations: The first position, called 'Sensor#1', is near the external surface of the refractory brick wall. The second position, called 'Sensor#2', is close to the internal surface of the refractory brick wall (near the brick wall-PCM interface) (Figure 5.4)

All inverse heat transfer simulations were launched with the following initial arbitrary guesses for the unknown parameters $P_{initial} = \left[2000\ ;\ 2000\ ;\ 5\ ;\ 0.33\ ;\ 0.33\ ;\ 3.33\right]$.

The simulations were executed with the Matlab software running on an Intel ® Core(TM) i5-2520M CPU @ 2.50GHz.

For the sake of comparing the 'estimated solution' obtained with the inverse model to the 'exact solution' generated by the 1-D direct model (FVM), the Relative Root-Mean-Square Error (RRMSE) and the estimation error of the parameters ($Error_P$) were employed. These errors are defined as follows:

$$\mathrm{RRMSE}_{E(t)} = 100 \times \sqrt{\frac{1}{I}\sum_{i=1}^{I}\left(\frac{E\left(t_i\right)_{estimated} - E\left(t_i\right)_{exact}}{E\left(t_i\right)_{exact}}\right)^2} \qquad (5.17)$$

$$Error_P\ \% = 100 \times \frac{\left|P_{exact} - P_{estimated}\right|}{\left|P_{exact}\right|} \tag{5.18}$$

$$Error_T\ \% = 100 \times \frac{\left|T_{exact} - T_{inverse}\right|}{\left|T_{exact}\right|} \tag{5.19}$$

*I* is the number of measurements. *E(t)* is the bank thickness.

The evolution of the least square norm Eq. (5.9) for the *Levenberg-Marquardt* Method (LMM) and for the *Levenberg-Marquardt* Method combined with *Broyden* method (LMM/BM) is shown in Figure 5.6. It is seen that the solution is achieved more efficiently with the LMM/BM. The LMM/BM calls the FVM 93 times while the LMM requires 512 calls. As a result, the CPU time for the LMM/BM is only 1612.6 s while that for the LMM is 8750.5 s.

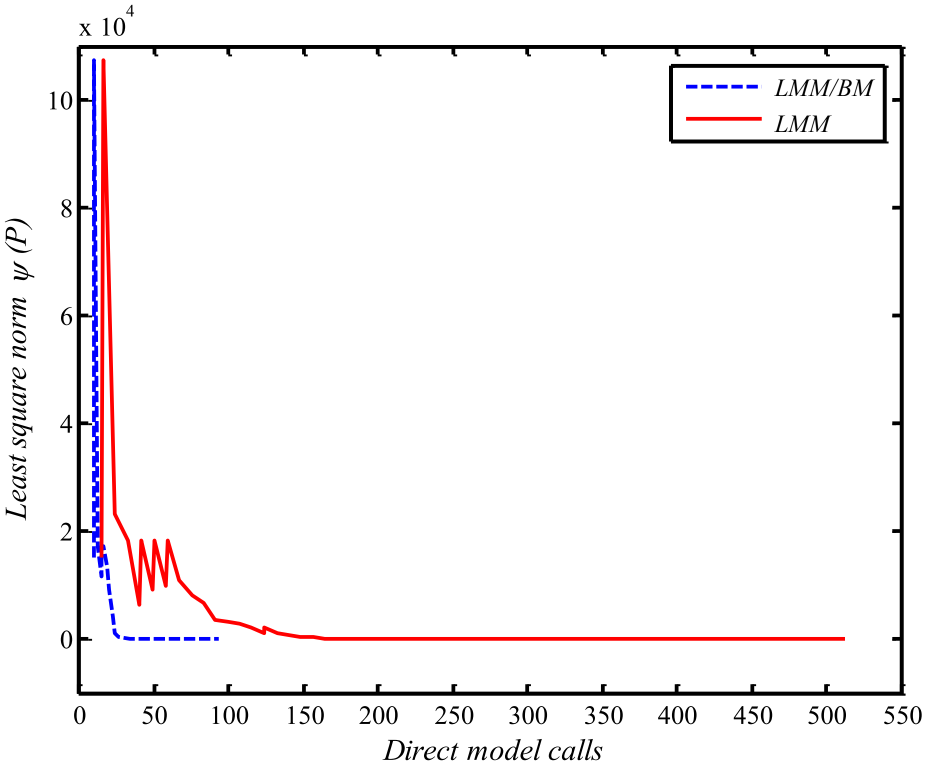

**Figure 5.6** Evolution of least square norm.

The convergence of the unknown parameters $P=\left[q_0;\ q_1;\ h_\infty;\ k_l;\ k_{s_0};\ k_{s_1}\right]$ is depicted in Figure 5.7.

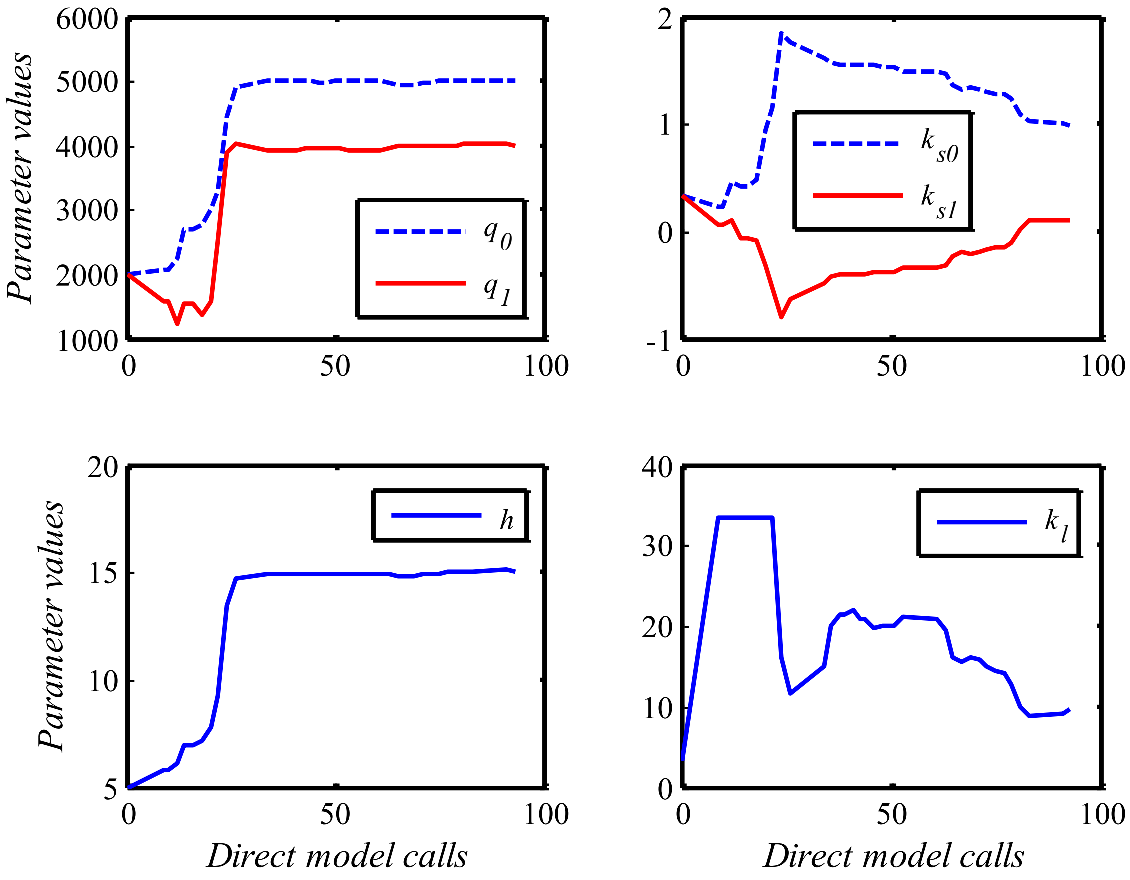

**Figure 5.7** Evolution of the parameter values.

The inverse predictions for the temperature distribution ‘estimated from the inverse model’ and for the corresponding $Error_T$ ‘defined by Eq. (5.19)’ are depicted in Figure 5.8. It is observed that $Error_T$ remains smaller than 0.1% for the entire furnace.

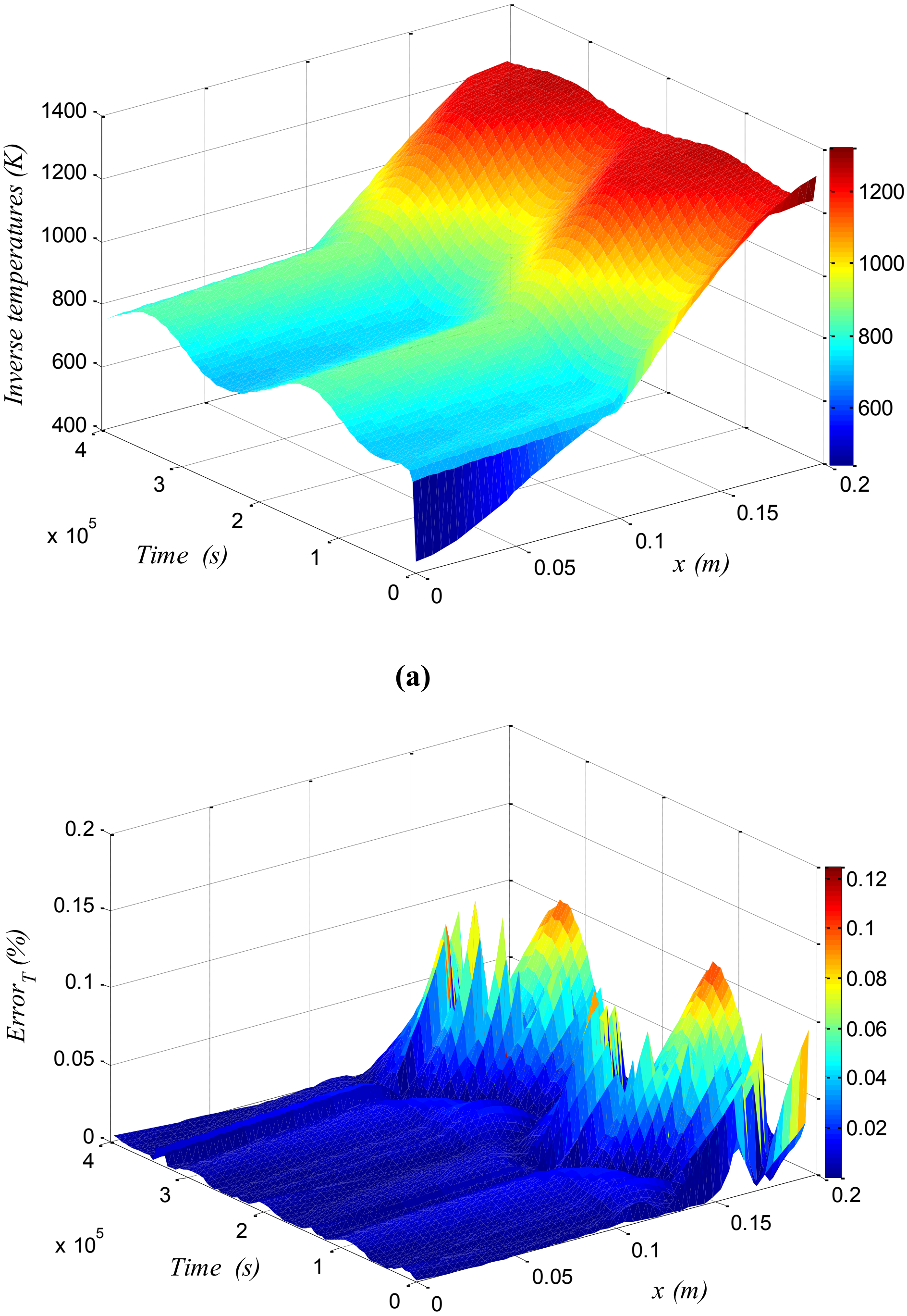

(a)

(b)

**Figure 5.8** Inverse predictions of the temperature distribution (a) and *Error*$_T$ (b).

Table 5.2 summarises the effect of the sensor location and of the data-capture-frequency on the estimation of the unknown parameters. The results are relatively accurate. The relative errors vary from 0.0 to 20.0 %. The largest discrepancy occurs in the prediction of $k_{s_1}$ (80 %). This is due to its small value with respect to the other conductivities [34, 76]. It is also seen that the use of sensor#2 with data-capture-frequency of 4000 measurements provides the best parameter estimation (case 4) [156].

**Table 5.2** Effect of the sensor location and of the data-capture-frequency.

| | | **2000 measurements** | | **4000 measurements** | |
|---|---|---|---|---|---|
| | | $P_{inverse}$ | $Error_P\%$ | $P_{inverse}$ | $Error_P\%$ |
| | | **Case 1** | | **Case 2** | |
| **Sensor#1** | $q_0$ | 4977.86 | 0.4 | 4992.29 | 0.2 |
| | $q_1$ | 3976.12 | 0.6 | 3995.24 | 0.1 |
| | $k_l$ | 11.99 | 19.9 | 10.36 | 3.6 |
| | $k_{s_0}$ | 1.07 | 7.0 | 1.01 | 1.0 |
| | $k_{s_1}$ | 0.02 | 80.0 | 0.09 | 10.0 |
| | $h_\infty$ | 14.93 | 0.5 | 14.98 | 0.1 |
| | | **Case 3** | | **Case 4** | |
| **Sensor#2** | $q_0$ | 5015.86 | 0.3 | 5000.44 | 0.0 |
| | $q_1$ | 4016.64 | 0.4 | 4001.84 | 0.0 |
| | $k_l$ | 9.11 | 8.9 | 9.75 | 2.5 |
| | $k_{s_0}$ | 0.98 | 12.0 | 0.99 | 1.0 |
| | $k_{s_1}$ | 0.12 | 20.0 | 0.11 | 10.0 |
| | $h_\infty$ | 15.06 | 0.4 | 15.00 | 0.0 |

Figure 5.9 shows that the effect of the location of the temperature sensor (sensor#1 and sensor#2) on the accuracy of the predicted bank thickness *E(t)* is insignificant [17, 34]. This result is of interest to the process industry. Indeed, it is much easier and safer to embed a sensor near the external surface of the lateral brick wall. Sensor#1 is therefore recommended over sensor#2. For the remainder of the discussion, sensor#1 will be retained.

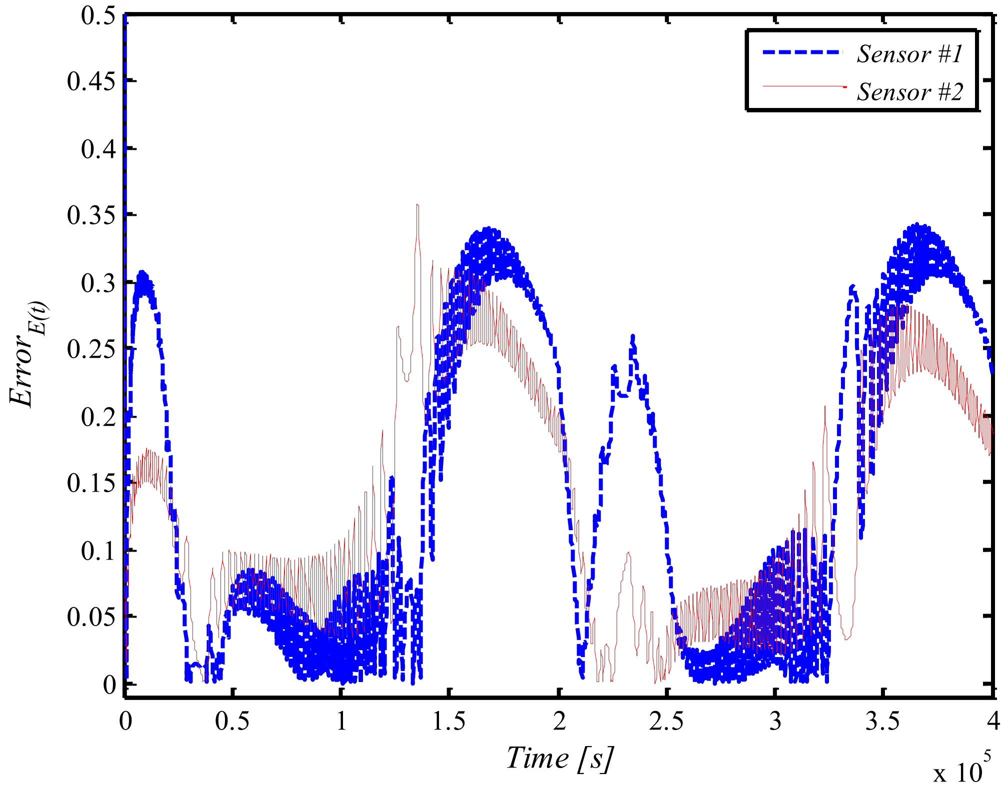

**Figure 5.9** Effect of the sensor position, (no noise).

Noisy experimental measurements were also simulated by adding an error to the exact temperature $\vec{T}_{exact}$ generated by the 1-D direct model:

$$\vec{T}(t_i) = \vec{T}_{exact}(t_i) + \sigma\vec{\omega}_i \tag{5.20}$$

$\sigma$ is the standard deviation of the measurement errors, which may take the value of 0.0 (no noise) and $2\% \, T_{max}$. $T_{\max}$ is the maximum temperature measured by the sensor. $\vec{\omega}_i$ is a random number. This number is generated with the '*randn*' function (standard normal distribution) from Matlab.

Figure 5.10 compares the measured temperatures generated with the 1-D direct model with noise ($2\%\ T_{\max}$) to the estimated temperatures calculated by the inverse model. The confidence bounds $\pm 2.576\ \sigma_{\hat{P}_j}$ are also shown.

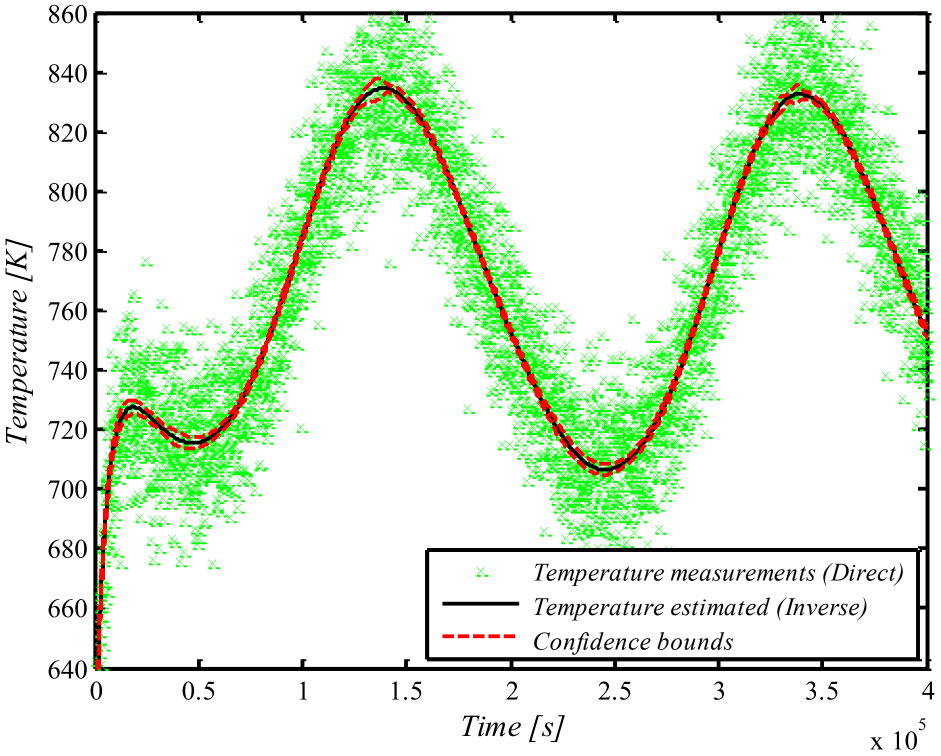

**Figure 5.10** Measured temperatures, inverse temperature and confidence bounds (Sensor#1, $\sigma = 2\%\ T_{\max}$).

Figure 5.11 illustrates the effect of the noise level on the predicted time-varying thickness of the protective bank *E(t)*. As expected, a slight discrepancy appears when the noise level rises to $2\%\ T_{max}$. For example, the $\mathrm{RRMSE}_{E(t)}$ value increases form (0.05 %, no noise) to (1.42 %, $\sigma = 2\%\ T_{max}$). It is also noted that the noise increases the CPU time. Nevertheless, the inverse method remains stable and accurate.

The effect of the data-capture-frequency (the total number of measurements) on the predicted RRMSE of the bank thickness is illustrated in Figure 5.12. As expected, the accuracy improves when the data-capture-frequency increases. On the other hand, when the noise level rises to $2\%\ T_{max}$, the predictions worsen. In any cases, the higher the data-capture-frequency, the better.

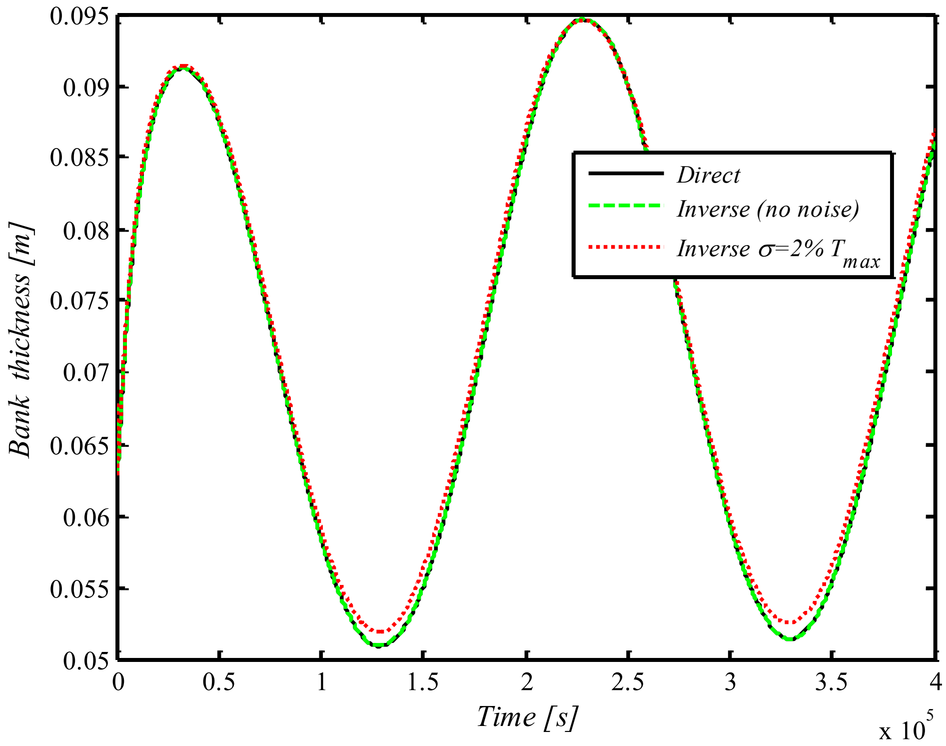

**Figure 5.11** Effect of noise on the predicted Bank thickness.

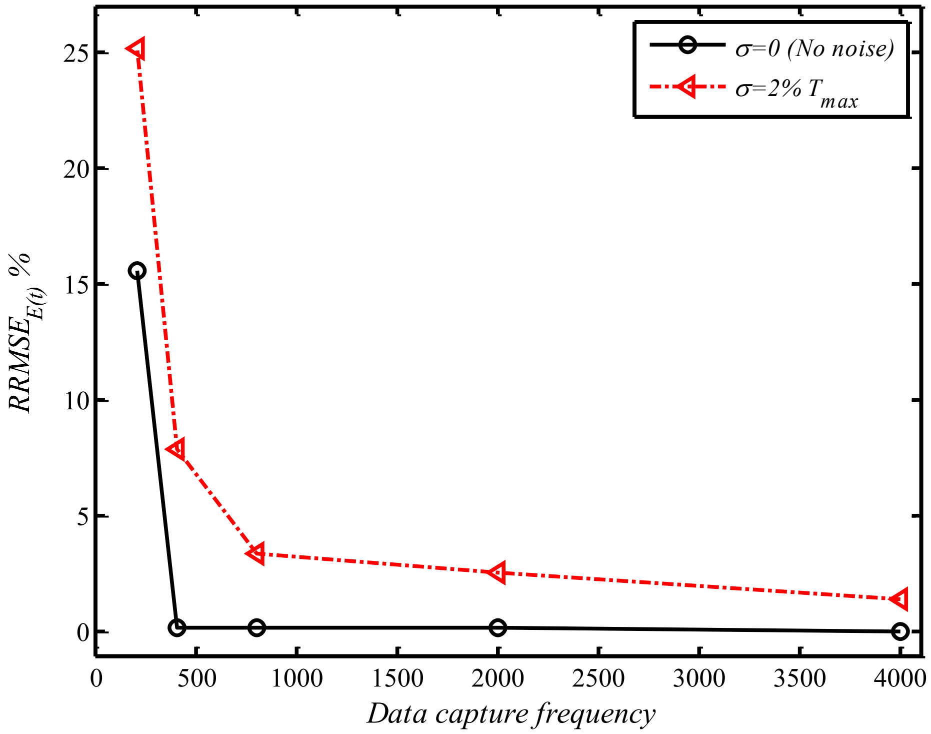

**Figure 5.12** Effect of data-capture-frequency on the predicted of the $\mathrm{RRMSE}_{E(t)}$ .

## 5.5. Conclusion

An inverse heat transfer procedure was presented for predicting simultaneously the operating and thermal parameters of a melting furnace. These parameters are the external heat transfer coefficient, the thermal conductivity of the phase change material (PCM) and the time-varying heat load of the furnace. Once these parameters are estimated, the time-varying thickness of the protective PCM bank that coats the internal surface of the furnace wall may be predicted. The melting and solidification of the PCM is modeled with the enthalpy method. The inverse problem is handled with the *Levenberg-Marquardt* Method (LMM) combined to the *Broyden* method (BM). The models were validated and the effect of the position of the temperature sensor embedded in the furnace wall, of the data capture frequency and of the measurement noise was investigated. A statistical analysis for the parameter estimation was also carried out. Recommendations were made concerning the preferred location of the embedded sensor and the required data capture frequency.

## Acknowledgements

The authors are grateful to the Natural Sciences and Engineering Research Council of Canada (NSERC) for the financial support.

# 6. TRANSFERT DE CHALEUR INVERSE EN CRYOCHIRURGIE

## Avant-propos

**Auteurs et affiliation :**
**M. Hafid** : Étudiant au doctorat, Université de Sherbrooke, Faculté de génie, Département de génie mécanique.
**M. Lacroix** : Professeur, Université de Sherbrooke, Faculté de génie, Département de génie mécanique.
**Date de soumission** : 5 Avril 2017
**Revue :** Journal of Thermal Biology
**Référence :** [37]

## Titre français

Prédiction par transfert inverse de l'évolution temporelle de l'interface de congélation pendant la cryochirurgie.

## Résumé français

Cet article présente une procédure inverse de transfert de chaleur pour surveiller le mouvement du front de congélation à partir d'une cryosonde. A l'aide d'un thermocouple implanté dans la partie de tissu indésirable, la méthode inverse prédit simultanément le taux de perfusion sanguine, la conductivité thermique du tissu congelé et celle du tissu non-congelé. Une fois que ces paramètres sont prédits, la distribution de température dans le tissu et l'évolution temporelle du front de congélation sont calculées à l'aide du modèle direct. L'effet des actions et des paramètres suivants sur les prédictions inverses est étudié: (1) l'initialisation des paramètres polynomiaux inconnus dans la méthode de *Levenberg-Marquardt* ; (2) la température de la cryosonde ; (3) le coefficient de transfert de chaleur extérieur ; et (4) le bruit sur les mesures de température. Dans tous les scénarios de cryothérapie simulés, la méthode inverse a permis de restituer fidèlement le mouvement du front de congélation. Comparée aux techniques d'imagerie par ultrasons ou par résonance magnétique (IRM), la méthode inverse proposée est une alternative prometteuse et bon marché.

## Mots clés

Cryochirurgie, Transfert de chaleur inverse, Interface de changement de phase, Méthode de *Levenberg-Marquardt*, Propriétés thermiques, Equation de *Pennes*, Méthode enthalpique.

# Title

Fast inverse prediction of the freezing front in cryosurgery.

# Abstract

This article presents an inverse heat transfer method for monitoring the motion of the freezing front from a cryoprobe. With the help of a thermocouple pressed against the layer of diseased tissue, the inverse heat transfer method estimates simultaneously the blood perfusion rate and the thermal conductivities of both frozen and unfrozen tissues. This information is then fed to the *Pennes* bioheat equation that (1) calculates the time-varying temperature distribution inside the layer of tissue and (2) predicts the motion of the freezing front. The effect of the most influential parameters on the inverse predictions is investigated. These parameters are (1) the initial guesses for the unknown *Levenberg-Marquardt* polynomial parameters of the thermo-physical properties; (2) the temperature of the cryoprobe; (3) the heat transfer coefficient of the impinging jet of liquid nitrogen; and (4) the noise on the temperature data recorded by the thermocouple probe. Results show that the proposed inverse method is a viable alternative to ultrasound and Magnetic Resonance Imaging (MRI) for monitoring the motion of the freezing front during cryosurgery. For all the cryogenic scenarios simulated, the predictions of the inverse model remain accurate and stable.

# Keywords

Inverse heat transfer; Phase change interface; *Levenberg-Marquardt* Method; Thermal properties; Bioheat transfer; *Pennes* equation; Cryosurgery; Enthalpy method.

# Nomenclature

| | |
|---|---|
| $c$ | specific heat [J/kg°C] |
| $dt$ | time step [s] |
| $f_s$ | solid fraction |
| $h$ | heat transfer coefficient [W/m$^2$ °C] |
| $I$ | total number of measurements |
| $J$ | Jacobian matrix |
| $k$ | thermal conductivity [W/m °C] |
| $L$ | latent heat of freezing [J/kg] |
| $L_t$ | thickness of tissue [m] |
| $N$ | number of unknown parameters |
| $\vec{P}$ | vector of unknown parameter |
| $Q_m$ | metabolic heat generation[$W/m^3$] |
| $RRMSE$ | relative root-mean-square errors [%] |
| $Error$ | estimation errors [%] |
| $s(t)$ | freezing front position [m] |
| $t$ | time [s] |
| $\hat{T}$ | estimated temperature [°C] |
| $T_b$ | arterial blood temperature [°C] |
| $T_c$ | cryogenic probe temperature [°C] |
| $x$ | Cartesian spatial coordinate [m] |
| $Y$ | measured temperature [°C] |
| $w_b$ | blood perfusion rate [$ml/s\ ml$] |

**Greek symbols**

| | |
|---|---|
| $\alpha$ | thermal diffusivity |
| $\varepsilon$ | small number |
| $\mu$ | damping parameter |
| $\rho$ | density of tissue [kg/m$^3$] |
| $\sigma$ | standard deviation of the measurement error |
| $\sigma_{\hat{P}_j}$ | standard deviation of the estimated parameter |
| $\Psi$ | sum of squares norm |
| $\xi$ | small number |
| $\delta H$ | enthalpy [J/m$^3$] |
| $\Delta$ | difference |
| $\Omega^k$ | diagonal matrix |
| $\lambda$ | Neumann's parameter |
| $\omega$ | random number |

**Subscripts**

| | |
|---|---|
| $\infty$ | ambient |
| b | blood |
| exact | exact solution |
| $f$ | frozen region |
| $liq$ | liquidus |
| max | maximum |
| $u$ | unfrozen region |
| $P$ | parameter |
| $sol$ | solidus |
| $T$ | temperature |

**Superscripts**

| | |
|---|---|
| $k$ | time iteration number |
| $T$ | transposed matrix |
| ^ | estimated parameter |
| → | vector |
| ↔ | matrix |

## 6.1. Introduction

Cryosurgery is the use of extreme cold in surgery to destroy abnormal or diseased tissue. Warts, moles, skin tags and small skin cancers are candidates for cryosurgical treatment. Internal disorders, including cancers, are also treated with cryosurgery.

Cryosurgery is a minimally invasive procedure. It is often preferred to more traditional kinds of surgery because it minimizes pain and scarring, and its costs are relatively low [174, 175].

Cryosurgery works by taking advantage of the destructive effect of freezing temperatures on cells. When their temperature sinks beyond a certain level, ice crystals begin forming inside the cells. Due to their lower density, the ice crystals tear apart the cells. They also harm the blood vessels that supply the malignant tissue.

A common method of freezing lesions is using liquid nitrogen as the cooling solution. This very cold liquid, its temperature is -196 $^{0}C$, may be sprayed on the diseased tissue or circulated through a cryoprobe [176, 177]. The cryoprobe is a tube placed in contact with the tumor. Ultrasound or magnetic resonance imaging (MRI) is used to guide the cryoprobe and monitor the freezing of the cells [178, 179]. This helps in limiting damage to adjacent healthy tissues and, more of a concern, avoiding damage to nerve tissue.

But ultrasound and MRI monitoring techniques are not always readily available. The alternative then is to resort to the mathematical modeling and the numerical simulation of the heat transfer and freezing processes that take place inside the biological tissues [180-183]. This computational monitoring technique is convenient and relatively inexpensive. Its predictions are reliable provided, however, that the thermal properties of the tissues, such as the blood perfusion and the thermal conductivities, are well defined. Unfortunately, the thermal properties of the biological tissues are often poorly known. Moreover, they change as the tissues freeze up [184, 185].

It is possible to determine experimentally the thermal properties of biological tissues [32, 115]. But the measurement techniques are not without complications and they require sophisticated equipment that can hardly be employed during cryosurgery.

A promising approach for handling this problem rests on inverse heat transfer techniques [151, 186]. Investigations based on inverse methods have been carried out in the past for estimating the thermal parameters of living tissues. [187] estimated the blood perfusion coefficient for the one-dimension *Pennes* equation using the Tikhonov regularization method. [188] determined the unknown time-dependent surface heat flux in a living skin tissue using the conjugate gradient method. [121] predicted the size and the location of the tumor in a one-dimensional tissue by inverse analysis. Similar studies were also conducted by [120, 122, 123, 189]. Other investigations focused on the simultaneous estimation of various thermo-physical properties of tissues using inverse methods [125, 153, 190-192].

The *Pennes* model of bioheat transfer equation, which describes the heat transfer in living biological tissues, is widely adopted in variety of biological researches [193-195].

Another mathematical problem that arises during the cryosurgery is the phase change phenomena of the tissue. Indeed, the prediction of thermo-physical properties during the phase change process by inverse method is also a challenging task [166, 196-198].

In all the aforementioned studies however, the prediction of the thermo-physical properties of the biological tissues was not carried out during cryosurgery. The present paper remedies this shortcoming. Its objective is to pursue the previous studies by developing an inverse method capable of estimating the unknown thermo-physical properties during cryosurgery. Once the unknown properties are determined, the isotherms and the moving freezing front are predicted and, as a result, the cryosurgical procedure may be monitored and controlled.

This paper is organized as follows. First, a Finite-Volume Method (FVM) based on the *Pennes* bioheat equation and the phase change enthalpy method is developed. The FVM is then validated with an analytical solution available in the open literature. Next, an inverse technique based on the *Levenberg-Marquardt* Method (LMM) is presented. The (LMM) is combined to the *Broyden* Method (BM) in order to speed the computations. Finally, the inverse method is thoroughly tested for several freezing scenarios. The effect of the most influential parameters on the inverse predictions and on the course of the cryosurgery is investigated. These parameters are (1) the initial guesses for the unknown *Levenberg-Marquardt* polynomial parameters; (2) the temperature of the cryoprobe; (3) the heat transfer coefficient of the impinging jet of liquid nitrogen; and (4) the noise on the temperature data recorded by the thermocouple probe.

## 6.2. Problem statement and assumptions

Figure 6.1 illustrates a schematic of the system under study. The thickness of the diseased tissue layer is $\boldsymbol{L_t}$. A cryoprobe is pressed against the layer of tissue (the left boundary at $x = 0$). At time $t=0$, the cryogenic probe temperature is suddenly set equal to the sub-freezing temperature $T_c$. As a result, heat is transferred from the diseased tissue to the cryoprobe. The temperature of the tissue decreases rapidly and starts freezing on the surface of the cryoprobe. As time passes, the thickness of the frozen layer $s(t)$ increases. The freezing procedure continues until the entire layer of diseased tissue has been deeply frozen and its tumor cells destroyed.

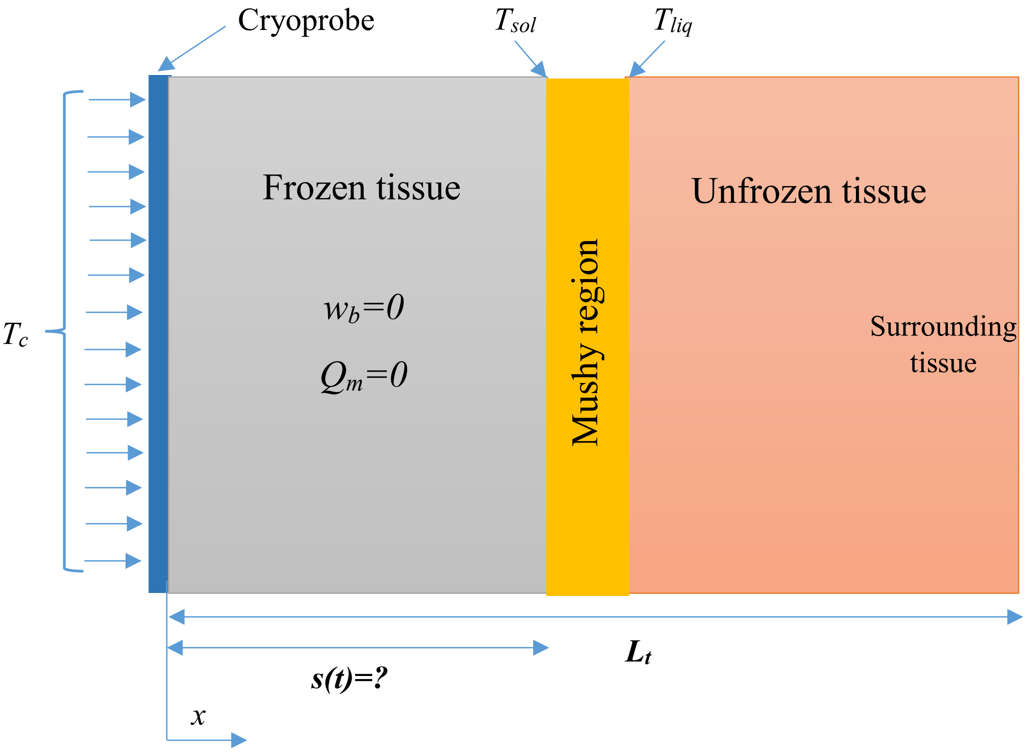

**Figure 6.1** Schematic of the system. The time-varying position of the freezing front is $s(t)$.

The prediction of the heat transfer and of the freezing processes that take place inside the layer of tissue is carried out with a mathematical model that rests on the following assumptions:

- ✓ Heat is predominantly transferred from the tissue to the cryoprobe. As a result, a one-dimensional heat transfer model is retained [199].
- ✓ The heat transfer inside the tissue is conduction-dominated [29, 200].

- ✓ The phase change process is non-isothermal. It is characterized by three zones: a frozen solid zone, a mushy zone and an unfrozen zone (Figure 6.1).
- ✓ The blood perfusion and the metabolic heat generation are uniform through time and space. These phenomena vanish, however, in the frozen and in the mushy regions.
- ✓ The blood temperature is set equal to $T_b=37\ °C$.
- ✓ The heat transfer between the tissue and the blood takes place in the capillaries. The effect of large blood vessels is neglected [201, 202].
- ✓ The liquidus temperature $T_{liq}$ (the upper limit) and the solidus temperature $T_{sol}$ (the lower limit) of the biological tissue are set equal to (-1 °*C*) and (-8 °*C*), respectively [203, 204].

## 6.3. The direct problem

In the direct problem, the thermo-physical properties, the initial and the boundary conditions are all known. The mathematical model for the heat transfer in the tissue layer rests on the following *Pennes* bio-heat equation [103]:

$$\rho c \frac{\partial T}{\partial t} = \frac{\partial}{\partial x}\left(k \frac{\partial T}{\partial x}\right) + \rho_b c_b w_b \left(T_b - T\right) + Q_m + \delta H \frac{\partial f_s}{\partial t} \tag{6.1}$$

*ρ, c* and *k* are the density, the specific heat and the thermal conductivity of the tissue, respectively. The subscript *'b'* refers to the blood characteristics. $w_b$ and $Q_m$ represent the blood perfusion rate and the metabolic heat generation in the tissue, respectively. *T* is the tissue temperature and $T_b$ is the arterial blood temperature.

The last term on the right-hand side of Eq. (6.1) represents the solid/liquid phase change of the biological tissue during cryosurgery. $\delta H$ and $f_s$ are the enthalpy and the solid fraction during phase change, respectively. The enthalpy $\delta H$ is defined as $\delta H = \rho(c_{solid} - c_{liquid})T - \rho L.$ The solid fraction may be expressed as

$$f_s = F\left(T\right) = \begin{cases} 0 & T \geq \mathrm{T}_{liq} \quad \left(\text{Unfrozen zone}\right) \\ \dfrac{T - T_{liq}}{T_{sol} - T_{liq}} & \mathrm{T}_{sol} < T < \mathrm{T}_{liq} \left(\textit{Mushy}\text{ zone}\right) \\ 1 & T \leq \mathrm{T}_{sol} \quad \left(\text{Frozen solid zone}\right) \end{cases} \tag{6.2}$$

At each time-step, the solid fraction $f_s$ is updated iteratively as follows

$$f_s^{k+1} \approx f_s^k + \left(\frac{dF}{dT}\right)^k \left(T^{k+1} - F^{-1}\left(f_s^k\right)\right) \tag{6.3}$$

$F^{-1}$ is the inverse function of $F$.

The boundary conditions in Figure 6.1 are set to

$$\frac{\partial T\left(x = L_t,\ \mathrm{t}\right)}{\partial x} = 0 \tag{6.4}$$

$$T\left(x = 0,\ \mathrm{t}\right) = T_c \tag{6.5}$$

The initial condition is given by

$$T\left(x,\ \mathrm{t{=}0}\right) = 37\ {}^{0}\mathrm{C} \tag{6.6}$$

Eq. (6.1) is solved with a finite-volume method. An implicit time-discretization scheme is adopted. The resulting set of algebraic equations is solved with a Tri-Diagonal-Matrix-Algorithm (TDMA) [143].

### 6.3.1. Validation of the direct model

The accuracy of the above mathematical model was first checked with Neumann's solution for the semi-infinite freezing problem [205]. The Neumann's problem was simulated numerically by setting the heat generation and the blood perfusion rate equal to zero in Eq. 6.1 ($Q_m = w_b = 0$). The initial temperature was set equal to $T_0 = 37\ °C$. The temperature of the freezing point $T_f$ was set equal to the solidus temperature $T_{sol}$ (the lower limit). At the left boundary ($x = 0\ m$), the temperature of the cryoprobe was imposed $T_c$. The analytical solution for the time-varying freezing front $s(t)$, provided by Neumann, is:

$$s(t) = 2\lambda\sqrt{\left(\alpha_f\right)t} \tag{6.7}$$

The parameter $\lambda$ is obtained from the solution of the following transcendental equation

$$\frac{1}{\exp\left(\lambda^2\right) \times erf\left(\lambda\right)} - \upsilon\left(\frac{k_u}{k_f}\right)\left(\frac{T_0 - T_f}{T_f - T_c}\right)\left(\frac{\exp\left(-\upsilon^2\lambda^2\right)}{erfc\left(\upsilon\lambda\right)}\right) = \left(\frac{\lambda L\ \sqrt{\pi}}{c_f\left(T_f - T_c\right)}\right) \tag{6.8}$$

where $\upsilon = \sqrt{\dfrac{\alpha_f}{\alpha_u}}$. $\alpha_f$ and $\alpha_u$ are the thermal diffusivities in the frozen and unfrozen regions, respectively. $L$ is the latent heat of fusion. *erf* and *erfc* are the error functions.

The length of semi-infinite region $\left(0 \le x \le L_t\right)$ was set equal to $L_t=0.05\ m$. The numerical simulation was carried out with a grid made of uniform space increments $\Delta x=3.125*10^{-4}\ m$ and for a constant time-step $\Delta t = 10\ s$ . Simulations conducted with finer grid sizes and smaller time-steps yielded the exact same results.

As an example, Figure 6.2 depicts the time-varying freezing front for different temperatures of the cryoprobe $T_c$. It is seen that the agreement between the numerical predictions achieved with the direct model and the analytical solution remains, for all cases, excellent.

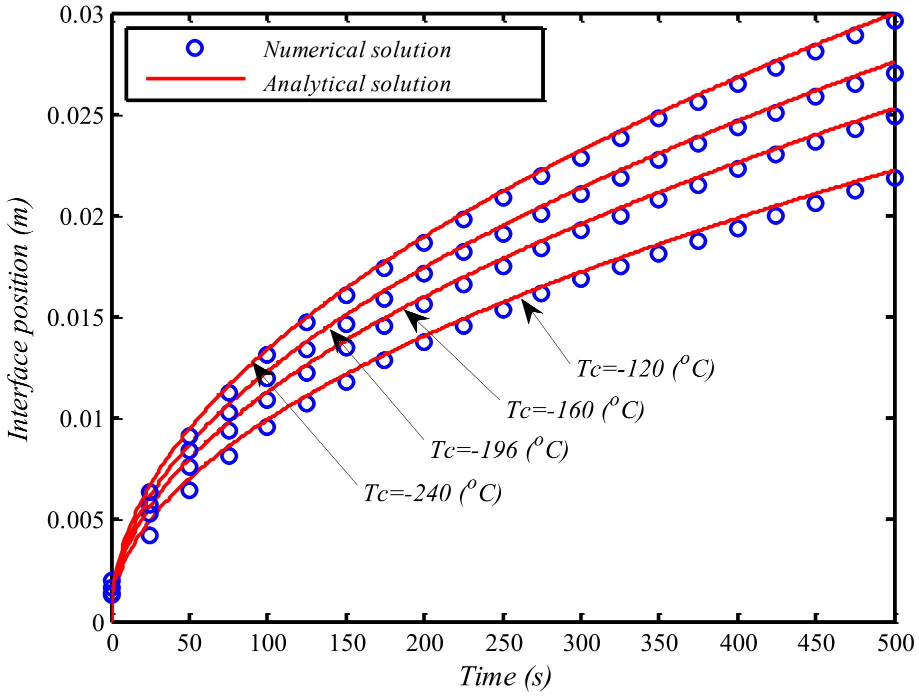

**Figure 6.2** Time-varying freezing front position for different temperatures of the cryoprobe.

## 6.4. Inverse model

In the inverse model, the blood perfusion rate $w_b$, and the thermal conductivities of the frozen and of the unfrozen layers of tissue $k_f$ and $k_u$ are all unknown. These properties are estimated with the inverse model. Once they have been obtained, they are fed to the direct model (section 6.3 above) that calculates the time-varying temperature distribution $T(x,t)$ and predicts the motion of the freezing front $s(t)$.

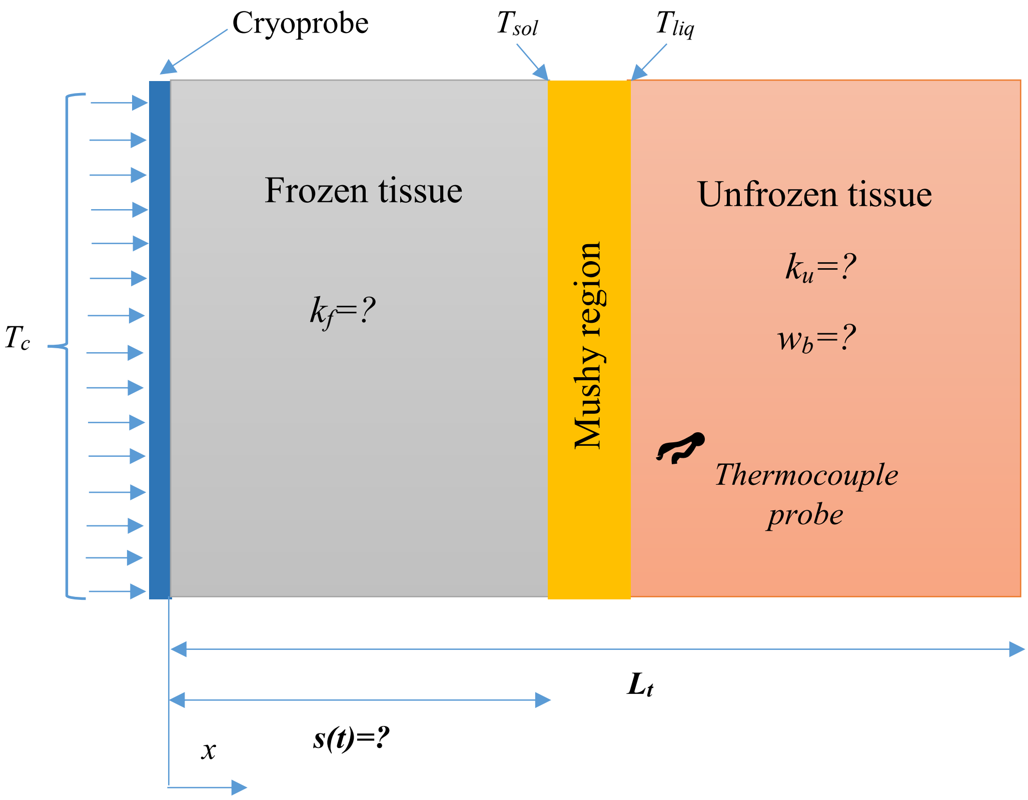

**Figure 6.3** The inverse problem. $w_b$ , $k_u$ and $k_f$ are unknown. They are estimated from the temperatures recorded by thermocouple probe.

So the objective of the inverse model is to determine the unknown thermal properties of the biological tissue, i.e., $w_b$, $k_f$ and $k_u$. To achieve this task, a thermocouple probe is pressed against the diseased tissue (Figure 6.3). It records the time-varying temperatures $Y\left(t_i\right)$. This information is fed to the inverse model that minimizes the least square norm $\Psi\left(\vec{P}\right)$:

$$\Psi\left(\vec{P}\right)=\sum_{i=1}^{I}\left[Y\left(t_i\right)-\hat{T}\left(t_i,\vec{P}\right)\right]^2 \tag{6.9}$$

$\hat{T}\left(t_i,\vec{P}\right)$ is the vector of the estimated temperatures obtained with the inverse model. $P = (w_b, k_f, k_u)$ is the set of the unknown thermal parameters. $I$ is the total number of recorded temperatures. The temperatures recorded by the thermocouple probe, $Y(t_i)$, are called the *'direct temperatures'*. For the sake of the present study, these temperatures are 'generated' from the solution of the direct problem for which the parameters $P = (w_b, k_f, k_u)$ are completely specified. Later, these temperatures will be 'contaminated' with random noise so as to mimic the effect of measurement errors (see section 6.5.4).

The *Levenberg–Marquardt* method is adopted for the solution of the present inverse problem [117, 124]. In this iterative method, the incremental value of the unknown thermal parameters $\Delta P$, is expressed as

$$\Delta\vec{P} = \left[ \left(\overleftrightarrow{J}^k\right)^T \overleftrightarrow{J}^k + \mu^k \overleftrightarrow{\Omega}^k \right]^{-1} \left(\overleftrightarrow{J}^k\right)^T \left(\vec{Y} - \vec{T}\left(\vec{P}^k\right)\right) \tag{6.10}$$

The superscripts "$\leftrightarrow$" and "$\rightarrow$" refer to the matrix and the vector notation, respectively. The superscript "T" denotes the transpose of the matrix. $\mu^k$ is a positive scalar, named '*Damping parameter'*. The choice and the update of this parameter are discussed in [150]. $\overleftrightarrow{\Omega}^k = diag\left[\left(\overleftrightarrow{J}^k\right)^T \overleftrightarrow{J}^k\right]$ is a diagonal matrix. $\overleftrightarrow{J}^k$ is the Jacobian matrix, also called the *'sensitivity matrix'* . It is written as

$$\overleftrightarrow{J}\left(\vec{P}\right) = \begin{pmatrix} \dfrac{\partial T_1}{\partial w_b} & \dfrac{\partial T_1}{\partial k_f} & \dfrac{\partial T_1}{\partial k_u} \\ \dfrac{\partial T_2}{\partial w_b} & \dfrac{\partial T_2}{\partial k_f} & \dfrac{\partial T_2}{\partial k_u} \\ \vdots & \vdots & \vdots \\ \dfrac{\partial T_I}{\partial w_b} & \dfrac{\partial T_I}{\partial k_f} & \dfrac{\partial T_I}{\partial k_u} \end{pmatrix} \tag{6.11}$$

The Jacobian matrix plays a crucial role in the estimation of the thermal parameters. There are several approaches for computing the Jacobian [151]. In the present study, the Jacobian matrix is expressed with a finite difference approximation

$$J_{ij} = \frac{\partial \hat{T}_i}{\partial P_j} \cong \frac{\hat{T}\left(t_i\ ; P_1, \ldots, P_j + \left(\delta P_j\right), \ldots P_N\right) - \hat{T}\left(t_i\ ; P_1, \ldots, P_j - \left(\delta P_j\right), \ldots P_N\right)}{2\left(\delta P_j\right)} \tag{6.12}$$

The subscripts $i$ and $j$ represent the time and the parameter, respectively. The parameter perturbation $\left(\delta P_j\right)$ is set to $\xi\left(1+\left|P_j\right|\right)$, where $\xi$ is a small number.

At each iteration, the approximation of the sensitivity coefficients of the Jacobian matrix ( $\overleftrightarrow{J} \in R^{I*\mathrm{N}}$ where: $I$=50 and $N$=3) requires the solution of the direct problem six times. As a result, the computation of the Jacobian matrix using a finite difference approximation may become time-consuming.

In order to reduce the computational effort, the Jacobian matrix is updated using the *Broyden* method [152]:

$$J_k = J_{k-1} + \frac{\left(\left(\hat{T}_k - \hat{T}_{k-1}\right) - J_{k-1}\Delta P_{k-1}\right)\Delta P_{k-1}^T}{\Delta P_{k-1}^T \Delta P_{k-1}} \tag{6.13}$$

$J_k$ and $J_{k-1}$ are the Jacobian matrices at the current and at the previous iteration, respectively. $\Delta P_{k-1}$ is the incremental value of the unknown parameters. Further details on this calculation method are provided in [34, 35].

The algorithms for the direct model and for the inverse model are summarized in Figure 6.4

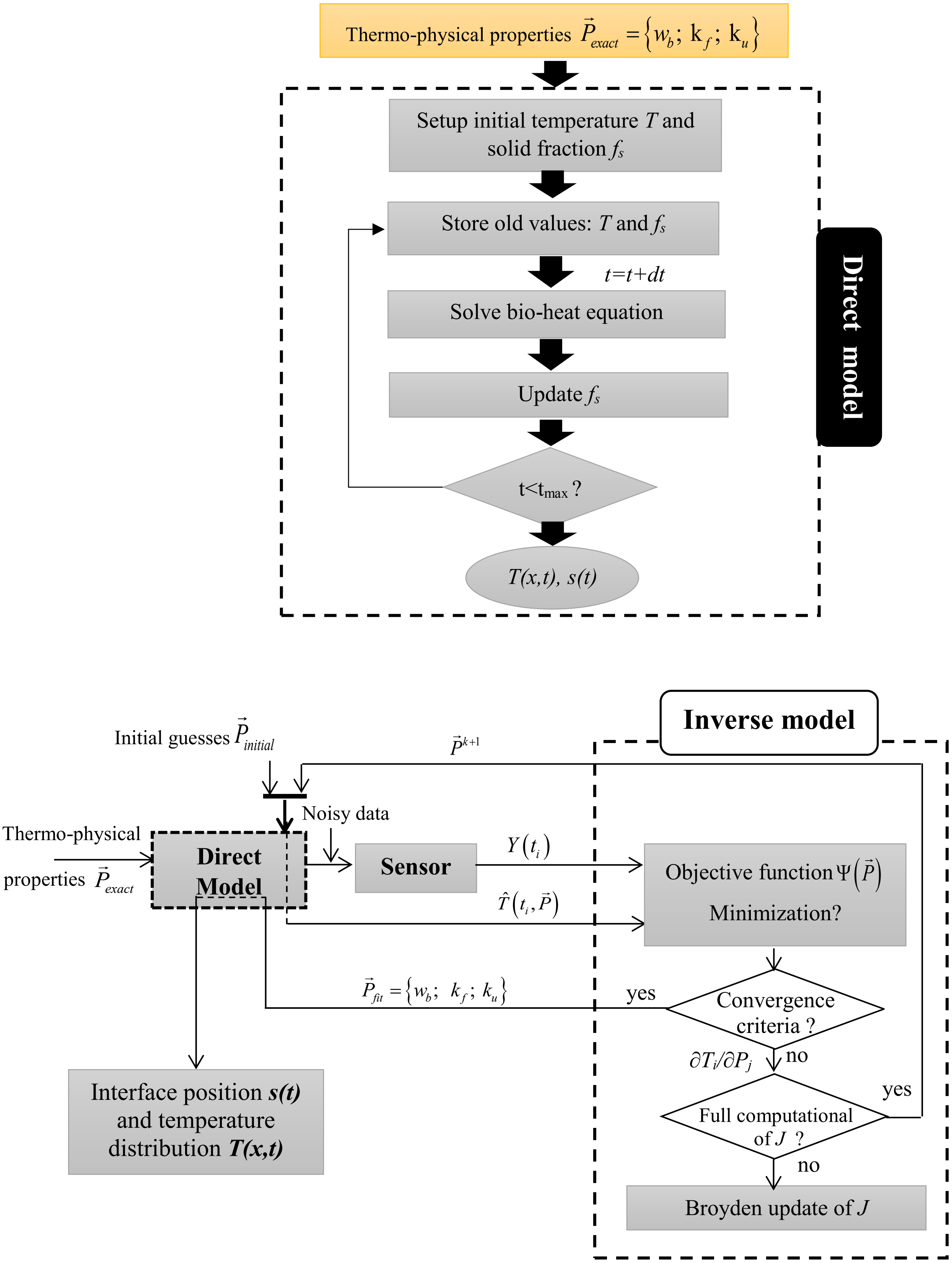

**Figure 6.4** Direct and inverse heat transfer algorithms.

## 6.5. Results and discussion

In order to monitor the motion of the freezing front during cryosurgery, the blood perfusion rate $w_b$ and the thermal conductivities in the frozen and the unfrozen tissues, $k_f$ and $k_u$, are first estimated with the inverse model of section 6.4. This information is then passed to the direct model (section 6.3) that calculates the temperature distribution $T(x,t)$ and predicts the time-varying position of the freezing front $s(t)$.

The following numerical simulations were all conducted for a *0.05 m* thick biological tissue. The temperature of the cryoprobe was fixed at $T_c$= -196 *°C*, and the duration of cryosurgery was limited to 500 *s*. The physical properties of the biological tissue retained for the simulations are summarized in Table 6.1 [108, 206].

Numerical simulations were carried out for a grid space of $\Delta x=2.5*10^{-4}$ *m* and a time step of $dt$=10 *s.* Additional simulations were also conducted to ensure that the predictions are grid space and time step independent.

All simulations were performed with the Matlab software running on an Intel ® Core(TM) i5-2520M CPU @ 2.50GHz.

**Table 6.1** Properties of the biological tissue.

| | Symbol | Value | Unit |
|---|---|---|---|
| Thermal conductivity of unfrozen tissue | $k_u$ | 0.5 | W/m °C |
| Thermal conductivity of frozen tissue | $k_f$ | 2 | W/m °C |
| Specific heat of unfrozen tissue | $c_u$ | 3600 | J/kg °C |
| Specific heat of frozen tissue | $c_f$ | 1800 | J/kg °C |
| Density of unfrozen tissue | $\rho_u$ | 1000 | kg/m$^3$ |
| Density of frozen tissue | $\rho_f$ | 1000 | kg/m$^3$ |
| Latent heat of freezing | $L$ | 250 | kJ/kg |
| Lower phase transition temperature | $T_{sol}$ | −8 | °C |
| Upper phase transition temperature | $T_{liq}$ | −1 | °C |
| Blood perfusion rate | $w_b$ | 0.0005 | ml/s ml |
| Metabolic heat generation | $Q_m$ | 4200 | W/m$^3$ |
| Specific heat of blood | $c_b$ | 3640 | J/kg °C |
| Density of blood | $\rho_b$ | 1000 | kg/m$^3$ |
| Blood temperature | $T_b$ | 37 | °C |

To characterize the accuracy of the proposed inverse method, three errors are defined and computed:

$$Error_P\ \% = 100 \times \frac{\left|P_{exact} - P_{inverse}\right|}{\left|P_{exact}\right|} \tag{6.14}$$

$$Error_T\ \% = 100 \times \frac{\left|T_{exact} - T_{inverse}\right|}{\left|T_{exact}\right|} \tag{6.15}$$

$$\mathrm{RRMSE}_{s(t)}\ \% = 100 \times \sqrt{\frac{1}{I}\sum_{i=1}^{I}\left(\frac{s(t_i)_{exact} - s(t_i)_{inverse}}{s(t_i)_{exact}}\right)^2} \tag{6.16}$$

*P* and *T* stand for the unknown thermal parameter and temperature, respectively. The subscript *'exact'* refers to the solution obtained from the direct model. The subscript *'inverse'* refers to the solution estimated with the inverse model. *I* is the total number of temperature data recorded by the thermocouple probe during cryosurgery. In the present study, this number was set equal to $I = 50$.

## 6.5.1. Effect of the initial guesses

This section examines the effect of the initial guesses for the thermal properties $\vec{P}_{ini} = \left[ w_b;\ k_f;\ k_u\ \right]$ on the convergence and the accuracy of the inverse predictions. The initial guesses were taken as 1/3, 1/5 and 1/7 of that of the exact parameter value (i.e., case#1, case#2 and case#3, respectively). The results of the calculations are shown in Figure 6.5 and are summarized in Table 6.2. It is seen that the inverse estimations are good for all cases. The largest discrepancy occurs in the estimation of the blood perfusion rate $w_b$ (4.8%). This is due to its small value with respect to the other thermal properties ($k_f$ and $k_u$) considered here [76].

For the remainder of this paper, the initial parameter guesses of case#2 will be retained in all simulations.

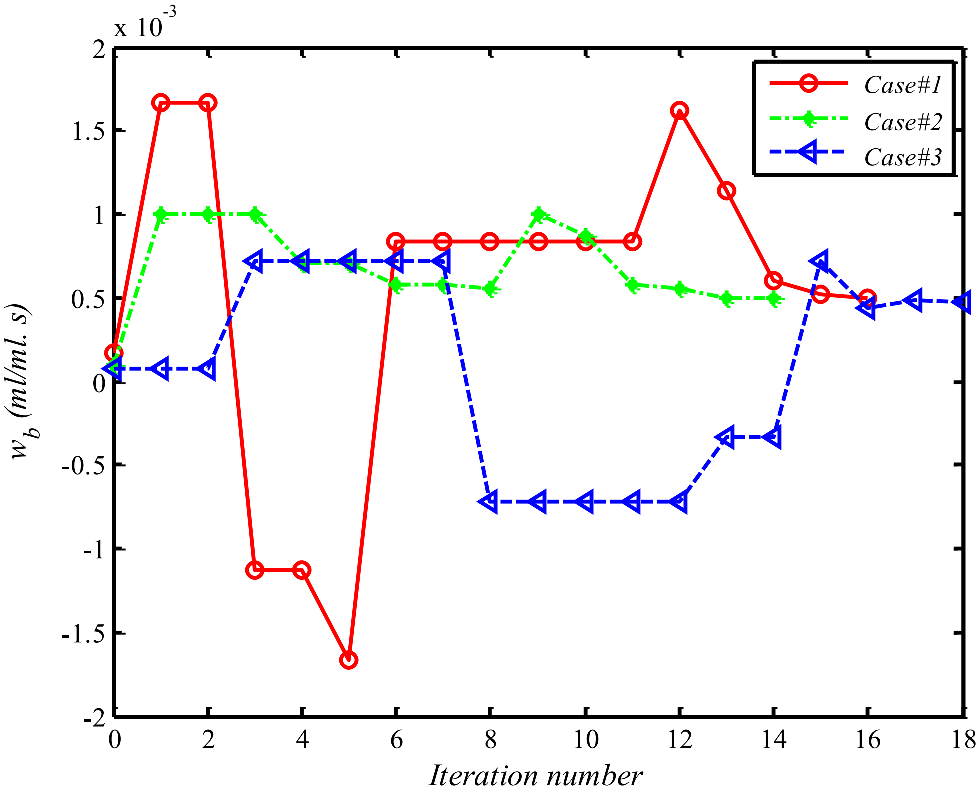
x 10^-3
2
1.5
1
0.5
0
-0.5
-1
-1.5
-2
w_b (ml/ml. s)
0
2
4
6
8
10
12
14
16
18
Iteration number
Case#1
Case#2
Case#3

(a)

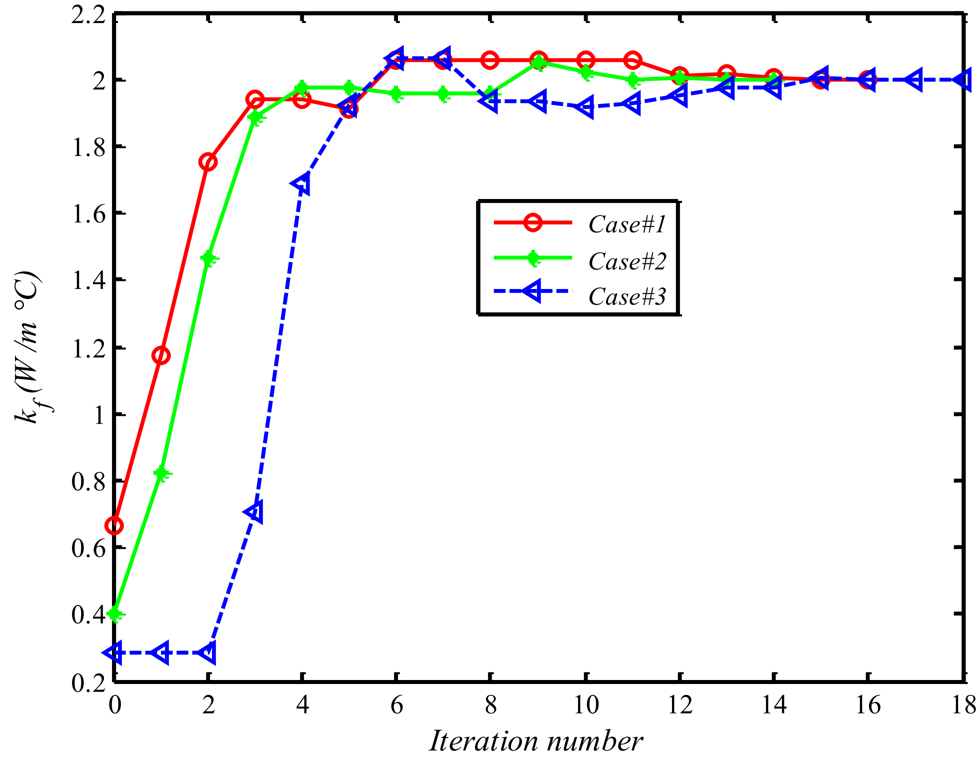
2.2
2
1.8
1.6
1.4
1.2
1
0.8
0.6
0.4
0.2
k_f (W/m °C)
0
2
4
6
8
10
12
14
16
18
Iteration number
Case#1
Case#2
Case#3

(b)

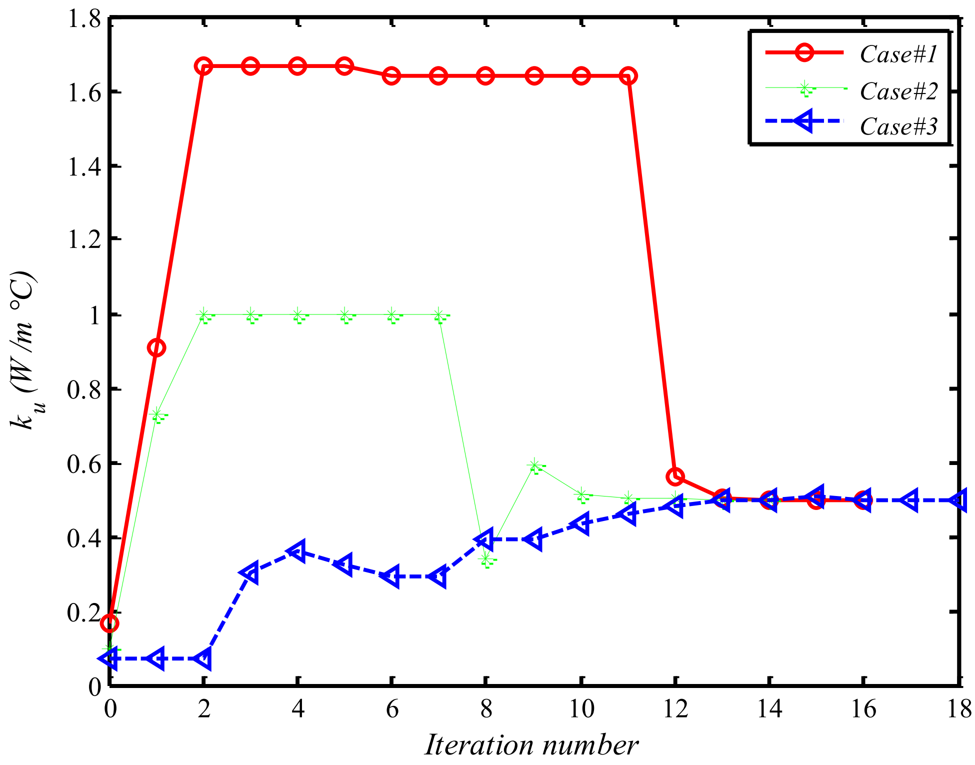

(c)

**Figure 6.5** Convergence of the unknown thermal parameters.

**Table 6.2** Effect of the initial guesses on the predictions of the thermal parameters.

| | | ***Case#1***<br>$P_{initial} = P_{exact}/3$ | | ***Case#2***<br>$P_{initial} = P_{exact}/5$ | | ***Case#3***<br>$P_{initial} = P_{exact}/7$ | |
|---|---|---|---|---|---|---|---|
| | $P_{exact}$ | $P_{inverse}$ | $Error_P\%$ | $P_{inverse}$ | $Error_P\%$ | $P_{inverse}$ | $Error_P$ |
| $w_b$ (ml/ml*s) | $5*10^{-4}$ | $4.92*10^{-4}$ | 1.6 | $4.96*10^{-4}$ | 0.8 | $4.76*10^{-4}$ | 4.8 |
| $k_f$ (W/m °C) | 2 | 1.9998 | 0.01 | 1.9999 | 0.005 | 1.9992 | 0.04 |
| $k_u$ (W/m °C) | 0.5 | 0.5 | 0 | 0.4999 | 0.02 | 0.4997 | 0.06 |

The inverse predictions for the temperature distribution and for the corresponding $Error_T$ are illustrated in Figure 6.6. It is observed that $Error_T$ remains smaller than *1.5%* during the entire duration of the cryosurgical procedure. The maximum value of $Error_T$ occurs in the mushy zone, that is, in the region where Eq. (6.1) is nonlinear.

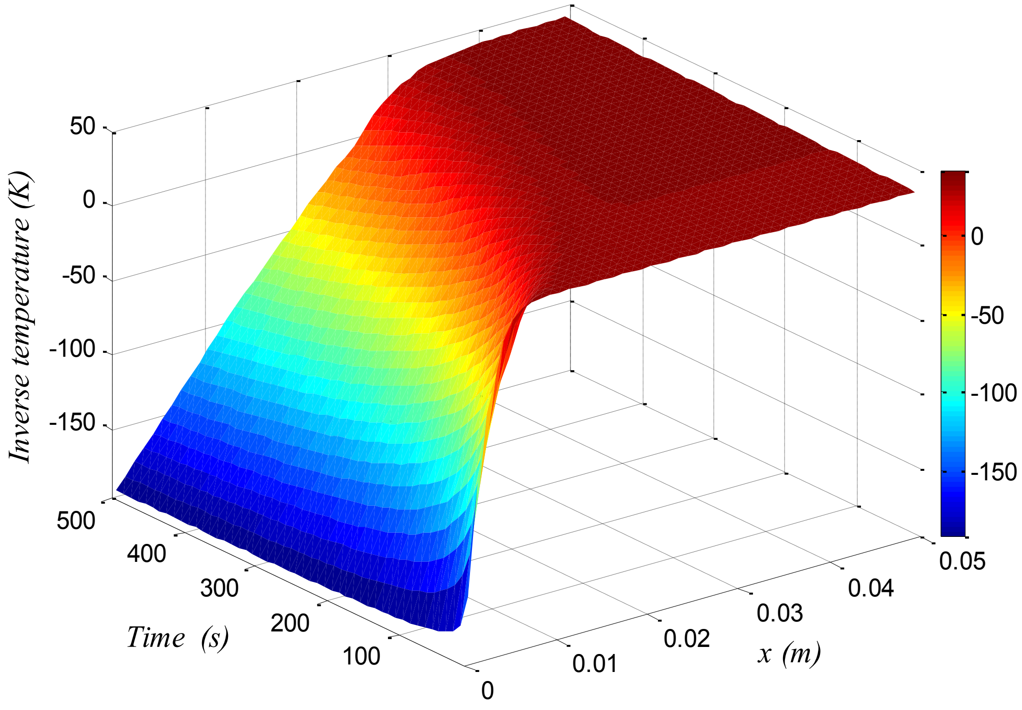

**(a)**

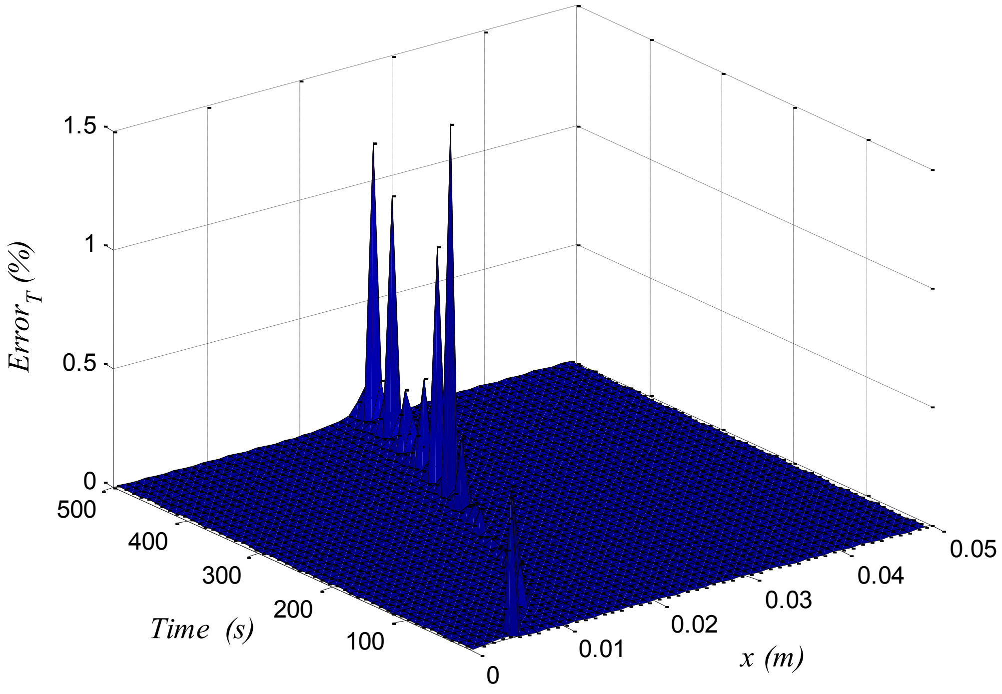

**(b)**

**Figure 6.6** Inverse predictions of the temperature distribution **(a)** and $Error_T$ **(b)**.

The freezing fronts predicted from the direct model and estimated with the inverse model are compared in Figure 6.7. Examination of this figure reveals that both solutions are in perfect agreement. The corresponding temperature contours calculated with the inverse model are depicted in Figure 6.8.

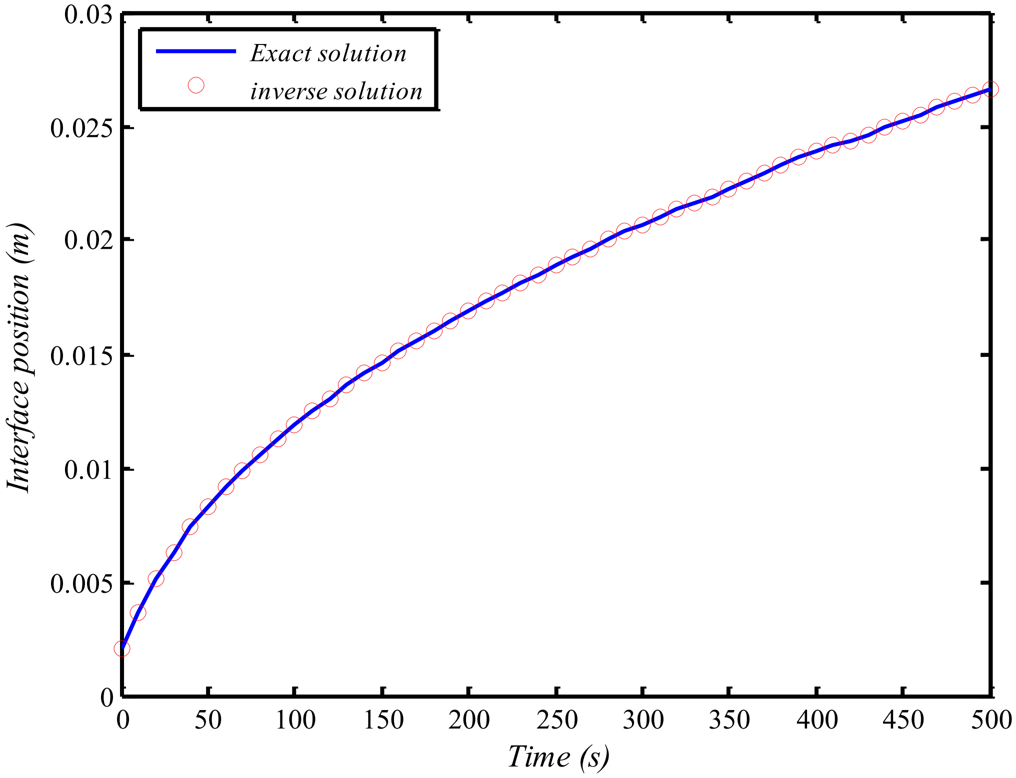

**Figure 6.7** Predicted freezing front without noise.

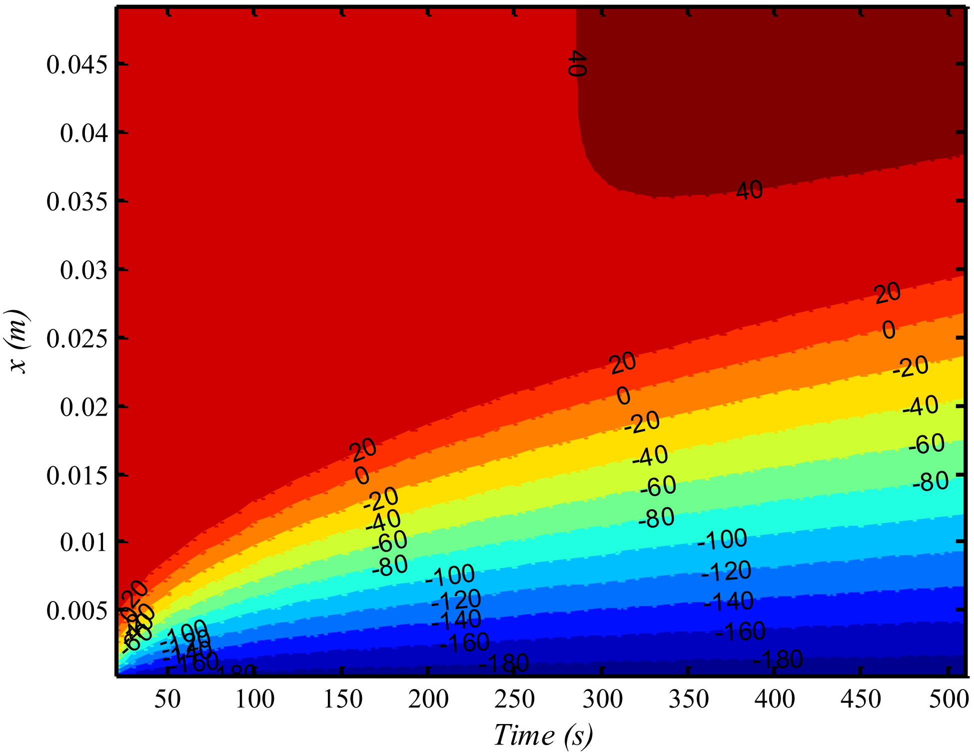

**Figure 6.8** Temperature contours predicted with the inverse model.

### 6.5.2. Effect of the freezing temperature

The effect of the freezing temperature $T_c$ on the inverse predictions was also checked. Table 6.3 and Figure 6.9 show that the inverse method remains stable and accurate in all cases. The temperature contours predicted with the inverse model for $T_c$= -140 and -*230 °C* are also illustrated in Figure 6.10. As expected, the size of the frozen region increases as the freezing temperature $T_c$ drops.

**Table 6.3** Effect of the freezing temperature on the parameter estimation.

| | | $T_c$=-140 °C | | $T_c$=-196 °C | | $T_c$=-230 °C | |
|---|---|---|---|---|---|---|---|
| | $P_{Exact}$ | $P_{Inverse}$ | Error% | $P_{Inverse}$ | Error% | $P_{Inverse}$ | Error% |
| $w_b$ | $5*10^{-4}$ | $4.93*10^{-4}$ | 1.4 | $4.96*10^{-4}$ | 0.8 | $4.97*10^{-4}$ | 0.6 |
| $k_f$ | 2.00 | 1.9998 | 0.01 | 1.9999 | 0.005 | 2 | 0 |
| $k_u$ | 0.50 | 0.4999 | 0.02 | 0.4999 | 0.02 | 0.4999 | 0.02 |

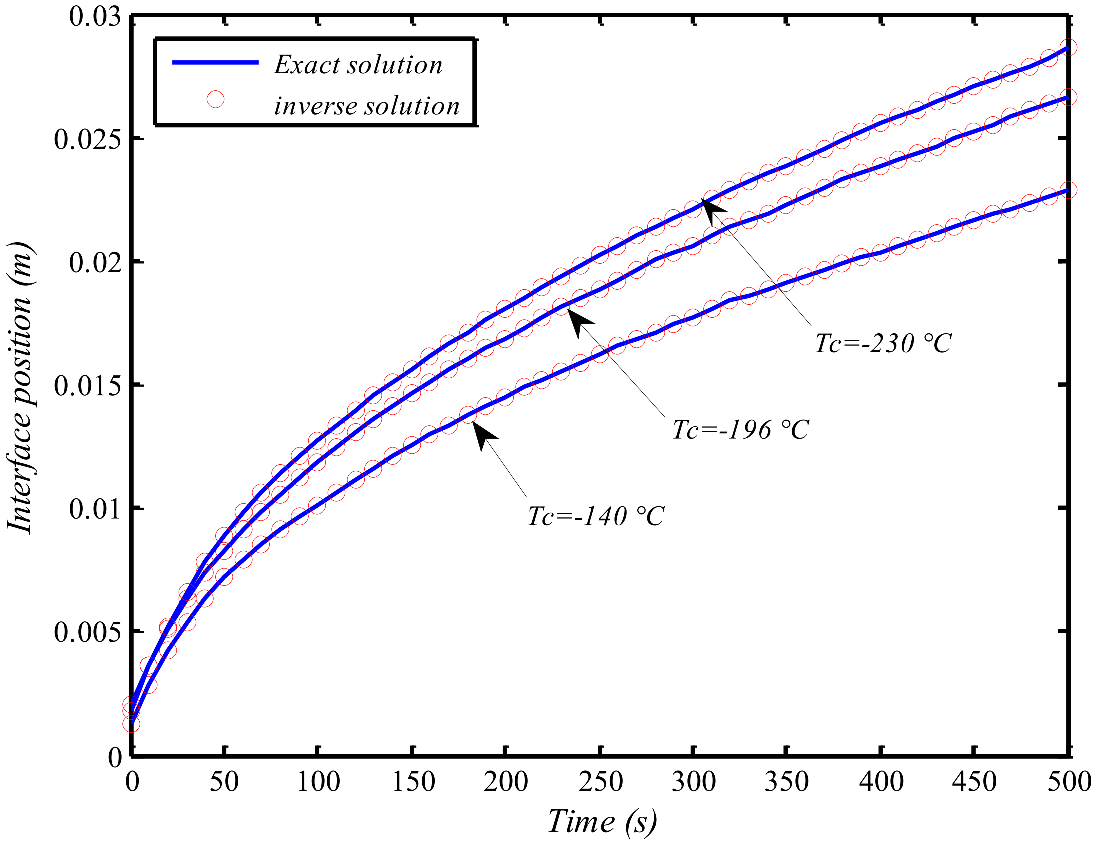

**Figure 6.9** Motion of the freezing front for different temperatures $T_c$.

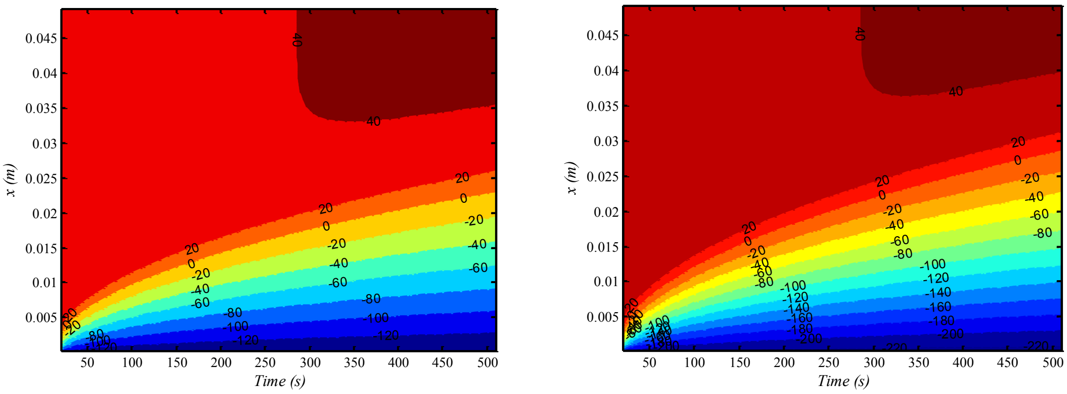

*Tc=-140 °C*

*Tc=-230 °C*

**Figure 6.10** Isotherms predicted with the inverse model.

### 6.5.3. Effect of heat transfer coefficient *h* on the inverse estimations

For external tumors such as ear and skin tumors, and for cysts, the cryogenic probe is not in direct contact with the surface of the tissue. The surface of the tissue is maintained at a constant sub-freezing temperature $T_c$ by resorting to an impinging jet of liquid nitrogen. In such cases, the temperature field across the layer of tissue and the time-varying location of the freezing front depend on the heat transfer coefficient of the impinging jet [207].

The effect of the external heat transfer coefficient on the predictions of the inverse model was examined by imposing the following boundary condition at $x = 0$ (Figure 6.1):

$$-k\frac{\partial T\left(x=0,\ \mathrm{t}\right)}{\partial x}=-h\left(T\left(0,t\right)-T_{\infty}\right) \tag{6.17}$$

$T_\infty$ is the temperature of liquid nitrogen. It is fixed at $T_\infty=-196\ °C$ [176].

Figure 6.11 illustrates the time evolution of the freezing front, predicted with both the direct and the inverse models, for different values of the heat transfer coefficient *h*. Once again, the agreement between both models is excellent. The relative root-mean-square error for the freezing front $RRMSE_{s(t)}$ remains, in all cases, below *1%*. It is also seen, as expected, that the size of the frozen region increases as the heat transfer coefficient augments. The corresponding temperature contours predicted with the inverse model for $h=250$ and $h=3000\ W/m^2\ °C$ are depicted in Figure 6.12.

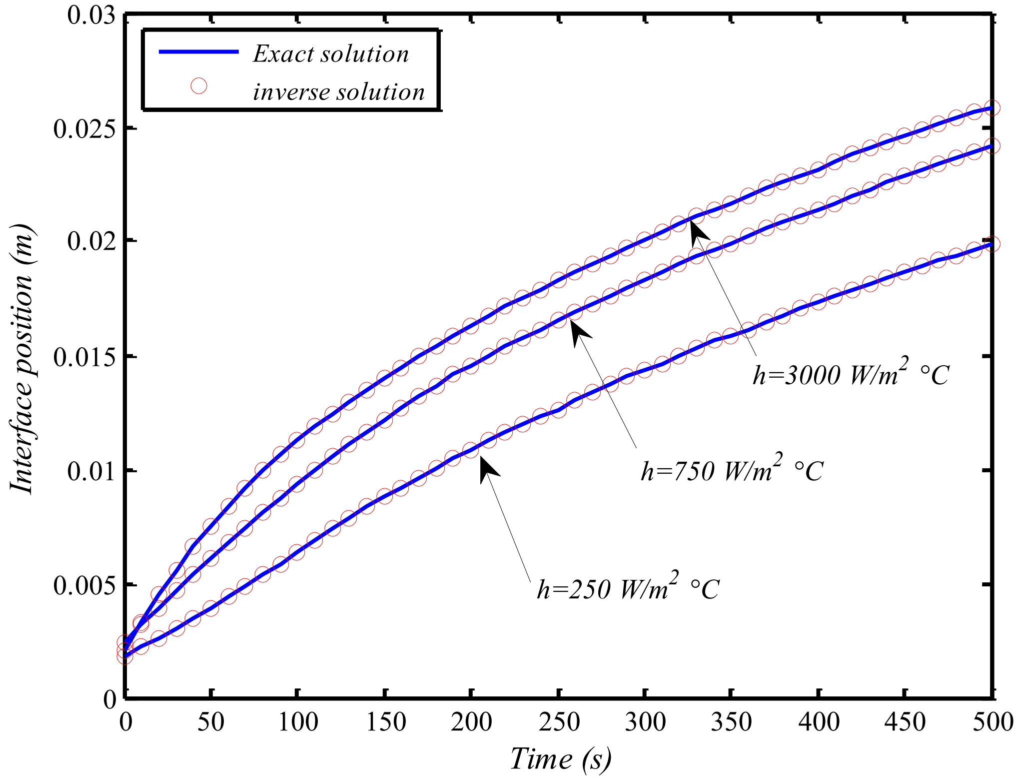

**Figure 6.11** Effect of the heat transfer coefficient.

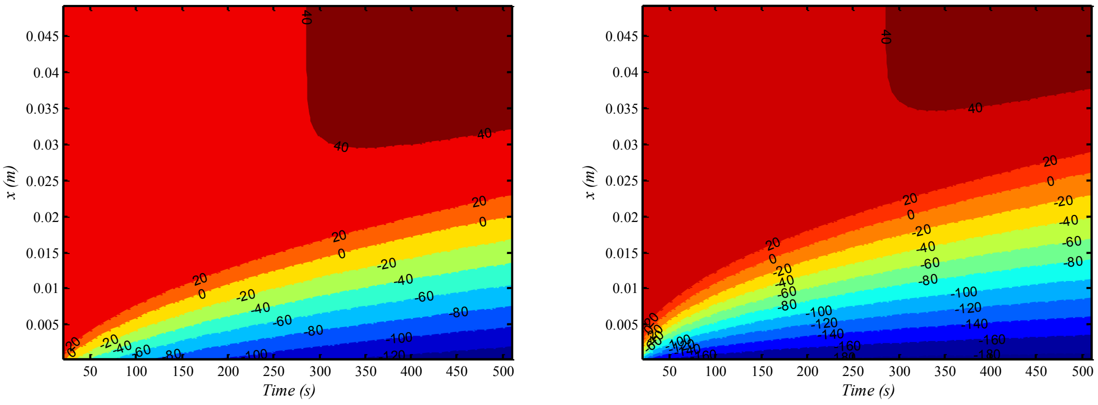

h=250 W/m$^2$ °C

h=3000 W/m$^2$ °C

**Figure 6.12** Temperature contours predicted with the inverse model.

### 6.5.4. Effect of noise on the inverse predictions

In order to assess the accuracy of the inverse solution and to obtain the confidence bounds, a statistical analysis for the unknown parameters was performed. Moreover, the temperatures recorded by the thermocouple probe may be contaminated with measurement errors. For distributed measurement errors with zero mean and a constant variance $\sigma^2$, the standard deviation of the estimated parameters can be expressed as

$$\sigma_{\hat{P}_j} = \sigma \sqrt{diag\left\{ \left( \frac{\partial T^T}{\partial P} \right) \left( \frac{\partial T}{\partial P^T} \right) \right\}^{-1}} \tag{6.18}$$

Assuming a normal distribution for the errors on the temperatures recorded and 99% confidence, the intervals for the computed parameters $P_j$ are given as

Probability:

$$\left\{ \left( \hat{P}_j - 2.576\ \sigma_{\hat{P}_j} \right) < P_{j,exact} < \left( \hat{P}_j + 2.576\ \sigma_{\hat{P}_j} \right) \right\} \cong 99\% \tag{6.19}$$

$\hat{P}_j$ are the estimated values of the unknown polynomial thermal parameters, $P_{j,exact}$, for (*j=1, 2, 3*), and $\sigma_{\hat{P}_j}$ are the standard deviations given by Eq. (6.18).

Let us examine the case with noisy experimental data. The temperatures recorded by the thermocouple probe were contaminated with '*measurement errors*' (or noise) using the random number generator (*randn*) $\vec{\omega}_i$. This measurement error is added to the recorded temperature, which, in the present study, is the temperature provided by the direct model $\vec{T}_{exact}$:

$$\vec{T}(\mathrm{t}_i) = \vec{T}_{exact}(\mathrm{t}_i) + \sigma\vec{\omega}_i \tag{6.20}$$

σ is the standard deviation of the measurement errors. The value for σ is arbitrarily set equal to $1\%T_{max}$ and to $2\%T_{max}$. $T_{max}$ is the maximum temperature measured by the thermocouple probe.

Figure 6.13 compares the measured noisy temperatures (the temperatures generated with the direct model that are contaminated with noise of $2\%T_{max}$) to the estimated temperatures (the temperatures predicted from the inverse model). The confidence bounds of ±2.576 $\sigma_{\hat{P}_j}$ are also shown. Once again, and in spite of the noisy data, the predictions of the inverse model remain accurate and reliable.

The effect of noise on the predictions of the freezing front is depicted in Figure 6.14. As expected, when the noise level rises from $1\%T_{max}$ to $2\%T_{max}$, the relative root-mean-square error for the phase change interface $RRMSE_{s(t)}$ slightly increases (from 0.25% to 0.32%). The computational time for noisy data also augments. Nonetheless, the inverse method remains stable and relatively accurate in all cases.

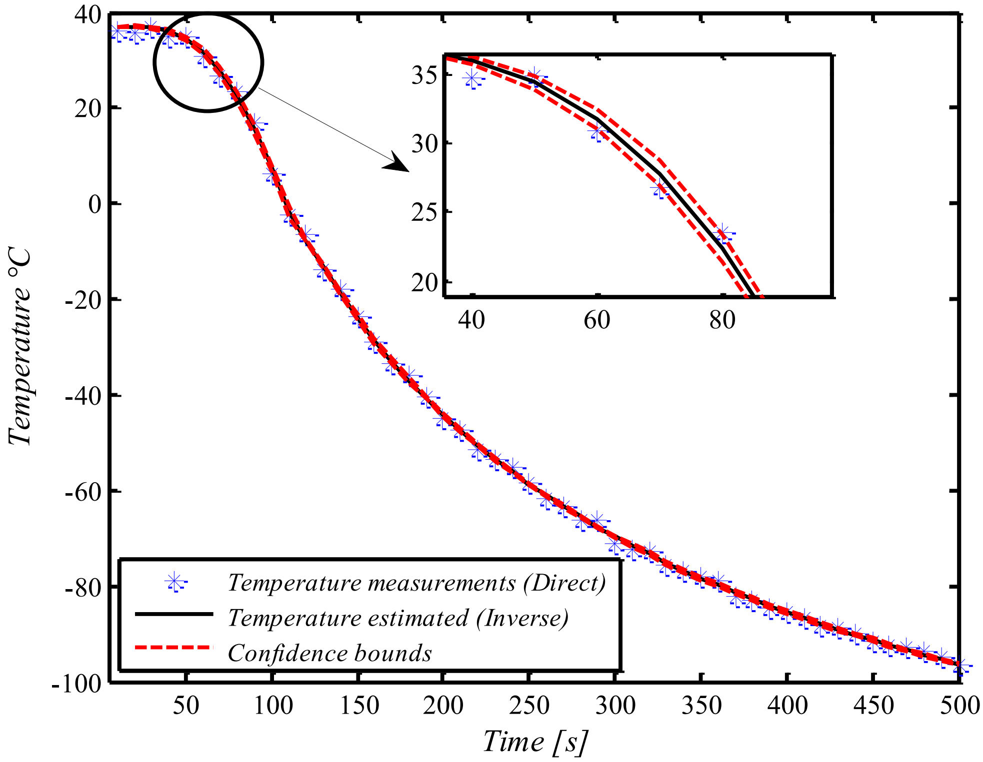

**Figure 6.13** Measured and predicted inverse temperatures.

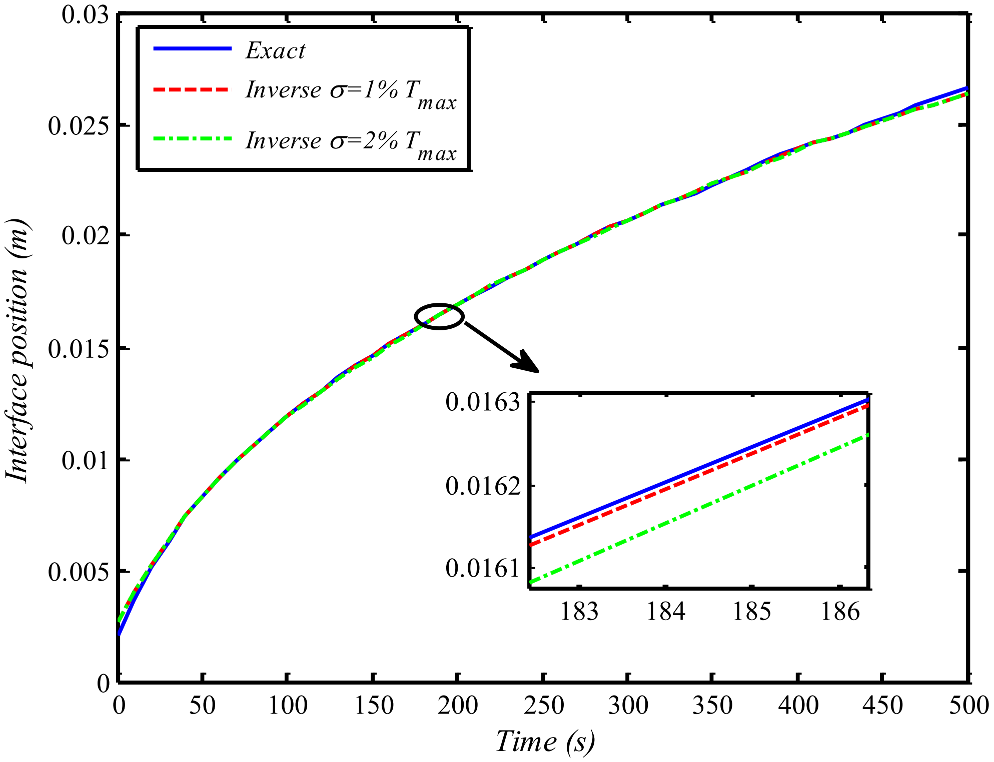

**Figure 6.14** Predicted position of the freezing front with noise.

## 6.6. Conclusion

This article presented an inverse heat transfer method for monitoring the motion of the freezing front from a cryoprobe. With the help of a thermocouple pressed against the layer of diseased tissue, the inverse heat transfer method is able to estimate simultaneously the blood perfusion rate and the thermal conductivities of both frozen and unfrozen tissues. This information is then fed to the *Pennes* bioheat equation that (1) calculates the time-varying temperature distribution inside the layer of tissue and (2) predicts the motion of the freezing front. The effect of the most influential parameters on the inverse predictions was investigated. These parameters are (1) the initial guesses for the unknown *Levenberg-Marquardt* polynomial parameters of the thermo-physical properties; (2) the temperature of the cryoprobe; (3) the heat transfer coefficient of the impinging jet of liquid nitrogen; and (4) the noise on the temperature data recorded by the thermocouple probe. Results have shown that the proposed inverse method is a viable alternative to ultrasound and MRI for monitoring the motion of the freezing front during cryosurgery. For all cryogenic scenarios investigated, the predictions of the inverse remained accurate and stable.

## Acknowledgements

The authors are grateful to the Natural Sciences and Engineering Research Council of Canada (NSERC) for the financial support.

# 7. CONCLUSION

## 7.1. Sommaire

Ce projet de recherche a permis de développer de nouveaux modèles numériques basés sur le transfert de chaleur inverse pour (1) prédire l'évolution temporelle de la couche protectrice qui recouvre les parois internes de briques réfractaires dans les réacteurs métallurgiques à haute température ; (2) prédire l'évolution temporelle de l'interface de congélation dans les tissus biologiques et évaluer la distribution de la température pendant la cryochirurgie. Si les problématiques abordées proviennent de domaines d'application différents, elles partagent, en revanche, des phénomènes thermiques semblables.

### 7.1.1. Les réacteurs métallurgiques

La première problématique a poursuivi des travaux entamés à l'université de Sherbrooke dont l'objectif est de développer des méthodes inverses afin de prédire l'épaisseur de la couche protectrice dans les réacteurs métallurgiques. Tout d'abord, un modèle monodimensionnel de changement de phase non-isotherme basé sur l'équation de conservation de l'énergie et la méthode enthalpique a été développé. Le système d'équations a été discrétisé à l'aide de la méthode des volumes finis. Ensuite, une validation numérique du modèle a été effectuée à l'aide des résultats disponibles dans la littérature.

Par la suite, le problème inverse a été posé. Il repose sur la méthode de *Levenberg-Marquardt* (LM). Pour réduire le temps de calcul associé à la mise en œuvre du problème inverse, la méthode de *Levenberg-Marquardt* a été combinée à la méthode de *Broyden*.
Les articles qui ont été publiés ont permis de répondre à la première problématique. Les objectifs qui ont été fixés pour cette problématique ont été atteints, soit :

(1) Une méthode inverse a été développée afin de prédire l'épaisseur de la couche protectrice à partir de mesures non-invasives de température provenant d'un seul capteur situé dans les parois extérieures du réacteur.

(2) Le phénomène d'érosion des parois internes de briques réfractaires a été détecté sans recourir aux modèles complexes de l'érosion. Le modèle inverse développé a permis de prévoir la profondeur d'érosion de la paroi intérieure en utilisant un seul thermocouple intégré dans la paroi extérieure de briques.

(3) La méthode inverse développée permet aussi de prédire simultanément les propriétés physiques et thermiques du réacteur telles que la conductivité thermique de la paroi de la brique réfractaire, la conductivité thermique de la couche protectrice, la conductivité thermique de la matière en fusion et le flux de chaleur dans le réacteur.

(4) La résistance thermique de contact entre la brique réfractaire et la couche protectrice et le flux de chaleur au centre du réacteur ont été estimées simultanément.

(5) Les paramètres polynomiaux de la conductivité thermique de MCP ont été déterminés en fonction de la température, du coefficient de transfert thermique extérieur et du flux de chaleur à l'intérieur du réacteur.

Les travaux de recherche effectués ont conduit également à des conclusions intéressantes, dont l'intérêt consiste à développer des techniques non-invasives au sein de l'industrie métallurgique. Par exemple, la position de thermocouple dans la paroi de briques a peu d'influence sur les prédictions inverses. Par conséquent, il est recommandé d'installer le thermocouple près de la paroi extérieure de brique réfractaire. En pratique, sa mise en place est plus facile et moins risquée. Toutefois, si le coefficient de convection extérieur est élevé, il est plutôt recommandé d'enfoncer le capteur dans le mur de brique. Par ailleurs, il a été conclu que l'augmentation de la fréquence d'acquisition du capteur améliore les prédictions inverses.

### 7.1.2. La cryochirurgie

Les objectifs relatifs à la deuxième problématique ont également été atteints.

(1) Premièrement, un modèle monodimensionnel basé sur l'équation de *Pennes* et la méthode enthalpique a été développé, puis validé par la solution analytique de *Neumann*.

(2) La méthode inverse, basée sur l'algorithme de *Levenberg-Marquardt* combinée à la méthode de *Broyden*, a été adaptée afin d'évaluer l'évolution temporelle du front de congélation ainsi que la distribution de température dans les tissus biologiques.

(3) La méthode inverse développée permet de prédire simultanément les propriétés thermo-physiques d'un tissu biologique telles que le taux de perfusion sanguine, la conductivité thermique de tissu congelé et celle de tissu non-congelé.

(4) La chaleur métabolique et le taux de perfusion sanguine d'un tissu malade ont été également estimés simultanément. La méthode inverse a été appliquée sur deux types de tumeurs (tumeur du poumon et tumeur du sein).

(5) L'effet des actions et des paramètres qui pourraient influencer les prédictions inverses telles que l'initialisation des paramètres polynomiaux inconnus dans la méthode de *Levenberg-Marquardt*, la température de la cryosonde, le bruit sur les mesures de température, le coefficient de transfert de chaleur extérieur, et le type de tumeur a été également examiné. Pour tous les scénarios cryogéniques simulés, il a été constaté que les prédictions du modèle inverse demeurent précises et stables.

Finalement, les résultats montrent que la méthode inverse proposée pourrait être une alternative viable aux ultrasons et à l'imagerie par résonance magnétique (IRM) pour assister la cryochirurgie.

## 7.2. Limites du projet de recherche et travaux futurs

Lors des travaux de recherche effectués dans le cadre de ce projet de thèse, des nouvelles problématiques ont été soulevées. Elles pourraient faire l'objet de travaux futurs.

### 7.2.1. La méthode inverse

Malgré le succès de la méthode inverse de *Levenberg-Marquardt* dans la prédiction des paramètres inconnus, elle est relativement gourmande en temps de calcul. Par conséquent, elle ne permet pas de contrôler en temps réel (1) l'épaisseur de la couche protectrice au sein des réacteurs métallurgiques et (2) l'interface de congélation pendant la cryochirurgie. Pour pallier à ce problème, des travaux futurs porteront sur l'utilisation des méthodes inverses d'estimation en temps réel telles que les réseaux de neurones artificiels [208].

Dans le contexte des méthodes inverses, la position de capteur de température et/ou de flux de chaleur doit être connue avec précision [151]. Toutefois, si celle-ci est erronée, quelles seraient les répercussions sur les prédictions inverses ? Des travaux futurs pourraient mettre l'accent sur ce problème ayant recours aux méthodes basées sur l'analyse statistique.

### 7.2.2. Les réacteurs métallurgiques

Toutes les études réalisées dans le cadre de la première problématique ont considéré un modèle monodimensionnel basé sur l'hypothèse des gradients de températures plus élevés dans la direction $x$ (Figure 1.2). En effet, ce modèle compte beaucoup de limitation, à savoir les pertes thermiques qui demeurent ignorées au niveau de la croûte et de la cathode (voir Figure 1.2). Par conséquent, le développement des modèles 2D et 3D est nécessaire pour prédire le profile réel de la couche protectrice.

En outre, le modèle développé est purement thermique. Il ignore, entre autres, les phénomènes électromagnétiques et mécaniques qui surgissent dans les réacteurs métallurgiques. Des travaux futurs porteront sur des modèles plus réalistes qui tiennent en compte les effets mécaniques et électromagnétiques en utilisant des codes commerciaux (CFX et ANSYS) couplés à la méthode inverse.
Le dernier point dans cette partie consistera en la validation expérimentale de la méthode inverse pour l'industriel.

### 7.2.3. La cryochirurgie

Les travaux réalisés ici constituent un point de départ pour le transfert de chaleur inverse en cryothérapie. L'intégration de cette approche de modélisation dans certaines applications médicales (lutte contre le cancer) pourrait servir au développement thérapeutique dédié à la cryochirurgie. Pour sa mise en œuvre, plusieurs points devraient être considérés, notamment :

- ✓ Le recours aux modèles 2D et 3D qui est également incontournable surtout pour des organes vitaux présentant des géométries complexes.
- ✓ La localisation de point d'intervention au sein de la tumeur lors de l'insertion de la cryosonde est à la fois une tâche délicate et cruciale. La taille de la tumeur doit être identifiée avec précision. Pour ce faire, une méthode inverse sera développée pour prédire en premier temps la position de la cryosonde par rapport aux dimensions de la tumeur, et par la suite évaluer l'interface de congélation.
- ✓ Malgré que le modèle de *Pennes* ait connu un grand succès dans la modélisation des tissus biologique, il compte beaucoup de limitations, entre autres, (1) il ne tient pas compte l'effet de la géométrie vasculaire des vaisseaux (la ramification et le rétrécissement de diamètre des vaisseaux) et (2) il ne considère pas l'effet de la

direction de la perfusion sanguine dans le tissu. Pour franchir ces limites, l'utilisation des modèles plus développés, à savoir le modèle de *Wulff* (1974) et le modèle de *Kreith* (2000) [209], [101], fera l'objet d'une étude ultérieure.

- ✓ Dans toutes les études réalisées ici, un seul cycle de congélation a été considéré. Or, plusieurs études antérieures ont montré que l'utilisation de cycles 'gel-dégel' permet d'améliorer la cryothérapie [29, 204, 210]. Dans ce contexte, des travaux futurs porteront sur la prédiction des paramètres inconnus pendant la cryochirurgie gel-dégel.
- ✓ Finalement, tous ces modèles numériques devraient être validés expérimentalement afin de s'assurer de la crédibilité de l'approche inverse en cryochirurgie. Faute de temps et de moyens, on n'a pas pu poursuivre davantage les travaux de recherche sur le transfert inverse en cryochirurgie.

## 7.3. Contributions scientifiques du projet de recherche

### 7.3.1. Articles publiés dans les journaux avec comité de lecture

1. Hafid M. et Lacroix M., " **Inverse heat transfer prediction of the state of the brick wall of a melting furnace**." *Applied Thermal Engineering*, vol. 110, p. 265-274, ***(2017).***
2. Hafid M. et Lacroix M., "**An inverse heat transfer method for predicting the thermal characteristics of a molten material reactor**." *Applied Thermal Engineering*, vol. 108, p. 140-149, ***(2016).***
3. Hafid M. et Lacroix M., "**Inverse Heat Transfer Analysis of a Melting Furnace Using Levenberg-Marquardt Method**." *International Journal of Mechanical, Aerospace, Industrial, Mechatronic and Manufacturing Engineering*, vol. 10, no 7, p. 1196-1203, ***(2016).***
4. Hafid M. et Lacroix M., "**Prediction of the Thermal Parameters of a High-Temperature Metallurgical Reactor Using Inverse Heat Transfer.**", *International Journal of Mechanical, Aerospace, Industrial, Mechatronic and Manufacturing Engineering*, vol. 10, no 6, p. 907-913, ***(2016).***

### 7.3.2. Articles soumis pour publication

5. Hafid M. et Lacroix M., " **Multi-parameter Estimation of a Melting Furnace by Inverse Heat Transfer**", soumis au *Applied Thermal Engineering,* Décembre ***2016***.
6. Hafid M. et Lacroix M., " **Fast inverse prediction of the freezing front in cryosurgery**", soumis au *Journal of Thermal Biology*, Avril ***2017***.
7. Trabelsi S., Hafid M., Poncet S., Poirier M., Lacroix M., " **Rheology of Ethylene- and Propylene-Glycol Ice Slurries: experiments and ANN model** ", soumis au *International Journal of Refrigeration, Mars* ***2017***.

### 7.3.3. Actes de colloques avec comité de lecture

8. 19th International Conference on Biophysical and Biomedical Engineering*, 25-26 Juin* ***2017****,* Paris, France.
9. 25ème Congrès Français de Thermique, 30 mai-2 juin ***2017***, Marseille, France.
10. 18th International Conference on Heat Transfer and Applications, *14-15 Juillet,* ***2016***, Montréal, Canada.
11. 18th International Conference on Fluid Mechanics and Thermodynamics, *6-7 Juin,* ***2016***, New York, USA.

### 7.3.3. Autres contributions sans comité de lecture

12. 84e Congrès de l'Acfas, *9-13 Mai,* ***2016***, Montréal, Canada.
13. 2e assemblée annuelle du CREEPIUS, *8 Janvier,* ***2015***, Sherbrooke, Canada.

# ANNEXE A : PRÉDICTION PAR TRANSFERT INVERSE DES PARAMÈTRES THERMIQUES D'UNE CUVE D'ÉLECTROLYSE.

## Avant-propos

**Auteurs et affiliation :**

**M. Hafid** : Étudiant au doctorat, Université de Sherbrooke, Faculté de génie, Département de génie mécanique.

**M. Lacroix** : Professeur, Université de Sherbrooke, Faculté de génie, Département de génie mécanique.

**Conférence :** *18th* International Conference on Fluid Mechanics and Thermodynamics, *6-7 Juin, **2016***, New York, USA.

**Revue :** Int. Journal of Mechanical, Aerospace, Industrial, Mechatronic and Manufacturing Engineering.

**État de l'acceptation :** Version finale publiée.

**Référence :** [38]

# Title

Prediction of the Thermal Parameters of a High-Temperature Metallurgical Reactor Using Inverse Heat Transfer.

# Abstract

This study presents an inverse analysis for predicting the thermal conductivities and the heat flux of a high-temperature metallurgical reactor simultaneously. Once these thermal parameters are predicted, the time-varying thickness of the protective phase-change bank that covers the inside surface of the brick walls of a metallurgical reactor can be calculated. The enthalpy method is used to solve the melting/solidification process of the protective bank. The inverse model rests on the *Levenberg-Marquardt* Method (LMM) combined with the *Broyden* method (BM). A statistical analysis for the thermal parameter estimation is carried out. The effect of the position of the temperature sensors, total number of measurements and measurement noise on the accuracy of inverse predictions is investigated. Recommendations are made concerning the location of temperature sensors.

# Keywords

Inverse heat transfer, phase change, metallurgical reactor, *Levenberg–Marquardt* method, *Broyden* method, bank thickness.

## A.1. Introduction

High-temperature metallurgical reactor such aluminum-electrolysis-cells (Figure A.1) are used for material processing that requires high powers and elevated temperature. Their applications are in the production of aluminum and the smelting of materials such as steel, copper and nickel calcine.

A fascinating solid/liquid phase change phenomenon that arises in these metallurgical reactors is the formation of a bank that covers the inside surface of the refractory brick wall. The presence of this bank is extremely important. It protects the inner lining of the refractory brick wall from the highly corrosive slag. On the other hand, too thick a bank is detrimental to the industrial production as the volume available for smelting is reduced. Therefore, keeping a bank of optimal thickness is crucial for the safe and profitable operation of the metallurgical reactor.

Due to the hostile conditions that prevail inside these reactors, it is however very difficult and risky to measure the bank thickness using probes submerged into the corrosive slag (The standard method). Additionally, the transient formation of the bank depends on the boundary conditions, the power input, and the thermos physical properties of the slag. Consequently, predicting the transient formation of the protective bank inside high-temperature metallurgical reactor is a challenging problem. To address this problem, an inverse heat transfer procedure is proposed. The prediction of the bank formation with inverse heat transfer methods has been the subject of few investigations in the past. These methods rest on the conjugate gradient method [17, 47, 64, 65], the Kalman filter method [58-62] and the LMM [66]. In all of these studies, the focus was on the inverse prediction of the time-varying heat flux at ($x=L_{Brick} + L_{PCM}$) using the transient temperature measurements, or heat flux measurements, taken at a specified location inside the refractory brick wall (Figure A.2). Once the heat flux had been predicted, the time-varying bank thickness $E(t)$ was calculated using the direct model.

The objective of the present study is to extend these previous studies by predicting simultaneously several unknown quantities of interest that is the time-varying heat flux $q''(t)$, the thermal conductivity in liquid PCM, the thermal conductivity in solid PCM and the thermal conductivity of refractory brick wall (Figure A.4).

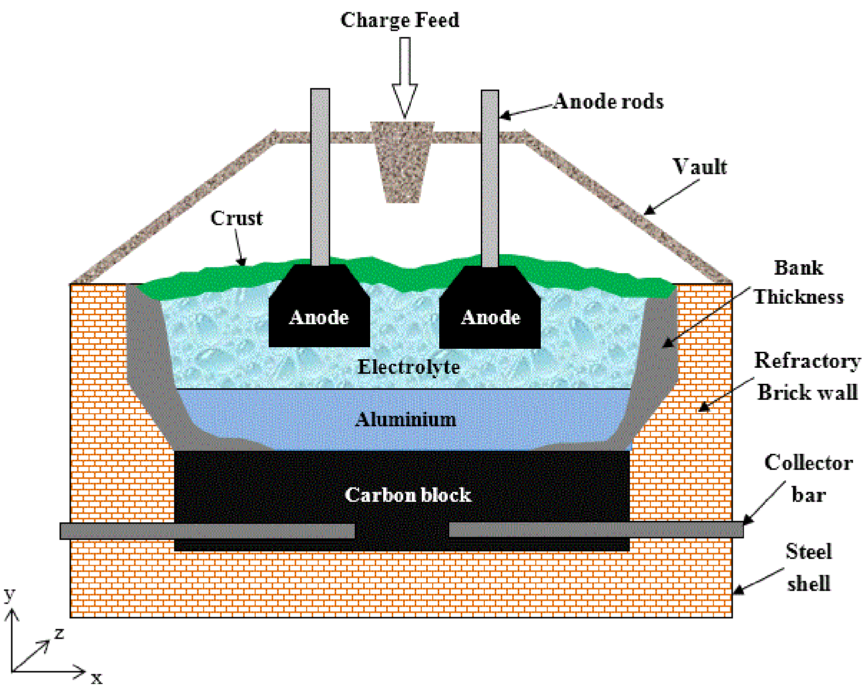

**Figure A.1** Cross view of a typical high-temperature metallurgical reactor.

## A.2. Problem Statement and Mathematical Model

The one-dimensional phase-change problem for a High-temperature Metallurgical Reactor is depicted in Figure A.2.

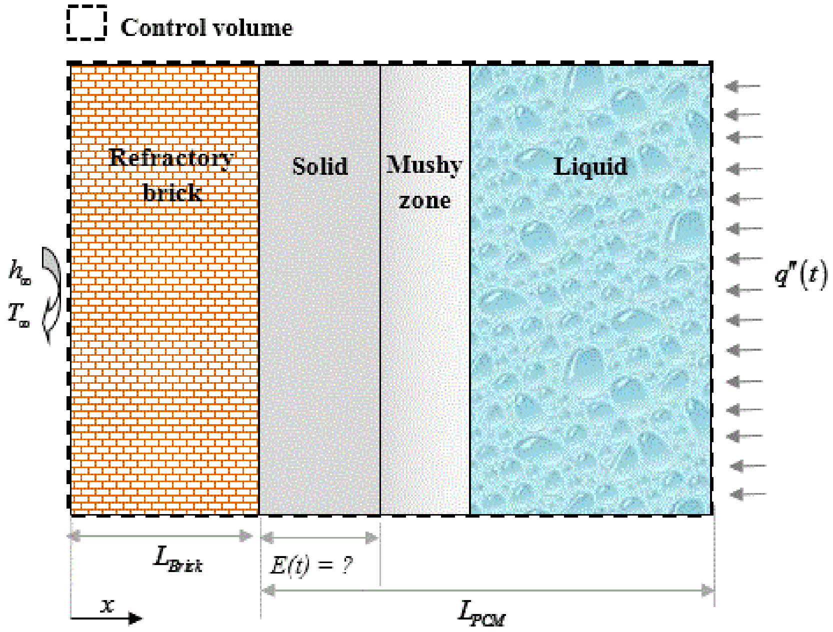

**Figure A.2** Schematic of a one-dimensional phase-change problem for a high-temperature metallurgical reactor.

The inner lining of the brick wall ($x=L_{Brick}$) is coated with a protective bank whose thickness is $E(t)$. $E(t)$ represents the position of the solidification front for the Phase Change Material (PCM). The outer surface of the brick wall ($x=0$) is cooled with an air stream. The outside temperature is $T_\infty$ and the convective heat transfer coefficient $h_\infty$. At ($x= L_{Brick} + L_{PCM}$), a time-varying heat flux $q''(t)$ is imposed over the time interval $t\epsilon[0, 400000\ (s)]$.

The proposed mathematical model rests on the following assumptions [17, 58-61]:

- ✓ The temperature gradients in the $x$ direction are much larger than those in the other directions. As a result, a one-dimensional analysis can be applied.
- ✓ The heat transfer inside the liquid phase of the PCM is conduction dominated [142].
- ✓ The thermal properties of the phase change material (PCM) are temperature independent.
- ✓ The phase change problem is non-isothermal. The melting process is depicted by three zones: a solid phase, a mushy zone and a liquid phase.
- ✓ The thermal contact resistance between the refractory brick wall and the PCM is neglected.

Based on these assumptions, the governing heat diffusion equation is expressed as:

$$\rho C_p \frac{\partial T}{\partial t} = \frac{\partial}{\partial x}\left(k\frac{\partial T}{\partial x}\right) - \delta H \frac{\partial f}{\partial t} \tag{A.1}$$

where $\delta H$ and $f$ are the enthalpy and the liquid fraction, respectively. The enthalpy $\delta H$ is defined as

$$\delta H = \rho(C_{p,liquid} - C_{p,solid})T + \rho\lambda \tag{A.2}$$

The liquid fraction $f$ varies linearly between the solidus $T_{sol}$ and the liquidus $T_{liq}$ in the following manner:

$$f = F(T)\begin{cases} 0 & T \le \mathrm{T}_{sol} \quad (\textit{Solid}\ \text{region}) \\ \dfrac{T-T_{sol}}{T_{liq}-T_{sol}} & \mathrm{T}_{sol} \le T \le \mathrm{T}_{liq}\ (\textit{Mushy}\ \text{region}) \\ 1 & T \ge \mathrm{T}_{liq} \quad (\textit{Liquid}\ \text{region}) \end{cases} \tag{A.3}$$

At each time-step, the liquid fraction $f$ is updated iteratively in the following manner [141]:

$$f^{k+1} \approx f^{k} + \left(\frac{dF}{dT}\right)^{k}\left(T^{k+1} - F^{-1}\left(f^{k}\right)\right) \tag{A.4}$$

$F^{-1}$ is the inverse function of $F$. The boundary conditions at the left and right sides of Figure A.2 are:

$$\begin{cases} \left(-k\dfrac{\partial T}{\partial x}\right)_{x=0} = \bar{h}\left(T\left(0,t\right) - T_{\infty}\right) \\ \left(-k\dfrac{\partial T}{\partial x}\right)_{x=L_{Brick}+L_{PCM}} = q''\left(t\right) \end{cases} \tag{A.5}$$

Equations (A.1)-(A.5) are solved numerically using a Finite-Volume Method (FVM). The scheme adopted for the time discretization is implicit. The resulting set of algebraic equations is solved using the Tri-Diagonal-Matrix-Algorithm (TDMA) [143].

The mathematical model was first validated using the one-dimensional test case for the solidification of the binary Al–4.5% Cu alloy reported in [140, 168]. In this example, a Dirichlet boundary condition of $T=573$ *(K)* is assumed at the boundary $x=L_{Brick}$ (Figure A.2). The width of the PCM layer is set equal to $L_{PCM}=0.5$ *(m)* and the initial temperature is fixed at $T_{in}= 969$ *(K)*. Figure A.3 shows the predicted time-varying phase front are in excellent agreement with the source-based numerical method [141] and the semi-analytical heat balance integral method [140].

Next, the direct model was implemented for the entire metallurgical reactor i.e. the refractory brick wall and the PCM (Figure A.2). The operating thermal conditions of the metallurgical reactor are similar to those reported in [58, 60]. The brick wall is set equal to $L_{Brick}=0.1(m)$ and the PCM layer (solid, mushy, and liquid) is set equal to $L_{PCM}=0.1(m)$ (Figure A.2). The surrounding temperature is set equal to $T_{\infty}=300$ *(K)* and the outside average heat transfer coefficient is fixed at $h_{\infty}=15$ *(W/m$^2$ K)*.

The time-varying heat flux $q''(t)$ at ($x=L_{Brick}+L_{PCM}$) is given by

$$q''(t) = Q_0 + Q_1 * \sin^2\left(\frac{3\pi.t}{t_{\max}}\right) \tag{A.6}$$

It is also assumed that the PCM thermal conductivity in the solid and liquid phases is temperature independent. The thermo-physical properties of the metallurgical reactor (brick wall and PCM) are provided in Table A.1 [58, 60].

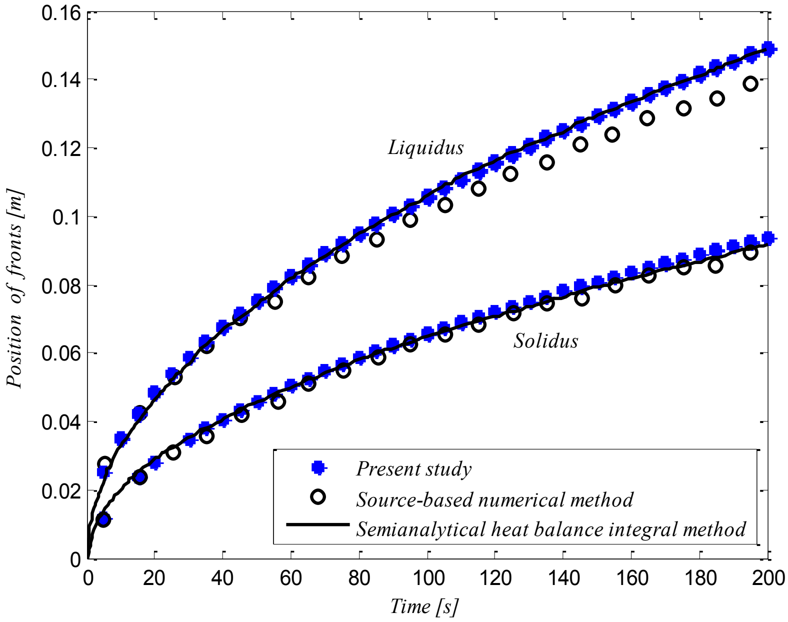

**Figure A.3** Solidification of a binary Al–4.5%-Cu alloy.

**Table A.1** Thermo-physical Properties of the Brick Wall and PCM.

| Parameter | Value | Unit |
|---|---|---|
| $k_{BRICK}$ | 16.8 | W/m K |
| $C_{p, BRICK}$ | 875 | J/kg K |
| $\rho_{BRICK}$ | 2600 | kg/m$^3$ |
| $k_{PCM,solid}$ | 1 | W/m K |
| $k_{PCM,liquid}$ | 10 | W/m K |
| $C_{p, PCM,solid}$ | 1800 | J/kg K |
| $C_{p, PCM,liquid}$ | 1800 | J/kg K |
| $\rho_{PCM}$ | 2100 | kg/m$^3$ |
| $\lambda_{PCM}$ | 5.1 x 10$^5$ | J/kg |
| $T_{sol}$ | 1213 | K |
| $T_{liq}$ | 1233 | K |

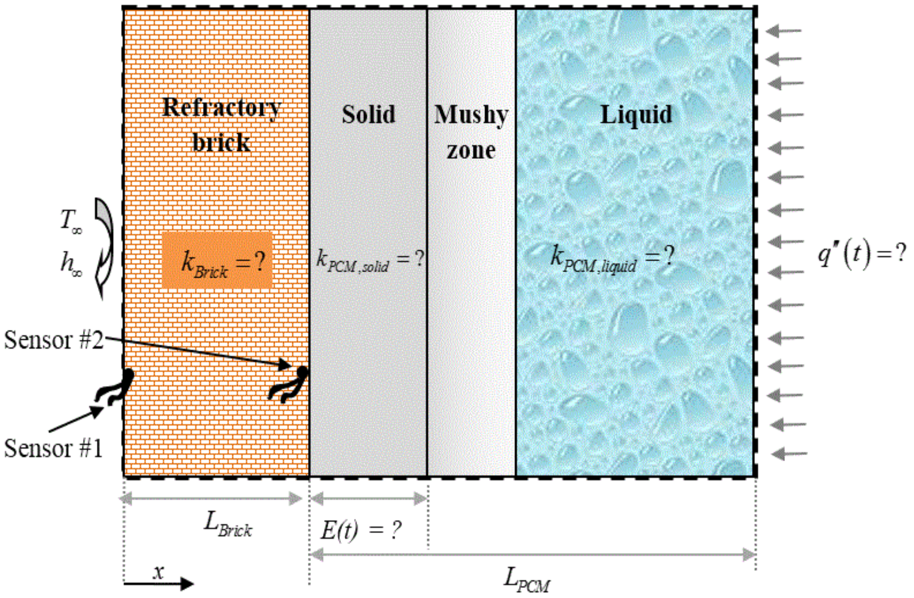

**Figure A.4** The inverse problem: $k_{Brick}$, $k_{PCM,solid}$, $k_{PCM,liquid}$ and $q''(t)$ are unknown. They are determined from temperatures taken by probes (sensor #1 or sensor #2) embedded into the brick wall.

## A.3. The Inverse Model

In the direct model presented above, all the physical and the geometrical properties are known. For the inverse model, it is assumed that the parameters of: the heat flux $q''(t)$, the thermal conductivity of the brick wall $k_{Brick}$, the thermal conductivity in the solid PCM $k_{PCM,solid}$ and in the liquid PCM $k_{PCM,liquid}$ are unknown (Figure A.4).

The objective of the inverse model is to determine the unknown thermal parameters for $q''(t)$ and thermal conductivities, i.e. $\vec{P} = \left[Q_0;\ Q_1;\ k_{brick};\ k_{PCM,solid};k_{PCM,liquid}\right]$. The additional information required for the estimation of these thermal parameters, is the time-varying temperature recorded by a sensor (thermocouple) embedded into the refractory brick wall Figure A.4. Once the thermal parameters are estimated, the bank thickness $E(t)$ is determined from the direct model presented above.

The estimation of the thermal parameters from measured can be constructed as a problem of minimization of the least square norm $\Psi\left(\vec{P}\right)$:

$$\Psi\left(\vec{P}\right) = \sum_{i=1}^{I}\left[Y\left(t_i\right) - \hat{T}\left(t_i,\vec{P}\right)\right]^2 \tag{A.7}$$

$P = (P_1, P_2, ...P_5)$ is the set of the unknown thermal parameters. $I$ is the total number of measurements. $Y(t_i)$ are the temperatures measured by the sensor. In the present study, these temperatures are 'generated' from the solution of the direct model. $\hat{T}\left(t_i, \vec{P}\right)$ are the estimated temperatures from the inverse model.

The *Levenberg–Marquardt* Method was adopted for minimizing the least square norm, (A.7). The incremental value of the unknown parameter $\Delta P$, is expressed as:

$$\Delta\vec{P} = \left[\left(\overleftrightarrow{J}^k\right)^T \overleftrightarrow{J}^k + \mu^k \overleftrightarrow{\Omega}^k\right]^{-1} \left(\overleftrightarrow{J}^k\right)^T \left(\vec{Y} - \vec{T}\left(\vec{P}^k\right)\right) \tag{A.8}$$

$\mu^k$ is a positive damping parameter. More details on the choice and the update of this parameter are provided in [150]. $\overleftrightarrow{\Omega}^k$ is the diagonal matrix of $\left(\overleftrightarrow{J}^k\right)^T \overleftrightarrow{J}^k$. The superscript 'T' denotes the transpose of the matrix. The superscripts "$\leftrightarrow$" and"$\rightarrow$" refer to the matrix and vector notation, respectively. $\overleftrightarrow{J}^k$ is the Jacobian matrix. It is given by:

$$\overleftrightarrow{J}\left(\vec{P}\right) = \begin{pmatrix} \frac{\partial T_1}{\partial P_1} & \frac{\partial T_1}{\partial P_2} & \frac{\partial T_1}{\partial P_3} & \frac{\partial T_1}{\partial P_4} & \frac{\partial T_1}{\partial P_5} \\ \frac{\partial T_2}{\partial P_1} & \frac{\partial T_2}{\partial P_2} & \frac{\partial T_2}{\partial P_3} & \frac{\partial T_2}{\partial P_4} & \frac{\partial T_2}{\partial P_5} \\ \vdots & \vdots & \vdots & \vdots & \vdots \\ \frac{\partial T_I}{\partial P_1} & \frac{\partial T_I}{\partial P_2} & \frac{\partial T_I}{\partial P_3} & \frac{\partial T_I}{\partial P_4} & \frac{\partial T_I}{\partial P_5} \end{pmatrix} \tag{A.9}$$

The Jacobian matrix (the sensitivity matrix) plays a very important role in the estimation of the parameters. There are several approaches for computing the sensitivity coefficients $\partial T_i/\partial P_j$ [151]. In this study, the sensitivity coefficients are approximated with a finite difference:

$$J_{ij} = \frac{\partial \hat{T}_i}{\partial P_j} \cong \frac{\hat{T}\left(t_i; P_1, ..., P_j + \left(\delta P_j\right), ...P_N\right) - \hat{T}\left(t_i; P_1, ..., P_j - \left(\delta P_j\right), ...P_N\right)}{2\left(\delta P_j\right)} \tag{A.10}$$

The parameter perturbation $\left(\delta P_j\right)$ is set to $\xi\left(1 + \left|P_j\right|\right)$. $\xi$ is a small number. The subscripts $i$ and $j$ represent the time and the parameter respectively.

In order to diminish the computational effort, the Jacobian matrix is updated using the *Broyden* update expression [152].

For the first iteration, for every 2*N iterations and for iterations that satisfy $\Psi(P+\Delta P) > \Psi(P)$, the sensitivity coefficients $\partial T_i/\partial P_j$ of the Jacobian matrix are estimated with (A.10). For every other iteration, the Jacobian matrix is updated using the *Broyden* expression:

$$J_k = J_{k-1} + \frac{\left(\left(\hat{T}_k - \hat{T}_{k-1}\right) - J_{k-1}\Delta P_{k-1}\right)\Delta P_{k-1}^T}{\Delta P_{k-1}^T \Delta P_{k-1}} \tag{A.11}$$

$\Delta P_{k-1}$ is the incremental value of the unknown parameters. $J_k$ and $J_{k-1}$ are the Jacobian matrices at the current and previous iteration, respectively.

Convergence of the LMM is declared when one of the following criteria is satisfied

$$\begin{cases} J^T \left\| Y(t_i) - \hat{T}\left(t_i, \vec{P}\right) \right\| < \varepsilon_1 \\ \left( \dfrac{P^{k+1} - P^k}{P^{k+1}} \right) < \varepsilon_2 \\ \Psi\left(P^{k+1}\right) < \varepsilon_3 \end{cases} \tag{A.12}$$

$(\varepsilon_1;\ \varepsilon_2;\ \varepsilon_3)$ are small numbers.

The *Levenberg–Marquardt* computational procedure for the inverse problem is summarized as:

*Step 1:* Solve the direct problem (A.1)-(A.5) in order to obtain the temperature field $T_{exact}$.

*Step 2:* Compute the least square norm $\Psi(P)$ from (A.7).

*Step 3:* Compute the sensitivity coefficients according to (A.10) or the *Broyden* update expression (A.11).

*Step 4:* Compute the increment $\Delta P$ of the estimated parameters from (A.8).

*Step 5:* Solve the direct problem with the new estimate $P^{k+1}$ in order to find $T(P^{k+1})$. Then compute $\Psi\left(P^{k+1}\right)$ as defined in step 2.

*Step 6:* Check for convergence as defined in (A.12). If convergence is not achieved, go back to Step 3, update the sensitivity coefficients and $\Psi(P)$.

Once the vector of the thermal parameters has been estimated, the bank *E(t)* is easily determined from the direct model.

## A.4. Statistical Analysis for Parameters Estimation

In order to assess the accuracy and the uniqueness of the solution and to obtain confidence intervals, a statistical analysis for parameter estimation was performed. Moreover, it was assumed that the signal temperature is contaminated with measurement errors. For distributed measurement errors with zero mean and constant variance $\sigma^2$, the standard deviation of the estimated parameters can be defined as [151]

$$\sigma_{p_j} = \sigma\sqrt{diag\left\{\left(\frac{\partial T^T}{\partial P}\right)\left(\frac{\partial T}{\partial P^T}\right)\right\}^{-1}} \tag{A.13}$$

Assuming a normal (or Gaussian) distribution for temperature measurement errors and 99% confidence, the bounds for the computed quantities $P_j$ are determined as

Probability:

$$\left\{\left(\hat{P}_j - 2.576\ \sigma_{\hat{P}_j}\right) < P_{j,exact} < \left(\hat{P}_j + 2.576\ \sigma_{\hat{P}_j}\right)\right\} \cong 99\% \tag{A.14}$$

$\hat{P}_j$ are the estimated values of the unknown parameters, $P_{j,exact}$, for *(j=1…5)*, and $\sigma_{\hat{P}_j}$ are the standard deviations obtained from (A.13).

## A.5. Results and Discussion

The above inverse heat transfer computational procedure was employed to predict simultaneously the heat flux *q"(t)* and the thermal conductivities ($k_{Brick}$, $k_{PCM,solid}$ and $k_{PCM,liquid}$) inside a high-temperature metallurgical reactor (Figure A.4). Once these parameters are estimated, the time-varying bank thickness *E(t)* is calculated from the direct model presented in section A.2.

The measured temperatures were collected with a sensor embedded into the refractory brick wall at two different locations: The first location, called ‘Sensor#1’, is near the outer surface of the brick wall. The second position, ‘Sensor#2’, is close to the molten material

PCM (Figure A.4). The total number of temperature measurements $I$ during the interval $t\epsilon[0, 400000\ (s)]$ is 2000.

Note that the uniqueness and the accuracy of the inverse procedure have been thoroughly tested with noisy data and for different positions of the sensor. These results are not reported here.

For the sake of comparing the inverse predictions '*Inverse model*' to the exact solution '*Direct model'*, three different estimation errors are defined in the following manner:

$$\text{Error}_{E(t_i)} = 100 \times \frac{\left|E(t_i)_{exact} - E(t_i)_{inverse}\right|}{\left|E(t_i)_{exact}\right|} \tag{A.15}$$

$$\text{RRMSE}_{E(t)}\,\% = 100 \times \sqrt{\frac{1}{I}\sum_{i=1}^{I}\left(\frac{E(t_i)_{exact} - E(t_i)_{inverse}}{E(t_i)_{exact}}\right)^2} \tag{A.16}$$

$$Error_P\ \% = 100 \times \frac{\left|P_{exact} - P_{inverse}\right|}{\left|P_{exact}\right|} \tag{A.17}$$

The effect of the sensor location (Sensor#1 and Sensor#2) on the estimation of the unknown parameters is summarized in Table A.2. It is seen that the error on the parameters estimation is less than 0.7%. It is also observed that sensor#2 (embedded deeper into the brick wall) provides the best parameter estimation.

The convergence for the unknown thermal parameters $\vec{P} = \left[Q_0;\ Q_1;\ k_{brick};\ k_{PCM,solid};k_{PCM,liquid}\ \right]$ is plotted in Figure A.5.

**Table A.2** Effect of the sensor position.

| | | *Sensor#1* | | *Sensor#2* | |
|---|---|---|---|---|---|
| | $P_{Exact}$ | $P_{Inverse}$ | $Error_P$ % | $P_{Inverse}$ | $Error_P$ % |
| $Q_0$ $(W/m^2)$ | 6000 | 5998.29 | 0.03 | 6001.84 | 0.03 |
| $Q_1$ $(W/m^2)$ | 5000 | 5003.46 | 0.07 | 5001.17 | 0.02 |
| $k_{brick}$ $(W/m\ k)$ | 16.8 | 16.88 | 0.48 | 16.85 | 0.30 |
| $k_{solid}$ $(W/m\ k)$ | 1 | 1.00 | 0.00 | 1.00 | 0.00 |
| $k_{liquid}$ $(W/m\ k)$ | 10 | 9.93 | 0.70 | 9.99 | 0.10 |

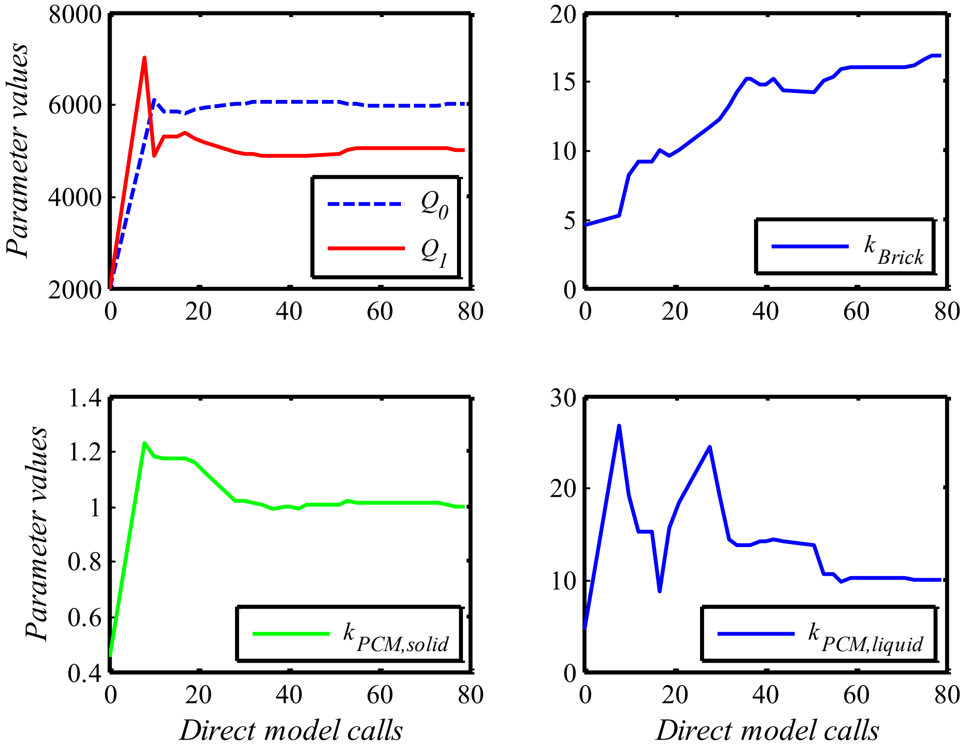

**Figure A.5** Convergence of the parameter values (Sensor#1, no noise).

The finite-difference approximation of the sensitivity coefficients, (A.9), requires the solution of the direct problem five times (number of unknown parameters) per iteration. As a result, the computations may quickly become prohibitive. To alleviate the computational effort, the sensitivity matrix was updated with the BM [152]. This strategy has already been applied successfully in the field of inverse heat transfer (IHTP) [154, 155]. Table A.3 shows that the solution using the LMM combined with BM (LMM/BM) is achieved more efficiently than that with the LMM.

**Table A.3** The convergence of LMM and LMM/BM.

| | *Direct model calls* | *CPU time (s)* |
|---|---|---|
| *LMM* | 90 | 4468.92 |
| *LMM/BM* | 79 | 3502.98 |

All simulations were conducted with the Matlab software running on an Intel ® Core(TM) i5-2520M CPU @ 2.50 GHz. The effect of the temperature-sensor location on the accuracy of the predicted bank thickness *E(t)* is depicted in Figure A.6. For both sensors, i.e., sensor#1 and sensor#2, the $Error_{E(t)}$ on the predicted bank thickness remains less than

0.1%. The effect of the sensor location appears to be insignificant [17]. Therefore, for practical reasons, sensor#1 is recommended over sensor#2. It is indeed much safer and easier to embed a sensor near the outer surface of the refractory brick wall. This result should be of interest to the process industry.

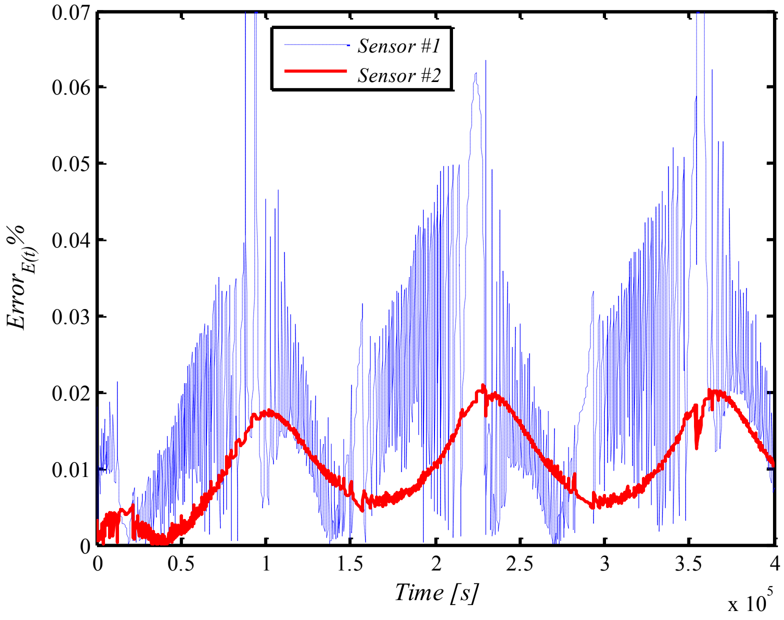

**Figure A.6** Effect of the sensor position on the predicted bank thickness *E(t)*.

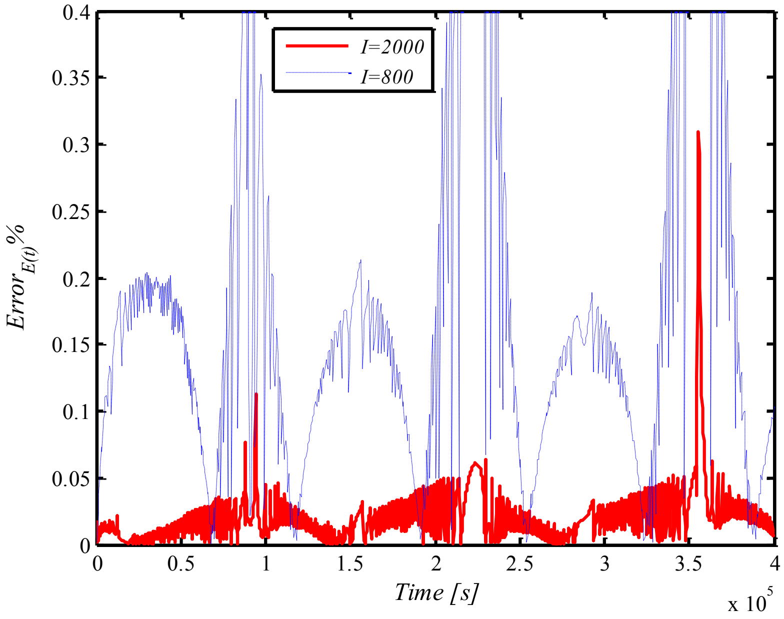

**Figure A.7** Effect of the total number of measurements on the $Error_{E(t)}$.

Figure A.7 shows the effect of the total number of measurements *I* on the accuracy of the predictions for the bank thickness. Accuracy improves when the total number of measurements is raised from *I=800* to *I=2000*. The higher the total number of measurements, the better.

In order to mimic temperature measurement errors, a random error noise $\vec{\omega}_i$ is added to the exact temperature $\vec{T}_{exact}$ generated by the direct model in the following manner:

$$\vec{T}(\mathrm{t}_i) = \vec{T}_{exact}(\mathrm{t}_i) + \sigma\vec{\omega}_i \tag{A.18}$$

$\sigma$ is the standard deviation of the measurement errors, which may take the value of *2%* $T_{max}$ and *4%* $T_{max}$. $T_{max}$ is the maximum temperature measured by the sensor.

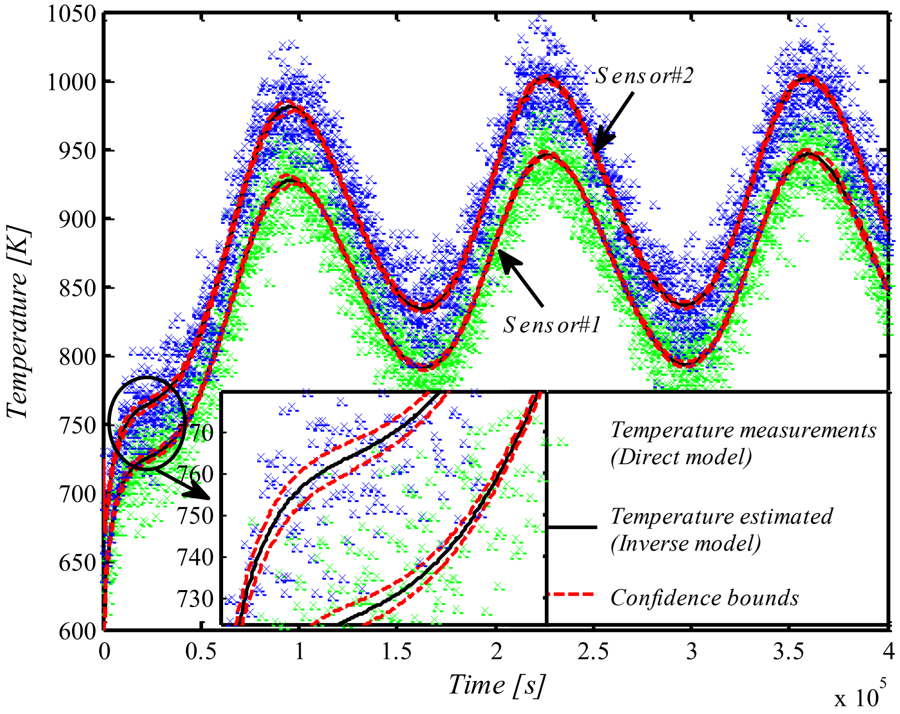

**Figure A.8** Measured and inverse temperature (Sensor#1 and Sensor#2, *σ=2%* $T_{max}$).

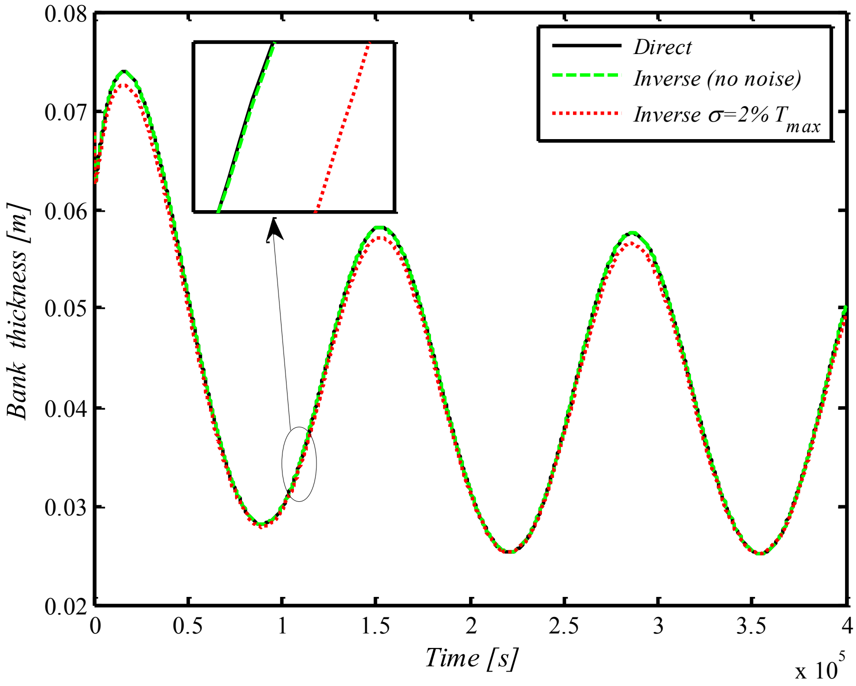

**Figure A.9** Effect of the noise on the predicted bank thickness from sensor #1.

Figure A.8 compares the measured temperatures provided by the direct model with $\sigma=2\%T_{max}$ to the estimated temperatures predicted by the inverse model with both sensors. The confidence intervals $\pm 2.576\ \sigma_{\hat{P}_j}$ are also shown.

Figure A.9 illustrates the effect of the noise level on the predicted bank thickness $E(t)$ using sensor #1. As expected, when the noise level rises to $2\%T_{max}$, the relative root-mean-square error for the bank thickness $RRMSE_{E(t)}$ increases form 0.03% to 1.43%. Nevertheless, the inverse model remains stable and accurate with experimental noise.

## A.6. Conclusion

An inverse heat transfer method was presented for predicting the time-varying thickness of the protective bank inside a high-temperature metallurgical reactor. It was shown that the inverse method may predict simultaneously the heat flux $q''(t)$, the thermal conductivity of the brick wall $k_{Brick}$ and the thermal conductivity of the solid and liquid phases of the PCM ($k_{PCM,solid}$ and $k_{PCM,liquid}$). The proposed inverse method rests on the LMM/BM. It was shown that LMM/BM is computationally more efficiently than the LMM. The effect of the measurement noise, of the location of the temperature sensors and of the total number of measurements on the inverse predictions was investigated. Recommendations were made concerning the location of the sensor embedded into the refractory brick wall.

## Acknowledgment

The authors are grateful to the Natural Sciences and Engineering Research Council of Canada (NSERC) for their financial support.

# ANNEXE B : PRÉDICTION INVERSE DE L'ÉROSION DANS UN FOUR DE FUSION EN UTILISANT LA MÉTHODE DE LEVENBERG-MARQUARDT

## Avant-propos

**Auteurs et affiliation :**

**M. Hafid** : Étudiant au doctorat, Université de Sherbrooke, Faculté de génie, Département de génie mécanique.

**M. Lacroix** : Professeur, Université de Sherbrooke, Faculté de génie, Département de génie mécanique.

**Conférence :** *18th* International Conference on Heat Transfer and Applications, *14-15 Juillet, **2016***, Montréal, Canada

**Revue :** Int. Journal of Mechanical, Aerospace, Industrial, Mechatronic and Manufacturing Engineering.

**État de l'acceptation :** Version finale publiée.

**Référence :** [39]

## Title

Inverse Heat Transfer Analysis of a Melting Furnace Using *Levenberg-Marquardt* Method.

## Abstract

This study presents a simple inverse heat transfer procedure for predicting the wall erosion and the time-varying thickness of the protective bank that covers the inside surface of the refractory brick wall of a melting furnace. The direct problem is solved by using the Finite-Volume model. The melting/solidification process is modeled using the enthalpy method. The inverse procedure rests on the *Levenberg-Marquardt* method combined with the *Broyden* method. The effect of the location of the temperature sensors and of the measurement noise on the inverse predictions is investigated. Recommendations are made concerning the location of the temperature sensor.

## Keywords

Melting furnace, inverse heat transfer, enthalpy method, *Levenberg–Marquardt* Method.

## B.1. Introduction

Melting furnaces, such as electric arc furnaces (Figure B.1), are used for material processing that requires high powers and elevated temperatures. Their main applications are the smelting of materials such as copper, steel and nickel calcine. An interesting solid/liquid phase change phenomenon that arises in these melting furnaces is the formation of solid layer, called a bank, that covers the inside surface of the refractory brick wall. This bank plays a crucial role in these furnaces. It protects the brick walls from the highly corrosive molten bath. Keeping a bank of optimal size is therefore crucial for the safe and profitable operation of the smelting furnace. It is very difficult to measure the bank thickness using probes submerged into the molten bath. The hostile conditions that prevail in the melt damage the probes and may even destroy them. This method is time consuming, risky and often inaccurate. Moreover, formation of the bank is the most complex process that depends on the boundary conditions.

In recent years, the problem of bank formation inside high-temperature melting furnaces has been tackled with various inverse heat transfer methods such as the *Levenberg-Marquardt* method [66], the Kalman-filter method [58-62] and the conjugate gradient method with the adjoint equation [17, 47, 64, 65]. In all the aforementioned studies, the focus is on the inverse prediction of the time-varying heat load of the furnace i.e. the heat flux $q''(t)$ at ($x=L_{Brick} + L_{PCM}$) (Figure B.2). Once the heat load is determined, the time-varying bank thickness $E(t)$ that covers the inside surface of the refractory brick wall can be calculated.

Another problem that arises inside these furnaces is the erosion-corrosion of the inner surface of the refractory brick wall. This problem occurs when the bank is lost and the inside lining of the wall suddenly becomes exposed to the hostile molten material. Predicting the erosion-corrosion wear is a crucial factor for determining the active life of the furnace. But, this task is very challenging due to the physical and chemical conditions that prevail inside the furnace [84, 85].

In the present study, an inverse heat transfer procedure is proposed for predicting simultaneously the erosion-corrosion thickness $L_{Erosion}$ with the unknown time-varying heat flux $q''(t)$. Once these parameters are estimated, the time-varying protective PCM bank that coats the internal surface of the furnace wall can be predicted. The solid/liquid phase change problem is modeled with the enthalpy method. The inverse problem is handled with the *Levenberg-Marquardt* Method (LMM) combined to the *Broyden* method (BM).

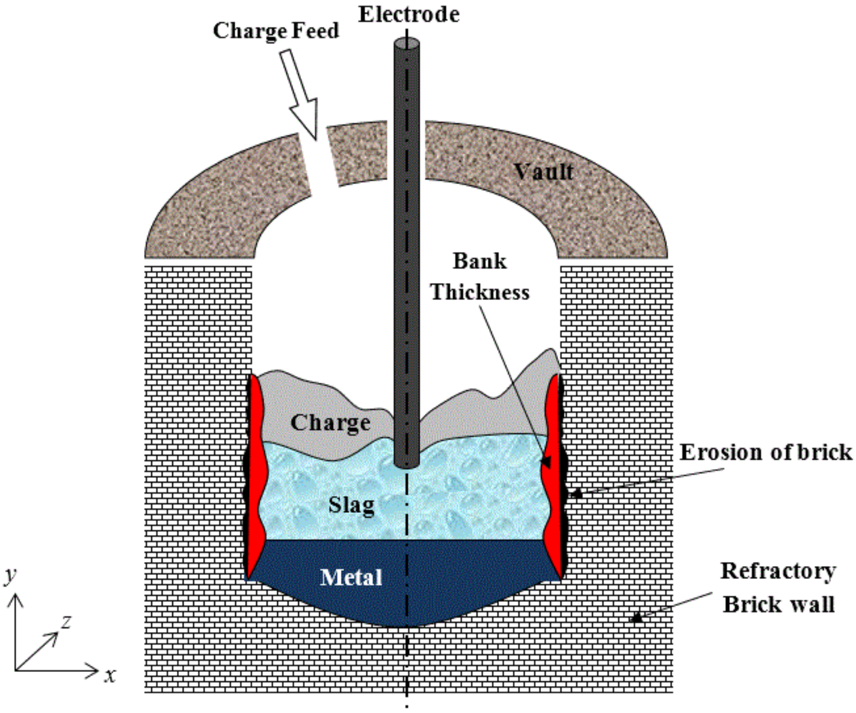

**Figure B.1** Cross view of a typical melting furnace.

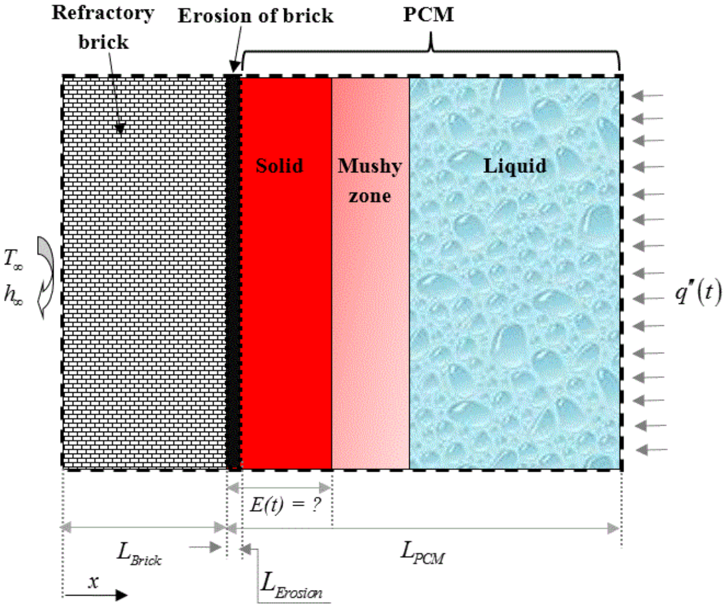

**Figure B.2** Schematic of the direct problem. *E(t)* is unknown. It is predicted numerically with the FVM.

## B.2. Finite-Volume Model (FVM) of The Melting Furnaces

Figure B.2 shows a schematic of the 1-D non-isothermal phase change problem. Here, the PCM is composed of a solid layer, a mushy zone and liquid layer. The inner surface of the refractory brick wall is covered by a protective bank whose time-varying thickness is *E(t)*. *E(t)* shows the position of the solidification front of the PCM.

The mathematical model for the melting furnace rests on the following assumptions [17, 58, 59, 61-64]

- ✓ The temperature gradients in the $x$ direction are much larger than those in the other directions. Consequently, a one-dimensional analysis can be applied (Figure B.2).
- ✓ The thermal contact resistance between the refractory brick wall and the PCM is neglected.
- ✓ The heat transfer inside the liquid phase of the PCM is conduction dominated [17, 142].
- ✓ The thermal properties of the phase change material (PCM) are temperature independent.
- ✓ The phase change problem is non-isothermal. The PCM is depicted by three zones: a solid phase, a mushy zone and a liquid phase (Figure B.2).

The governing heat diffusion equation for the refractory brick wall and the PCM is expressed as

$$\rho C_p \frac{\partial T}{\partial t} = \frac{\partial}{\partial x}\left( k \frac{\partial T}{\partial x} \right) - \delta H \frac{\partial f}{\partial t} \tag{B.1}$$

Where $\delta H$ and $f$ are the enthalpy and the liquid fraction, respectively. The enthalpy $\delta H$ is defined as

$$\delta H = \rho (C_{p,liquid} - C_{p,solid}) T + \rho \lambda \tag{B.2}$$

The liquid fraction *f* is given by

$$f = F(T) = \begin{cases} 0 & T \le \mathrm{T}_{sol} \quad (\textit{Solid} \text{ region}) \\ \dfrac{T - T_{sol}}{T_{liq} - T_{sol}} & \mathrm{T}_{sol} \le T \le \mathrm{T}_{liq} \, (\textit{Mushy} \text{ region}) \\ 1 & T \ge \mathrm{T}_{liq} \quad (\textit{Liquid} \text{ region}) \end{cases} \tag{B.3}$$

The liquid fraction *f* is updated iteratively at each time-step in the following manner [141]

$$f^{k+1} \approx f^k + \left(\frac{dF}{dT}\right)^k \left(T^{k+1} - F^{-1}\left(f^k\right)\right) \tag{B.4}$$

$F^{-1}$ is the inverse function of *F*. The boundary conditions at the left and at the right (Figure B.2) are:

$$\begin{cases} \left(k\dfrac{\partial T}{\partial x}\right)_{x=0} = h_\infty \left(T(0,t) - T_\infty\right) \\ \left(k\dfrac{\partial T}{\partial x}\right)_{x=L_{Brick}+L_{PCM}} = q''(t) \end{cases} \tag{B.5}$$

Equations (B.1)-(B.5) are solved numerically by using a time-implicit finite-volume method. The resulting set of algebraic equations is then solved by using the Tri-Diagonal-Matrix-Algorithm (TDMA).

The accuracy of the FVM was first validated by using the one-dimensional solidification of the binary Al–4.5% Cu alloy with properties reported in [140, 141]. A Dirichlet boundary condition of T=573 K is assumed at the boundary $x=L_{Brick}$ (Figure B.2). The width of the PCM layer is set equal to $L_{PCM}$=0.5 m and the initial temperature is set equal to $\mathrm{T}_{\mathrm{in}}$= 969 K.

The predicted liquidus and solidus fronts are presented in Figure B.3. It is seen that the predictions of the present model (FVM) are in excellent agreement with the semianalytical heat balance integral method [140] and the source-based numerical method [141].

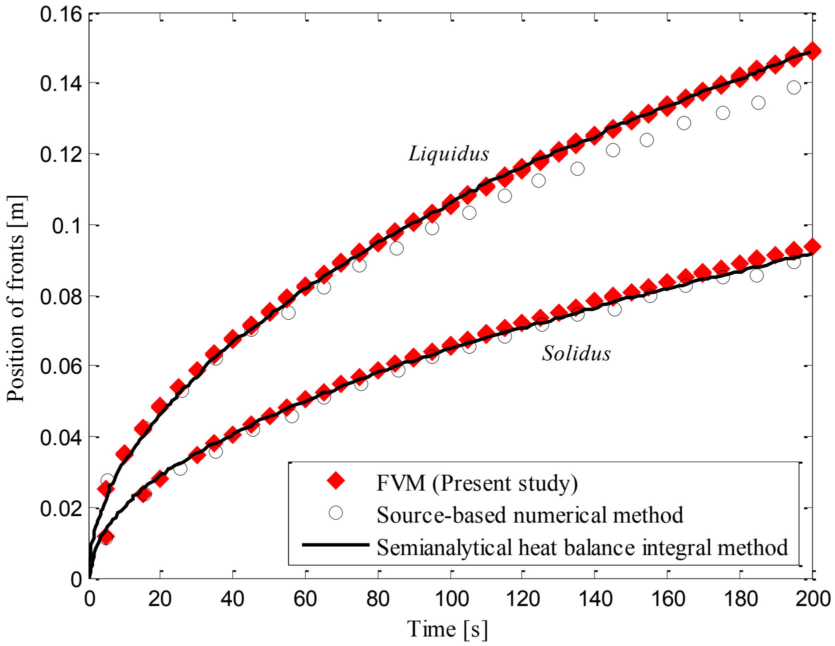

**Figure B.3** Solidification of a binary Al–4.5%-Cu alloy: Comparison with the results reported in [140, 141].

## B.3. The Direct Model

For the direct problem, all the physical and the geometrical properties are known. The objective of the direct model is to determine the temperature field *T(x,t)* and the time-varying thickness of the protective bank *E(t)* using the FVM presented above.

The direct model was implemented for the entire melting furnace i.e. the refractory brick wall and the PCM. The operating thermal conditions of the furnace are similar to those reported in [58, 61]. The refractory brick wall is set equal to $L_{Brick}$=0.1 m and the PCM layer (solid, mushy, and liquid) is set equal to $L_{PCM}$=0.1 m (Figure B.2). The external temperature is set equal to $T_\infty$=300 K and the outside average heat transfer coefficient is fixed at $h_\infty$=15 W/m$^2$. K. At $x=L_{Brick}+L_{PCM}$, the time-varying heat flux $q''$(t) is given by

$$q''(t) = P_1 + P_2 * \sin^2\left(\frac{2\pi . t}{t_{\max}}\right) \tag{B.6}$$

When the protective bank is lost, the inside surface of the refractory brick wall suddenly comes into direct contact with the molten material. Consequently, the exposed brick wall is attacked and becomes vulnerable to erosion-corrosion.

Indeed, erosion of refractory brick walls is a slow process [86, 89]. Therefore, the eroded portion of the wall may be considered time-independent within the time-intervals simulated here, $t\epsilon[0, 400000\ (s)]$. The eroded portion of the refractory wall $L_{\text{Erosion}}$ is set to

$$L_{Erosion} = 0.01\ (m) = P_3 \tag{B.7}$$

The coefficients are given by

$$\begin{cases} P_1 = 9000 & \left(\text{W/m}^2\right) \\ P_2 = 8000 & \left(\text{W/m}^2\right) \\ P_3 = 0.01 & (m) \end{cases} \tag{B.8}$$

The thermophysical properties of the melting furnace (brick wall and PCM) are summarized in Table B.1 [58, 61].

All numerical simulations were conducted with a grid size of 200 uniformly distributed control volumes inside the PCM layer and the refractory brick wall. The time step was set equal to 100 s.

**Table B.1** Thermo Physical Properties of the Refractory Brick Wall and of the PCM [58, 61].

| Parameter | Value | Unit |
|---|---|---|
| $k_{BRICK}$ | 16.8 | W/m K |
| $C_{p,BRICK}$ | 875 | J/kg K |
| $\rho_{BRICK}$ | 2600 | kg/m$^3$ |
| $k_{PCM,solid}$ | 1 | W/m K |
| $k_{PCM,liquid}$ | 100 | W/m K |
| $C_{p,PCM,solid}$ | 1800 | J/kg K |
| $C_{p,PCM,liquid}$ | 1800 | J/kg K |
| $\rho_{PCM}$ | 2100 | kg/m$^3$ |
| $\lambda_{PCM}$ | 5.1 x 10$^5$ | J/kg |
| $T_{sol}$ | 1213 | K |
| $T_{liq}$ | 1233 | K |

## B.4. The Inverse Model

For the inverse problem, it is assumed that the time-varying heat flux (at $x=L_{Brick}+L_{PCM}$) and the thickness of the eroded wall ($L_{Erosion}$) are unknown; i.e., $P_1$, $P_2$, and $P_3$ are unknown. The objective of the inverse analysis is to determine the unknown thermal parameters by using temperature measurements taken from a sensor located inside brick wall (Figure B.4). Once the time-varying heat flux $q''(t)$ and the thickness of the eroded wall $L_{Erosion}$ are determined, the time-varying thickness $E(t)$ of the protective bank may be estimated from the direct model (FVM) presented above.

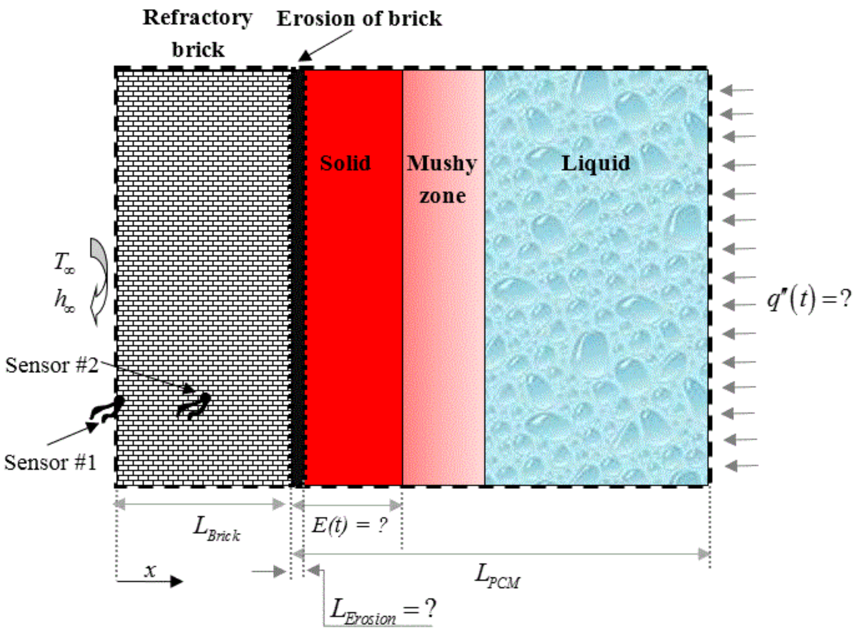

**Figure B.4** The inverse problem. $q''(t)$ and $L_{Erosion}$ are unknown. They are determined from sensor#1 or sensor#2.

The solution for the inverse problem consists of minimizing the least square norm $\Psi(\vec{P})$:

$$\Psi(\vec{P})=\sum_{i=1}^{I}\left[Y(t_i)-\hat{T}(t_i,\vec{P})\right]^2 \tag{B.9}$$

where $P=(P_1, P_2, P_3)$ is the set of the unknown parameters. Here $Y(t_i)$ are the temperatures measured i.e. temperatures generated from the solution of the direct problem wherein the parameters vector $P=(P_1, P_2, P_3)$ are known. $\hat{T}(t_i,\vec{P})$ are the estimated temperatures from the inverse model. $I$ is the total number of measurements.

The inverse problem is solved with the *Levenberg–Marquardt* Method (LMM). The incremental value of the unknown parameters ΔP, is given by:

$$\Delta\vec{P} = \left[\left(\vec{J}^k\right)^T \vec{J}^k + \mu^k \vec{\Omega}^k\right]^{-1} \left(\vec{J}^k\right)^T \left(\vec{Y} - \vec{T}\left(\vec{P}^k\right)\right) \tag{B.10}$$

Here $\mu^k$ is a positive damping parameter. The choice and the update of this parameter is discussed in [150]. $\vec{\Omega}^k = diag\left[\left(\vec{J}^k\right)^T \vec{J}^k\right]$ is a diagonal matrix. The superscript "T" denotes the transpose of the matrix. $\vec{J}^k$ is the Jacobian matrix and it is defined as

$$\vec{J}\left(\vec{P}\right) = \begin{pmatrix} \frac{\partial T_1}{\partial P_1} & \frac{\partial T_1}{\partial P_2} & \frac{\partial T_1}{\partial P_3} \\ \frac{\partial T_2}{\partial P_1} & \frac{\partial T_2}{\partial P_2} & \frac{\partial T_2}{\partial P_3} \\ \vdots & \vdots & \vdots \\ \frac{\partial T_I}{\partial P_1} & \frac{\partial T_I}{\partial P_2} & \frac{\partial T_I}{\partial P_3} \end{pmatrix} \tag{B.11}$$

The Jacobian $\vec{J}^k$ is approximated with a finite difference approximation [151]. For example, the sensitivity coefficient is given by:

$$J_{ij} = \frac{\partial \hat{T}_i}{\partial P_j} \cong \frac{\hat{T}\left(t_i\ ; P_1, \ldots, P_j + \left(\delta P_j\right), \ldots P_N\right)}{2\left(\delta P_j\right)} - \frac{\hat{T}\left(t_i\ ; P_1, \ldots, P_j - \left(\delta P_j\right), \ldots P_N\right)}{2\left(\delta P_j\right)} \tag{B.12}$$

The parameter perturbation $\left(\delta P_j\right)$ is set to $\xi\left(1 + \left|P_j\right|\right)$, where $\xi$ is a small number. The subscripts *i* and *j* represent the time and the parameter respectively.

In order to reduce the computational effort, the Jacobian matrix is updated using BM [152]. For the first iteration, for every *2*N* iterations and for iterations where $\Psi(P + \Delta P) > \Psi(P)$, the sensitivity coefficients of the Jacobian matrix are estimated with (B.12). For every other iteration, the Jacobian matrix is updated with the expression proposed by *Broyden* [152]:

$$J_k = J_{k-1} + \frac{\left(\left(\hat{T}_k - \hat{T}_{k-1}\right) - J_{k-1}\Delta P_{k-1}\right)\Delta P_{k-1}^T}{\Delta P_{k-1}^T \Delta P_{k-1}} \tag{B.13}$$

$\Delta P_{k-1}$ is the incremental value of the unknown parameters given by (B.10).

Convergence of the LMM is declared when

$$\begin{cases} J^T \left\| Y\left(t_i\right) - \hat{T}\left(t_i, \vec{P}\right) \right\| < \varepsilon_1 \\ \left( \dfrac{P^{k+1} - P^k}{P^{k+1}} \right) < \varepsilon_2 \\ \Psi\left(P^{k+1}\right) < \varepsilon_3 \end{cases} \tag{B.14}$$

$\{\varepsilon_1;\ \varepsilon_2;\ \varepsilon_3\}$ are a small number.

The overall computational procedure using LMM and BM is as follows:

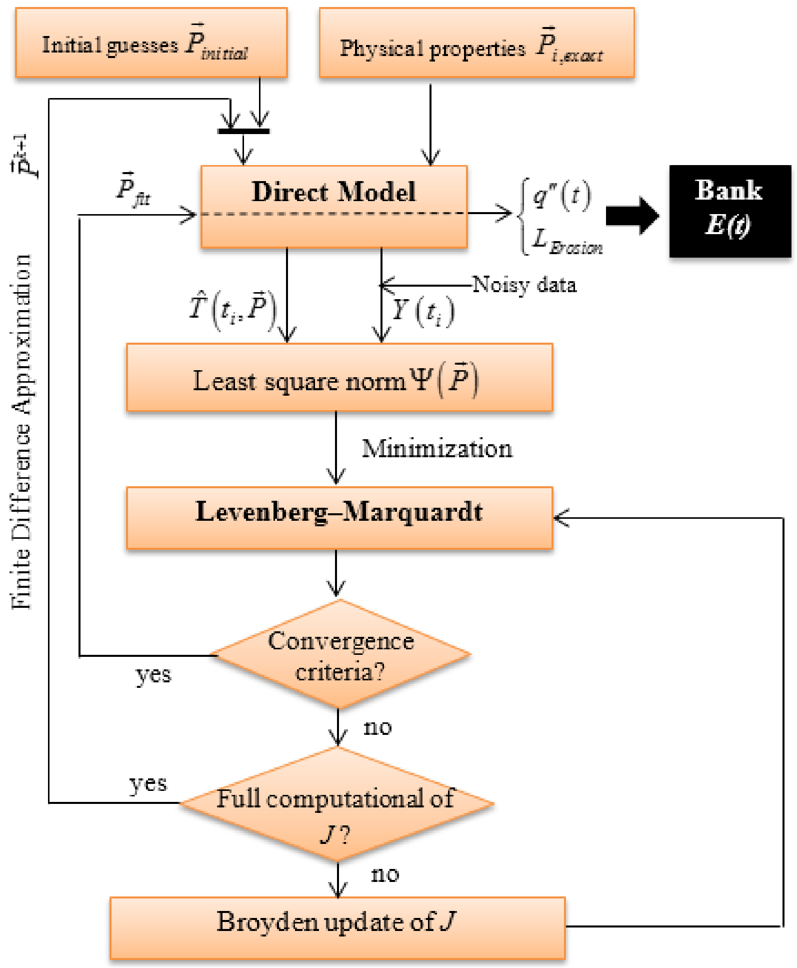

**Figure B.5** Overall algorithm for the inverse method.

## B.5. Results and Discussion

The inverse procedure proposed in Figure B.5 was employed for predicting simultaneously the unknown time-varying heat flux *q*"(t) and the unknown thickness of the eroded wall $L_{Erosion}$ (Figure B.4).

Once the heat flux *q*"(t) and the thickness of the eroded refractory wall $L_{Erosion}$ are estimated, the bank *E(t)* is easily determined from the FVM presented in Section B.2 above.

The temperatures measurements $Y_i$ were taken with a sensor located inside the brick wall at two different locations: The first position, called '*Sensor#1*', is near the outside surface of the brick wall. The second position, '*Sensor#2*', is in the middle of the brick wall (Figure B.4).

The data-capture-frequency (the total number of temperature recordings during an experiment, t=0 to 400000 s) is *I*=800.

In order to assess the accuracy and the uniqueness of the inverse analysis, the inverse procedure has been thoroughly tested with noisy measurements and for different positions of the embedded sensor.

In order to mimic measurement errors, a random error noise $\vec{\omega}_i$ is added to the exact temperature $\vec{T}_{exact}$ generated by the direct model:

$$\vec{T}(\mathrm{t}_i) = \vec{T}_{exact}(\mathrm{t}_i) + \sigma\vec{\omega}_i \tag{B.15}$$

$\sigma$ is the standard deviation of the measurement errors, which may take the value of 2% $T_{max}$ and 4% $T_{max}$. $T_{max}$ is the maximum temperature measured by the sensor.

To demonstrate the accuracy of the present inverse method for predicting the bank thickness, two cases (different heat flux *q*"(t)) were examined:

| | **Heat flux at $x=L_{Brick}+L_{PCM}$** |
|---|---|
| **Case#1** | $q''(t) = P_1 + P_2 * \sin^2\left(\dfrac{2\pi.t}{t_{\max}}\right)$ |
| **Case#2** | $q''(t) = P_1 + P_2 * \left(1 - \exp\left(-\dfrac{t}{t_{\max}}\right)\right)$ |

The exact values for the direct model, are $P_{exact} = \left\{ P_1 = 9000 \text{ w/m}^2 \ ; P_2 = 8000 \text{ w/m}^2 \right\}$

For the sake of comparing the inverse solution (inverse model) to the exact solution (direct model), two estimation errors are defined:

$$\text{Error}_{E(t)} = \frac{\left| E(t_i)_{inverse} - E(t_i)_{exact} \right|}{\left| E(t_i)_{exact} \right|} \tag{B.16}$$

$$Error_P \ \% = 100 \times \frac{\left| P_{inverse} - P_{exact} \right|}{\left| P_{exact} \right|} \tag{B.17}$$

Table B.2 illustrates the effect of the sensor location on the estimation of the unknown parameters. It is seen that the relative errors vary from 0 to 10.5%. The largest discrepancy, i.e., 10.5%, occurs in the prediction of $P_3$ (the erosion thickness). $P_3$ is the smallest and therefore the most sensitive parameter [76]. It is observed that sensor#2 provides the best parameter estimation.

Figures B.6 and B.7 compare the measured noisy temperatures (generated with the 1-D direct model with noise of 2% $T_{max}$) to the estimated temperatures predicted by the inverse model using sensor#1.

**Table B.2** Effect of the Sensor Location.

| | | | **Sensor#1** | | **Sensor#2** | |
|---|---|---|---|---|---|---|
| | | $P_{Exact}$ | $P_{Inverse}$ | $Error_P$ | $P_{Inverse}$ | $Error_P$ |
| ***Case 1*** | $P_1$ ($W/m^2$) | 9000 | 9065.7 | 0.7 | 9065.4 | 0.7 |
| | $P_2$ ($W/m^2$) | 8000 | 7896.7 | 1.3 | 7898.2 | 1.3 |
| | $P_3$ (mm) | 10 | 9.27 | 7.3 | 9.31 | 6.9 |
| ***Case 2*** | $P_1$ ($W/m^2$) | 9000 | 8999.5 | 0.0 | 8983.1 | 0.2 |
| | $P_2$ ($W/m^2$) | 8000 | 8035.5 | 0.4 | 8018.6 | 0.2 |
| | $P_3$ (mm) | 10 | 8.95 | 10.5 | 9.14 | 8.6 |

Figures B.8 and B.9 show the effect of the noise level on the predicted time-varying thickness of the protective bank *E(t)* for both cases. The erosion of the refractory brick wall is depicted by the negative bank thickness. As expected, a slight discrepancy appears when the noise level increase from 2% $T_{max}$ to 4% $T_{max}$. Nevertheless, it is seen that the predictions remain stable and accurate even for noisy signals.

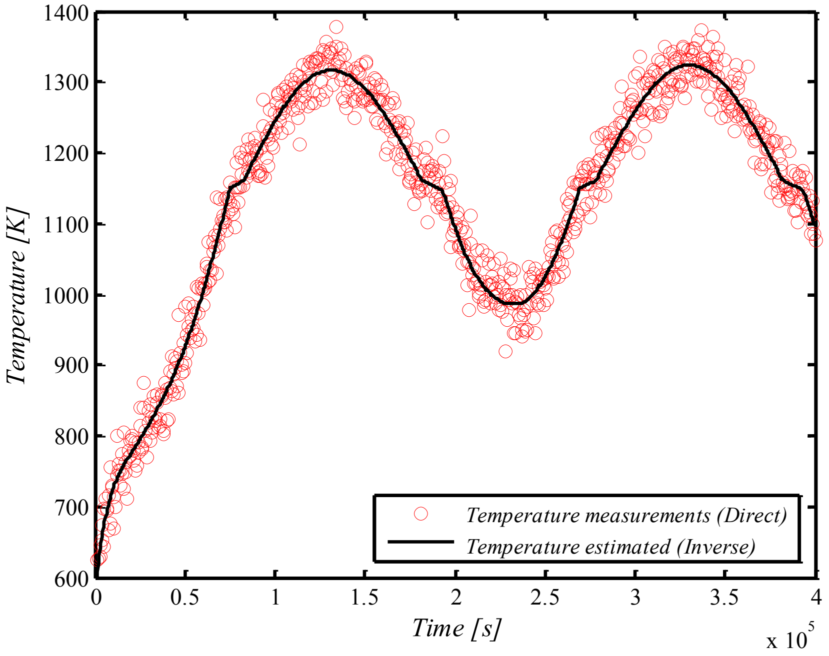

**Figure B.6** Measurements and inverse predictions (Case#1).

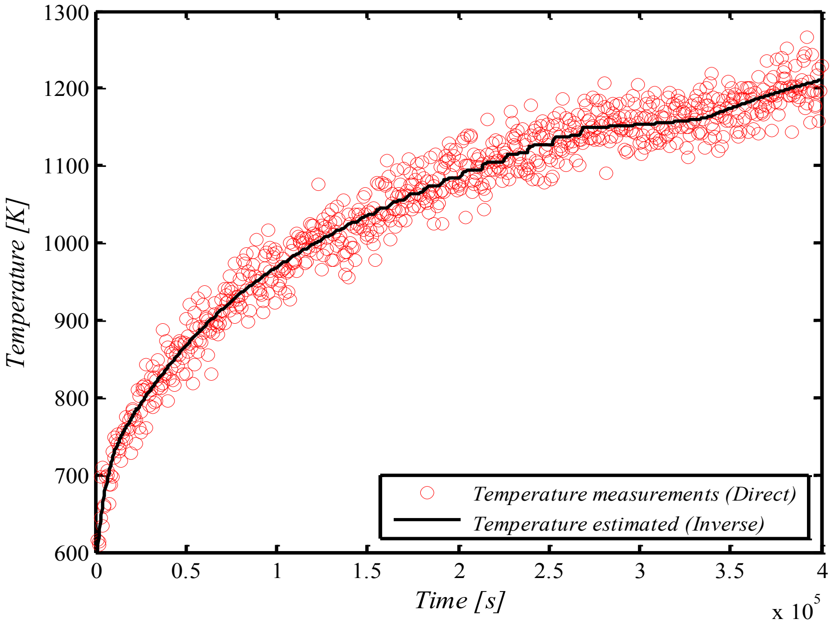

**Figure B.7** Measurements and inverse predictions (Case#2).

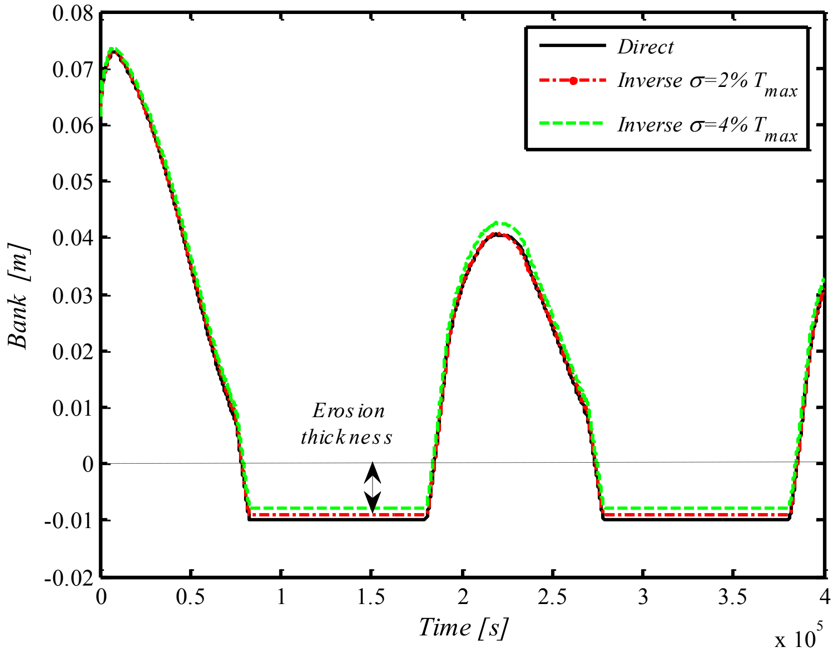

**Figure B.8** Predicted bank thickness with erosion (Case#1).

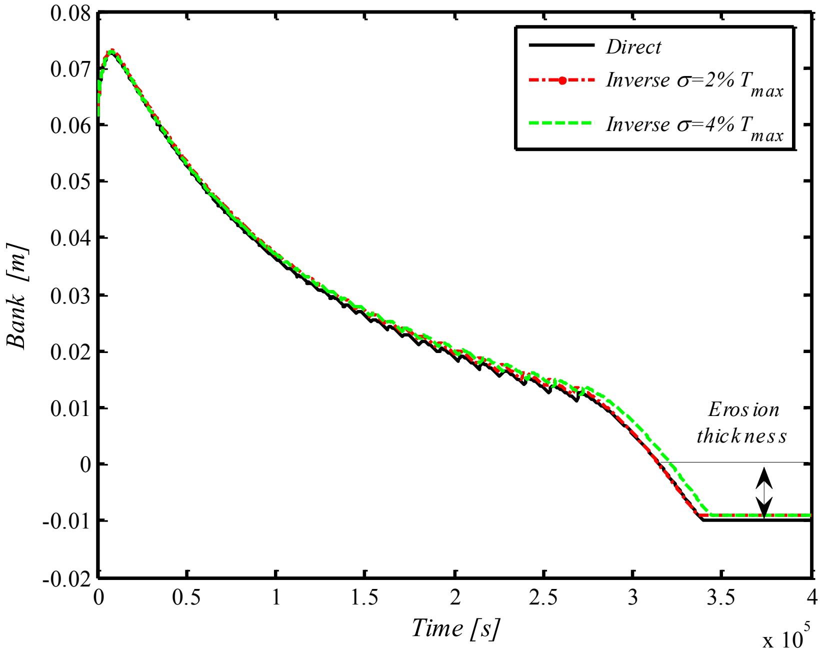

**Figure B.9** Predicted bank thickness with erosion (Case#2).

Figures B.10 and B.11 show the effect of the temperature sensor position (sensor#1 and sensor#2) on the accuracy of the predicted bank thickness *E(t)*. It is seen that the effect of the sensor position is insignificant [17]. Therefore, sensor#1 is recommended over sensor#2. This result is of interest to the process industry. Indeed, it is much safer and easier to embed a sensor near the external surface of the refractory brick wall.

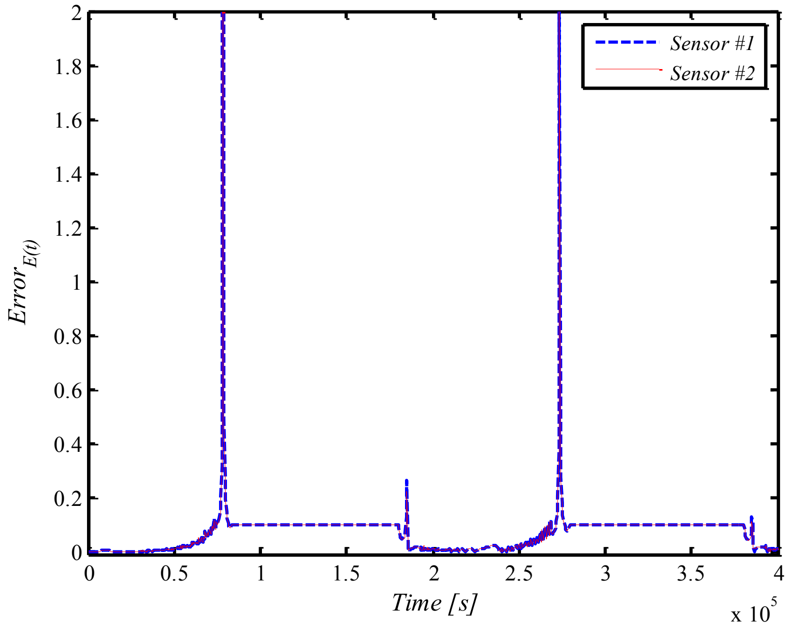

**Figure B.10** Effect of the sensor position on the predicted bank thickness *E(t)*, case 1.

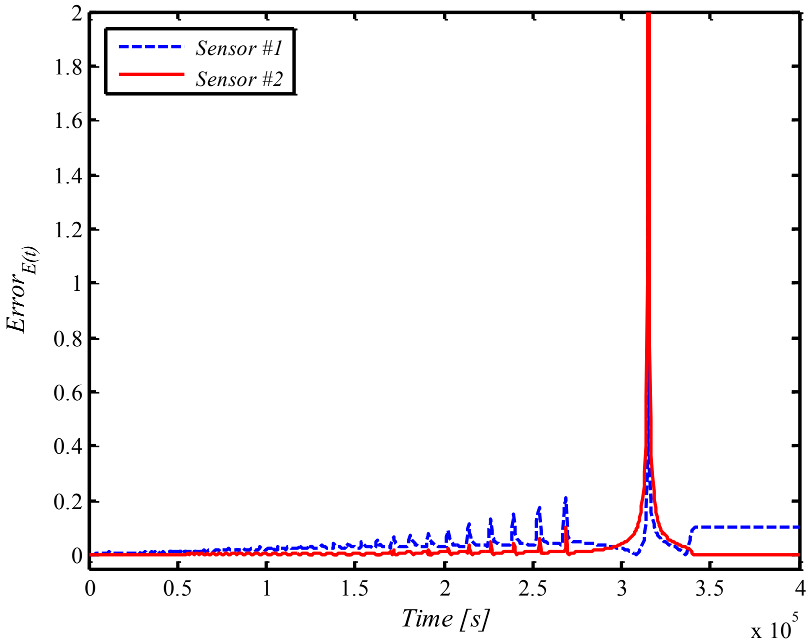

**Figure B.11** Effect of the sensor position on the predicted bank thickness *E(t)*, case 2.

It is noted that the approximation of the sensitivity coefficients of the Jacobian matrix, (B.12), requires the solution of the direct problem six times per iteration (2 times for each unknown parameter). As a result, the finite difference approximation is computationally expensive. In order to reduce the computation time, the sensitivity matrix was updated using BM [152]. This strategy has been applied successfully in the field of inverse heat transfer problems (IHTP) [38, 154, 155]. LMM combined with BM (LMM/BM) calls the direct model 20 times while LMM requires 35 calls. Consequently, the CPU time for the LMM/BM is only 715.5 s while that for the LMM is 1311.9 s.

The simulations were executed with the MATLAB software running on an Intel ® Core(TM) i5-2520M CPU @ 2.50GHz.

## B.6. Conclusion

An inverse heat transfer analysis was presented for predicting the wall erosion and the time-varying thickness of the protective bank inside a melting furnace. It was shown that the inverse analysis may also predict simultaneously the time-varying heat flux and the eroded portion of the refractory brick wall. The proposed inverse method rests on the LMM/BM. Using this combination of methods, the computation time was halved. The effect of the measurement noise and of the location of the temperature sensors on the inverse predictions was investigated. Recommendations were made concerning the location of the sensor embedded in the brick wall. Finally, this study illustrates how the inverse heat transfer can be used successfully for preventive maintenance of an industrial facility.

## Acknowledgment

The authors are grateful to the Natural Sciences and Engineering Research Council of Canada (NSERC) for their financial support.

# ANNEXE C : PRÉDICTION INVERSE DES PROPRIÉTÉS THERMIQUES DES TUMEURS DURANT LA CRYOCHIRURGIE

## Avant-propos

**Auteurs et affiliation :**

**M. Hafid** : Étudiant au doctorat, Université de Sherbrooke, Faculté de génie, Département de génie mécanique.

**M. Lacroix** : Professeur, Université de Sherbrooke, Faculté de génie, Département de génie mécanique.

**Conférence :** *19th* International Conference on Biophysical and Biomedical Engineering, *25-26 Juin **2017**,* Paris, France.

**Date de soumission** : 27 Mars 2017

**Référence :** [40]

# Title

An inverse heat transfer algorithm for predicting the thermal properties of tumors during cryosurgery.

# Abstract

This paper presents an inverse heat transfer approach for predicting the time-varying freezing front and the temperature distribution of tumors during cryosurgery. Using a temperature probe pressed against the layer of tumor, the inverse approach is able to predict simultaneously the metabolic heat generation and the blood perfusion rate of the tumor. Once these thermal properties are determined, the temperature-field and time-varying freezing front are predicted with the direct model. The direct problem is handled with the *Pennes* bioheat equation and the enthalpy method. The inverse model rests on the *Levenberg-Marquardt* Method (LMM) combined to the *Broyden* Method (BM). The effect (1) of the initial guesses for the unknown thermal properties; (2) of the thermal properties of the diseased tissues; (3) of the data capture frequency; and (4) of the noise on the recorded temperatures is investigated. It is shown that the proposed inverse method remains accurate and stable for all the cases investigated.

# Keywords

Cryosurgery, Inverse heat transfer, *Levenberg-Marquardt* Method, Thermal properties, *Pennes* model, Enthalpy method.

## C.1. Introduction

Cryosurgery has become a well-established technique for the ablation of undesirable tissues such as tumors and cancers. It is an effective treatment for external tumors such as ear tumors and skin tumors, and for internal tumors such as lung tumors and breast tumors. Cryosurgery is often preferred to the traditional surgery due to the fact that it is minimally invasive and that the hospitalization time is reduced.

Cryosurgery resorts to extreme cold for destroying diseased tissues. It works by taking advantage of the destructive effect of freezing temperatures on living cells. The instrument used to freeze the tissues is a cryoprobe. The low temperatures are obtained by circulating liquid nitrogen through the cryoprobe.

As illustrated in Figure C.1, the cryoprobe is inserted in such a way as to optimize the freezing of the tumor. When the rate of cooling is very high, ice crystals form inside the cells. These ice crystals damage the cell membrane and leads to the destruction of the tumor. Furthermore, the formation of ice crystals harm the blood vessels that supply the tumor tissue.

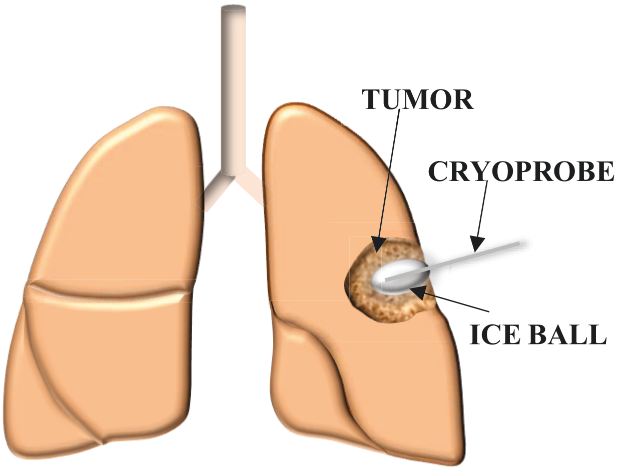

**Figure C.1** Cryosurgery of lung tumor.

Destroying the diseased tissues while minimizing the damages to the surrounding healthy tissues is however a challenging task. Sophisticated imaging techniques such as Magnetic Resonance Imaging (MRI) or ultrasounds must be used to guide the cryoprobe and monitor the freezing of the cells [178, 179]. But these imaging techniques are often unavailable. Moreover, they cannot reproduce the time-varying temperature distribution inside the layer of tissue. An alternative to MRI or ultrasounds is the mathematical modeling of the heat transfer and the freezing processes that take place inside the tissues [180-183]. But in order to perform the mathematical analysis, the thermal properties of the tissues, such as the metabolic heat generation and the blood perfusion, must be known. Measuring these properties with experimental techniques is however a complicated task [32, 115]. They require sophisticated equipment that can hardly be employed during cryosurgery. This is where inverse heat transfer methods come to the rescue [151]. In these methods, the unknown thermal properties may be determined by means of temperatures recorded by a temperature probe pressed against the layer of tissue.

Many studies based on inverse methods have been carried out in the past for predicting the blood perfusion coefficient [187], the unknown time-dependent surface heat flux in a living skin tissue [188], and the size and the location of the tumor [120-123, 189]. Studies also focused on the simultaneous estimation of various other thermo-physical properties using inverse approach [125, 190-192].

In all the aforementioned investigations however, the prediction of the thermal properties of the biological tissues during cryosurgery was not carried out.

The main purpose of the present paper is to pursue the aforementioned studies by developing an inverse method capable of estimating the unknown metabolic heat generation rate and the blood perfusion rate during cryosurgery. Once these unknown parameters are determined, the temperature-field and the moving freezing front are predicted. Overall, the proposed method may become, one day, a viable alternative to more expensive imaging techniques that are used in cryosurgery.

This paper is organized as follows. First, a one-dimensional finite-volume model based on the *Pennes* bioheat equation and the non-isothermal phase change enthalpy method is developed. The model is then validated with an analytical solution available in the open literature. Second, an inverse procedure based on the *Levenberg-Marquardt* Method (LMM) combined to the *Broyden* Method (BM) is presented. Finally, the proposed inverse procedure is thoroughly tested for several freezing scenarios.

## C.2. Problem Statement and Assumptions

Figure C.2 illustrates the one-dimensional phase change problem for cryosurgery. Three regions are considered: (1) the frozen zone whose time-varying interface position is *s(t)*, (2) the mushy zone and (3) the intact (unfrozen) zone. The lower and upper phase change interfaces are defined as the distance that separates the cryoprobe from the solidus temperature $T_{sol}$ and the liquidus temperature $T_{liq}$, respectively. A freezing temperature $T_c$, which represents the temperature of the cryoprobe, is imposed on the left boundary condition (at $x = 0$). At the right boundary ($x=L_t$), the temperature gradient is set equal to zero. No heat is transferred as this boundary is far removed from the cryoprobe. The thickness of the tissue is set equal to $L_t$=0.05 m.

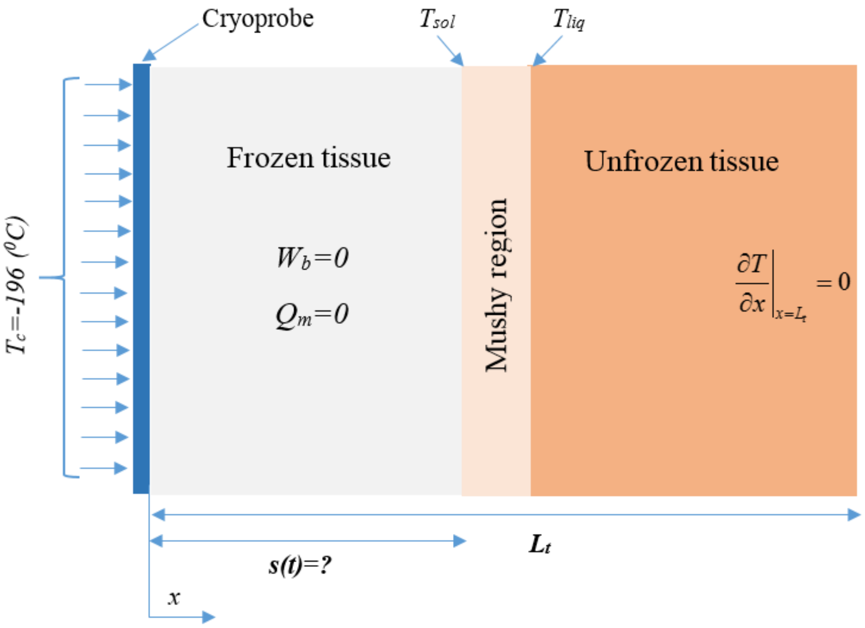

**Figure C.2** One-dimensional problem of cryosurgery.

The mathematical model of cryosurgery rests on the following assumptions:

- ✓ Heat is predominantly transferred from the tissue to the cryoprobe. Thus, a one-dimensional heat transfer model can be applied [199].
- ✓ The blood perfusion rate and the metabolic heat generation are assumed to be uniform through time and space.
- ✓ The blood perfusion rate and the metabolic heat generation are set equal to zero in the frozen and in the mushy regions.

- ✓ The blood temperature is set equal to $T_b=37\ °C$.
- ✓ The phase change of the diseased tissue is non-isothermal. The freezing process is characterized by three zones: a frozen solid zone, a mushy zone and an unfrozen zone (Figure C.2).
- ✓ The liquidus temperature $T_{liq}$ (the upper limit) and the solidus temperature $T_{sol}$ (the lower limit) of the biological tissue are set equal to (-1 *°C*) and (-8 *°C*) respectively [203, 204].
- ✓ The heat transfer inside the diseased tissue is conduction dominated [29, 200].
- ✓ The effect of large blood vessels is neglected [201, 202].

# C.3. The Direct Problem

For the direct problem, all the thermo-physical properties, the initial and the boundary conditions are known. The mathematical model for the heat transfer inside the biological tissue is given by the fundamental *Pennes* bio-heat equation [103]:

$$\rho c \frac{\partial T}{\partial t} = \frac{\partial}{\partial x}\left( k \frac{\partial T}{\partial x} \right) + \rho_b c_b w_b \left( T_b - T \right) + Q_m + \delta H \frac{\partial f_s}{\partial t} \tag{C.1}$$

$\rho$, $c$ and $k$ are the density, the specific heat and the thermal conductivity of the tissue, respectively. The subscript '*b*' refers to the blood characteristics. $w_b$ and $Q_m$ represent the blood perfusion rate and the metabolic heat generation in the tissue, respectively. $T$ is the tissue temperature and $T_b$ is the arterial blood temperature.

The last term on the right-hand side of Eq. (C.1) represents the liquid/solid phase change of the tissue during cryosurgery. $\delta H$ and $f_s$ are the enthalpy and the solid fraction during the phase change, respectively. The enthalpy $\delta H$ is defined as $\delta H = \rho(c_{solid} - c_{liquid})T - \rho\lambda$ and the solid fraction may be expressed as

$$f_s = F(T) = \begin{cases} 0 & T \geq \mathrm{T}_{liq} \quad (Liquid) \\ \dfrac{T - T_{liq}}{T_{sol} - T_{liq}} & \mathrm{T}_{sol} < T < \mathrm{T}_{liq} \ (Mushy \text{ regions}) \\ 1 & T \leq \mathrm{T}_{sol} \quad (Solid) \end{cases} \tag{C.2}$$

At each time-step, the solid fraction $f_s$ is updated iteratively according the following approximation

$$f_s^{k+1} \approx f_s^k + \left(\frac{dF}{dT}\right)^k \left(T^{k+1} - F^{-1}\left(f_s^k\right)\right) \tag{C.3}$$

*F* is a function of the temperature *T*. $F^{-1}$ is the inverse function of *F*.

The boundary conditions at the right and left sides of Figure C.2 are defined by:

$$\begin{cases} \dfrac{\partial T\left(x = L_t,\ \mathrm{t}\right)}{\partial x} = 0 & \left(\text{Right boundary}\right) \\ T\left(x = 0,\ \mathrm{t}\right) = T_c & \left(\text{Left boundary}\right) \end{cases} \tag{C.4}$$

The initial condition is given by:

$$T\left(x,\ \mathrm{t{=}0}\right) = 37\ {}^0\mathrm{C} \tag{C.5}$$

The one-dimensional *Pennes* bio-heat equation (Eq. (C.1)) is solved by using a finite-volume method. The scheme adopted for the time discretization is implicit. The resulting set of algebraic equations is then solved by using the Tri-Diagonal-Matrix-Algorithm (TDMA) [143].

The mathematical model accuracy was validated by comparing it to the Neumann's solution. The freezing temperature was set equal to $T_c = -196\ {}^0C$. The metabolic heat generation and blood perfusion rate were set equal to zero. Figure C.3 compares the upper phase change interface position (liquidus temperature $T_{liq}$ ) predicted by the present model to the Neumann's solution. The agreement between both solutions is excellent.

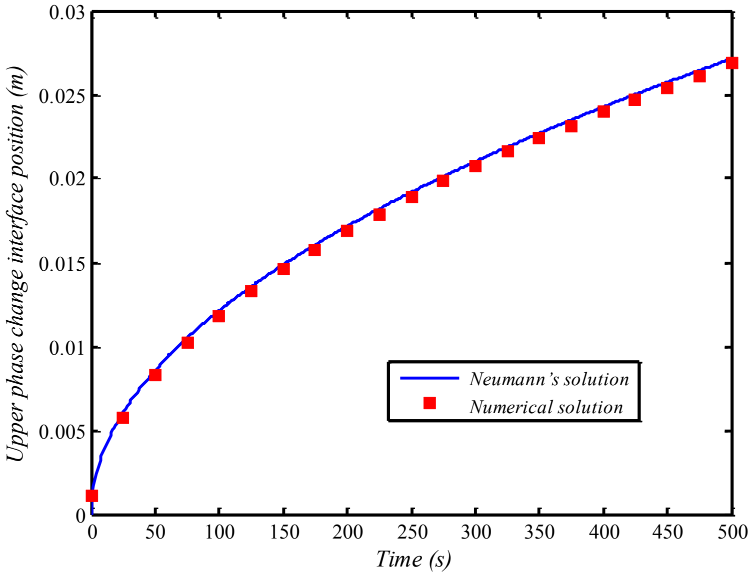

**Figure C.3** Comparison of the FVM with Neumann's solution.

## C.4. The Inverse Problem

In the inverse model, it is assumed that (1) the blood perfusion rate $w_b$ and (2) the metabolic heat generation $Q_m$ are unknown. They are estimated from the inverse method and then fed to the direct model that calculates the temperature distributions $T(x,t)$ and the phase change interface position $s(t)$.

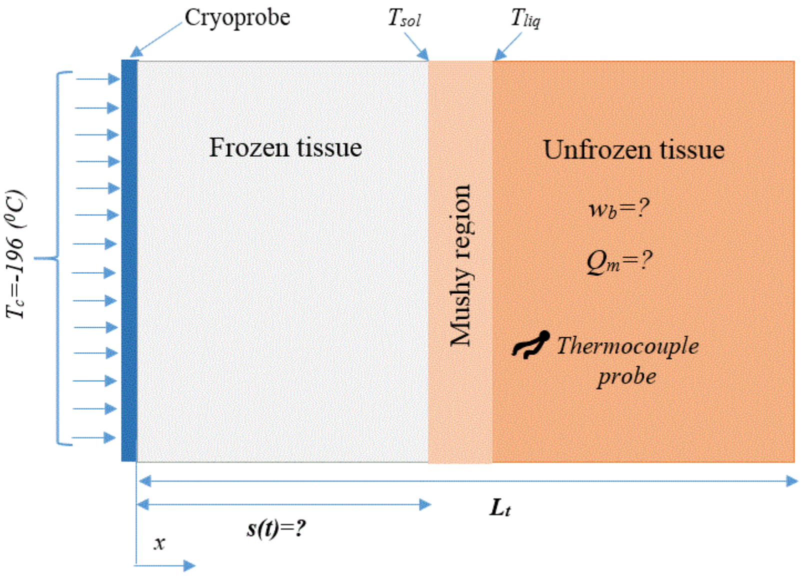

**Figure C.4** Inverse problem of cryosurgery. $w_b$ and $Q_m$ are unknown. They are estimated from temperature measurements provided by a temperature probe.

Therefore, the objective of the inverse method is to determine the unknown coefficients $\vec{P}=\{w_b,\ \mathrm{Q}_m\}$ by using temperature measurements taken from a temperature probe pressed against the diseased tissue (Figure C.4).

The estimation of these thermal properties can be constructed as a problem of minimization of the least square norm $\Psi\left(\vec{P}\right)$

$$\Psi\left(\vec{P}\right)=\sum_{i=1}^{I}\left[Y\left(t_i\right)-\hat{T}\left(t_i,\vec{P}\right)\right]^2 \tag{C.6}$$

where $P$ = *(w*$_b$*, Q*$_m$*)* is the set of unknown thermal parameters. $I$ is the total number of measurements. $Y(t_i)$ are the temperatures (also called the direct temperatures) measured with the temperature probe. In the present study, these temperatures are 'generated' from the solution of the direct problem wherein the parameters $P$ = *(w*$_b$*, Q*$_m$*)* are specified. $\hat{T}\left(t_i,\vec{P}\right)$ are the estimated temperatures from the inverse problem. Thus, the solution of the inverse problem is obtained when the least square norm (C.6) is minimized.

The *Levenberg–Marquardt* method is used for the solution of the present inverse problem. This method has been successfully applied to inverse problems in the past [117, 124]. In this iterative method, the incremental value of the unknown parameters $\Delta P$, is written as:

$$\Delta\vec{P}=\left[\left(\vec{J}^k\right)^T\vec{J}^k+\mu^k\vec{\Omega}^k\right]^{-1}\left(\vec{J}^k\right)^T\left(\vec{Y}-\vec{T}\left(\vec{P}^k\right)\right) \tag{C.7}$$

$\mu^k$ is a positive scalar, called the 'd*amping parameter'*. The choice and the update of this parameter are discussed in [150]. $\vec{\Omega}^k=diag\left(\vec{J}^k\right)^T\vec{J}^k$ is a diagonal matrix. $\vec{J}^k$ is the '*sensitivity matrix'*, also called the '*Jacobian matrix*'

$$\vec{J}=\begin{pmatrix}\dfrac{\partial T_1}{\partial w_b} & \dfrac{\partial T_1}{\partial Q_m}\\ \dfrac{\partial T_2}{\partial w_b} & \dfrac{\partial T_2}{\partial Q_m}\\ \vdots & \vdots\\ \dfrac{\partial T_I}{\partial w_b} & \dfrac{\partial T_I}{\partial Q_m}\end{pmatrix} \tag{C.8}$$

The *Jacobian matrix* plays a crucial role in the estimation of the thermal parameters. In fact, there are several approximations for computing the Jacobian matrix [151]. In the current study, the Jacobian matrix is approximated with a finite difference approximation

$$J_{ij} = \frac{\partial \hat{T}_i}{\partial P_j} \cong \frac{\hat{T}\left(t_i\ ; P_1,..,P_j + \left(\delta P_j\right),..P_N\right) - \hat{T}\left(t_i\ ; P_1,..,P_j - \left(\delta P_j\right),..P_N\right)}{2\left(\delta P_j\right)} \qquad \text{(C.9)}$$

The subscripts $i$ and $j$ represent the time and the parameter, respectively. The parameter perturbation $\left(\delta P_j\right)$ is set to $\xi\left(1+\left|P_j\right|\right)$, where $\xi$ is an arbitrary small number.

In order to reduce the computational effort, the Jacobian matrix is updated using the *Broyden* method [152].

$$J_k = J_{k-1} + \frac{\left(\left(\hat{T}_k - \hat{T}_{k-1}\right) - J_{k-1}\Delta P_{k-1}\right)\Delta P_{k-1}^T}{\Delta P_{k-1}^T \Delta P_{k-1}} \qquad \text{(C.10)}$$

$\left(\Delta P_{k-1}\right)$ is the incremental value of the unknown parameters. $\left(\hat{T}\right)$ are the estimated temperatures. Further details about this inverse method are provided in [34, 35, 38, 39].

The main steps involved in the computational procedure for the direct and the inverse problems are summarized in Figures C.5 and C.6 respectively.

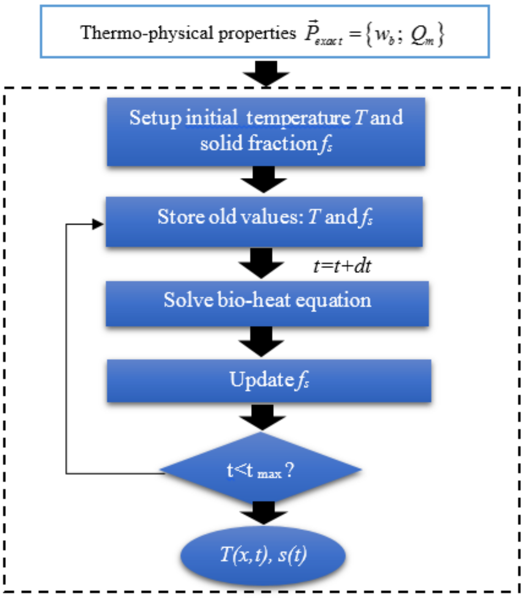

**Figure C.5** The direct problem.

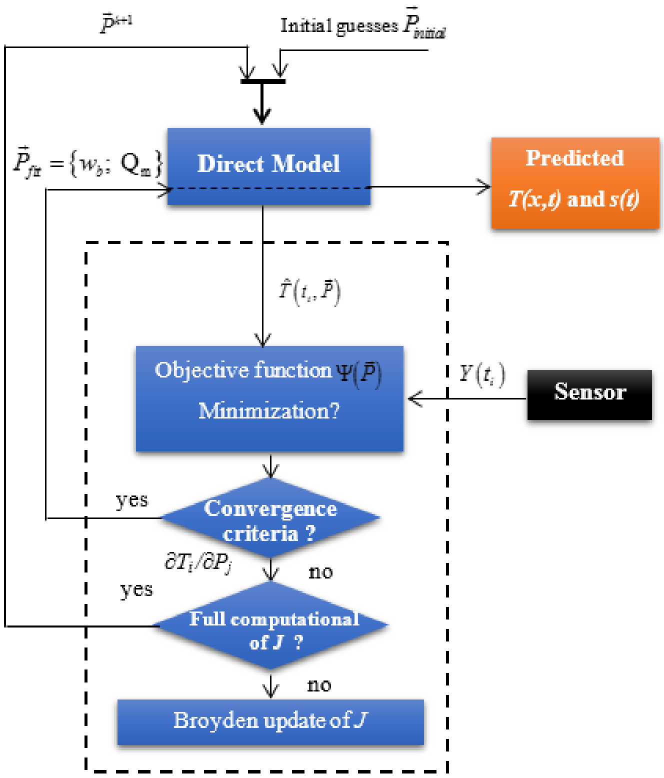

**Figure C.6** The inverse problem.

## C.5. Results and Discussion

In order to evaluate the temperature distribution *T(x,t)* and the time-varying phase change interface position *s(t)*, the unknown thermal properties of the biological tissue must first be determined. To achieve this task, the above inverse procedure (Figure C.6) was implemented. It predicts simultaneously the metabolic heat generation $Q_m$ and the blood perfusion rate $w_b$. Once these thermal parameters are obtained, the temperature distribution *T(x,t)* and the time-varying phase change interface position *s(t)* are calculated with the direct model described in section C.3.

The freezing temperature was fixed at $T_c$= -196 °*C* and the thickness of tissue was set equal to 0.05 *m*. The duration of cryosurgery was set equal to *t*= 500 s. The total number of measurements (temperatures recorded by the temperature probe during cryosurgery) is set equal to *I*=50.

All simulations presented here were conducted with a grid space of $dx=2.5*10^{-4}$ *m* and a time step of *dt*=10 *s*. Additional simulations were conducted to make sure that the predictions are grid space and time step independent. All simulations were performed using the Matlab software running on an Intel@ Core(TM) i5-2520M CPU@ 2.50 GHz.

In order to demonstrate the ability of the inverse method for determining the blood perfusion rate and the metabolic heat generation, two different diseased tissues (lung tumor and breast tumor) were considered. The thermal-physical properties of these diseased tissues are summarized in Table C.1 [106, 211, 212].

**Table C.1** Thermo-physical Properties of Tumors.

| | Symbol | Lung tumor | Breast tumor | Unit |
|---|---|---|---|---|
| Specific heat of unfrozen tumor tissue | $c_u$ | 4200 | 3600 | J/kg °C |
| Specific heat of frozen tumor tissue | $c_f$ | 1230 | 1800 | J/kg °C |
| Thermal conductivity of unfrozen tumor tissue | $k_u$ | 0.552 | 0.51 | W/m °C |
| Thermal conductivity of frozen tumor tissue | $k_f$ | 2.23 | 2 | W/m °C |
| Density of unfrozen tumor tissue | $\rho_u$ | 1000 | 1000 | kg/m$^3$ |
| Density of frozen tumor tissue | $\rho_f$ | 1000 | 1000 | kg/m$^3$ |
| Lower phase transition temperature | $T_{sol}$ | −8 | −8 | °C |
| Upper phase transition temperature | $T_{liq}$ | −1 | −1 | °C |
| Latent heat of freezing | $L$ | 333 | 335 | kJ/kg |
| Blood temperature | $T_b$ | 37 | 37 | °C |
| Blood specific heat capacity | $c_b$ | 3640 | 3640 | J/kg °C |
| Blood density | $\rho_b$ | 1000 | 1000 | kg /m$^3$ |
| Blood perfusion rate | $w_b$ | **0.002** | **0.009** | ml/s ml |
| Metabolic heat generation | $Q_m$ | **42000** | **29000** | W/m$^3$ |

To characterize the accuracy of the proposed inverse method, two relative errors 'for the blood perfusion rate and the metabolic heat generation' are used. These errors are defined as

$$Error_{w_b}\ (\%) = 100 \times \left| \frac{w_b^{exact} - w_b^{inverse}}{w_b^{exact}} \right| \tag{C.11}$$

$$Error_{Q_m}\ (\%) = 100 \times \left| \frac{Q_m^{exact} - Q_m^{inverse}}{Q_m^{exact}} \right| \tag{C.12}$$

The superscripts '*exact*' and '*inverse*' refer to the exact solution obtained with the direct model and the inverse solution predicted by the inverse model, respectively.

The effect of the initial guess values of the blood perfusion rate and of the metabolic heat generation on the convergence of the inverse model is shown in Figures C.7 and C.8, respectively. The initial guesses for *test#1, test#2, test#3* and *test#4* were set equal to 1/3, 1/5, 1/7 and 1/9 of that of the exact value respectively. It is seen that the convergence of the inverse method is excellent in all cases.

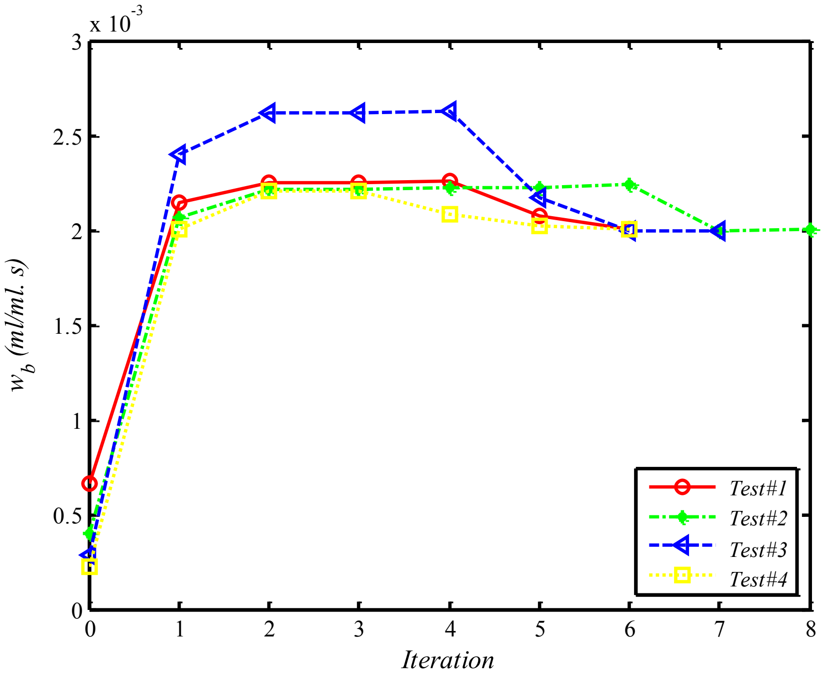

**Figure C.7** Convergence of blood perfusion rate (Lung tumor).

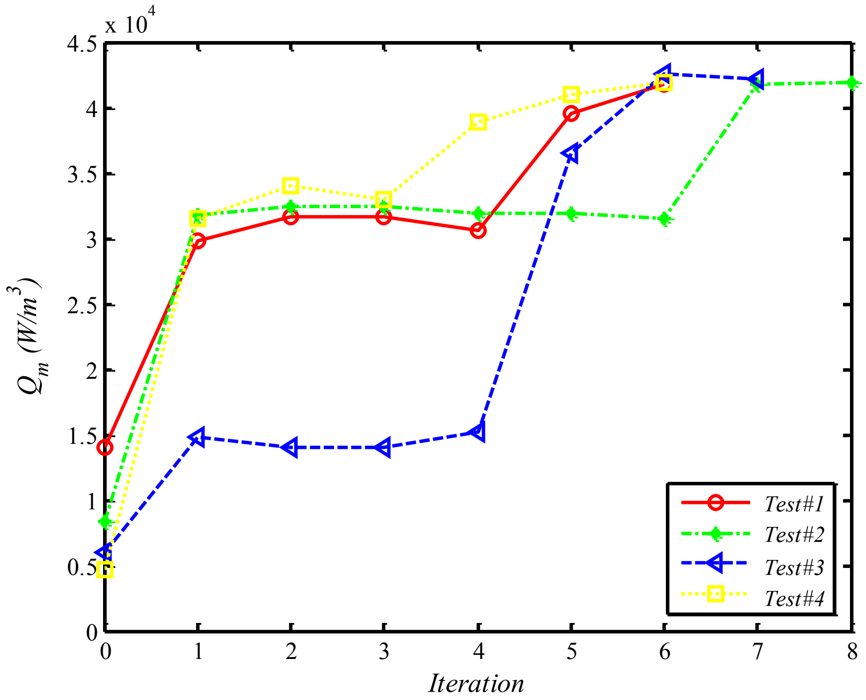

**Figure C.8** Convergence of metabolic heat generation (Lung tumor).

The results of the inverse predictions are summarized in Table C.2. Examination of this table reveals that the prediction of the blood perfusion rate and of the metabolic heat generation are good for the both tumors. The maximum recorded error is less than 0.7%.

**Table C.2** Inverse prediction of blood perfusion and metabolic heat generation.

| | Parameter | $P_{Exact}$ | $P_{Inverse}$ | Error% |
|---|---|---|---|---|
| Lung tumor | $w_b$ | $2*10^{-3}$ | $2.0*10^{-3}$ | 0 |
| | $Q_m$ | $4.2*10^4$ | $4.18*10^4$ | 0.48 |
| Breast tumor | $w_b$ | $9*10^{-3}$ | $9*10^{-3}$ | 0 |
| | $Q_m$ | $2.9*10^4$ | $2.88*10^4$ | 0.69 |

Figure C.9 compares the exact and the estimated motion of the lower phase change interface *s(t)* during the freezing process for the both tumors. It is seen that the inverse solution (the solution obtained from the inverse model) and the exact solution (the solution provided by the direct model) are in perfect agreement. One may observe that the phase change interface position in the lung tumor gets ahead of the breast tumor. This is due the smaller blood perfusion rate of the lung tumor (0.002 *ml/s.ml*) compared with the breast tumor (0.009 *ml/s.ml*). The temperature contours predicted with the inverse model for both tumors are also presented in Figure C.10.

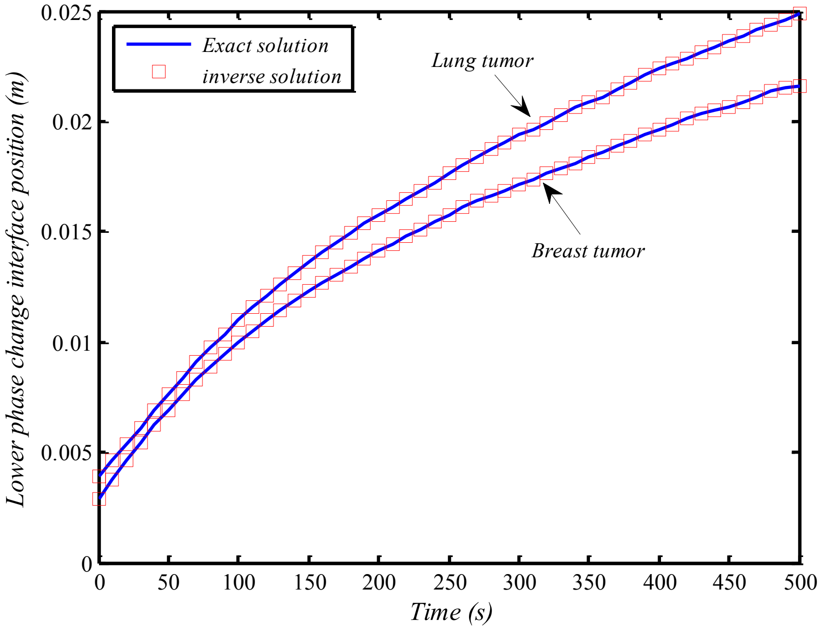

**Figure C.9** Lower phase change interface for both tumors.

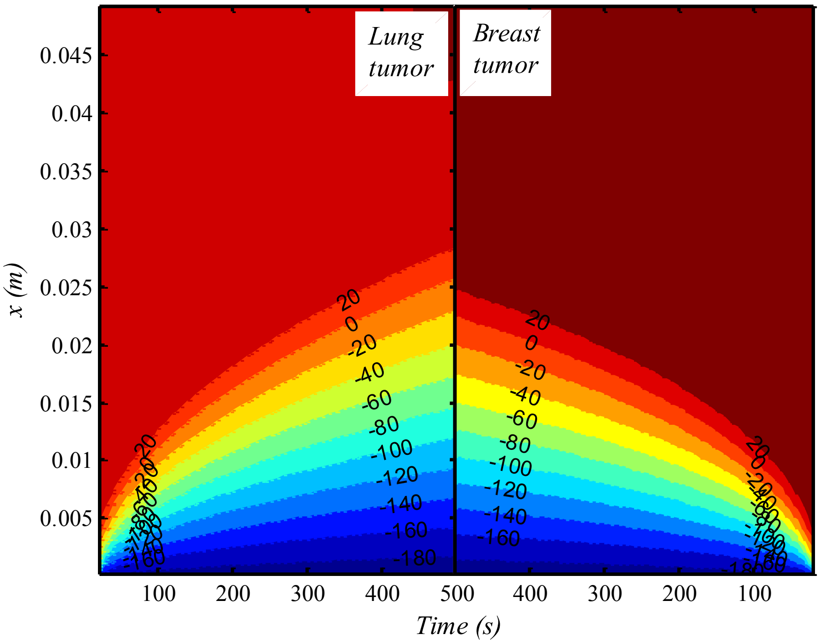

**Figure C.10** Temperature distribution for both tumors.

Table C.3 presents the effect of cryosurgery duration on the inverse predictions (Lung tumor). The duration of cryosurgery was set equal to 200, 500 and 800 (s). It is seen that the inverse predictions of the metabolic heat generation and of the blood perfusion rate are good for all cases. The relative error recorded is less than 0.5%. The corresponding temperature contours are depicted in Figure C.11. As expected, the freezing region expands with increasing duration of cryosurgery.

**Table C.3** Effect of cryosurgery duration on inverse predictions.

| Time (s) | Parameter | $P_{Inverse}$ | Error% |
|---|---|---|---|
| 200 | $w_b$ | $2.0*10^{-3}$ | 0 |
| | $Q_m$ | $4.198*10^{4}$ | 0.2 |
| 500 | $w_b$ | $2.0*10^{-3}$ | 0 |
| | $Q_m$ | $4.18*10^{4}$ | 0.48 |
| 800 | $w_b$ | $2.0*10^{-3}$ | 0 |
| | $Q_m$ | $4.19*10^{4}$ | 0.2 |

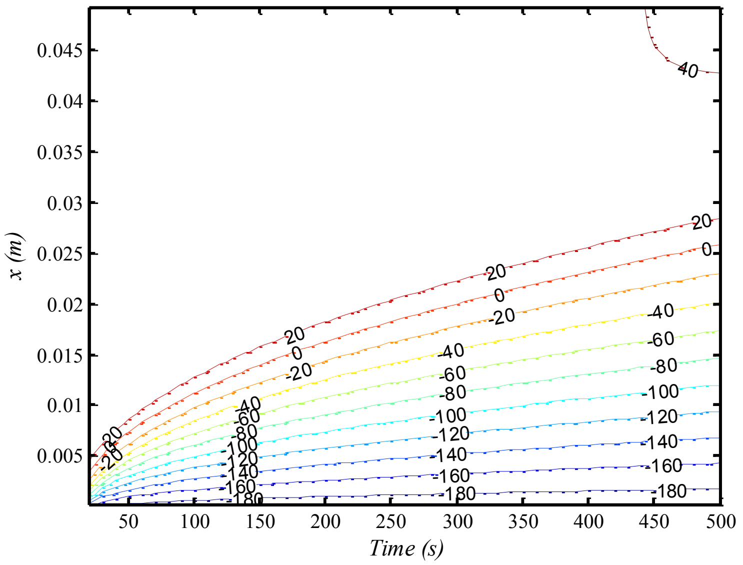

***t=500 s***

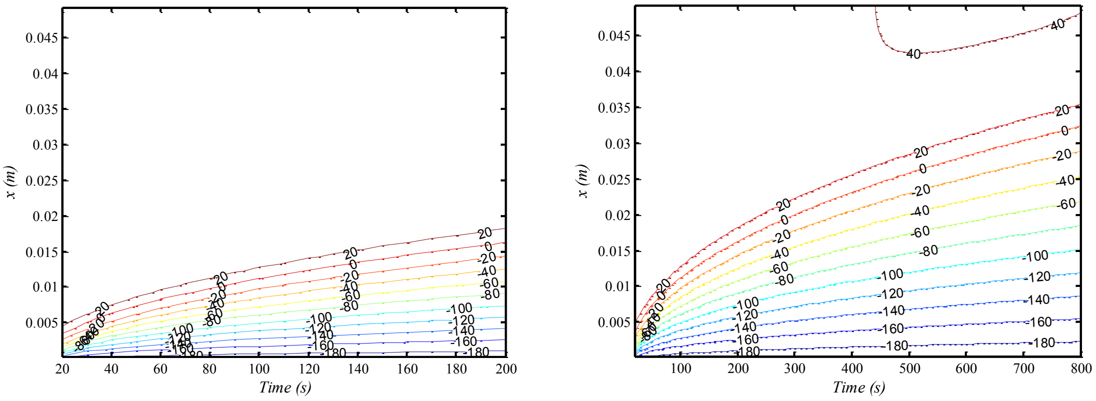

***t=200 s*** ***t=800 s***

**Figure C.11** Effect of cryosurgery duration on temperatures distribution.

## C.5.1. Effect of noise on the inverse predictions

In this section, the temperatures recorded by the temperature probe were contaminated with measurement errors (or noise) using a random number generator $(randn)\,\vec{\omega}_i$ These measurement errors are added to the recorded temperatures (the exact temperatures $\vec{T}_{exact}$ provided by the direct model):

$$\vec{T}_{\mathrm{noise}}(\mathrm{t}_i) = \vec{T}_{exact}(\mathrm{t}_i) + \sigma\ \vec{\omega}_i \qquad \text{(C.13)}$$

σ is the standard deviation of the measurement errors. The value for σ is arbitrarily set equal to *2%T<sub>max</sub>* and to *4%T<sub>max</sub>*. *T<sub>max</sub>* is the maximum temperature measured by the temperature probe.

Table C.4 summarizes the effect of the noise and of the total number of measurements *I* on the inverse predictions (Lung tumor). As expected, when the noise level rises from $2\%T_{max}$ to $4\%T_{max}$, the relative errors on the predicted blood perfusion rate and metabolic heat generation increase. Nevertheless, the inverse method remains stable and accurate. On the other hand, when the total number of measurements is increased from *I=50* to *I=100*, the relative errors drop.

**Table C.4** Effect of noise and of $I$ on the inverse predictions.

| | | *I=50* | *I=100* |
|---|---|---|---|
| σ=0% (no noise) | $Error_{\mathrm{wb}}$ | 0 | 0 |
| | $Error_{\mathrm{Qm}}$ | 0.48 | 0.23 |
| σ=2% | $Error_{\mathrm{wb}}$ | 7.11 | 5.10 |
| | $Error_{\mathrm{Qm}}$ | 18.05 | 7.04 |
| σ=4% | $Error_{\mathrm{wb}}$ | 31.56 | 5.41 |
| | $Error_{\mathrm{Qm}}$ | 36.55 | 18.39 |

## C.6. Conclusion

This paper presented an inverse heat transfer approach for predicting the time-varying phase change interface and the temperature distribution of diseased tissue during cryosurgery. Using a temperature probe pressed against the layer of diseased tissue, the inverse approach is able to determine simultaneously the metabolic heat generation and the blood perfusion rate. Once these thermal properties are obtained, the temperature distribution and the time-varying phase change interface may be predicted with the direct model. The direct problem is handled with the *Pennes* bioheat equation and the enthalpy method. The inverse model rests on the *Levenberg-Marquardt* Method (LMM) combined to the *Broyden* Method (BM). The effect (1) of the initial guesses for the unknown thermal properties; (2) of the thermal properties of the diseased tissues; (3) of the data capture frequency; and (4) of the noise on the recorded temperature was investigated. It was shown that the proposed inverse method remains accurate and stable for all the cases investigated.

## Acknowledgment

The authors are grateful to the Natural Sciences and Engineering Research Council of Canada (NSERC) for the financial support.

# LISTE DES RÉFÉRENCES

[1] Y. N. Toulouevski et I. Y. Zinurov, Innovation in electric arc furnaces, Springer-Verlag Berlin Heidelberg, 2010.

[2] K. Grotheim et H. Kvande, Introduction to Aluminum Electrolysis–Understanding the Hall-Heroult Process, Aluminium-Verlag, Düsseldorf: Germany, 1993.

[3] Y. N. Toulouevski et I. Y. Zinurov, Electric Arc Furnace with Flat Bath: Achievements and Prospects, Springer, 2015.

[4] P. Voisin, «Métallurgie extractive de l'aluminium,» Techniques de l'ingénieur, 1992.

[5] J. P. McGeer, «Electrolytic reduction cells for aluminium production,» *U.S. Patent No 4,592,820,* 1986.

[6] Y. Safa, Simulation numérique des phénomènes thermiques et magnétohydrodynamiques dans une cellule de Hall-Héroult, Thèse de doctorat: École Polytechnique Fédérale de Lausanne, Lausanne, Suisse, 2005.

[7] D. Patterson, D. Macdonald et C. Houle, «L'utilisation du volontarisme afin de contrôler les émissions de gaz à effet de serre du secteur industriel au Québec et au Canada: les cas des programmes VCR et ÉcoGESte,» chez *Politiques environnementales et accords volontaires: le volontarisme comme instrument de politiques environnementales au Quebec*, 2011, p. 75.

[8] «Émissions de gaz à effet de serre au Canada : progrès, perspectives et réductions,» Ottawa, Canada, 21 avril 2016.

[9] M. P. Taylor, B. J. Welch et M. J. O'sullivan, «Sidewall ledge dynamics in cells used for electrowinning aluminium,» chez *the Eleventh Australian Chemical Engineering Conference, Institution of Chemical Engineers*, 1983.

[10] M. P. Taylor, B. J. Welch et J. T. Keniry, «Influence of changing process conditions on the heat transfer during the early life of an operating cell,» *Light Metals,* pp. 437-447, 1983.

[11] J. S. Stevens McFadden , «Energy balance and cell dynamics : considerations,» *Proc. 6th Aust. Al. Smelting,* pp. 289-320, 1998.

[12] J. G. Peacey et G. W. Medlin, «Cell sidewall studies at Noranda aluminum,» chez *TMS Annual Meeting. TMS*, Warrendale, PA, USA, 1979.

[13] K. Grjotheim et B. J. Welch, Aluminium Smelter Technology--a Pure and Applied Approach, Dusseldorf: Aluminium-Verlag, 1988.

[14] K. Torklep et T. Nordbo, «Some applications of the elkem position probe,» chez *Proceedings of Sessions, TMS Annual Meeting. TMS*, San Francisco, CA, USA,, 1994.

[15] P. Boily, «Application des capteurs thermiques implantés pour la détection du profil de gelée dans la cuve d'électrolyse,» Université du Québec à Chicoutimi, Chicoutimi, 2001.

[16] O.P. Bonnardel et P. Homsi, «The Pechiney Semi-Continuous & Automatic Measurement Device (CMD),» chez *TMS Annual Meeting (A New Tool for Automatic Measurements)* , Warrendalc, PA, USA, 1999, p. 303-310.

[17] O. Tadrari et M. Lacroix, «Prediction of Protective Banks in High-Temperature Smelting Furnaces by Inverse Heat Transfer,» *Int. J. of Heat and Mass Transfer,* vol. 49, n° 13–14, p. 2180–2189, 2006.

[18] M. Lebreux, «Contrôle de l'épaisseur de gelée dans les réacteurs métallurgiques à haute température à l'aide d'un capteur virtuel,» Université de Sherbrooke, Sherbrooke, Québec, Canada, 2011.

[19] M. A. Marois, «Prédiction inverse d'un front de solidification dans un four de transformation à haute température,» Université de Sherbrooke, Sherbrooke, Québec, Canada, 2012.

[20] C. Bertrand, «Mesure et modélisation dynamique de la couche de gelée dans un réacteur métallurgique,» Université de Sherbrooke, Sherbrooke, 2014.

[21] Société canadienne du cancer, «Statistiques canadiennes sur le cancer,» Société canadienne du cancer, Gouvernement du Canada, Toronto (Ontario), 2016.

[22] Institut canadien d’information sur la santé, «Performance du système de santé canadien à l’international sur 50 ans : regard sur les années potentielles de vie perdues,» ON : ICIS, Ottawa, 2016.

[23] I. Paoli-Calmettes, «Les thermothérapies,» [En ligne]. Available: http://www.institutpaolicalmettes.fr/.

[24] M. C. BOULLIÉ, «CRYOTHÉRAPIE ET CRYOCHIRURGIE,» 13 février 2012. [En ligne]. Available: http://www.therapeutique-dermatologique.org/spip.php?article1357.

[25] L. Pauline, «Le froid s'affirme comme traitement contre le cancer,» Figaro-santé, 6 Juin 2014. [En ligne]. Available: http://sante.lefigaro.fr/actualite/2014/06/06/22428-froid-saffirme-comme-traitement-contre-cancer.

[26] B. L. Daniel, K. Butts et W. F. Block, «Magnetic resonance imaging of frozen tissues: temperature-dependent MR signal characteristics and relevance for MR monitoring of cryosurgery,» *Magnetic resonance in medicine,* vol. 41, n° 3, pp. 627-630, 1999.

[27] C. Thaokar et Y. Rabin, «Temperature field reconstruction for minimally invasive cryosurgery with application to wireless implantable temperature sensors and/or medical imaging,» *Cryobiology,* vol. 65, n° 3, pp. 270-277, 2012.

[28] J. C. Rewcastle, G. A. Sandison, L. J. Hahn, J. C. Saliken, J. G. McKinnon et B. J. Donnelly, «A model for the time-dependent thermal distribution within an iceball surrounding a cryoprobe,» *Physics in Medicine and Biology,* vol. 43 , n° 12, p. 3519, 1998.

[29] K. J. Chua, S. K. Chou et J. C. Ho, «An analytical study on the thermal effects of cryosurgery on selective cell destruction,» *Journal of biomechanics,* vol. 40, n° 1, pp. 100-116, 2007.

[30] G. J. Trezek et T. E. Cooper , «A probe technique for determining the thermal conductivity of tissue,» *Journal of Heat Transfer,* vol. 94, pp. 133-140, 1972.

[31] C. Svedman, G. W. Cherry , E. Strigini et T. J. Ryan, «Doppler imaging of skin microcirculation,» *ACTA DERMATOVENEREOLOGICA-STOCKHOLM,* vol. 78, pp. 114-118, 1998.

[32] M. Burger et F. V. Breukelen, «Construction of a low cost and highly sensitive direct heat calorimeter suitable for estimating metabolic rate in small animals,» *Journal of Thermal Biology,* vol. 38, n° 8, pp. 508-512, 2013.

[33] H. R. Schelbert, «PET contributions to understanding normal and abnormal cardiac perfusion and metabolism,» *Annals of biomedical engineering,* vol. 28, n° 8, pp. 922-929, 2000.

[34] M. Hafid et M. Lacroix, «An inverse heat transfer method for predicting the thermal characteristics of a molten material reactor,» *Applied Thermal Engineering,* vol. 108, pp. 140-149, 2016.

[35] M. Hafid et M. Lacroix, «Inverse heat transfer prediction of the state of the brick wall of a melting furnace,» *Applied Thermal Engineering,* vol. 110, pp. 265-274, 2017.

[36] M. Hafid et M. Lacroix, «Multi-Parameter Estimation of a Melting Furnace by Inverse Heat Transfer,» *Soumis au Applied Thermal Engineering,* 2016.

[37] M. Hafid et M. Lacroix, «Fast inverse prediction of the freezing front in cryosurgery,» *Journal of Thermal Biology,* vol. 69, pp. 13-22, 2017.

[38] M. Hafid et M. Lacroix, «Prediction of the Thermal Parameters of a High-Temperature Metallurgical Reactor Using Inverse Heat Transfer,» *Int. J. of Mechanical, Aerospace, Industrial, Mechatronic and Manufacturing Engineering,* vol. 10, n° 6, pp. 907-913, 2016.

[39] M. Hafid et M. Lacroix, «Inverse Heat Transfer Analysis of a Melting Furnace Using Levenberg-Marquardt Method,» *Int. J. of Mechanical, Aerospace, Industrial, Mechatronic and Manufacturing Engineering,* vol. 10, n° 7, pp. 1228-1235, 2016.

[40] M. Hafid et M. Lacroix, An inverse heat transfer algorithm for predicting the thermal properties of tumors during cryosurgery, Int. J. of Medical, Health, Biomedical, Bioengineering and Pharmaceutical Engineering, vol. 11, n° 6, pp. 298-306. 2017.

[41] P. Boily, L. I. Kiss, R.T. Bui et P. Desclaux, «Sensitivity analysis of the thermal detection of the Ledge profile in an aluminium reduction cell,» *Light Metals,* pp. 1209-1215, 2001.

[42] K. A. Rye, T. Eidet et K. Tørklep, «Dynamic ledge response in Hall-Heroult cells,» *LIGHT METALS,* pp. 347-352, 1999.

[43] C. Gau et R. Viskanta, «Melting and solidification of a metal system in a rectangular cavity,» *International Journal of Heat and Mass Transfer,* vol. 27, n° 1, pp. 113-123, 1984.

[44] Y. Wang, A. Amiri et K. Vafai, «An experimental investigation of the melting process in a rectangular enclosure,» *International Journal of Heat and Mass Transfer,* vol. 42, n° 19, pp. 3659-3672, 1999.

[45] J. Floquet, M. Désilets, P. Micheau et N. Quaegebeur, «Development of ultrasonic thickness measurements of solidification front inside metallurgical reactors,» *Mechanics & Industry,* vol. 16, n° 1, p. 111, 2015.

[46] J. Floquet, «Développement de mesures non destructives, par ondes ultrasonores, d'épaisseurs de fronts de solidification dans les réacteurs métallurgiques,» Université de Sherbrooke, Sherbrooke, 2013.

[47] C. Bertrand, M. A. Marois, M. Désilets, G. Soucy et M. Lacroix, « A combined 2D inverse predictions and experimental analysis for the bank formation inside a metallurgical reactor,» *International Journal of Heat and Mass Transfer,* vol. 59 , pp. 58-65, 2013.

[48] M. Dupuis, V. Bojarevics et J. Freilbergs, «emonstration thermo-electric and MHD mathematical models of a 500 kA aluminum electrolysis cell: Part 2,» *LIGHT METALS-WARRENDALE,* pp. 453-460, 2004.

[49] M. Dupuis et V. Bojarevics, «Weakly coupled thermo-electric and MHD mathematical models of an aluminium electrolysis cell,» *Light Metals,* vol. 1, pp. 449-454, 2005.

[50] M. Dupuis et V. Bojarevics, «Busbar sizing modeling tools: comparing an ANSYS® based 3D model with the versatile 1D model part of MHD-Valdis,» *GALLOWAY T J. Light Metals,* pp. 341-346, 2006.

[51] W. E. Haupin, «Calculating thickness of containing walls frozen from melt,» *TMS-AIME Annual Meeting,* vol. 23, n° 7, pp. 41-44, 1971.

[52] J. Thonstad et S. Rolseth, «Equilibrium between bath and side ledge,» *Light metals,* pp. 415-424, 1983.

[53] V. Gusberti, D. S. Severo, B. J. Welch et M. Skyllas-Kazacos, «Modeling the mass and energy balance of different aluminium smelting cell technologies,» *Light Metals,* pp. 929-934, 2012.

[54] E. Haugland, H. Borset, H. Gikling et H. Hoie, «Effects of ambient temperature and ventilation on shell temperature, heat balance and side ledge of an alumina reduction cell,» *LIGHT METALS-WARRENDALE, TMS,* pp. 269-276, 2003.

[55] J. N. Bruggeman et D. J. Danka, «Two-Dimensional Thermal Modeling of the Hall--Heroult Cell,» *Light Metals,* pp. 203-209, 1990.

[56] M. V. Romerio, M. Flueck, J. Rappaz et Y. Safa, «DETERMINATION AND INFLUENCE OF THE LEDGE SHAPE ON ELECTRICAL POTENTIAL AND FLUID MOTIONS IN A SMELTER,» *Light Metals TMS Annual Meeting,* pp. 461-468, 2005.

[57] S. Kalaiselvam, M. Veerappan, A. A. Aaron et S. Iniyan, «Experimental and analytical investigation of solidification and melting characteristics of PCMs inside cylindrical encapsulation,» *International Journal of Thermal Sciences,* vol. 47, n° 7, pp. 858-874, 2008.

[58] M. LeBreux, M. Désilets et M. Lacroix, «Fast Inverse Prediction of Phase Change Banks in High-Temperature Furnaces with a Kalman Filter Coupled with a Recursive Least-Square Estimator,» *Int. J. of Heat and Mass Transfer,* vol. 53, n° 23–24, p. 5250–5260, 2010.

[59] M. LeBreux, M. Désilets et M. Lacroix, «Control of the Ledge Thickness in High-Temperature Metallurgical Reactor using a Virtual Sensor,» *Inverse Problems in Sci. and Eng.,* vol. 20, n° 8, p. 1215–1238, 2012.

[60] M. LeBreux, M. Désilets et M. Lacroix, «Prediction of the Time-Varying Ledge Profile internal a High-Temperature Metallurgical Reactor with an Unscented Kalman Filter-Based Virtual Sensor,» *Numer. Heat Transfer A,* vol. 64, pp. 551-576, 2013.

[61] M. LeBreux, M. Désilets et M. Lacroix, «An unscented Kalman filter inverse heat transfer method for the prediction of the ledge thickness internal high-temperature metallurgical reactors,» *Int. J. of Heat and Mass Transfer,* vol. 57, n° 1, pp. 265-273, 2013.

[62] M. LeBreux, M. Désilets et M. Lacroix, «Is the performance of a virtual sensor employed for the prediction of the ledge thickness internal a metallurgical reactor affected by the thermal contact resistance?,» *WIT Transactions on Eng. Sci.,* vol. 83, pp. 517-526, 2014.

[63] M. LeBreux, M. Désilets et M. Lacroix, «To what extent do thermo physical properties of a metallurgical reactor affect the performance of a virtual sensor used for predicting the ledge profile?,» *Mechanics & Industry,* vol. 17, n° 6, p. 603, 2016.

[64] M. A. Marois, M. Désilets et M. Lacroix, «What is the Most Suitable Fixed Grid Solidification Method for Handling Time-Varying Inverse Stefan Problems in High Temperature Industrial Furnaces?,» *Int. J. of Heat and Mass Transfer,* vol. 55, p. 5471–5478, 2012.

[65] M. A. Marois, M. Désilets et M. Lacroix, «Prediction of the Bank Formation in High Temperature Furnaces by a Sequential Inverse Analysis with Overlaps,» *Numer. Heat Transfer A,* vol. 60, p. 561–579, 2011.

[66] M. A. Marois, M. Désilets et M. Lacroix, «Prediction of a 2-D Solidification Front in High-Temperature Furnaces by an Inverse Analysis,» *Numer. Heat Transfer A,* vol. 59, n° 3, p. 151–166, 2011.

[67] C. K. Chen et C. R. Su , «Inverse estimation for temperatures of outer surface and geometry of inner surface of furnace with two layer walls,» *Energy Conversion and Management,* vol. 49, n° 2, pp. 301-310, 2008.

[68] C. R. Su et C. K. Chen, «Geometry estimation of the furnace inner wall by an inverse approach,» *International Journal of Heat and Mass Transfer,* vol. 50, n° 19, pp. 3767-3773, 2007.

[69] S. Wang, S. C. Lin et Y. C. Yang, «Geometry estimation for the inner surface in a furnace wall made of functionally graded materials,» *International Communications in Heat and Mass Transfer,* vol. 67, pp. 1-7, 2015.

[70] C. R. Su, W. L. Liu et H. Y. Lai, «Estimation for inner surface geometry of furnace wall using inverse process combined with grey prediction model,» *International Journal of Heat and Mass Transfer,* vol. 52, n° 15, pp. 3595-3605, 2009.

[71] H. Farzan, S. M. H. Sarvari et S. H. Mansouri, «Inverse boundary design of a radiative smelting furnace with ablative phase change phenomena,» *Applied Thermal Engineering,* vol. 98, p. 1140–1149, 2016.

[72] J. G. Webster, The Measurement, Instrumentation, and Sensors: Handbook, Springer , 1999.

[73] J. S. Wilson, Sensor technology handbook, Elsevier, 2004.

[74] P. Wikström, W. Blasiak et F. Berntsson, «Estimation of the transient surface temperature and heat flux of a steel slab using an inverse method,» *Applied thermal engineering,* vol. 27, n° 14, pp. 2463-2472, 2007.

[75] P. Le Bideau, J. P. Ploteau et P. Glouannec, «Heat flux estimation in an infrared experimental furnace using an inverse method,» *Applied Thermal Engineering,* vol. 29, n° 14, pp. 2977-2982, 2009.

[76] B. Sawaf et M. N. Özisik, «Determining the constant thermal conductivities of orthotropic materials by inverse analysis,» *Int. communications in heat and mass transfer,* vol. 22, n° 2, pp. 201-211, 1995.

[77] M. Cui, X. Gao et J. Zhang, «A new approach for the estimation of temperature-dependent thermal properties by solving transient inverse heat conduction problems,» *International Journal of Thermal Sciences,* vol. 58, pp. 113-119, 2012.

[78] H. He, C. He et G. Chen, «Inverse determination of temperature-dependent thermophysical parameters using multiobjective optimization methods,» *International Journal of Heat and Mass Transfer,* vol. 85 , pp. 694-702, 2015.

[79] T. Telejko, «Analysis of an inverse method of simultaneous determination of thermal conductivity and heat of phase transformation in steels,» *Journal of materials processing technology,* vol. 155, pp. 1317-1323, 2004.

[80] R. C. Aster, B. Borchers et C. H. Thurber, Parameter estimation and inverse problems, New York: Elsevier, 2005.

[81] M. McClung et R. Zerkle, «Autopsy procedures and results at Century Aluminum of West Virginia,» *LIGHT METALS-WARRENDALE-PROCEEDINGS, TMS,* pp. 213-218, 2004.

[82] C. C. Wei, «Modelling of bath/ledge heat transfer in Hall-Heroult cells,» Thèse de doctorat, The University of Auckland, Auckland, New Zealand, 1996.

[83] L. Wu, H. Cheng, Y. Su et H. Feng, «Mathematical model for on-line prediction of bottom and hearth of blast furnace by particular solution boundary element method,» *Applied thermal engineering,* vol. 23, n° 16, pp. 2079-2087, 2003.

[84] Y. Zhang, R. Deshpande, D. F. Huang et P. Chaubal, «Numerical analysis of blast furnace hearth inner profile by using CFD and heat transfer model for different time periods,» *International journal of heat and mass transfer,* vol. 51, n° 1, pp. 186-197, 2008.

[85] C. M. Chang, W. T. Cheng, C. E. Huang et S. W. Du, «Numerical prediction on the erosion in the hearth of a blast furnace during tapping process,» *International Communications in Heat and Mass Transfer,* vol. 36, n° 5, pp. 480-490, 2009.

[86] A. M. GUZMÁN, D. I. MARTÍNEZ et R. GONZÁLEZ, «Corrosion–erosion wear of refractory bricks in glass furnaces,» *Engineering Failure Analysis,* vol. 46, pp. 188-195, 2014.

[87] H. Li, J. Cheng et L. Tang, «Corrosion of electrocast AZS refractories by CAS glass–ceramics melting,» *Journal of Non-Crystalline Solids,* vol. 354, n° 12, pp. 1418-1423, 2008.

[88] I. Crudu, M. P. Ionescu, V. Munteanu, I. F. Sandu et P. Nedelcu, «tribosystemic approach to refractory lining destruction in blast furnaces,» *Wear,* vol. 216, n° 2, pp. 251-261, 1998.

[89] M. Kaur, H. Singh et S. Prakash, «Surface engineering analysis of detonation-gun sprayed Cr 3 C 2–NiCr coating under high-temperature oxidation and oxidation–erosion environments,» *Surface and Coatings Technology,* vol. 206, n° 2, pp. 530-541, 2011.

[90] A. P. Luz, F. C. Leite, M. A. M. Brito et V. C. Pandolfelli, «Slag conditioning effects on MgO–C refractory corrosion performance,» *Ceramics International,* vol. 39, n° 7, pp. 7507-7515, 2013.

[91] A. Jakovics, I. Madzhulis, V. Frishfelds et B. Nacke, «Influence of melt flow and temperature on erosion of refractory and deposit formation in aluminium melting furnaces,» *Energy conversion and management,* vol. 43, n° 3, pp. 345-352, 2002.

[92] J. Poirier, F. Qafssaoui, J. P. Ildefonse et M. L. Bouchetou, « Analysis and interpretation of refractory microstructures in studies of corrosion mechanisms by liquid oxides,» *Journal of the European Ceramic Society,* vol. 28, n° 8, pp. 1557-1568, 2008.

[93] G. Onik, C. Cooper, H. I. Goldberg , A. A. Moss, B. Rubinsky et M. Christianson, «Ultrasonic characteristics of frozen liver,» *Cryobiology,* vol. 21, n° 3, pp. 321-328, 1984.

[94] J. C. Saliken, J. G. McKinnon et R. Gray, «Computed tomography for cryotherapy monitoring,» *Am. J. Radiol,* vol. 166, pp. 853-855, 1996.

[95] G. A. Sandison, M. P. Loye, J. C. Rewcastle, L. J. Hahn, J. C. Saliken, J. G. McKinnon et B. J. Donnelly, «X-ray CT monitoring of iceball growth and thermal distribution during cryosurgery,» *Physics in medicine and biology,* vol. 43, n° 11, p. 3309, 1998.

[96] N. E. Hoffmann et J. C. Bischof , «Cryosurgery of Normal and Tumor Tissue in the Dorsal Skin Flap Chamber: Part I—Thermal Response,» *Journal of Biomechanical Engineering,* vol. 123, n° 4, pp. 301-309, 2001.

[97] N. E. Hoffmann et J. C. Bischof, «Cryosurgery of normal and tumor tissue in the dorsal skin flap chamber: Part II—Injury response,» *Journal of biomechanical engineering,* vol. 123, n° 4, pp. 310-316, 2001.

[98] A. Aragon, «Contribution à l'étude de la cryothérapie en ophtalmologie vétérinaire: utilisation d'un système à azote liquide: l'Erbocryo-derm chez les carnivores domestiques,» Thèse de Médecine Vétérinaire, Ophtalmologie,, Lyon, 1998.

[99] J. Bickels, I. Meller et M. Malawer, «The biology and role of cryosurgery in the treatment of bone tumors,» *Musculoskeletal cancer surgery. Springer Netherlands,* pp. 135-145, 2004.

[100] P. B. Fretz et S. M. Barber , «rospective analysis cryosurgery as the sole treatment for equine sarcoids,» *The Veterinary clinics of North America, Small animal practice,* vol. 10, n° 4, pp. 847-859, 1980.

[101] W.J. Minkowycz, E.M. Sparrow et J.P. Abraham, Advances in Numerical Heat Transfer, USA: CRC Press , 2009.

[102] M. A. Dos Santos Bernardes, Developments in Heat Transfer, ISBN 978-953-307-569-3, InTech, 2011.

[103] H. H. Pennes , «Analysis of tissue and arterial blood temperatures in the resting human forearm,» *Journal of applied physiology,* vol. 1, n° 2, pp. 93-122, 1948.

[104] J. Bastacky et B. Rubinsky, «An analytical study of cryosurgery in the lung,» *Journal of biomechanical engineering,* vol. 114, pp. 467-472, 1992.

[105] J. Zhang, G. A. Sandison, J. Y. Murthy et L. X. Xu, «Numerical simulation for heat transfer in prostate cancer cryosurgery,» *Journal of biomechanical engineering,* vol. 127, n° 2, pp. 279-294, 2005.

[106] S. Kumar et V. K. Katiyar, «Numerical study on phase change heat transfer during combined hyperthermia and cryosurgical treatment of lung cancer,» *International Journal of Applied Mathematics and Mechanics,* vol. 3, n° 3, pp. 1-17, 2007.

[107] R. Magleby, A. Schallop, E. Shulman et J. Sterling, «The Effect of Vascularization and Tissue Type on Cryosurgical Procedures,» Cornell University, New York, 2008.

[108] Y. Rabin et A. Shitzer, «Numerical solution of the multidimensional freezing problem during cryosurgery,» *Journal of biomechanical engineering,* vol. 120, n° 1, pp. 32-37, 1998.

[109] G. Zhao, H. F. Zhang, X. J. Guo, D. W. Luo et D.Y. Gao, « Effect of blood flow and metabolism on multidimensional heat transfer during cryosurgery,» *Medical engineering & physics,* vol. 29, n° 2, pp. 205-215, 2007.

[110] S. Singh et S. Kumar, «A study on the effect of metabolic heat generation on biological tissue freezing,» *The Scientific World Journal,* 2013.

[111] R. I. Andrushkiw, «Mathematical modeling of freezing front propagation in biological tissue,» *Mathematical and Computer Modelling,* vol. 13, n° 10, pp. 1-9, 1990.

[112] P. K. Gupta, J. Singh et K. N. Rai, «Numerical simulation for heat transfer in tissues during thermal therapy,» *Journal of Thermal Biology,* vol. 35, n° 6, pp. 295-301, 2010.

[113] P. K. Gupta, J. Singh et K. N. Rai, «A numerical study on heat transfer in tissues during hyperthermia,» *Mathematical and Computer Modelling,* vol. 57, n° 5, pp. 1018-1037, 2013.

[114] S. Acharya, D. B. Gurung et V. P. Saxena, «Human males and females body thermoregulation: Perfusion effect analysis,» *Journal of thermal biology,* vol. 45, pp. 30-36, 2014.

[115] G. Delhomme, A. Dittmar, W. H. Newman, H. F. Bowman et M. Jouvet, «Thermal diffusion probes for tissue blood flow measurements,» *Sensors and Actuators B: Chemical,* vol. 6, n° 1-3, pp. 87-90. , 1992.

[116] C. Svedman, G. W. Cherry, E. Strigini et T. J. Ryan, «Laser Doppler imaging of skin microcirculation,» *ACTA DERMATOVENEREOLOGICA-STOCKHOLM,* vol. 78, pp. 114-118, 1998.

[117] J. Iljaž et L. Škerget, «Blood perfusion estimation in heterogeneous tissue using BEM based algorithm,» *Engineering Analysis with Boundary Elements,* vol. 39 p. 75-87, 2014.

[118] P. L. Ricketts, A. V. Mudaliar, B. E. Ellis, C. A. Pullins, L. A. Meyers, O. I. Lanz et T. E. Diller, «Non-invasive blood perfusion measurements using a combined temperature and heat flux surface probe,» *International journal of heat and mass transfer,* vol. 51, n° 23, pp. 5740-5748, 2008.

[119] Z. S. Deng et J. Liu, « Parametric studies on the phase shift method to measure the blood perfusion of biological bodies,» *Medical engineering & physics,* vol. 22, n° 10, pp. 693-702, 2000.

[120] K. Das et S. C. Mishra, «Non-invasive estimation of size and location of a tumor in a human breast using a curve fitting technique,» *International Communications in Heat and Mass Transfer,* vol. 56, pp. 63-70, 2014.

[121] K. Das, R. Singh et S. C. Mishra, «Numerical analysis for determination of the presence of a tumor and estimation of its size and location in a tissue,» *Journal of thermal biology,* vol. 38, n° 1, pp. 32-40, 2013.

[122] P. W. Partridge et L. C. Wrobel, «An inverse geometry problem for the localisation of skin tumours by thermal analysis,» *Engineering Analysis with Boundary Elements,* vol. 31, n° 10, pp. 803-811, 2007.

[123] K. Das et S. C. Mishra, « Simultaneous estimation of size, radial and angular locations of a malignant tumor in a 3-D human breast–A numerical study,» *Journal of thermal biology,* vol. 52, pp. 147-156, 2015.

[124] C. H. Huang et C. Y. Huang, « An inverse problem in estimating simultaneously the effective thermal conductivity and volumetric heat capacity of biological tissue,» *Applied mathematical modelling,* vol. 31, n° 9, pp. 1785-1797, 2007.

[125] A. Jalali, M. B. Ayani et M. Baghban, «Simultaneous estimation of controllable parameters in a living tissue during thermal therapy,» *Journal of thermal biology,* vol. 45, pp. 37-42, 2014.

[126] K. S. Jhajj, S. R. Slezak et K. J. Daun, «Inferring the specific heat of an ultra high strength steel during the heating stage of hot forming die quenching, through inverse analysis,» *Applied Thermal Engineering,* vol. 83, pp. 98-107, 2015.

[127] M. LeBreux, M. Désilets et M. Lacroix, «Prediction of the ledge thickness inside a high-temperature metallurgical reactor using a virtual sensor,» *Journal of Physics: Conference Series, IOP Publishing,* vol. 395, n° 1, p. 012077, 2012.

[128] J. Zhang et M.A. Delichatsios, «Determination of the convective heat transfer coefficient in three-dimensional inverse heat conduction problems,» *Fire Saf.,* vol. 44 , n° 5, pp. 681-690, 2009.

[129] C. H. Huang et Y. L. Tsai, «A transient 3-D inverse problem in imaging the time-dependent local heat transfer coefficients for plate fin,» *Applied Thermal Engineering,* vol. 25, n° 14-15, pp. 2478-2495, 2005.

[130] W. L. Chen, Y. C. Yang et H. L. Lee, «Inverse problem in determining convection heat transfer coefficient of an annular fin,» *Energy Convers. Manag.,* vol. 48, n° 4, pp. 1081-1088, 2007.

[131] A. S. Dogonchi et D. D. Ganji, «Convection-radiation heat transfer study of moving fin with temperature-dependent thermal conductivity, heat transfer coefficient and heat generation,» *Applied Thermal Engineering,* vol. 103, p. 705–712, 2016.

[132] J. Zueco, F. Alhama et C.F.G. Fernandez, «Inverse determination of temperature dependent thermal conductivity using network simulation method,» *Journal of Materials Processing Technology,* vol. 174, n° 1, pp. 137-144, 2006.

[133] M.I. Char, F.P. Chang et B.C. Tai, «Inverse determination of thermal conductivity by differential quadrature method,» *International Communications in Heat and Mass Transfer ,* vol. 35, n° 2, pp. 113-119, 2008.

[134] C.L. Chang et M. Chang, «Inverse determination of thermal conductivity using semi-discretization method,» *Applied Mathematical Modelling,* vol. 33, n° 3, pp. 1644-1655, 2009.

[135] F. L. Rodríguez et V. de Paulo Nicolau, « Inverse heat transfer approach for IR image reconstruction,» *Applied thermal engineering,* vol. 33, pp. 109-118, 2012.

[136] C. H. Huang et H. H. Wu, «An inverse hyperbolic heat conduction problem in estimating surface heat flux by the conjugate gradient method,» *Journal of Physics D: Applied Physics,* vol. 39, n° 18, p. 4087–4096, 2006.

[137] Y. Li, G. Wang et H. Chen, «Simultaneously estimation for surface heat fluxes of steel slab in a reheating furnace based on DMC predictive control,» *Applied Thermal Engineering,* vol. 80, pp. 396-403, 2015.

[138] C. H. Huang, P. Y. Wu et S. Kim, «A nonlinear inverse problem in estimating the polymerization heat source of bone cements by an iterative regularization method,» *Inverse Problems,* vol. 26, n° 6, p. 065009, 2010.

[139] Y. C. Yang et W. L. Chen, «A nonlinear inverse problem in estimating the heat flux of the disc in a disc brake system,» *Applied Thermal Engineering,* vol. 31, n° 14-15, pp. 2439-2448, 2011.

[140] V. R. Voller, «Development and application of a heat balance integral method for analysis of metallurgical solidification,» *Applied Mathematical Modelling,* pp. 3-11, 1989.

[141] V. R. Voller et C. R. Swaminathan, «General Source-Based Method for Solidification Phase Change,» *Numer. Heat Transfer,* vol. 19, p. 175–189, 1991.

[142] V. Guillaume, L. Gosselin et M. Lacroix, «An enhanced thermal conduction model for the prediction of convection dominated solid–liquid phase change,» *Int. J. of Heat and Mass Transfer, vol. 52, no. 7-8, pp. 1753-1760, 2009.*

[143] S. V. Patankar, Numerical Heat Transfer and Fluid Flow, New York: McGraw-Hill, 1980.

[144] R. Dou, Z. Wen et G. Zhou, «2D axisymmetric transient inverse heat conduction analysis of air jet impinging on stainless steel plate with finite thickness,» *Applied Thermal Engineering,* vol. 93, pp. 468-475, 2016.

[145] S. Zhao, W. Zhang, X. He, J. Li, Y. Yao et X. Lin, «Simultaneous reconstruction of thermal degradation properties for anisotropic scattering fibrous insulation after high temperature thermal exposures,» *Applied Thermal Engineering,* vol. 78, pp. 507-515, 2015.

[146] S. Rouquette, J. Guo et P. Masson , «Estimation of the parameters of a Gaussian heat source by the Levenberg–Marquardt method: application to the electron beam welding,» *Int. J. of Thermal Sciences,* vol. 46, n° 2, pp. 128-138, 2007.

[147] T. Xie, Y. L. He, Z. X. Tong, W. X. Yan et X. Q. Xie, «An inverse analysis to estimate the endothermic reaction parameters and physical properties of aerogel insulating material,» *Applied Thermal Engineering,* vol. 87, pp. 214-224, 2015.

[148] M. Cui, K. Yang, X. L. Xu , S. D. Wang et X. W. Gao, «A modified Levenberg–Marquardt algorithm for simultaneous estimation of multi-parameters of boundary heat flux by solving transient nonlinear inverse heat conduction problems,» *Int. J. of Heat and Mass Transfer,* vol. 97, pp. 908-916, 2016.

[149] E. García, D. Méresse, I. Pombo, S. Harmand et J. A. Sánchez, «Identification of heat partition in grinding related to process parameters, using the inverse heat flux conduction model,» *Applied Thermal Engineering,* vol. 66, n° 1-2, pp. 122-130, 2014.

[150] D. W. Marquardt, «An algorithm for least-squares estimation of nonlinear parameters,» *J. of the Society for Industrial and Applied Mathematics,* pp. 431-441, 1963.

[151] M. N. OZISIK et H. R. B. Orlande, Inverse Heat Transfer, New York: Taylor and Francis, 2000.

[152] C. G. Broyden, «A class of methods for solving nonlinear simultaneous equations,» *Mathematics of computation,* pp. 577-593, 1965.

[153] G. P. Flach et M. N. Özişik, «Inverse heat conduction problem of simultaneously estimating spatially varying thermal conductivity and heat capacity per unit volume,» *Numerical Heat Transfer,* vol. 16, n° 2, pp. 249-266, 1989.

[154] B. Moghadassian et F. Kowsary, «Inverse boundary design problem of natural convection–radiation in a square enclosure,» *Int. J. of Thermal Sci.,* vol. 75, pp. 116-126, 2014.

[155] K. W. Kim et S. W. Baek, «Inverse radiation–conduction design problem in a participating concentric cylindrical medium,» *Int. J. of Heat and Mass Transfer,* vol. 50, n° 13-14, pp. 2828-2837, 2007.

[156] S. Kumar et S. P. Mahulikar, «Reconstruction of aero-thermal heating and thermal protection material response of a Reusable Launch Vehicle using inverse method,» *Applied Thermal Engineering,* vol. 103, pp. 344-355, 2016.

[157] I. Istadi et Y. Bindar, «Improved cooler design of electric arc furnace refractory in mining industry using thermal analysis modeling and simulation,» *Applied Thermal Engineering,* vol. 73, n° 1, pp. 1129-1140, 2014.

[158] M. Carmona et C. Cortés, «Analysis of the thermal performance and convection effects in an aluminum holding furnace using CFD,» *Applied Thermal Engineering,* vol. 76, pp. 484-495, 2015.

[159] D. Fu, Y. Chen, Y. Zhao, J. D'Alessio, K. J. Ferron et C. Q. Zhou, «CFD modeling of multiphase reacting flow in blast furnace shaft with layered burden,» *Applied Thermal Engineering,* vol. 66, n° 1, pp. 298-308, 2014.

[160] C. E. Huang, S. W. Du et W. T. Cheng, « Numerical investigation on hot metal flow in blast furnace hearth through CFD,» *ISIJ international,* vol. 48, n° 9, pp. 1182-1187, 2008.

[161] J. M. Casal, J. Porteiro, J. L. Míguez et A. Vázquez, «New methodology for CFD three-dimensional simulation of a walking beam type reheating furnace in steady state,» *Applied Thermal Engineering,* vol. 86, pp. 69-80, 2015.

[162] A. G. Mombeni, E. Hajidavalloo et M. Behbahani-Nejad, «Transient simulation of conjugate heat transfer in the roof cooling panel of an electric arc furnace,» *Applied Thermal Engineering,* vol. 98, pp. 80-87, 2016.

[163] C. Yigit, G. Coskun, E. Buyukkaya, U. Durmaz et H. R. Güven, «CFD modeling of carbon combustion and electrode radiation in an electric arc furnace,» *Applied Thermal Engineering,* vol. 90 , pp. 831-837, 2015.

[164] A. Blaise, B. Bourouga, B. Abdulhay et C. Dessain, «Thermal contact resistance estimation and metallurgical transformation identification during the hot stamping,» *Applied thermal engineering,* vol. 61, n° 2, pp. 141-148, 2013.

[165] J. Choi, B. Sung, C. Kim et D. A. Borca-Tasciuc, «Interface engineering to enhance thermal contact conductance of evaporators in miniature loop heat pipe systems,» *Applied Thermal Engineering,* vol. 60, n° 1, pp. 371-378, 2013.

[166] T. Loulou, E. A. Artyukhin et J. P. Bardon, «Estimation of thermal contact resistance during the first stages of metal solidification process: I—experiment principle and modelisation,» *International Journal of Heat and Mass Transfer,* vol. 42, n° 12, pp. 2119-2127, 1999.

[167] S. C. Somé, D. Delaunay et V. Gaudefroy, «Vincent. Comparison and validation of thermal contact resistance models at solid–liquid interface taking into account the wettability parameters,» *Applied Thermal Engineering,* vol. 61, n° 2, pp. 531-540, 2013.

[168] V. R. Voller, «Fast implicit finite-difference method for the analysis of phase change problems,» *Numer. Heat Transfer B,* vol. 17, n° 2, pp. 155-169, 1990.

[169] C. H. Huang et Y. H. Chen, «An optimal design problem in determining non-uniform fin heights and widths for an impingement heat sink module,» *Applied Thermal Engineering,* vol. 63, n° 2, pp. 481-494, 2014.

[170] C. H. Huang et W. L. Chang, «An inverse design method for optimizing design parameters of heat sink modules with encapsulated chip,» *Applied Thermal Engineering,* vol. 40, pp. 216-226, 2012.

[171] S. K. Dhiman et J. K. Prasad, « Inverse estimation of heat flux from a hollow cylinder in cross-flow of air,» *Applied Thermal Engineering,* vol. 113, pp. 952-961, 2017.

[172] M. Cui, Y. Zhao, B. Xu et X. W. Gao, «A new approach for determining damping factors in Levenberg-Marquardt algorithm for solving an inverse heat conduction problem,» *International Journal of Heat and Mass Transfer,* vol. 107, pp. 747-754, 2017.

[173] Y. Wang, Wang, Y, X. Luo, Y. Yu et Q. Yin, «Evaluation of heat transfer coefficients in continuous casting under large disturbance by weighted least squares Levenberg-Marquardt method,» *Applied Thermal Engineering,* vol. 111, pp. 989-996, 2017.

[174] M. M. Malawer, J. Bickels, I. Meller, R. G. Buch, R. M. Henshaw et Y. Kollender, «Cryosurgery in the Treatment of Giant Cell Tumor: A Long term Followup Study,» *Clinical orthopaedics and related research,* vol. 359, pp. 176-188, 1999.

[175] N. N. Korpan, Basics of cryosurgery, Springer Science & Business Media, 2012.

[176] T. S. Ravikumar, G. Steele, R. Kane et V. King, «Experimental and clinical observations on hepatic cryosurgery for colorectal metastases,» *Cancer research,* vol. 51, n° 23, pp. 6323-6327, 1991.

[177] A. A. Gage et J. G. Baust, «Cryosurgery for tumors,» *Journal of the American College of Surgeons,* vol. 205, n° 2, pp. 342-356, 2007.

[178] S. O. Pfleiderer, M. G. Freesmeyer, C. Marx, R. Kühne-Heid, A. Schneider et W. A. Kaiser, «Cryotherapy of breast cancer under ultrasound guidance: initial results and limitations,» *European radiology,* vol. 12, n° 12, pp. 3009-3014, 2002.

[179] P. E. Huber, J. W. Jenne, R. Rastert, I. Simiantonakis, H. P. Sinn et H. J. Strittmatter, «A new noninvasive approach in breast cancer therapy using magnetic resonance imaging-guided focused ultrasound surgery,» *Cancer research,* vol. 61, n° 23, pp. 8441-8447, 2001.

[180] M. Jaeger et M. Carin, «The front-tracking ALE method: application to a model of the freezing of cell suspensions,» *Journal of Computational Physics,* vol. 179, n° 2, pp. 704-735, 2002.

[181] X. Zhao et K. J. Chua, «Studying the thermal effects of a clinically-extracted vascular tissue during cryo-freezing,» *Journal of Thermal Biology,* vol. 37, n° 8, pp. 556-563, 2012.

[182] M. A. Khanday et F. Hussain, « Explicit formula of finite difference method to estimate human peripheral tissue temperatures during exposure to severe cold stress,» *Journal of thermal biology,* vol. 48, pp. 51-55, 2015.

[183] M. Carin et M. Jaeger, «Numerical simulation of the interaction of biological cells with an ice front during freezing,» *The European Physical Journal Applied Physics,* vol. 16, n° 3, pp. 231-238, 2001.

[184] T. E. Cooper et G. J. Trezek, «Correlation of thermal properties of some human tissue with water content,» *Aerospace medicine,* vol. 42, n° 1, pp. 24-27, 1971.

[185] C. Y. Lee et J. Bastacky, «Comparative mathematical analyses of freezing in lung and solid tissue,» *Cryobiology,* vol. 32, n° 4, pp. 299-305, 1995.

[186] L. Gosselin, M. Tye-Gingras et F. Mathieu-Potvin, «Review of utilization of genetic algorithms in heat transfer problems,» *International Journal of Heat and Mass Transfer,* vol. 52, n° 9, pp. 2169-2188, 2009.

[187] D. Trucu, D. B. Ingham et D. Lesnic, «Reconstruction of the space-and time-dependent blood perfusion coefficient in bio-heat transfer,» *Heat Transfer Engineering,* vol. 32, n° 9, pp. 800-810, 2011.

[188] H. L. Lee, T. H. Lai, W. L. Chen et Y. C. Yang, «An inverse hyperbolic heat conduction problem in estimating surface heat flux of a living skin tissue,» *Applied Mathematical Modelling,* vol. 37, n° 5, pp. 2630-2643, 2013.

[189] R. Das, S. C. Mishra et R. Uppaluri, «Multiparameter estimation in a transient conduction-radiation problem using the lattice Boltzmann method and the finite-volume method coupled with the genetic algorithms,» *Numerical Heat Transfer,* vol. 53 , n° 12, pp. 1321-1338, 2008.

[190] J. M. Luna, R. Romero-Mendez, A. Hernandez-Guerrero et F. Elizalde-Blancas, «Procedure to estimate thermophysical and geometrical parameters of embedded cancerous lesions using thermography,» *Journal of biomechanical engineering,* vol. 134, n° 3, p. 031008, 2012.

[191] K. Yue, X. Zhang et F. Yu, «Simultaneous estimation of thermal properties of living tissue using noninvasive method,» *International Journal of Thermophysics,* vol. 28, n° 5, pp. 1470-1489, 2007.

[192] C. H. Huang et C. Y. Huang, «An inverse biotechnology problem in estimating the optical diffusion and absorption coefficients of tissue,» *International journal of heat and mass transfer,* vol. 47, n° 3, pp. 447-457, 2004.

[193] M. Dehghan et M. Sabouri, « A spectral element method for solving the Pennes bioheat transfer equation by using triangular and quadrilateral elements,» *Applied mathematical modelling,* vol. 36, n° 12, pp. 6031-6049, 2012.

[194] A. Fasano, D. Hömberg et D. Naumov, «On a mathematical model for laser-induced thermotherapy,» *Applied Mathematical Modelling,* vol. 34, n° 12, pp. 3831-3840, 2010.

[195] M. Jasiński, E. Majchrzak et L. Turchan, «Numerical analysis of the interactions between laser and soft tissues using generalized dual-phase lag equation,» *Applied Mathematical Modelling,* vol. 40, n° 2, pp. 750-762, 2016.

[196] E. Franquet, S. Gibout, J. P. Bédécarrats, D. Haillot et J. P. Dumas, «Inverse method for the identification of the enthalpy of phase change materials from calorimetry experiments,» *Thermochimica acta,* vol. 546, pp. 61-80, 2012.

[197] E. Franquet, J.P. Bedecarrats, D. Haillot et J. P. Dumas, «Determination of the enthalpy of phase change materials by inverse method from calorimetric experiments. Applications to pure substances or binary solutions,» *Journal of Physics: Conference Series,* p. 012135, 2012.

[198] T. Loulou, E. A. Artyukhin et J. P. Bardon, «Estimation of thermal contract resistance during the first stages of metal solidification process: II—experimental setup and results,» *International journal of heat and mass transfer,* vol. 42, n° 12, pp. 2129-2142, 1999.

[199] Y. T. Zhang et J. Liu, «Numerical study on three-region thawing problem during cryosurgical re-warming,» *Medical engineering & physics,* vol. 24, n° 4, pp. 265-277, 2002.

[200] H. Budman, A. Shitzer et J. Dayan, «Analysis of the inverse problem of freezing and thawing of a binary solution during cryosurgical processes,» *Journal of biomechanical engineering,* vol. 117, n° 2, pp. 193-202, 1995.

[201] E. H. Wissler, «Pennes' 1948 paper revisited,» *Journal of Applied Physiology,* vol. 85 , n° 1, pp. 35-41, 1998.

[202] T. L. Horng, T. L. Horng, W. L. Lin, C. T. Liauh et T. C. Shih, «Effects of pulsatile blood flow in large vessels on thermal dose distribution during thermal therapy,» *Medical physics,* vol. 34, n° 4, pp. 1312-1320, 2007.

[203] Y. Rabin et A. Shitzer, «Exact solution to the one-dimensional inverse-Stefan problem in nonideal biological tissues,» *Journal of Heat Transfer,* vol. 117, n° 2, pp. 425-431, 1995.

[204] K. J. CHUA et S. K. CHOU, «On the study of the freeze–thaw thermal process of a biological system,» *Applied Thermal Engineering,* vol. 29, n° 17, pp. 3696-3709, 2009.

[205] H. S. Carslaw et J. C. Jaeger, Conduction of heat in solids, 2 éd., Oxford: Clarendon Press, 1959.

[206] Z. S. Deng et J. Liu, «Numerical simulation of selective freezing of target biological tissues following injection of solutions with specific thermal properties,» *Cryobiology,* vol. 50, n° 2, pp. 183-192, 2005.

[207] J. Okajima, A. Komiya et S. Maruyama, «24-gauge ultrafine cryoprobe with diameter of 550µm and its cooling performance,» *Cryobiology,* vol. 69, n° 3, pp. 411-418, 2014.

[208] S. Trabelsi, M. Hafid, S. Poncet, M. Lacroix et M. Poirier, «Rheology of Ethylene- and Propylene-Glycol Ice Slurries: Experiments and ANN Model,» *Soumis au International Journal of Refrigeration,* 2017.

[209] Marco Aurélio dos Santos Bernardes, Developments in Heat Transfer, Croatia: InTech, 2016.

[210] A. A. Gage et J. Baust, «Mechanisms of tissue injury in cryosurgery,» *Cryobiology,* vol. 37, n° 3, pp. 171-186, 1998.

[211] A. Zhang, L. X. Xu, G. A. Sandison et J. Zhang, «A microscale model for prediction of breast cancer cell damage during cryosurgery,» *Cryobiology,* vol. 47, n° 2, pp. 143-154, 2003.

[212] F. J. González, «Thermal simulation of breast tumors,» *Revista mexicana de física,* vol. 53, n° 4, pp. 323-326, 2007.